Bloom phenology, mechanisms and future change in the Southern Ocean.

Joan Llort

Thése de doctorat de l'Université Pierre et Marie Curie - Paris 6

École Doctorale des Sciences de l'Environment (ED129)

Laboratoire LOCEAN - IPSL, UMR 7159

Bloom phenology, mechanisms and future change in the Southern Ocean

---

Par:

Joan LLORT JORDI

dirigée par Marina Lévy et Julien LeSommer

Spécialité: Océanographie

Presentée et soutenue publiquement le 9 janvier 2015,
devant un jury composé de:

M. Stéphane Blain	LOMIC - UPMC	Président du jury
M. Laurent Mémery	LEMAR - IUEM	Rapporteur
M. Tom Trull	CSIRO - UTAS	Rapporteur
M. Hervé Claustre	LOV	Examinateur
M. Laurent Bopp	LSCE - IPSL	Invité
Mme. Marina Lévy	LOCEAN - IPSL	Co-directrice
M. Julien Lesommer	LGGE	Co-directeur

LOCEAN - IPSL
4, place Jussieu
75252 Paris Cedex 05
Boite courrier 100

UPMC
Ecole Doctorale de Sciences de l'Environment (ED129)
4 place Jussieu
75252 Paris Cedex 05

Résumé

La production primaire (PP) dans l'Océan Austral joue un rôle crucial dans la capacité des océans à absorber le carbon atmosphérique. Elle est caractérisée par une forte limitation en Fer et par un cycle saisonnier très marqué, présentant un bloom planctonique en fin d'hiver, plus ou moins intense selon les régions. Ma thèse est centrée sur la compréhension des mécanismes qui contrôlent ce bloom et sa variabilité, ainsi que sur les éléments, présents et futurs, qui contrôlent son intensité. J'ai abordé le premier aspect (phénologie et mécanismes) en mettant en place une approche mécaniste basée sur une nouvelle configuration du modèle biogéochimique PISCES forcé par un environnement physique 1D idéalisé. Cette méthodologie m'a permis de réconcilier les différentes théories sur la formation des blooms aux hautes-latitudes, d'identifier les spécificités du bloom de l'Océan Austral et de proposer des critères adaptés à sa détection dans les observations. En outre, les résultats de cette étude de modélisation ont été confrontés à ceux issues d'une deuxième approche, basée sur des observations satellitaires, ce qui a permis la localisation géographique des différentes phénologies de bloom que j'ai identifiées dans l'Océan Austral. Pour répondre au deuxième aspect (altération et changements futurs), j'ai également suivi une double approche. J'ai d'abord examiné comment les limitations par la lumière et par le fer se combinent, via la variabilité du cycle saisonnier du mélange vertical, et pilotent ainsi la production primaire dans l'Océan Austral actuel à l'aide de la configuration idéalisée présentée plus haut. Dans un deuxième temps, cette analyse a permis d'aider à l'interprétation des variations de PP observées dans les projections climatiques issues de 8 modèles couplés (CMIP5). L'ensemble de mes résultats permet de mieux comprendre les processus physiques et biologiques qui contrôlent la croissance du phytoplancton dans l'Océan Austral et d'appréhender comment la modification de ces processus peut entraîner des altérations de la PP dans une région clé pour l'évolution future du climat.

Abstract

Primary production (PP) in the Southern Ocean (SO) plays a crucial role on atmospheric carbon uptake. PP in this ocean is highly iron-limited and presents a marked seasonal cycle. Such a seasonal cycle has a strong productive phase in late winter, called bloom, which distribution and intensity is highly variable. My PhD focus on two specific aspects of the PP in the SO: first, the mechanisms that drive such a bloom and its dynamics and, second, the elements able to control the bloom intensity at present and in the future. The first aspect (bloom phenology and mechanisms) was addressed by setting up a mechanistic approach based on a novel model configuration: a complex biogeochemical model (PISCES) forced by a 1D idealised physical framework. This methodology allowed me to conciliate the different bloom formation theories and to identify the SO bloom specificities. Moreover, I proposed how to use different bloom detection criteria to properly identify bloom from observations. Such criteria were then tested in a complementary observation-based approach (with satellite and in-situ data) to characterise different bloom phenologies and its spatial distribution in the SO. The second aspect (bloom intensity and future change) was also addressed by a twofold approach. First, using the 1D model, I studied how seasonal variability of vertical mixing combine light and Fe limitation to drive PP. Secondly, I used such an analysis to interpret PP trends observed in 8 coupled model climatic projections (CMIP5 models). My PhD thesis results allow for a better understanding of the physical and biological processes controlling phytoplankton growth. My conclusions also suggest how an alteration of these processes by Climate Change may influence PP in the whole SO, a key region for future climate evolution.

Remerciements

Ce n'est pas évident de remercier à sa juste valeur toutes les personnes qui m'ont accompagné (dans le sens le plus large du terme) pendant ces derniers trois ans. Dans les deux pages qui suivent, je vais essayer de tous les nommer. Malgré mes efforts, si jamais j'en oublie certaines, j'espère qu'elles se sont déjà senti remerciés un moment ou un autre par mes mots ou mes actes.

Tout d'abord je voudrais remercier Tom Trull et Laurent Mémery pour avoir accepté d'être les rapporteurs de mon manuscrit. Ses commentaires et corrections ont été d'une pertinence et justesse difficilement égalables. Ils m'ont permis de voir mes travaux sous un angle complètement nouveau avec un regard critique sur mes contributions au domaine la biogéochimie marine dans l'Océan Austral. Également, je veux remercier ici Stéphane Blain, Laurent Bopp et Hervé Claustre pour sa participation à mon jury de thèse. Ce fut un énorme plaisir et un privilège d'avoir cinq chercheurs de ce niveau qui acceptent de consacrer une partie de son temps à lire, écouter et commenter mes travaux de thèse. Cette chance ne s'est pas limitée à la fin de la thèse, car Stéphane et Laurent ont aussi fait partie de mon comité de thèse. Je les remercie de ses conseils et avis qui ont fortement contribué à renforcer les différentes questions et approches que j'ai abordé pendant mes travaux.

Sans aucun doute, c'est à mes deux encadrants que je tiens aussi à remercier. Marina et Julien m'ont donné l'occasion de m'introduire au métier de la recherche en océanographie (un rêve de longue date) sous les meilleures conditions possibles. Grâce à cette codirection, j'ai eu la chance de pouvoir découvrir deux façons très différentes de faire de la recherche, ainsi comme d'assister à des discussions scientifiques que, même si souvent elles échappaient le cadre de mon travail, m'ont permis d'acquérir une culture scientifique et une vision très large des multiples facettes qui font partie du métier de chercheur. Outre que l'inestimable contribution de Marina et Julien, une bonne partie de mes travaux de thèse aurait été impossible de réaliser sans les conseils, contributions et disponibilité de Sakina Ayata, Carolina Dufour et Aurélie Albert. Sans oublier bien-sûr Christian Ethé qui est toujours là pour vous ramener (toi et ton code) sur le droit chemin.

Mais en plus de tout ça, Marina et Julien m'ont aussi offert la possibilité d'interagir et collaborer avec d'autres chercheurs excellents. Ces collaborations ont démarré très tôt: le premier jour de ma thèse je prenais l'avion vers La Réunion pour participer à la campagne KEOPS2. Ma participation à cette campagne fût possible grâce à Stéphane Blain et Bernard Quéguiner qui ont accepté mon embarquement mais surtout à l'équipe OISO-CARAUS, et tout particulièrement à Claire LoMonaco. Lors de mes 58 jours au bord du Marion Dufresne et sous des conditions souvent pas "confortables", Claire a eu la patience de me montrer les secrets de l'océanographie observationnelle et de me donner la possibilité d'apprécier (souvent à coût de manque de sommeil et fatigue accumulée) l'effort qui se cache derrière chacune des mesures en mer. La campagne

KEOPS2 m'a aussi permis de connaître un grand nombre de chercheurs/ses dont plusieurs ont joué un rôle très important tout au long de ma thèse. Merci beaucoup Francesco pour tes conseils, bonne humeur et ton insatiable curiosité qui nous rappelle toujours quelle est la raison essentielle pour laquelle existe la science.

Les travaux de thèse que je présente sur ce manuscrit ne seraient pas les mêmes sans les deux extraordinaires chercheurs avec qui j'ai le plus collaboré lors de ma thèse. Je suis très conscient de la chance que j'ai eu de travailler à côté d'Alessandro Tagliabue et Jean-Baptiste Sallée et je veux les remercier d'abord pour sa générosité à l'heure de partager et communiquer son expertise qui ont été essentielles pour atteindre la qualité de mes travaux.

Mais il n'y a pas que des collaborations professionnelles dans la recherche (heureusement!). Je vais être succinct et je vais remercier (par ordre d'apparition) les personnes qui ont contribué à que ma thèse (et mon adaptation à la vie française qui allait avec) fût une expérience humaine profondément enrichissante. Tout d'abord merci à Jordi Isern-Fontanet pour avoir su me donner son avis de la façon la plus juste possible au moment où j'ai pris une des décisions les plus importantes pour mon avenir. Un grand merci pour Cédric pour tous les moments partagés dans la petite cabine du Marion et pour avoir été un super hôte qui m'a très bien montré tous les secrets de la vie au LOCEAN (et ses annexes gastronomico-alcoholiques!!). Merci à Camille, Marie-Paule, Anne-Julie et tous les membres de KEOPS2 grâce à qui les deux mois enfermés au milieu de l'Austral ont été une magnifique et super amusante expérience. Merci à Tom et Andy pour inviter David Bowie à bord et m'offrir un des plus beaux instants de ma vie en écoutant *Young Americans* entouré d'albatros. Merci beaucoup à toute la famille Bopp qui m'a accueilli comme "l'oncle-qui-parle-bizarre" lors de mon séjour à CapeTown et tout particulièrement à Annette pour nos échappées aux bloques les plus dangereux de l'Afrique du Sud! Thanks a million for my favourite blues woman on Earth! Sarah Niiiiiiicholson, I didn't even knew it was possible to feel so close to somebody living 10,000 km away from my continent. To spend the time with you (either in Africa, Europe or Asia) is an extraordinary pleasant experience. Thanks again to you (and Luke!!) for your painful job on correcting this manuscript! Merci Marion, ma soeur de joies et déprimes! Je demande comment tu feras pour ne pas mourir de faim sans mes biscuits aux céréales et comment moi je ferai en soirée sans mon amie riche qui m'invite à des gin-toniques... Merci bien à Véra et Johanna pour être des superbes copines de froid et obscurité dans le bureau 443 et pour avoir contribué à créer la meilleure table à thé jamais vue à LOCEAN! Karine, Sara(h)s, Laurène, Casimir, Jérôme, Pedro, Anthony, Lolo, Martin (et Lisa!), Clément, Maite, Olga, Julie, Hugo... je n'ai pas la place pour chacun d'entre vous mais vous savez que je vous aime trop et que la seule raison pour laquelle je ne voulais pas finir ma thèse c'était pour avoir toujours une excuse pour continuer à faire les plus belles soirées avec vous tous! Ça me paraît vraiment improbable que plus jamais j'arrive à trouver un groupe de gens si variés, drôles, intelligents et intensément vitales comme vous. Merci, merci, merci!! Et bien-sûr merci à notre famille adoptive en France: Guillaume, Marie, Marianne, Lucien, Cédric et Delphine! Vous avez

été les premiers à nous accueillir et à nous montrer les secrets de la vie 'à la française' (même sans fromage!) et vous nous accompagnez dans chacune des étapes de ce séjour qu'on n'arrive pas vraiment à clôturer. Merci à Paris aussi pour ses rares moments de joie extrême que cette ville sait si bien cacher derrière la grisaille, le froid et les fin de mois difficiles...

Faire la thèse en France a malgré tout des conséquences moins agréables. Depuis plus de 5 ans (et ça continue...) j'ai dû apprendre à vivre avec mes autres deux familles sous un autre ciel. Je veux remercier ma famille naturelle pour nous avoir soutenu lors de nos projets malgré qu'ils se déroulent bien loin de chez nous. Je veux également remercier mes amis de Tarragone, ma deuxième famille, celle qui n'arrête pas de croitre ces derniers temps! Merci pour nous rendre visite si souvent et pour avoir continué à nous traiter exactement pareil que comme quand on est parti.

Finalement, je veux remercier Ari sans qui j'aurais même pas osé démarrer toute cette aventure et avec qui, n'importe quelle autre aventure à venir, devient une excuse pour continuer partager ma vie avec toi.

Contents

Introduction

High latitude ecosystems evolve in environments characterised by a contrasted seasonal cycle. During the dark and cold winters, populations of photosynthetic organisms (or primary producers) remain low. After the winter solstice[1], days get longer, more solar radiation reaches the surface and temperatures start to rise. Terrestrial primary producers respond to these changes with a rapid increase in biomass accumulation led by an increase in cell division rates (Behrenfeld [2010]). Such a sudden increase often culminates with large and striking flowering events, known as *blooms*. For ocean primary producers (i.e., phytoplankton), things are not so simple.

In the ocean, blooms are large and rapid seasonal accumulations of phytoplankton organisms which are usually observed in early spring in higher latitudes. Blooms result in the ocean surface waters to become greener in colour, this property makes them easily visible and measurable by satellite. The importance of phytoplankton for ocean ecosystems and the intense nature of blooms, have made high-latitude blooms a subject of study for decades. One of the first documented scientific works addressing this question was published in 1926 (Bigelow [1926]) and since then, hundreds of publications have followed. The debate on the spring bloom has recently regained a lot of attention (Behrenfeld [2010], Chiswell [2011], Mahadevan et al. [2012], Taylor and Ferrari [2011]), in particular due to the increased availability of combined, high-resolution (in space and time) observations of phytoplankton and of their physical environment. Most of these publications (and especially the most influencing ones) have been based in the North-Atlantic, and a few other focused on the rest of high-latitude regions, such as the North Pacific and the Southern Ocean.

Despite these numerous studies, mechanisms underpinning bloom dynamics[2] are still under much debate. The bloom initiation is the cornerstone of this debate but the drivers of biomass accumulation, the vertical structure of the plankton ecosystem or the carbon export during the bloom; are some of the questions still waiting to be answered.

For the case of the Southern Ocean, an additional source of uncertainty comes into play: iron. This element is an essential micro-nutrient for phytoplankton growth. The scarcity of iron sources

[1] 21st of December in the Northern Hemisphere and 21st of July in the Southern Hemisphere

[2] Hereinafter, we will refer to "bloom dynamics" as the ensemble of physical and biological processes that take place during a bloom. The complex combination of these processes defines the bloom "shape" or bloom phenology.

in the majority of the Southern Ocean and the very specific ocean chemistry of this element, result in this oceanic region to be strongly iron limited (Martin et al. [1990]). Furthermore, the fact that Fe-reservoirs are found at deeper depth than other limiting macro-nutrients (such as nitrate or phosphate; Tagliabue et al. [2011]) stresses the importance of deep mixing for Southern Ocean bloom dynamics.

The magnitude and timing of blooms have important consequences on high-latitude ecosystems as phytoplankton constitute the first trophic level in the ocean and many grazers and carnivores depend on them (Longhurst [2007]). Moreover, high-latitude primary production plays a significant role in the global carbon cycle through its capacity to export atmospheric carbon to deep ocean layers (the so-called *biological pump*). Hence, high-latitudes blooms have an influence on Climate which, in turn, is likely to alter the environments where these blooms take place.

The general objective of the study presented in this manuscript is to understand the drivers of phytoplankton blooms in the Southern Ocean and to assess how they could be affected by climate change. This is all the more crucial as climate projections for the next century predict strong modifications of the physical environment in Southern Ocean.

General context

Chapter 1

General Context

In this introductory chapter, I will present the general context over which this study was founded. First, I will present a brief review on high-latitude blooms. Second, in section 1.2 I will present the Southern Ocean features which are likely to influence bloom dynamics at present and in the future. This will bring me to the presentation of the specific objectives of my PhD works and to detail the structure of this manuscript.

1.1 High-latitude bloom theories

The strong seasonality of primary production in the Southern Ocean is characteristic of high-latitude oceans. This seasonal cycle is characterised by a sudden increase in the population of phytoplankton (which surface imprint is usually observed in late winter, early spring), called *phytoplankton bloom* or simply, *bloom*.

Blooms are typical of high-latitude ocean regions and they have been widely studied, with special emphasis in the North-Atlantic (NA). One of the first (and inspiring) studies about NA blooms was made by Sverdrup in 1953. In it, Sverdrup proposed that blooms initiate in spring when the mixed layer (i.e., the upper-ocean layer which hydrographical properties -T and S- are homogeneously mixed) reaches a 'critical depth' at which integrated production overcomes the integrated losses associated with respiration and mortality (figure 1.1 a). The fundamental concepts in Sverdrup's hypothesis (usually referred to as the *Critical depth hypothesis*) were based on previous studies by Gran and Braarud [1935] and Riley [1942], but Sverdrup elaborated an apparently easy-testable and quantitative criteria that strongly appealed the oceanographic community. In his theory, seasonality of the mixed layer depth (MLD) has a major role on bloom initiation (figure 1.1.a[1]).

[1]Caption of figure 1.1: *Comparison of bloom hypotheses: (a) the critical depth hypothesis (CDH), (b) the critical turbulence hypothesis (CTH), and (c) the disturbance-recovery hypothesis (DRH). The seasonal cycle in each plot*

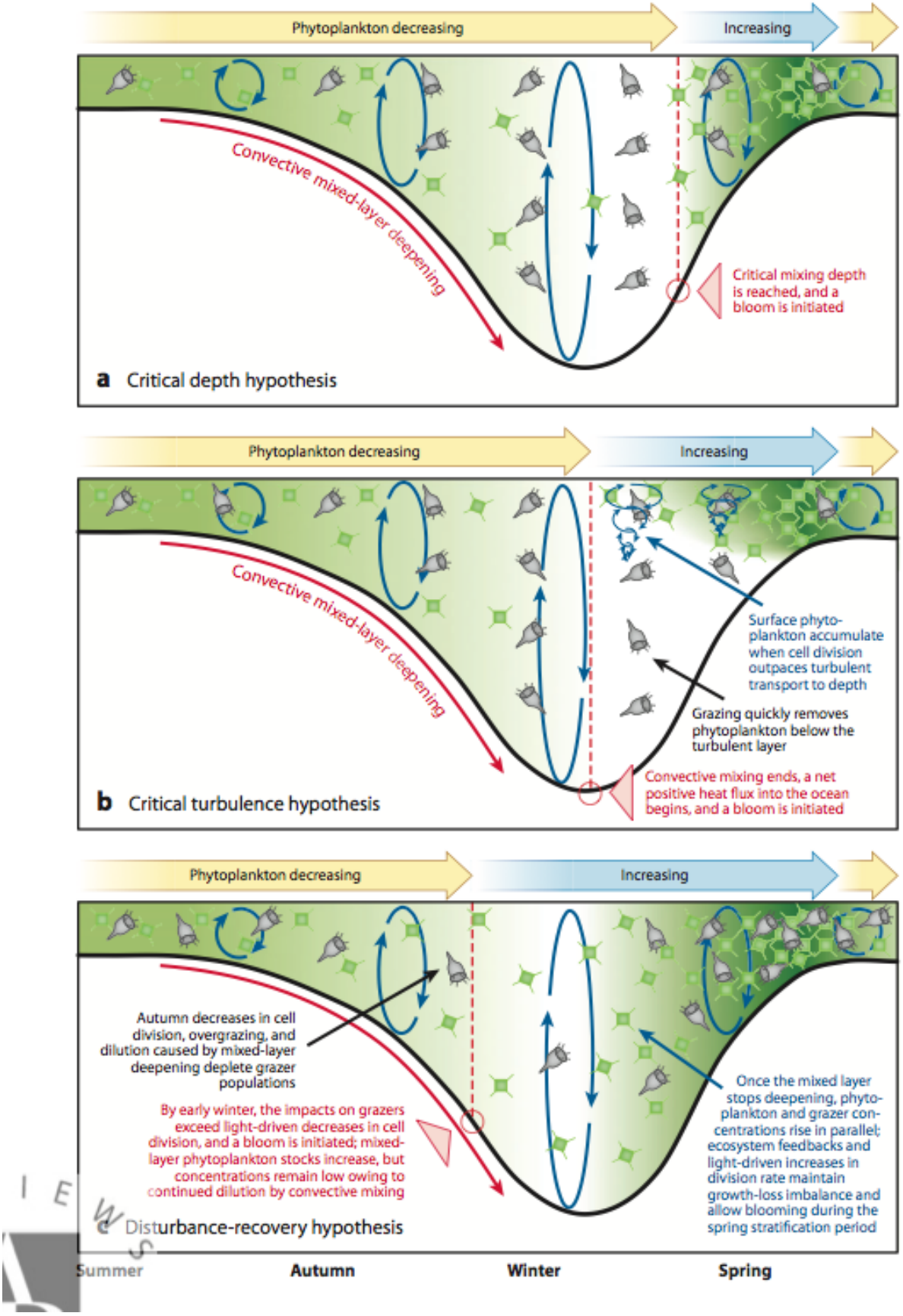

FIGURE 1.1: See footnote in next page

Since the *Critical depth hypothesis* was published sixty years ago, a number of works have adapted Sverdrup bloom's conceptual model to experimental data in different high-latitude regions (Nelson and Smith [1991]; Obata et al. [1996]; Siegel [2002]). At the same time, some others have documented cases where a bloom developed in absence of stratified waters (Townsend et al. [1992]; Dale et al. [1999]). Such apparently controversial results motivated some authors to propose a refinement of Sverdrup's theory regarding the use of a "mixing depth" rather than a mixed-layer depth: the *Critical tubulence hypothesis* (Brainerd and Gregg [1995]; Chiswell [2011]; Taylor and Ferrari [2011]). According to these authors, surface blooms appear when vertical turbulence weakens (in late winter, due to weaker winds and net positive heat fluxes) creating stratified upper layers that maintain phytoplankton close to the enlightened zone (i.e., the euphotic layer) of the water-column (figure 1.1.b).

Both the critical depth and the critical turbulence hypotheses emphasised a 'bottom up' control (i.e., by light and nutrients) of phytoplankton population. An alternative 'top down' view of phytoplankton bloom dynamics (based on the ideas of Cushing [1962]) has also gained prominence in recent years (Banse [1992]; Behrenfeld [2010], Behrenfeld et al. [2013a]). This view suggests that initiation of blooms is due to subtle imbalances in predator–prey relationships that occur over winter (due to deep mixed layer dilution of populations; figure 1.1.c). The bloom theories review by Behrenfeld and Boss [2014] called this 'top-down' view as the *Disturbance – Recovery Hypothesis* (hereinafter DRH) and sustained it by experimental and model data. When assuming DRH, bloom onset are always found in winter, much earlier than onset predicted by Sverdrup's based theories.

In this work, high-latitude phytoplankton blooms were studied not in the North-Atlantic but in Southern Ocean waters. Except for the fact that both regions are situated at similar latitudes (thus, both receive a similar solar radiation throughout the year), these two oceanic regions present many more differences than similarities. At first (satellite) sight, one of the most striking differences, is that bloom variability (in space, timing and magnitude) is much higher in the Southern Ocean. For instance, while in the North-Atlantic spring surface bloom emergence is apparently propagated from south to north in a quasi-zonal pattern (figure 1.2 (a); Siegel [2002] and Henson et al. [2009]), remote-sensing observations in the Southern Ocean reveal strong asymmetries and latitudinal variations (figure 1.2 (b); Thomalla et al. [2011]).

With the aim to understand the whole dynamics (i.e., at surface and at depth) behind Southern Ocean blooms, our approach was based on two assumptions: first, we assumed that North-Atlantic and Southern Ocean blooms were driven by the same fundamental mechanisms; second, we assumed that the strong bloom variability observed in the Southern Ocean was due to the specificities that differentiate this ocean from the North-Atlantic. In the next section, I will

begins with summer on the left. Thick black lines indicate mixed-layer depth (MLD). From Behrenfeld and Boss [2014]

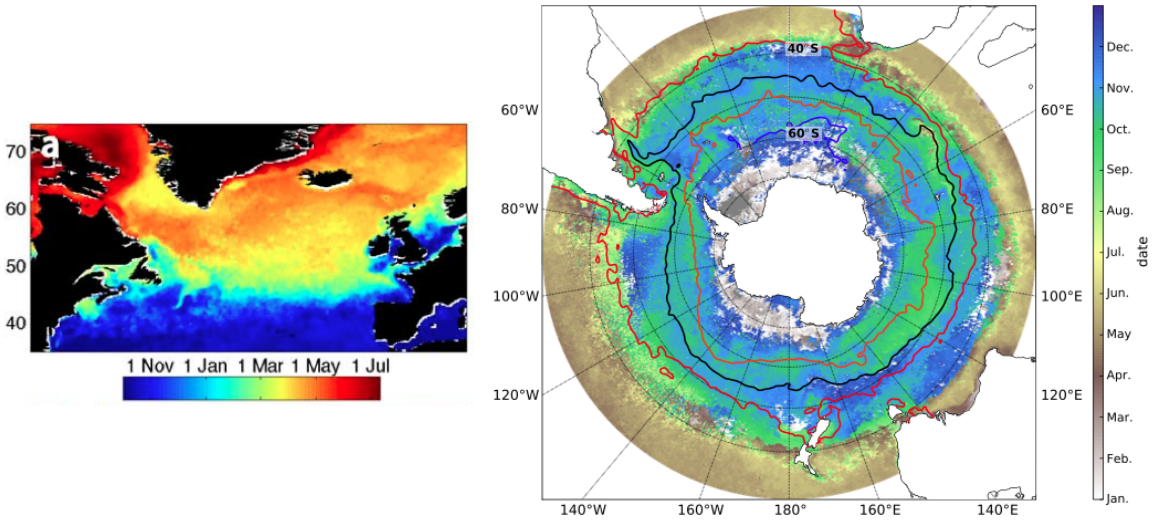

FIGURE 1.2: Left: *Mean (1998–2004) start date of the phytoplankton bloom estimated from SeaWiFS chlorophyll data in the North-Atlantic.* From Henson et al. [2009]. Right: *Date of the phytoplankton bloom initiation in the Southern Ocean south of 30°S. Mean (1998-2007) frontal positions contours shown for the STF (red), the SAF (black), the PF (orange) and the SACCF (blue).* From Thomalla et al. [2011].

resume some of these Southern Ocean specificities, especially those likely to influence bloom dynamics at the present and in the future.

1.2 The Southern Ocean

General circulation and frontal dynamics

The Southern Ocean is the only ocean in the world free of latitudinal boundaries. It forms a 21,000km perimeter circumference around the Antarctic continent (i.e., annular) which surface represents the 20% of global ocean surface. Besides this particular geography, powerful and persistent westerly winds drive the Antarctic Circumpolar Current (ACC), a strong and voluminous current that flows from west to east enclosing the Antarctic continent (figure 1.3a).

On the northern edge of the ACC, subtropical gyres flow counterclockwise, and their intense and energetic western boundary currents join the northern branches of the ACC in the western Atlantic, Indian, and Pacific basins (figure 1.3a). The ACC and the western boundary currents have a profound influence on the physical and geochemical characteristics of the Southern Ocean (Rintoul et al. [2010]). They form meridional dynamical barriers (Sallée et al. [2008]) that receive the name of fronts, and divide the Southern Ocean into four annular regions (figure 1.3b). These zones are, from north to south:

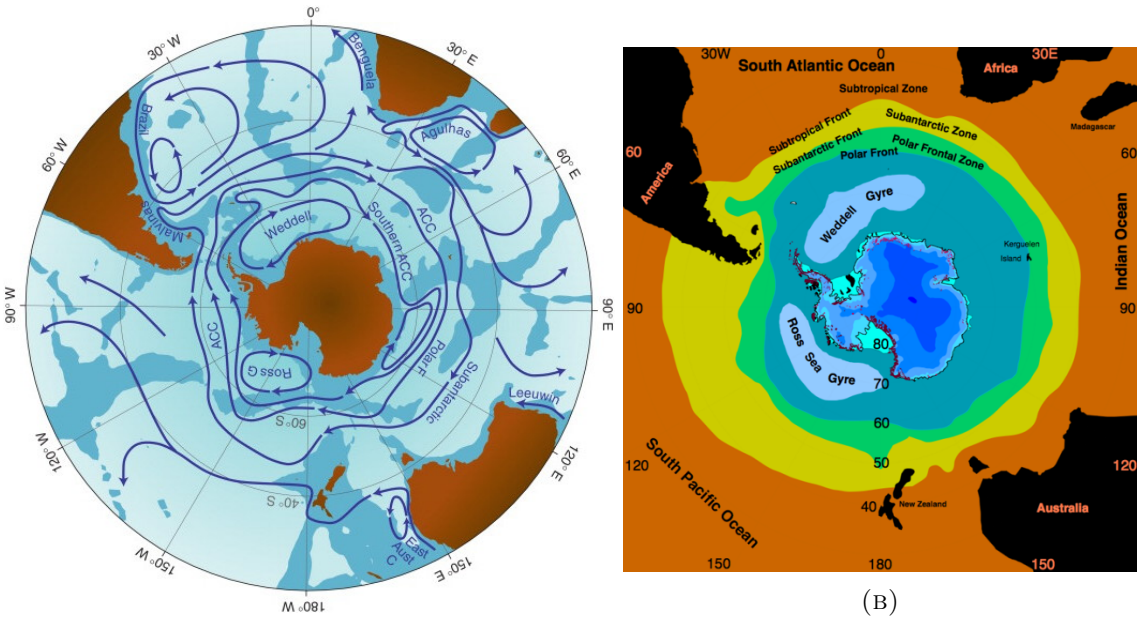

(A) (B)

FIGURE 1.3: Left: *A schematic view of the major ocean currents of the Southern Hemisphere oceans south of 201°S. Depths shallower than 3500m are shaded. C, current; G, gyre; F, front; ACC, Antarctic Circumpolar Current.* From [Rintoul, 2009]. Right: A schematic view of the ocean frontal system in the Southern Ocean. From H.Grobe, Alfred Wegener Institute.

- The subtropical zone, around 30°S, characterized by stratified surface layers, and relatively weak wind and buoyancy forcing; delimited at south for the sub-tropical front.
- The sub-Antarctic zone, directly north of the ACC, which is characterized by very deep mixed-layers, intense winds, large buoyancy forcing, and the presence of the energetic western boundary currents.
- The ACC (or Polar Frontal) zone, characterized by the top-to-bottom and large circumpolar current.
- The subpolar zone, south of the Polar Front, characterized by the seasonal presence of sea-ice, and a relatively stratified surface layer.

In addition to this upper-ocean circulation, the density gradient associated to ACC together with the influence of strong heat and freshwater fluxes provides a low-resistance pathway from the deep ocean to the surface (upwelling). The combination of both horizontal and vertical water displacements creates a complex circulation in the Southern Ocean that has an important implication for the global ocean circulation. At Weddell Sea, the low buoyancy of the surface waters masses and the bathymetric slope create the appropriate conditions for deep water formation. This surface to bottom transport constitutes the southern limb of the Meridional Overturning Circulation (MOC).

Mixed layer and seasonal variability

In the Southern Ocean, the MLD presents a large spatial variability with some regions where the seasonal cycle is highly marked. Summer MLDs reach about 100m in the vicinity of the ACC. Winter cooling destabilises the water column and increases the MLD. The deepest winter mixed layers (and largest seasonal cycles) are found north of the Antarctic Circumpolar Current, particularly in the eastern Indian and Pacific Oceans. The loss on buoyancy during autumn and winter gradually deepens the mixed layer between January and September. Warming during spring and early summer rapidly re-establishes the shallow summer mixed layer. The amplitude of the seasonal cycle exceeds 400 m in some locations north of the ACC (figure 1.4).

The intra-seasonal and interannual variability of MLD about this large seasonal cycle is substantial, with values exceeding several hundred meters and a standard deviation for the whole Southern Ocean (35–65°S) of 20 m in summer and 60 m in winter.

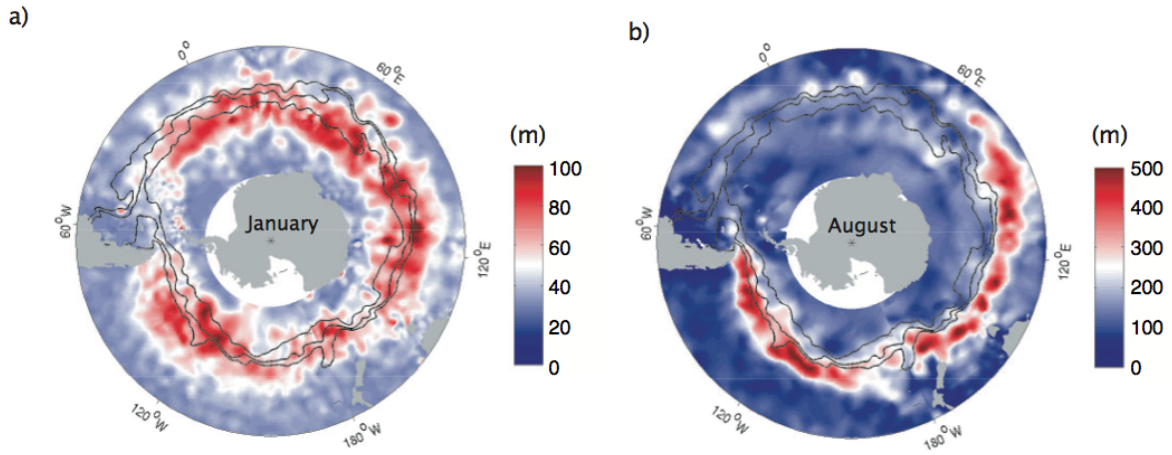

FIGURE 1.4: *Seasonal cycle of mixed-layer depth. (a) Summer (January) and (b) winter (August) mean depth of the Southern Ocean mixed layer.* From Sallée et al. [2008].

This estimation of the MLD seasonal cycle and spatial distribution in the Southern Ocean has been extracted from Sallée et al. [2008]. In their work, mixed layer was estimated using temperature and salinity measurements of the water-column acquired by autonomous floats (Argo floats). MLD was extracted from these measurements using a density criterion of $\Delta\rho \leq 0.03\ kg/m^3$. Such a criterion has been shown to be the most appropriate for Southern Ocean characteristics (Dong et al. [2008], Sallée et al. [2006]) and allows to quantify the upper-ocean layer where the effect of mixing has homogenised the water column. The MLD is a useful concept to address the state of the water-column physical properties however, as shown by Huisman et al. [1999], Chiswell [2011] or Taylor and Ferrari [2011], the MLD fails to correctly represent the processes that control phytoplankton vertical distribution. To overcome this issue, a new concept, the mixing layer depth, has appeared in recent years in the oceanographic community. The concept of mixing layer depth (which will recurrently appear throughout this manuscript) refers to the upper ocean layer that

is actively mixed due to strong turbulence. This magnitude (with m^2/s units) is a quantification of the small scale vertical motions that drive phytoplankton inside the water-column. The mixing layer depth is much more sensitive to changes in air-sea fluxes (Taylor and Ferrari [2011]) than the MLD. In consequence, seasonal evolution of the mixing depth is strongly perturbed by short intra-seasonal events and can be decoupled from the MLD seasonal cycle (especially in early spring). An important part of the debate on the *Critical depth hypothesis* comes (as recently proposed by Franks [2014] in an excellent work exclusively consecrated to this topic) from the ambiguity of Sverdup's words and a posterior misinterpretation of his main assumptions. In words of Franks [2014], *Sverdrup (1953) wrote about a "mixed layer", though he was clearly referring to a "turbulent layer", the waters that are kept in motion through turbulence.*(...)

Primary production and iron

Annual primary production in the Southern Ocean is generally low with a strong seasonal cycle amplitude (60 mgC/m2/d in August -winter- to 400 mgC/m2/d in December -summer- (Moore and Abbott [2000], Arrigo et al. [2008]) in phase with MLD seasonal cycle (Sallée et al. [2010a]). The coupling between MLD and primary production suggests an important role of light limitation and nutrient resupply that influence phytoplankton growth. However, with exception of subtropical latitudes (30° to 40°), main phytoplankton nutrients concentrations (i.e., N and P) in the surface layer of the Southern Ocean are significantly above common nutrient limiting concentrations, even during winter (Sarmiento and Gruber [2006]). This apparent paradox states the Southern Ocean as the vastest High-Nutrient Low-Chlorophyll (HNLC) region of global ocean. This paradox was resolved by Martin et al. [1990] who demonstrated that phytoplankton in HNLC regions is limited by iron (Fe)[2].

Primary production in the Southern Ocean presents a large-scale spatial variability (figure 1.5, where sChl is used as a "proxy" for primary production). The highest summer values of surface Chl concentration are mainly observed in the sub-tropical zone where iron is horizontally advected from continental platforms or supplied from terrestrial dust deposition. High values are also observed downwards sub-antarctic islands (p.e., islands in the Atlantic sector) and over regions of shallow bathymetry (p.e., Kerguelen Plateau at 50°S-80°E). In these regions, currents interact with bathymetry resupplying surface layers with iron (Blain et al. [2007], Borrione and Schlitzer [2013]). A third system where high Chl is measured in summer is the marginal ice zone, close to the Antarctic coasts (Arrigo and van Dijken, 2004). Another characteristic of the Chl patterns observed in figure 1.5 is the apparent interaction of Chl with frontal dynamics. These interactions have been associated with mesoscale activities able to maintain a nutrient flux towards surface waters (Moore and Abbott [2002]). Other authors suggested that fronts may create dynamical

[2]Fe essential micro-nutrient for photosynthetic organisms such as phytoplankton.

branches and filaments that shape different waters of elevated chlorophyll (Sokolov and Rintoul [2007]).

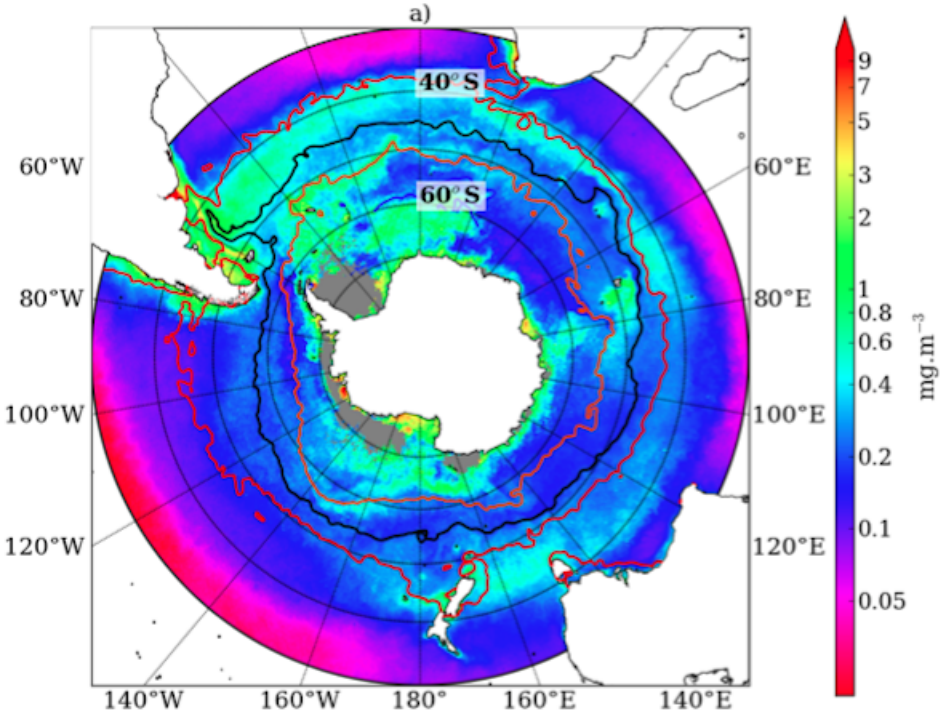

FIGURE 1.5: *Spatial distribution of mean chlorophyll concentrations for the Southern Ocean south of 30°S for summer–January. Mean January (1998–2007) frontal positions calculated from MADT contours are shown for the STF (red), the SAF (black), the PF (orange) and the SACCF (blue).* From Thomalla et al. [2011]

Far from coasts and the Antarctic continent (i.e., in the so-called Permanent Open Ocean Zone or POOZ), upper layers iron supply is mainly driven by the coupling between the depth of winter mixing and the depth of the iron stock: the ferricline. Dissolved iron is affected by specific biochemical processes (p.e., scavenging) that reduce iron availability in upper layers and shift ferricline to very deep layers, usually deeper than nutricline and average winter mixing depths (figure 1.6).

The ensemble of these elements seems to suggest that, even if it is well known that phytoplankton blooms result from an interaction of multiple bottom-up (light, upper ocean layers mixing, iron supply) and top-down (grazers, virus) controls (Boyd et al. [2012b]; Banse [1992]), is still poorly understood which of these processes drive bloom dynamics in the Southern Ocean. Moreover, the physical environment where these blooms develop is likely to be significantly altered by Climate Change. In next section, we will sketch the current knowledge on the influence of Climate Change over the Southern Ocean physical dynamics.

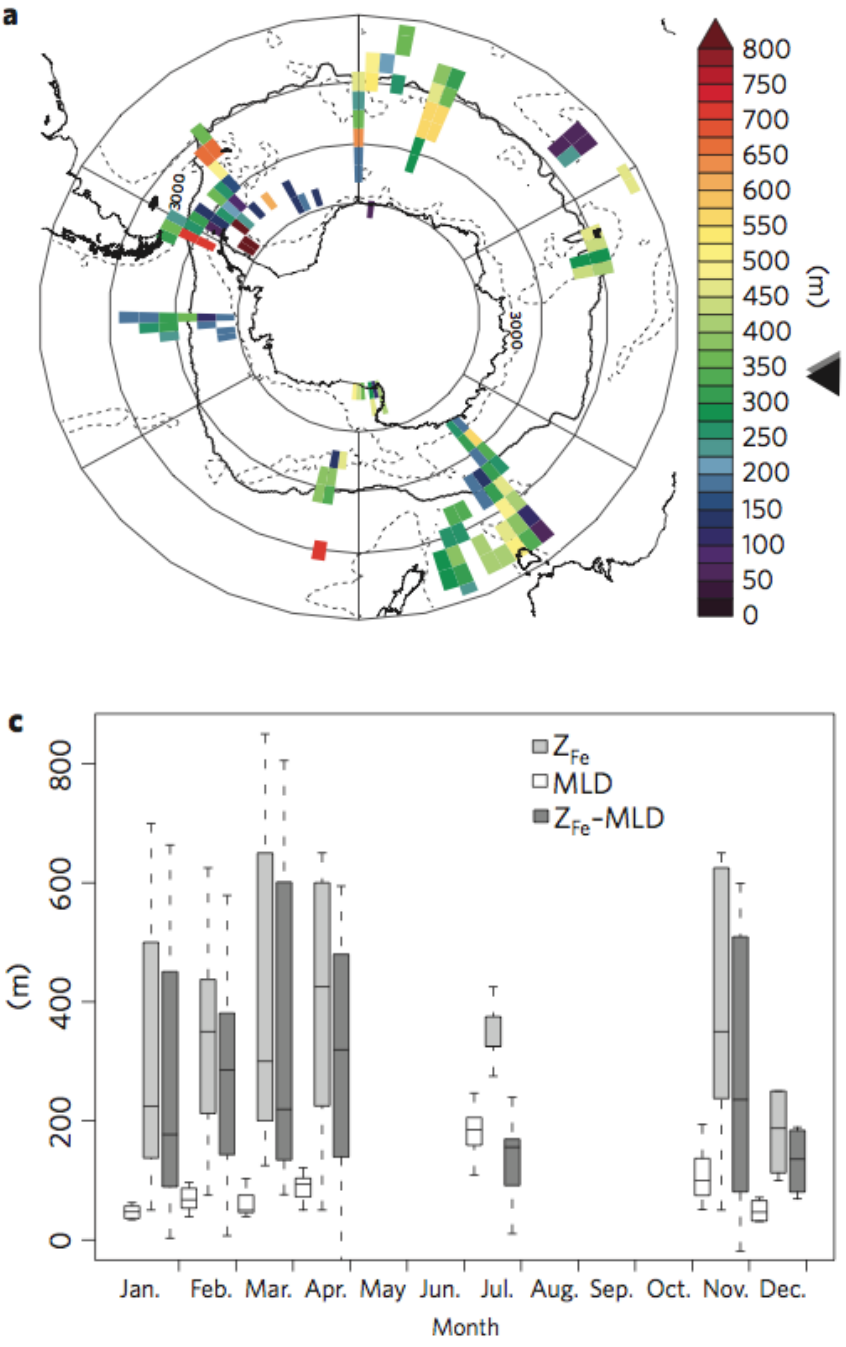

FIGURE 1.6: *Depths of the ferricline and its seasonal evolution. TOP: The depth of the ferricline (m), black and grey triangles denote the mean and median, respectively. The 3,000 m isobath and the mean Polar Front position (black line) are also shown. BOTTOM: Box and whisker plots of the seasonal cycle in MLD, ZFe and ZFe-MLD (the size of the box represents the quartiles 1–3, with the vertical bar corresponding to the median and the whiskers representing 1.5 times the inter-quartile range).* From **?**

Impacts of Climate Change in the Southern Ocean

The upwelling, surface transformation and subsequent subduction of large volumes of water in the Southern Ocean play a crucial role on global climate due to its implications for carbon cycle and transport of nutrients at the global scale (Heinze [2002], Sarmiento et al. [2004]). Thus, any alteration on the physical drivers (i.e., surface wind, heat fluxes, ice melting) of Southern Ocean circulation is likely to have strong climatic implications (Lenton and Matear [2007], Le Quéré et al. [2007]). Amongst these drivers the principal mode of variability of the atmospheric circulation in the Southern Hemisphere, the Southern Annular Mode (or SAM), plays a major role. The SAM presents an annular distribution around the Antarctic continent with low atmospheric pressures centred over the continent and a ring of high pressures surrounding the continent. The difference between the atmospheric pressure (or the geopotential height) over the Antarctic continent and at a lower latitude allows to define the SAM index. During a positive phase of SAM, pressures over Antarctica are "anomaly" low and, on the contrary, pressures at lower latitudes are "anomaly" high. SAM index has been measured since 1955 but, during the last two decades a clear persistence on the SAM positive phase has been observed. Such persistent positive trend (which seems related to natural and anthropic forcing; Cai et al. [2005], Lenton and Matear [2007]) causes the strengthen and poleward shift of surface winds that drive Southern Ocean circulation. Moreover, such an alteration on wind regimes has a significant impact on the physics (sea surface temperature, sea-ice, eddy activity; Sen Gupta et al. [2009]; Dufour et al. [2013]) and biogeochemistry (Lovenduski and Gruber [2005]) and, consequently, on the carbon cycle (Le Quéré et al. [2007], Lenton and Matear [2007]).

Addressing how the climate - Southern Ocean relationship will evolve in future decades is however a tough question to face. Both systems dynamics emerge from the combination of complex mechanisms involving physical circulation and thermodynamics of the ocean and atmosphere (and cryosphere), complex biogeochemical cycles (i.e., iron dynamics, phytoplankton diversity, virus...) and uncertain future trends of human activities influencing greenhouse effect gases concentration. Meijers [2014] states this problematic and a strategic solution in a clear way:

> (...) Although much progress has been made in recent years towards understanding the interplay of these factors through vastly increased numbers of high-quality observations and concerted modelling efforts, the response of the system to projected anthropogenic climate forcing still has a great deal of uncertainty. One way of addressing this uncertainty is through the use of large numbers of climate models and looking for robust trends to emerge across the ensemble.

Climate models, or Earth System Models (ESM), aim to simulate all these processes able to influence on global climate creating a sort of "virtual" planet. To do so, models representing

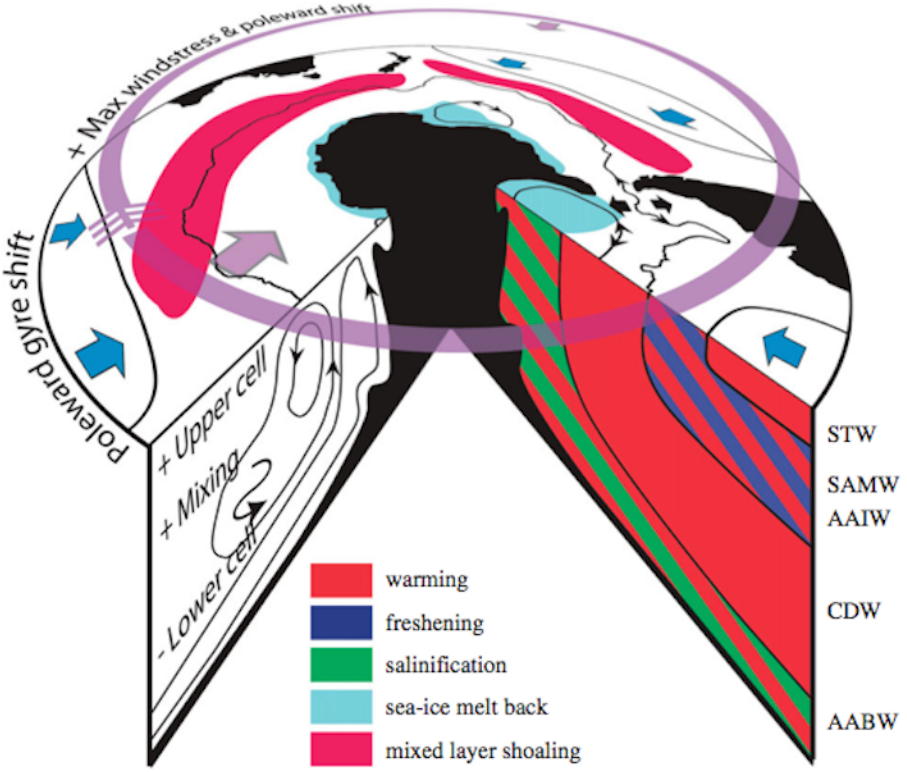

FIGURE 1.7: *Schematic showing the impact of climate forcing in CMIP5 models in the Southern Ocean by the end of the twenty- first century. See text for more details. Arrows in both directions for the ACC and subpolar gyres indicate significant changes in transport of both signs within the model ensemble.* From Meijers [2014]

the ocean, the atmosphere, the emerged lands, the cryosphere, etc. are coupled all together to allow feedback and realistic projections. Currently, there exists an international effort[3] to create a consistent and coherent ensemble of ESMs: the Coupled Model Intercomparison Project (CMIP5; Taylor et al. [2012] and http://cmip-pcmdi.llnl.gov/).

In this PhD, we used some of the CMIP5 model outputs to address the future trend on primary production in the Southern Ocean (see chapter 6). Here, we will briefly expose the main CMIP5's projected changes over the physical components of the Southern Ocean as they have been resumed in Meijers [2014].

Under future forcing, all models show a poleward shift in the westerly wind stress maxima and a general increase in westerly strength, characteristic of a more positive SAM (figure 1.7). The subtropical gyres have a coherent poleward shift in response to climate forcing. Moreover, most of the models also present a warming of the whole water column and shallower MLD. However, these two trends seem to be affected by a generalised MLD bias amongst most of the models (Sallée et al. [2013]).

[3]This international modelling effort is coordinated and leaded by the International Panel on Climate Change (IPCC; http://www.ipcc.ch/)

1.3 Specific objectives and structure

The main aim of my works was to investigate **the mechanisms that control primary production in the Southern Ocean.** I addressed this question from a mechanistic and from an integrated point of view.

The mechanistic point of view focused on the seasonal scale to answer two specific questions:

- What are the mechanisms driving phytoplankton bloom dynamics in the Southern Ocean?
- How do these mechanisms combine to produce the bloom diversity observed in the Southern Ocean?

The integrated point of view focused on the net effect of the environment over annual primary production. From this alternative point of view I addressed a third specific question:

- How is Southern Ocean primary production likely to be influenced by an altered environment due to Climate Change?

This manuscript is structured in four parts and seven chapters.

The beam of complementary approaches used to answer each of the precedent questions will be presented in the second part of this manuscript. In chapter 2, I will present the ensemble of observational data I used. As will be presented, I have been exploiting multiple sources of observation data, both for model set-up/validation and for the study of the Southern Ocean bloom variability. However, my engagement with observational approaches went beyond the simple exploitation: I was lucky to contribute to the acquisition and pre-treatment of carbon cycle related variables during a 2-month collaboration at OISO-KEOPS2 sea survey. This experimental work led to the publication of the scientific paper presented in Appendice A.

In the second chapter dedicated to methodology, chapter 3, I will details the three types of modelling tools I manipulated: CMIP5 *coupled*[4] models, Southern Ocean *forced* configurations and a novel water-column (i.e., 1D) biogeochemical configuration.

The third part of this manuscript is constituted of three chapters. Each of them aimed to answer one of the specific question presented above.

In chapter 4, I addressed the mechanisms that drive bloom dynamics using a novel 1D configuration. This model configuration consisted in a very simple physical seasonal cycle created to force a biogeochemical complex model. Relationships between physical environment and bloom

[4]Here we refer to coupled models when both ocean and atmosphere dynamics are computed. On the contrary, in *forced* models, the atmosphere is pre-scribed and used as forcing to simulate ocean dynamics.

dynamics were statistically established thanks to an ensemble of 1,200 modelled blooms issued from the 1D configuration. Thanks to this strategy we identified 3 important bloom phases and we concluded which factors (physical and biological) control each bloom phase. Our methodology allowed us to test and contrast different bloom theories and bloom detection methods. Interestingly, we concluded that any of them were completely wrong or completely right and that an important part of the debate was due to vague definitions of certain concepts. This study was synthesised as a scientific article (included in the chapter) that we submitted (currently reviewed with minor revisions) to *Journal of Marine Science* for the *Sixty years since Sverdrup's critical depth hypothesis* special issue.

We then used results and conclusions from bloom dynamics study as starting point to understand how bloom mechanisms combine to create the diversity of bloom phenology observed in the Southern Ocean. Using both observations and a biogeochemical forced model, we addressed the diversity of phytoplankton seasonal cycles (i.e., bloom phenology) observed in the Southern Ocean as well as the drivers which sustain such diversity. The observational-based part of this work will be presented in the first half of chapter 5 in the form of a scientific article, which I co-authored with J.B.Sallée, and that we also submitted to JMS special issue. The second part of chapter 5 constitutes a model-based approach equivalent to the observations-based study. We applied the same methodology as for observations to a biogeochemical forced model of the Southern Ocean. The richness of model data has allowed us to contrast conclusions issued from observations and to estimate at which degree such conclusions depended on the methodology. Furthermore, the regional 3D model supplies a much realistic representation of the relationship between phytoplankton vertical distribution and the mixed layer depth, questioning some assumptions widely applied when using observation and proposing new directions to potential observational programs in the Southern Ocean.

In chapter 6, a wider look is adopted with the aim to explore how the drivers of primary production in the Southern Ocean are likely to be influenced by the Climate Change. To do so, we compared the drivers of primary production at annual scale (identified with the idealised 1D model configuration) to long-term trends projected by an ensemble of Earth System models (ESMs) under Climate Change influence. On one hand, outputs from the ESMs allow to identify potential drivers of change (or stressors) that merit to be monitored. On the other hand, the idealised model allow to quantify the isolated impact of some of these stressors in the current and future Southern Ocean. Combining both approaches allowed us to speculate which stressors may influence future primary production in the Southern Ocean. Moreover, it allowed us to identify possible bias on the averaged signal of climate projections and to point out some model weaknesses able to cause such bias. This study (carried out in collaboration with L. Bopp) is currently being prepared to be submitted as a scientific paper to *Biogeosciences*.

The last chapter of this manuscript, chapter 6.5, constitutes a general summary of the ensemble of conclusions and a compilation of research perspectives identified from our works.

Methods

Chapter 2

Observations

2.1 Introduction

Study of Southern Ocean has been historically constrained by a lack of observations. This data deficiency was due to intrinsic features of the Southern Ocean: isolation and rough sea conditions which hinder navigation and scientific research surveys, sea-ice winter coverage at high-latitudes (southwards 65°S, on average) and vast dimensions. The lack of good ocean biogeochemistry data is even more severe. This is due to the necessity of special methods and instruments to sample iron (the main limiting nutrient in the Southern Ocean; Martin et al. [1990]) and to the existence of specific phytoplankton species (Boyd et al. [2010]; Johnson et al. [2013]).

In the lasts decades, a renewed interest on understanding the Southern Ocean together with new remote and autonomous sampling technologies have enormously increased available observations. Interestingly, the introduction of new sampling techniques have not substituted, but complemented older or more "traditional" techniques. It is very often necessary to use a specific source of data to resolve a specific question.

In this chapter, I will present the sources of observational data and how they were used in this manuscript. The ensemble of these different data sources has been grouped in three types to structure this chapter: *in-situ* and regionally specific data, remotely sensed data and Argo floats data. The first group, detailed in section 2.2, contains *in-situ* observational data obtained by three different research programs all of them occurring around (and above) the Kerguelen Plateau: KERFIX station program, KEOPS project and autonomous data from elephant seals mounted sensors. These three research programs provide "high-quality"[1] data sets all through the water column for some very specific domains. The reliability and vertical coverage of these data sets made them appropriate to be used as "reference" to validate and initialize the different model

[1] Carefully calibrated sensors and recurrent use of laboratory techniques for measurements.

configurations presented in section 3. However, these data sets became insufficient when we focused on bloom phenology over the whole Southern Ocean (chapter 5) due to its limited spatial and seasonal coverage. The study on Southern Ocean bloom phenology required data covering large extents of the Southern Ocean and a significant number of seasonal cycles (in a fairly good time resolution) to capture main features of different bloom phenologies. Satellite estimations of surface chlorophyll data (i.e., ocean colour data) satisfied the required conditions: they covered a large domain of Southern Ocean at 5 days frequency and for more than 10 years (1998-2011). The ocean colour data set we used will be detailed in section 2.3. The third group of data, Argo floats, were useful when we get interested on the seasonal distribution of phytoplantkon in the water column was investigated. Several works have recently shown (Behrenfeld and Boss [2013], Ferrari et al. [2014]) that surface Chl estimations are not sufficient to properly address high-latitude phytoplankton seasonal cycles. These cycles are tightly related to changes in mixing and density gradients in ocean upper layers (i.e., stratification). An estimation of upper ocean stratification and its seasonal variability in the Southern Ocean is now possible due to the data provided by autonomous floats (i.e., Argo floats); this source of observational data will be briefly described in section 2.4.

2.2 Observations in the Indian Sector of the Southern Ocean

2.2.1 KERFIX station

KERFIX project (Jeandel et al. [1998]) aimed to monitor ocean-atmosphere CO2 and O2 exchanges and related processes with a time series station located at 50°40' S–68°25'E, 60 miles southwest of the Kerguelen Islands (see black triangle in map 2.1) . From January 1990 to March 1995, regular monthly measurements of temperature, salinity, P, Si, NO3, NH4, Chl-a and others variables[2]; were carried out in KERFIX station.

The mean N, Si and P profiles and the monthly Chl-a surface data (available from 1992 to 1995) were used to initialise some of our model configurations (see chapter 3). Chl-a was collected at 12 depths in the upper 300m. and analysed "by dipping them in 90% acetone (Nuclepore membranes) followed by an extraction period of 12h at 5°C (Fiala et al. [1998]). KERFIX station is assumed to be representative of the Permanent Open Ocean Waters (POOZ) where surface Fe supply is mainly due to winter mixing (**?**). Chl-a time series were used to validate the water column model presented in 3 and 4.

[2]More information in Jeandel et al. [1998] and http://www.obs-vlfr.fr/cd_rom_dmtt/kfx_main.htm

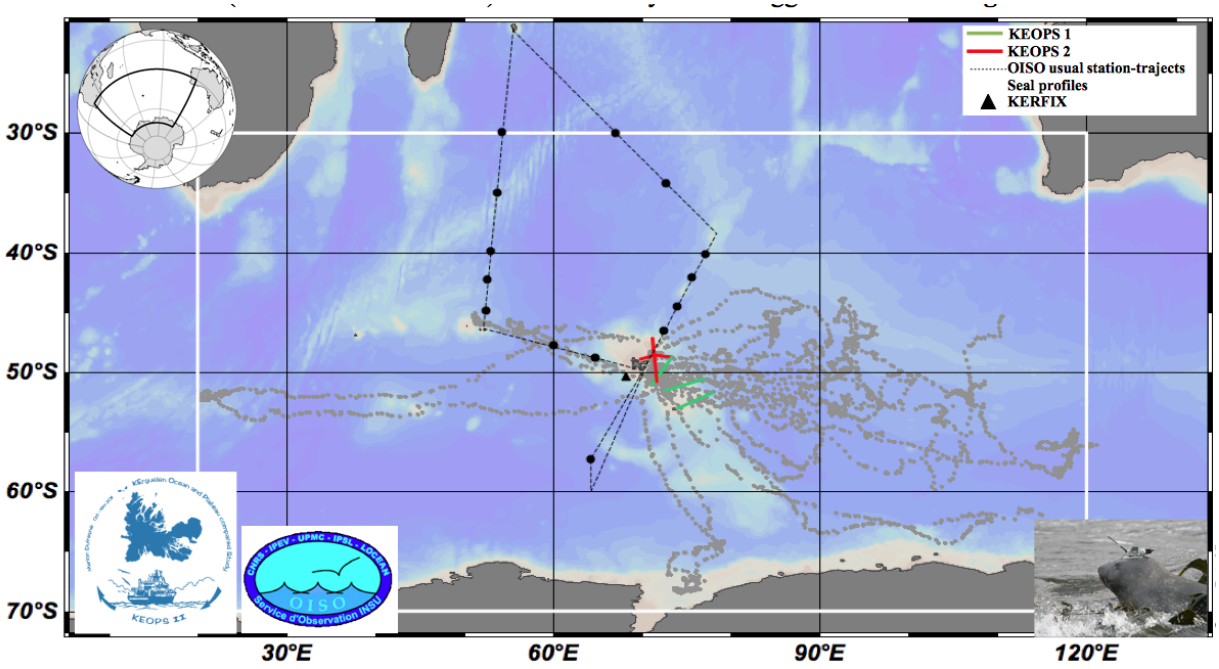

FIGURE 2.1: Map of Southern Ocean Indian Sector; Kerguelen Island is located right in the middle of the map. Blue to white background colour represents bathymetry; dark grey for land. Observational programs detailed in the text are represented: black dots-line marks usual stations and transect of OISO program, green lines mark the position of KEOPS I transects, red lines mark the position of KEOPS II main transects, the black triangle mark position of KERFIX station and grey dots mark locations of elephant seal profiles. In bottom right corner of the map, a picture of an elephant seal equipped with a data logger.

2.2.2 KEOPS project

KEOPS[3] project (Blain et al. [2004]), based around the Kerguelen Plateau and Archipelago, is a multi-disciplinary study aimed at understanding phytoplankton bloom dynamics, relating CO2 air-sea fluxes and consequent carbon export in an naturally iron fertilized region. KEOPS aims to cover all processes that couple physics and biogeochemistry during bloom formation and evolution. With this aim two oceanographic campaigns have been conducted (KEOPS I, in January-February 2005, and KEOPS II, in October-November 2011; see map in 2.1).

Sampling of primary production and carbon-cycle related variables from KEOPS I and II constitutes an exceptional data base to address high-latitude bloom and iron limitation studies. During my PhD works, KEOPS project has been an essential source of data (e.g., Fe vertical profiles and transport to validate 3D models) and knowledge to understand Fe limited primary production and bloom formation.

Furthermore, I have been my own actively involved in KEOPS II oceanographic campaign as an assistant of C.LoMonaco, for the continuum sampling of sea surface pCO2. Such measurements were conducted during KEOPS II onboard *R/V Marion Dufresne* but they also form part of a

[3] http://www.obs-vlfr.fr/keops2

long-term observational effort on CO2 fluxes in the Southern Ocean; the OISO[4] program (black circles in map 2.1 with black circles). The experimental work I carried out during the KEOPS II - OISO 20 sea campaign resulted in a scientific paper submitted to KEOPS 2 special issue in Biogeosciences journal[5]; submitted version of this paper is presented in A.

2.2.3 Kerguelen elephant seals

Kerguelen Island hosts one of the biggest populations of southern elephant seals (*Mirounga leonina*) with more than 120,000 individuals (Guinet et al. [1992]). These animals are one of the major predators of the Southern Ocean. They travel large distances (McConnell et al. [1992]) and dive up to 2000-m depths (Hindell et al. [1991]; Dragon et al. [2010]) on their quest for food. Moreover, elephant seals spend almost the entire year at sea with the exception of two 1-month periods spent on land: at austral spring, for reproduction, and at late summer, for moulting.

Since 2003, around 100 of Kerguelen elephant seals have been equipped with a data logger that integrate multiple oceanographic sensors and a transmitter relays data via the Argo satellite system (see section 2.4 for more information on Argo program). Data loggers can be positioned by satellite triangulation. The data loggers are equipped with sensors measuring temperature, salinity, water fluorescence and recently, accelerometers (Guinet et al. [2013]). While elephant seals travel hundreds of miles at open sea and dive to ocean interior, these sensors measure properties of the water column. When the animal reaches the surface, this information is transmitted to the satellite allowing a near real-time monitoring of ocean properties. Sampling occurs throughout the year and specially during winter periods, when sampling in the Southern Ocean is almost impossible by other means (i.e., research vessels due to hard navigation conditions and satellite data due to cloud coverage and short day-light length).

Chl estimations from elephant seals fluorometers have been used to evaluate the vertical and horizontal extent of phytoplankton concentration downstream Kerguelen island and plateau. Due to work on calibrating elephant seals fluorometers (Guinet et al. [2013]), Chl concentration values are much more accurate than current surface Chl satellite estimations.

2.3 Ocean colour data in the Southern Ocean

Three databases of ocean colour data are available for the Southern Ocean: the Sea-viewing Wide Field-of-view Sensor (SeaWiFS), the Moderate Resolution Imaging Spectroradiometer (MODIS-Aqua) and GlobColour (see figure 2.2.A). The latter is an European Space Agency (ESA) project that produces global ocean colour products by merging together data from multiple sensors

[4] more information in http://caraus.ipsl.jussieu.fr/oiso-accueil.html
[5] http://www.biogeosciences-discuss.net/special_issue133.html

(SeaWiFS, MODIS and others). GlobColour data has a spatial resolution of 1/4°x1/4° and a temporal resolution of 8 days, thus each calendar year has 46 time steps. Combining the data from different sensors increases the daily coverage of the oceans to ≈30% whereas individual sensors cover 8-16% of the globe (Durand [2007]). Such an increase of coverage is critical in high-latitudes (e.g., Southern Ocean) where sea-ice, short winter day length and cloudiness cause scarcity of valid data, specially in winter.

Data gaps in winter and early spring makes seasonal cycle detection of phytoplankton difficult (Cole et al. [2012]). We carried out some diagnostics to address the regional and temporal coverage available from GlobColour database in the Southern Ocean. A reasonably accurate detection of the whole Chl seasonal cycle from space requires sufficient valid year-long data and a relatively homogeneous distribution of valid data through the year. With the aim to quantify these two conditions, we defined the Largest Data Gap (LDG) index per pixel as:

$$\text{LDG} = \frac{\text{Largest consecutives data gaps per time period (timesteps)}}{\text{Timesteps per time period}}. \tag{2.1}$$

Using GlobColour database, we measured LDG index over all year long and from September to February (during the intense phase of the seasonal cycle). For instance, the LDG index for year 1998 (represented in 2.2.B) clearly states how, at latitudes higher than 60°S (and lower in the Atlantic sector) the phytoplankton seasonal cycle can not be monitored using ocean colour data. Therefore, LDG index is a year-dependent criteria to exclude those insufficiently sampled pixels, for which a robust reproduction of seasonal cycle is impossible. For the observation-based bloom study presented in chapter 5, we imposed that LDG <45 days within the 4 months centred on the detected onset. Such a restriction ensured that onset detection was really based on observed data.

Underestimation of surface Chl concentration in the Southern Ocean

Ocean colour satellites and databases use different algorithms to transform the radiative signal into surface Chl estimates. Such algorithms are carefully created through years of work on data validation for each new sensor. However, recent studies have shown that standard algorithms of SeaWiFS and MODIS are not adapted to Southern Ocean bio-optical proprieties (Szeto et al. [2011]). It has been repeatedly shown that remote sensing Chl estimates were underestimed by a factor two when compared to *in-situ* accurate (i.e., HLPC techniques) measurements (Kahru and Mitchell [2010], Guinet et al. [2013]). Recently, Johnson et al. [2013] created new algorithms to improve Chl estimates of SeaWiFS, MODIS and GlobColour in the Southern Ocean. SeaWiFS and MODIS estimates were considerably improved using Johnson et al. [2013] algorithms: Chl concentrations increased all over Souhtern Ocean, specially on high summer Chl spots (i.e., East coast of South America, downstream sub-Antactic islands, New Zealand), where difference with respect to standard algorithms was higher than 1mg/m^3.

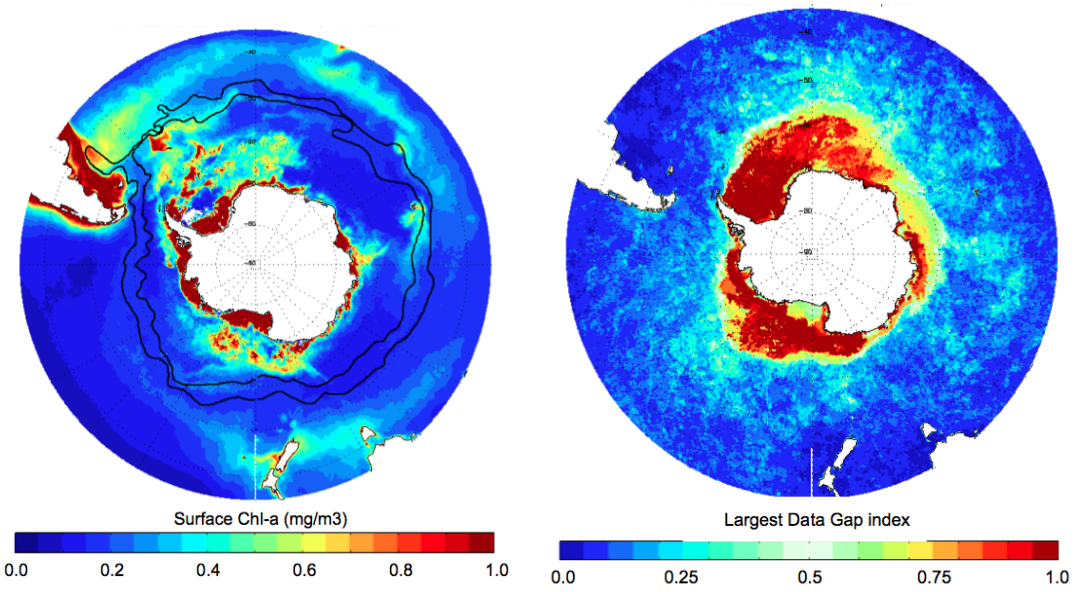

FIGURE 2.2: Left: Climatological Chl mean (Globcolour, standard algorithm). Right: Map of LDG index computed during austral spring-summer (Sept. 1998 to February 1999).

2.4 Argo floats

Argo is a global array of more than 3,000 free-drifting profiling floats that measures physical properties in the upper 2000m of the ocean. Floats cycle to 2000m depth every 10 days, measuring temperature and salinity during its ascent and position at surface (from which current velocity can be derived). Once at the surface, measurements are transmitted to satellites and to data centres allowing a real-time monitoring of the upper ocean.

The array of Argo floats provides 100,000 temperature/salinity (T/S) profiles and velocity measurements per year distributed over the global oceans at an average 3-degree spacing. For instance, in the Southern Ocean (where density of floats is still very low) Argo program contribute about half of the Southern Ocean profiles (http://wocesoatlas.tamu.edu/). The 4-5 years autonomous life of these floats allow including Southern Ocean winter.

As stated in the introduction, we used Argo floats data to properly address Southern Ocean bloom phenology (work presented in chapter 5). The information of the water column provided by Argo database (i.e., mixed layer depth estimations) was crucial to interpret and distinguish the phenology regimes. From this database, we calculated the mixed layer depth with a surface-density-difference criterion of $\Delta\sigma \leq 0.03$ kg m^{-3}[6].

Our aim was initially to co-locate (in time and space) individual Argo profiles to satellites surface Chl estimations to have an accurate reconstruction of stratification in the water column at the "precise" moment (+/- 5 days) at which sChl had been measured. However, the number of ocean

[6] Sallée et al. [2006] tested a number of methods and shows that this particular criterion is well adapted to localized the base of the seasonal mixed-layer in the Southern Ocean.

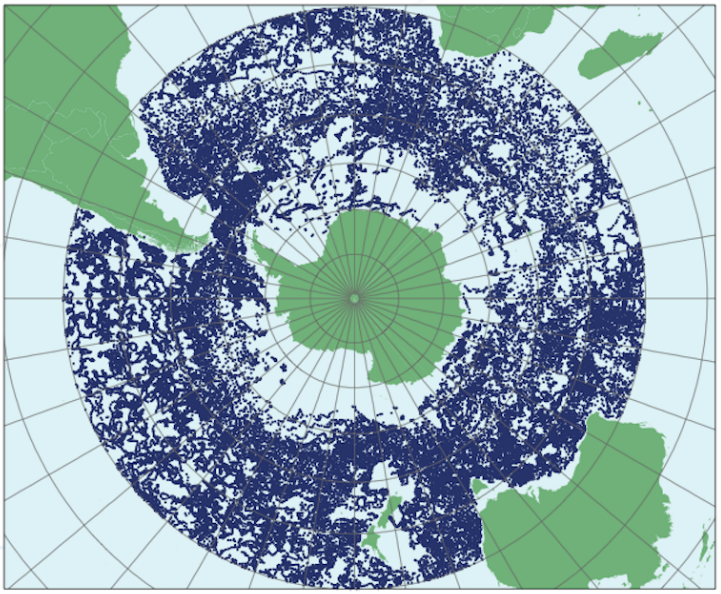

FIGURE 2.3: Location of more than 60,000 Argo profiles collected during the 24 months of the International Polar Year (2007-2009). From M.Balbeoch, JCOMMOPS

colour data pixels available during a 5-days window was huge compared to the number of individual Argo profiles. Thus, co-localisation strategy forced us to discard an important amount of satellite data reducing the statistical weight of our results. To circumvent this issue, we complement individual profiles with an Argo-based dataset with a much higher coverage (in time and space): the EN3 reanalysis dataset from the UK Met-Office (http://www.metoffice.gov.uk/hadobs/en3/). The EN3 product consists of objective analyses of assimilated ship and Argo profiles[7]. EN3 reanalysis provide monthly-analysed fields of full-depth temperature and salinity profiles on a one-degree grid.

[7]To ensure that Argo observations in the Southern Ocean had been integrated in the EN3 reanalysis, only data from year 2002 was used.

Chapter 3

Models

3.1 Introduction

An important part of the work carried out was based on the study of biogeochemical processes in Southern Ocean using modelling tools. Even though such modelling approaches were often developed in parallel to observations-based approaches, our aim was not to exactly reproduce observations using models but to use models to address ocean processes from a virtual perspective. This virtual perspective allowed us, for example, to create huge virtual data sets with measurements on fine scale plankton related processes (work presented in chapter 4), to test theoretical hypotheses (see results on Sverdrup's hypothesis at the end of chapter 4), to contrast results based on observations (second part of chapter 5) or to explore possible future changes in the Southern Ocean (chapter 6).

In this chapter, I will present the different models I used, together with the motivations and technical issues encountered to set up these different configurations. The chapter will be divided in three sections focused on three types of modelling strategies: from the most realistic and holistic to the most idealised and mechanistic.

In first place, I will present the "coupled" or Earth System Models (ESMs). These type models are meant to represent as climate-related processes as possible. ESMs simulate different compartments of the climate machine (i.e., atmosphere, ocean, vegetation, etc.) and couple these compartments together resulting in very complex and realistic simulations. With the aim to study Climate Change influence over Southern Ocean primary production, I used 8 ESMs from the latest CMIP5[1] exercise. These models will be presented in section 3.3 of this chapter, while the study on Climate Change impact over Southern Ocean primary production will be presented in chapter 6.

[1] CMIP5 states for the 5th phase of the Coupled Model Intercomparison Project. For more details refer to section 3.3.

Section 3.4 will be focused on regional "forced" models (the atmospheric processes are not computed; the ocean is forced by a pre-scribed atmosphere) representing physical and biogeochemical processes occurring in the Southern Ocean. These models have been set-up by A.Albert and J.LeSommer (MEOM team, in Grenoble) but I have actively participated to its improvement and validation. My contribution to these models will be presented in section 3.4. Some of these model configurations have been exploited to the study presented in the second part of chapter 5.

At last, in section 3.5, I will present a novel and idealised biogeochemical model configuration which I set-up during my PhD. Thus configuration was aimed not to produce realistic simulations but to resolve in the detail the mechanics of phytoplankton bloom. The model is based on an idealised physical framework used to force a complex biogeochemical model (PISCES). The work on set-up and following exploitation of this configuration will be presented in section 3.5. The results produced by this modelling approach contributed to the studies presented in chapter 4 and chapter 6.

To avoid ambiguities, hereinafter *model* will be referred to as an ensemble of routines aimed to simulate an environment (e.g., the ocean or the climate), *model configuration* or, simply, *configuration* stands for a specific grid or domain represented for a specific model. *experience* will be used when different code versions are used for a given configuration. Finally, *run* is the result of executing a model for a specific configuration and under specific conditions (i.e., duration, outputs frequency...). A model can have several configurations and from one configuration we can set-up different experiences. From an experience is possible to obtain multiple runs (e.g., one-year run with daily outputs or 100-years run with monthly outputs).

With the exception of some of the Earth System Models (ESMs), all the model configurations created were based on the NEMO modelling environment (Nucleus for European Modelling of the Ocean, Madec [2008]). In next section, I will briefly describe the general environment of NEMO modelling system putting the emphasis on its biogeochemical compartment (i.e., PISCES model).

3.2 NEMO modelling environment

NEMO is an ocean modelling environment principally developed in Institute Pierre Simon-Laplace (ISPL), France, with the participation of several European research centres[2]. Its main core is the OPA model, for ocean dynamics and thermodynamics (Madec [2008]). OPA is a primitive equation model aimed to cover from regional to global ocean scales and to be coupled to models representing important ocean-related processes as sea-ice dynamics and thermodynamics (LIM model) or passive tracers dynamics (TOP). Ocean biogeochemical cycles are also

[2]NERC (UK), MetOffice (UK), CMCC (Italy), INGV (Italy), CNRS (France) and Mercator (France)

represented in NEMO environment thanks to PISCES model (Aumont and Bopp [2006]), which is embedded in TOP.

NEMO system is used for a wide range of applications: from studies on fundamental physical oceanography (e.g. studies on turbulence and ocean energetics) and ocean and ice biogeochemistry, to operational forecast (e.g. ECMWF and Mercator) and global Climate Change projections. Actually, NEMO constitutes the ocean component of several Earth System Models (ESM) as IPSL one, the IPSL-CM5 (Dufresne et al. [2013] and http://www.icmc.ipsl.fr).

Biogeochemical parametrisations in PISCES

The PISCES biogeochemical model (Aumont [2012]) aims to simulate processes governing ocean primary production and other carbon cycle related processes. PISCES resolves 24 prognostic variables (see figure 3.1), including two phytoplankton (nanophytoplankton and diatoms), two zooplankton (micro- and mesozooplankton) and the main limiting nutrients in the global ocean (N, P, Si and Fe). The PISCES formulation is based on the assumption that marine organic matter is present in the global ocean in a relatively constant composition: for each atom of P there is 16 atoms of N and 106 of C [3]. Phytoplankton growth is limited by the external concentrations of these three nutrients. Such assumptions are the foundations of *Monod* type of biogeochemical models (Monod [1942]). However, PISCES is not a fully *Monod* model as Si and Fe quotas are variable[4]. The nutrient-depending formulation allows for the adaptation of PISCES to a large number biogeochemical environments and so, to better represent global ocean variability.

Prognostic equation for each phytoplankton group concentration (i=1,2) is:

$$\frac{\delta P_i}{\delta t} = \mu_i P_i - g_i^Z(P_i)\ Z - g_i^M(P_i)\ M - m_i P_i + \frac{\partial}{\partial z}\left[\kappa_z \frac{\partial P_i}{\partial z}\right] \qquad i = 1,2 \tag{3.1}$$

where P_i stands for biomass of group i, μ_i is the growth rate, g_i represents the grazing rate and m_i the mortality rate. The last right hand side term is the effect of vertical diffusion over biomass due to vertical mixing of intensity κ_z. Phytoplankton growth rate (μ_i) depends on the availability of N, P, Fe and Si (only for diatoms); but also on light and temperature:

$$\mu_i \ = \ \mu_{max}^i\ g(Z_{mxl})\ \left(\ 1\ -\ \exp\left(\frac{-\alpha_i\ Q_i^{Chl}\ PAR_i}{\mu_{max}\ L_i}\right)\right)\ L_i, \qquad i = 1,2 \tag{3.2}$$

where $\mu_{max}^i \ = \ \mu_{max}^0\ f_i(T)$ ($f_i(T)$ is the dependency of the growth rate with temperature; Eppley [1972]), $g(Z_{mxl})$ a penalisation term for deep mixing (detailed in next section, equation

[3] This empirical relationship was established by Redfield (Redfield [1934]) from which receives its name, the *Redfield ratio*

[4] BGCM models assuming variable ratios are known as *quota* models; Droop [1983]

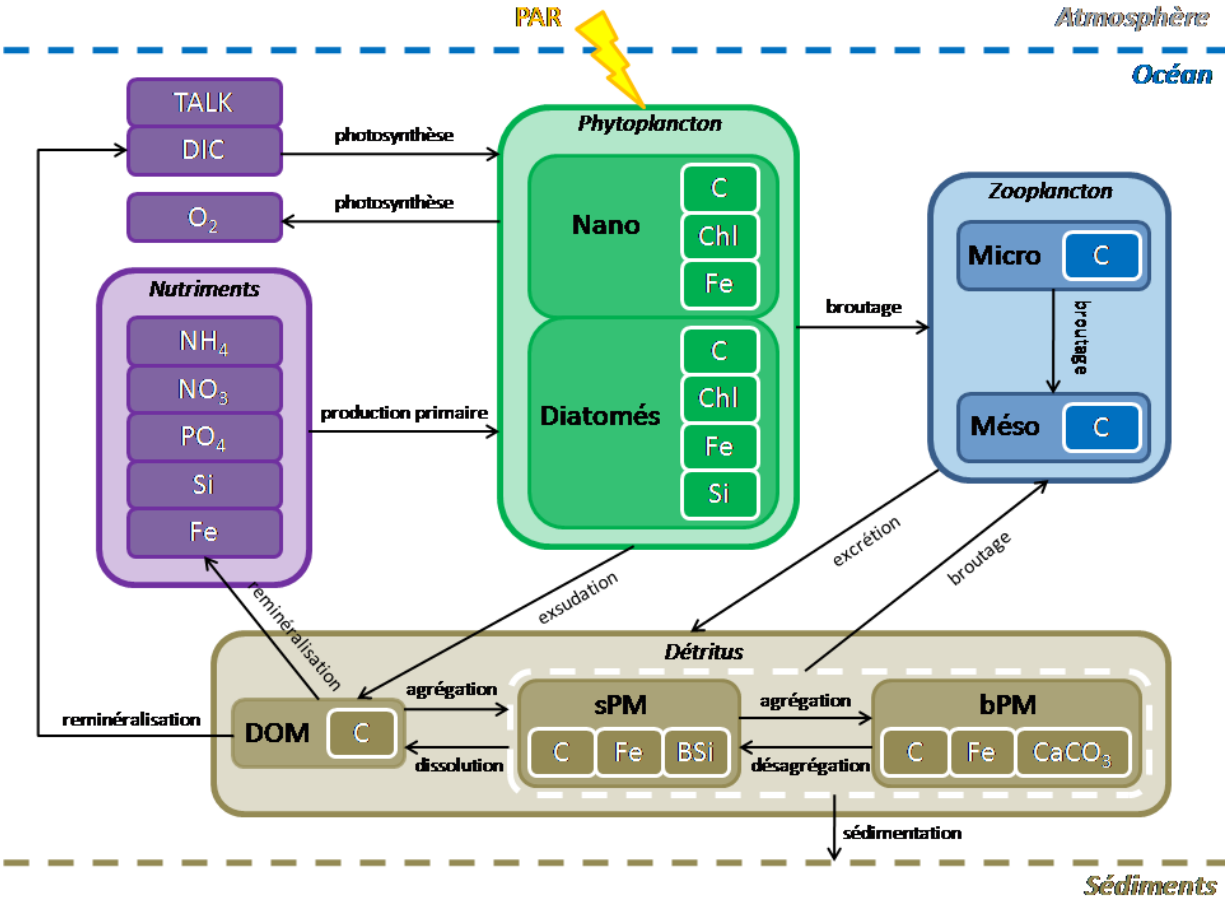

FIGURE 3.1: PISCES architecture (in French). From Dufour [2011]

3.5), PAR_i is function of the shortwave radiation at the surface, α_i is the initial slope of the P-I curve, Q_i^{Chl} the Chl:C quota for each phytoplankton and L_i is the nutrient limitation. Nutrients limitation in our set-up can only be due to Fe, so $L_i \equiv L_i^{Fe}$ where:

$$L_i^{Fe} = min\left(1,\ max\left(0,\ \frac{Q_i^{Fe} - Q_{i,min}^{Fe}}{Q_{i,opt}^{Fe}}\right)\right). \tag{3.3}$$

Iron limitation is formulated following a *Quota* approach (Droop [1983]) with the term $Q_{i,opt}^{Fe}$ allowing luxury uptake (as in Buitenhuis and Geider [2010]).

Alternative formulation for phytoplankton growth rate: the *newprod* option

PISCES is a flexible tool intended to represent the large variability of biogeochemical conditions existing in the global ocean. There are close to 100 parameters which allow users to tune the model and adapt it to a large diversity of environments and experimental data. Most of these parameters define values for empirical constants (e.g. the minimum half-saturation constant for each nutrient or the phytoplankton mortality rate). Other parameters are used to allow model user to chose amongst alternative code formulations of a specific mechanism. An example of these second type of parameters is the *olprod*/*newprod* option which I will present in next paragraph.

As stated, in PISCES phytoplankton growth rate is computed by equation 3.2. However, throughout this chapter I will present two alternative formulations of equation 3.2 and I will show the impact of each formulation over phytoplankton seasonal cycle. The first of these alternative formulations I will present is the *oldprod*/*newprod* option. In the most recent PISCES code version (Aumont [2012]), user can choose amongst two possible formulations for phytoplankton growth rate: the"original" or "by-default" one, expressed in equation 4.1 and hereinafter referred as *oldprod*, and a new one, called *newprod* and computed as follows:

$$\mu_i \;=\; \mu^i_{max}\; f(L_{day})\; g(Z_{mxl}) \left(1 \;-\; \exp\left(\frac{-\alpha_i\; Q^{Chl}_i\; PAR_i}{f(L_{day})\; (\mu_{ref} + b_{resp})} \right) \right) \; L_i, \qquad i = 1,2 \quad (3.4)$$

the differences with respect to 3.2 are in red and L_{day} is the normalised ([0,1]) day length, μ_{ref} a reference growth rate and b_{resp} a small respiration rate. The addition of $f(L_{day})$[5] in equation 3.4 causes growth rate to be dependent of day length, which is expected to slightly modify primary production in latitudes where the day length significantly changes through the year (i.e., medium to high latitude winters), penalising winter production and enhancing it in summer.

3.3 Coupled Earth system models

CMIP5 ensemble models: Climate Change projections

Climate change derived impacts on ecosystem and human societies all around the globe constitute one of the major challenges of current times. To understand, evaluate and face such challenges, international efforts have started some decades ago involving different actors of the society as politics, economists or climate related researchers. The most important of this international cooperation is the International Panel for Climate Change (IPCC). It was founded in 1988 by the United Nations Environmental Programme (UNEP) and the World Meteorological Organization (WMO). As described in its official website[6],

> (...) It reviews and assesses the most recent scientific, technical and socio-economic information produced worldwide relevant to the understanding of climate change. It does not conduct any research nor does it monitor climate related data or parameters.

Such a mission is conducted through the creation of quinquennial IPCC's Assessment Reports (AR): an up-to-date condensed summary of research works related to climate change. The aim of these reports (the fifth one has been published in 2014) is to create a solid review of current knowledge on climate (from regional to global scales) and on all those human activities

[5] Defined as $f(L_{day}) \;=\; 1.5 \frac{L_{day}}{0.5 + L_{day}}$

[6] http://www.ipcc.ch/

related to it at present, identifying and evaluating potential impacts and threats. The range of disciplines covered by these reports goes from geophysics to economic and public health and they are addressed to policymakers, even if documents access are opened to general public. Latest IPCC report (published between 2013 and 2014) was divided in three volumes:

- The Physical Science Basis
- Impacts, Adaptation and Vulnerability
- Mitigation of Climate Change

First volume is focused on synthesizing research works presented during the last 5 years that provided new knowledge on physical climate mechanisms. Studies based on Earth System Models (ESM) constitute an important part of this volume content as they are a unique tool to explore past and future climate. ESMs are complex to set up and require important sums of computational (and economical) resources. Such drawback was one of the motivations to unify efforts amongst modelling community that resulted on the Climate Model Inter-comparison Project (CMIP5, for the latest version; Taylor et al. [2012]).

CMIP5 consists on an ensemble of 20 latest generation ESMs which are run under similar conditions (e.g., same period of "pre-industrial" control or same future trends on CO2 emissions) with the aim to obtain comparable results. This strategy allow to statistically minimise results uncertainty on future climate evolution: single model bias are supposed to be compensated when averaging over the ensemble of models. Future climate projections are a tricky problem to face as they are strongly dependent of both Earth system complex dynamics and future greenhouse gases emissions from human activities. CMIP5 adopt an additional strategy to represent the widest range possible of future climate evolutions: 4 radiative forcing future scenarios (the so-called RCPs) are estimated assuming four different global trends on greenhouse emissions (Moss et al. [2010]; van Vuuren et al. [2011]). These scenarios are labelled according to the additional radiative forcing level in 2100 with CO2 concentrations reaching 936, 670, 538 and 421 ppm,i.e., RCP8.5, RCP6.0, RCP4.5 and RCP2.6 respectively (figure 3.2). While RCP2.6 reproduces a scenario of strong global politics on Climate Change mitigation, with a decline on CO2 emission starting as soon as 2050 (not realistic); RCP8.5 simulates a planet where CO2 emission continue to raise throughout the 21st century.

I used the results from 8 CMIP5 models under the strongest scenario (RCP8.5) to address the impact of Climate Change over Southern Ocean primary production. This study is a step forward from Henson et al. [2013] and Bopp et al. [2013] works who, from a global analysis of CMIP5 projections, concluded that a high inter-model uncertainty on primary production trends in the Southern Ocean. Our study, conducted in collaboration with L.Bopp and J.B.Sallée, will be presented in chapter 6.

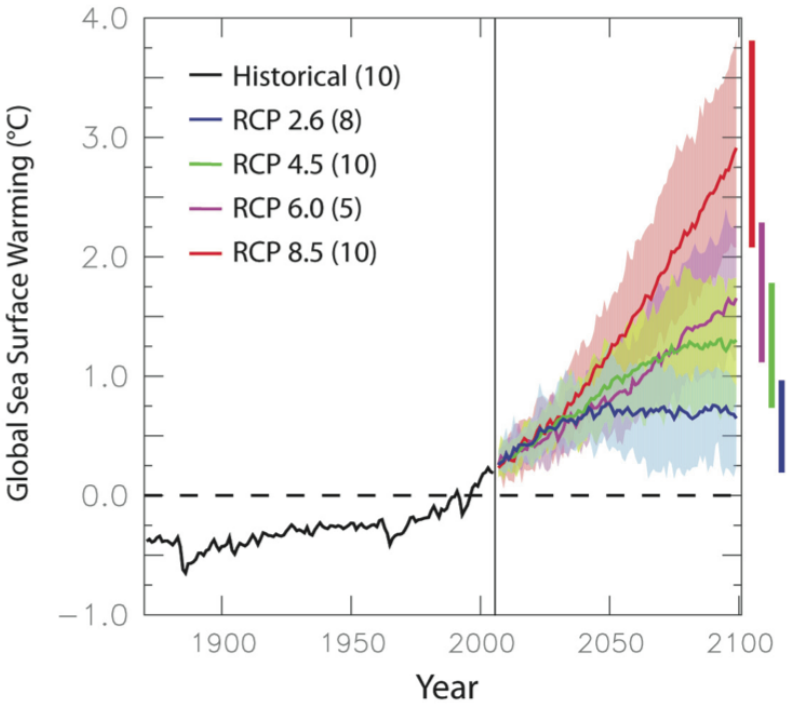

FIGURE 3.2: Model-mean time series of global sea surface warming (°C) over 1870–2100 (relative to 1990–1999 mean) using historical simulations and the four RCPs scenarios explored by CMIP5. Shading indicates one inter-model standard deviation. Adapted from Bopp et al. [2013]

3.4 Regional forced models

The ensemble of configurations we set up were motivated (and some of them based) on the works of Dufour [2011] and Mathiot [2009]. The latter created a regional circumpolar extraction of the Southern Ocean and Antarctic coasts from a global configuration at 0.5° of resolution (ORCA05). The southern frontier was extended until 70°S to fully represent Wedell and Ross seas while, at north, model grid started at 30°S. This configuration, called PERIANT05, covered the whole Southern Ocean and southern edge of subtropical gyres (see figure 3.3).

From this modelling framework, Dufour [2011] set up configurations coupling ocean physics and biogeochemistry, forced by atmospheric inputs. These configurations were called BIOPERIANT05 and resulted in an important set of runs that Dufour [2011] used to answer a number of questions regarding carbon cycle and its link with Southern Ocean dynamics (Dufour [2011] and Dufour et al. [2013]). The ensemble of configurations and experiences created were based on Dufour's BIOPERIANT05 reference experience, called HIST05.

Three new configurations were set up: one 1D configuration, one 3D configurations representing the Southern Ocean Indian Sector (from 20°E to 120°E; called BIOSINDIAN05) and one 3D periantarctic configuration (BIOPERIANT05-GAA95b). Here I will detail the work I carried out

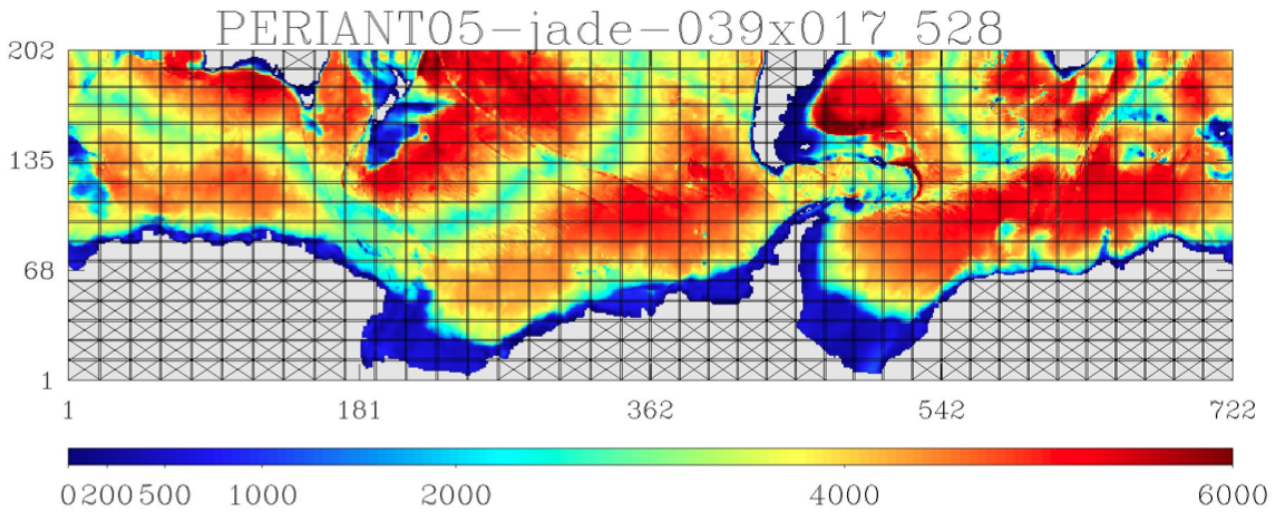

FIGURE 3.3: PERIANT05 domain and computational decomposition. Grid dimensions were 722x202 points with a resolution of 0.5°cos(latitude) x 0.5°. Colourbar represent bathymetry.

on the development of the two 3D configurations; the 1D configuration will be described in detail in the next section 3.5.

BIOSINDIAN05 configuration covered the domain 20°E-120°E/30°S-70°S (named SINDIAN in figure 3.4) using the grid, resolution and bathymetry of PERIANT05. BIOSINDIAN05 configuration was aimed to improve HIST05 based on the flaws identified by Dufour [2011], specially the inconsistencies on phytoplankton seasonal cycle (timing and magnitude) compared to observations (see section 3.4 for details). Three reasons motivated the zoom in the Indian Sector for BIOSINDIAN05 configuration:

1. A number of observation data was available for this sector, especially, around Kerguelen's Plateau. *In-situ* observations are a precious element to validate and test new biogeochemical configurations, specially for the Southern Ocean where ocean colour data is biased (Johnson et al. [2013]).

2. Reducing the model grid also reduced the computing time and allowed testing different configurations with different growth rate formulations.

3. Future configurations at higher-resolution were planned for this region. Hence, a reference run for Indian sector at 0.5° was necessary to use as foundation for next configurations.

3D configurations main features are detailed in table 3.1, together BIOPERIANT05 reference configuration from Dufour [2011], added for comparison (in grey). In addition, while this manuscript is being written, two new configurations at higher resolution are being developed.

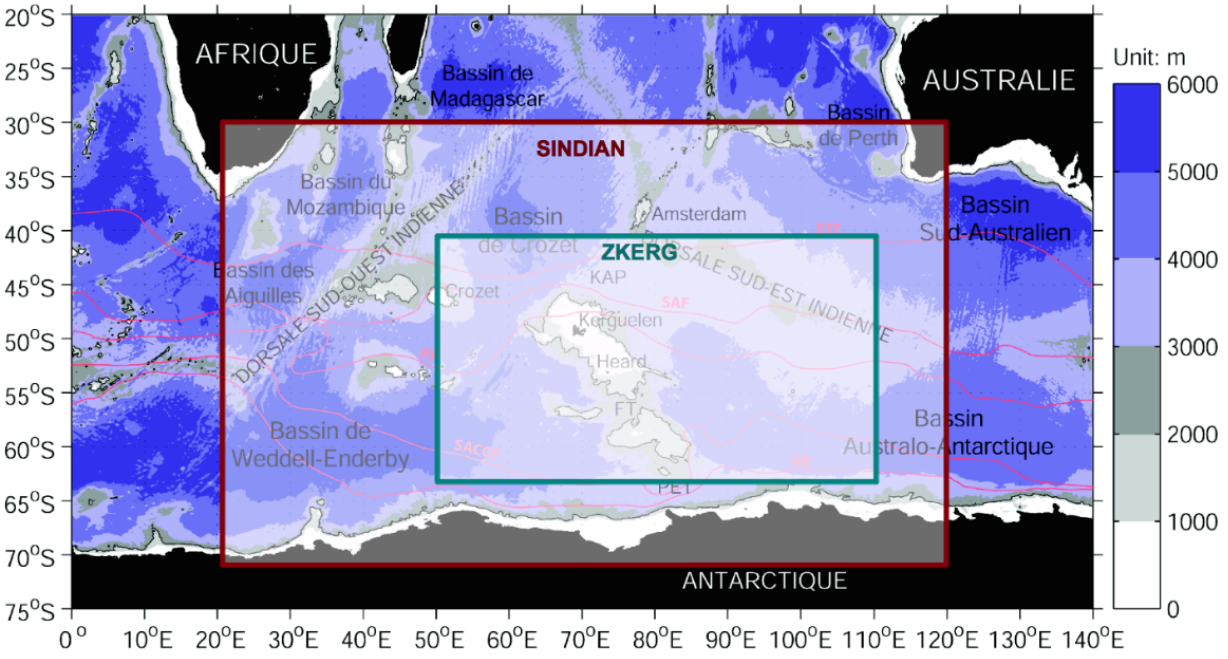

FIGURE 3.4: Map of the Southern Ocean Indian Sector. The domain covered by BIOSINDIAN05 configuration is represented by the box SINDIAN. Box ZKERG stands for a smaller domain for future high-resolution models. Colourbar represents bathymetry.

CONFIGURATION (resolution)	DOMAIN	DIMENSIONS	PHYSICS
BIOSINDIAN05-GAASIN (0.5°)	[20°-120°E, 30°-70°S]	(203, 202, 46)	NEMO v3.4
BIOPERIANT05-GAA95b (0.5°)	[0°-360°E, 30°-70°S]	(722, 202, 46)	NEMO v3.4
BIOPERIANT05-HIST05 (0.5°)	[0°-360°E, 30°-70°S]	(722, 202, 46)	NEMO v3.2.2

TABLE 3.1: Table presenting the main feature of biogeochemical configurations set up.

Seasonal cycle sensitivity to growth rate formulation: BIOSINDIAN05 experiences

Outputs from HIST05 broadly reproduced the spatial patterns of surface Chlorophyl-a (sChl) through the year (see figure 3.5, only months of bloom formation and apex are represented). However, Dufour [2011] identified three relevant aspects to be improved:

1. sChl patterns north of the ACC presented significantly stronger concentrations than the ones estimated by SeaWiFs.

2. Blooms downstream of the sub-Antarctic islands (i.e., South Georgia, Kerguelen) were very weak in the model compared to satellite measurements.

3. Bloom timing in the model seemed to be shifted around 1 to 2 months earlier with respect to satellite observations.

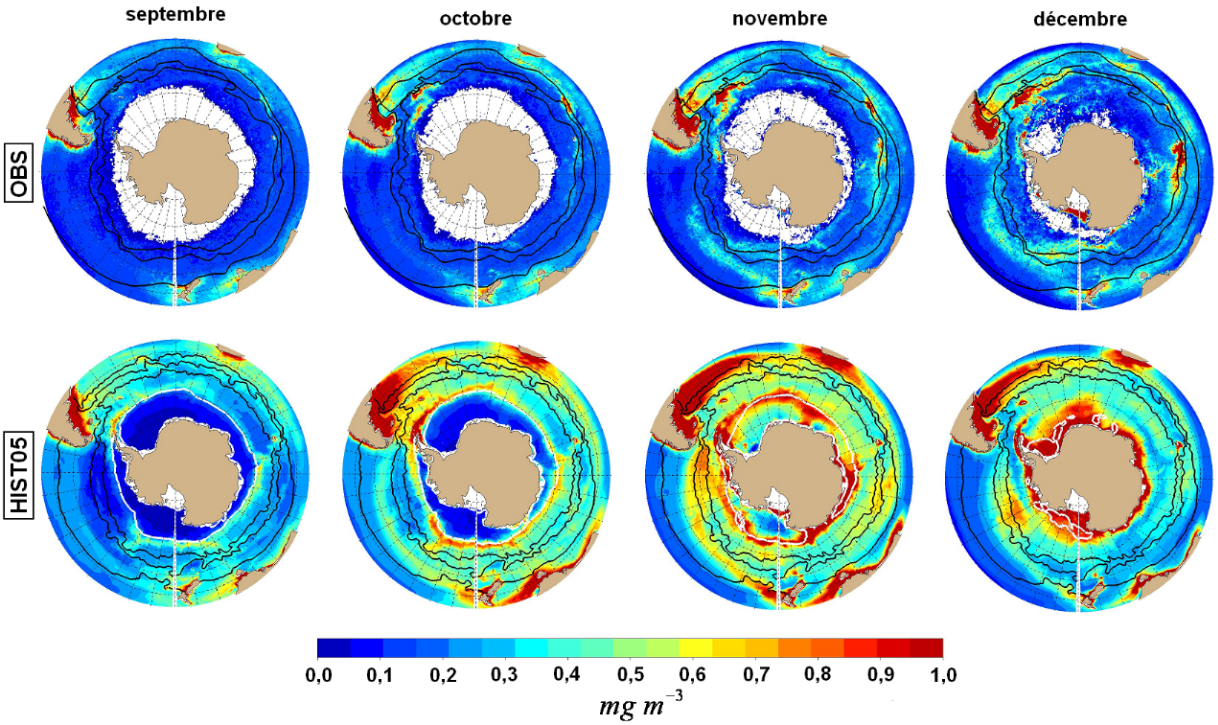

FIGURE 3.5: Periantartic maps of surface Chl. concentration estimated by SeaWiFs and by HIST05 configuration. From Dufour [2011]

Although some of these flaws were related to ocean physics representations (e.g., mixed layer), we focused on production and surface Chl sensitivity to variations on growth rate (μ) PISCES formulation. BIOSINDIAN05 configuration was used to implement the different formulations (i.e., experiences), that were called BIOS05_eN (N stands for the experience number). Each experience produced a 10 years run (5 days and monthly outputs) with a different version of growth rate formulation, over the whole Indian Sector.

To test and compare BIOSINDIAN05 experiences with observational data, we zoomed in on two domains at the west and east of the Kerguelen Plateau (identified as red boxes in figure 3.6). To work with small domains permitted to better identify mechanisms driving the bloom that could be biased by a large scale spatial average and, in addition, to contrast sets of outputs not only to ocean colour satellite data but also to confident *in-situ* measurements (i.e., west of Kerguelen thanks to KERFIX station time series; and at east thanks to elephant seals database -see chapter **??** for details-). Indeed, each of these domains represented a different biogeochemical regions: at the eastern side, typical open ocean water conditions with winter vertical iron supply; at the western side, situated downstream Kerguelen, hence with iron mainly supplied by advection and dynamical instabilities). In the interests of clarity, west domain will be hereinafter referred as KERFIX domain, while east domain as BLOOM domain.

As a reference framework with which to compare BIOSINDIAN05 experiences, we will firstly illustrate the bias on bloom timing and magnitude identified by Dufour [2011] at the KERFIX

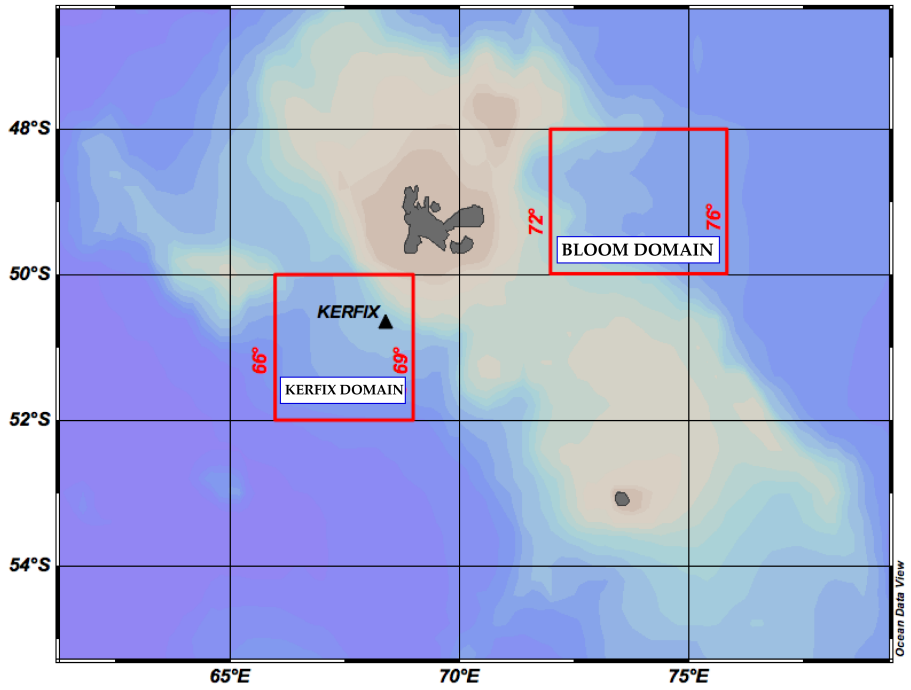

FIGURE 3.6: The Kerguelen Islands and Plateau and KERFIX and BLOOM domains where experiences were compared to ocean colour and *in-situ* data.

and BLOOM domains. The HIST05 15-years mean seasonal cycle was compared to GlobColor 13-years mean satellite estimations (blue and black dashed lines respectively, in figure 3.7). At the KERFIX station sChl concentration begins to rise as early as July (to reach its maximal value around 15th November) while GlobColor estimations do not show an increase in sChl concentration until September and the peak of the cycle arrives on 15th December. The magnitude is very similar for both estimations but it must be remembered that the GlobCoulour algorithms are known to underestimate sChl concentration in the Southern Ocean (Johnson et al. [2013]). A more confident measure of sChl is the KERFIX station time series (1992-1995, Jeandel et al. [1998]). The 3-years averaged data (red line in figure 3.7) shows a seasonal cycle with a narrow and marked peak that starts in mid-September and reaches maximal value between November and December. The KERFIX station measurements show how sChl starts to increase earlier in the model and that, in fact, the whole modelled seasonal cycle of sChl is smoother (i.e., low maximal concentration, high minimal concentration and low rates of change) compared to *in-situ* data. The BLOOM domain shows a similar issue in terms of timing but the under-representation of bloom magnitude is much more exaggerated in this case. The extremely weak maximal sChl concentration in this case is mainly due to a lack of iron transport downstream the Kerguelen Plateau (as Dufour [2011] had already identified for all sub-Antarctic islands). We expect this bias to be reduced in the upcoming configurations at higher resolution (1/12° and 1/36°)

The sChl seasonal cycle was weaker than in observations contrasted with the modelled MLD mean seasonal cycles (bottom panels in figure 3.7): compared to MLD estimated from Argo/ship

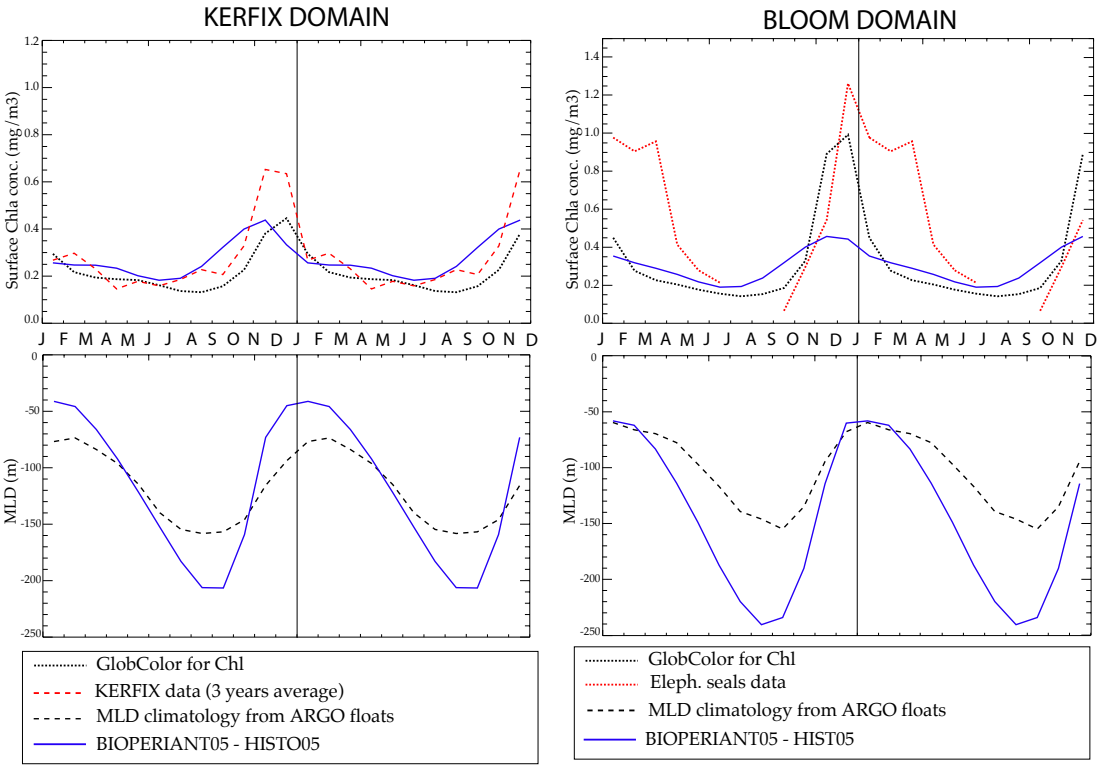

FIGURE 3.7: HIST05 configuration sChl seasonal cycle compared to observational data at KERFIX (left) and BLOOM (right) domains.

data (Sallée et al. [2008]). MLD in HIST05 model was much deeper in winter and shallower in summer resulting on high rates of (des-)stratification. In figure 3.7, the surface bloom starts when the MLD is maximal in HIST05 and the sharp MLD shallowing, from October to December, has a very weak impact on sChl. Such a premature bloom onset suggested that light limitation in PISCES was too weak in winter (or too strong in summer) eluding its impact over the phenology of the bloom. In conclusion improvement in both physics and biogeochemistry were necessary to bring model data closer to observations.

The work to better represent mixed layer seasonal cycle was exclusively conducted by MEOM team (in particular, by A.Albert). Different tests were carried out to reduce winter MLD. Amongst these tests, an improved formulation and parametrisation of TKE turbulent closure scheme in NEMO, had a major impact on reducing penetration of turbulent winter mixing and, consequently, reducing winter MLD (results will be presented in concluding figure 3.9, at the end of this section).

Unlike improvement in physics, I actively collaborated with MEOM team to improve PISCES skills on better reproducing phytoplankton cycle in the Southern Ocean. Based on BIOSINDAN05 configuration we set-up a series of experiences to test different PISCES formulations. Outputs produced by these experiences were contrasted with observational data at KERFIX and

BLOOM domains. To properly quantify the impact of new formulations, we first created a "reference" experience (named BIOS05_e0) in which the PISCES code version was equivalent to one used by C.Dufour in HIST05 configuration.

The first experience (BIOS05_e1) was a test with the alternative growth rate formulation provided in PISCES code: the *newprod* parametrisation presented in section 3.2. As stated, *newprod* formulation added a factor to the growth rate equation (equations 3.2 and 3.4) to take into account the day length. Thus, such an additional penalisation was meant to have a more notable influence in winter, when days shorten (specially in high-latitudes). However, as figure 3.8 shows, experience BIOS05_e1 presented a lower sChl than the reference experience, not only in winter but also throughout the entire seasonal cycle. As a consequence, the bloom timing remained earlier than observations and the bias on the undervalued sChl concentration increased.

From BIOS05_e1 results we concluded that, to efficiently shift the bloom timing, it was necessary to apply a factor of strict winter penalisation. In fact, PISCES code already contains a factor with similar effect: the g(Z_{mxl}) term in growth rate computation. Term $g(Z_{mxl})$, present in equations 3.2 and 3.4, penalises phytoplankton the growth rate when MLD deepens below the euphotic layer[7] (Z_{eu}). Such penalisation is intended to take into account the time that algae spends without receiving enough light to do photosynthesis and is especially effective in winter when the mixed layer is deep and euphotic layer is shallow (due to low solar radiation). The $g(Z_{mxl})$ penalisation term is expressed in PISCES "standard" version (hereinafter *oldpenal*) as

$$g(Z_{mxl}) \;=\; 1 \;-\; \frac{T_{dark}}{T^{P}_{dark} + T_{dark}}, \tag{3.5}$$

with Z_{mxl} representing mixed layer depth (or MLD) and $T_{dark} = (max(0, Z_{mxl} - Z_{eu}))^2/86400$. Parameter T^{P}_{dark}, defined by user, is equal to the number of days that phytoplankton can survive without light (by default, values are 3 days for nanophytoplankton and 4 for diatoms). With the aim to increase such penalising effect over winter growth rate, we recovered a similar factor defined by Lévy et al. [1998] for a study in Mediterranean Sea. This alternative formulation, that will be referred as *newpenal*, can be expressed as:

$$g^{*}(Z_{mxl}) \;=\; 1 \;-\; f_P \;\times \left(\frac{Z_{mxl}}{Z_{eu}} \;-\; 1 \right), \tag{3.6}$$

where parameter f_P is equal to 0.9 nanophytolpankton and 0.8 for diatoms. Such a new computation was coded inside the *p4zprod.F90* routine, were growth rate is computed.

BIOSINDIAN05 experiences with *newpenal* formulation (BIOS05_e2 and BIOS05_e3) did showed a significant change on bloom timing (figure 3.8). For both BIOS05_e2 and BIOS05_e3 where the only difference was the *newprod*/*oldprod* option respectively, surface bloom onset was delayed until July at the KERFIX domain and August at the BLOOM domain (more than one month later

[7] In PISCES, the depth of the euphotic layer is defined as the depth at which there is a 1‰ of surface PAR

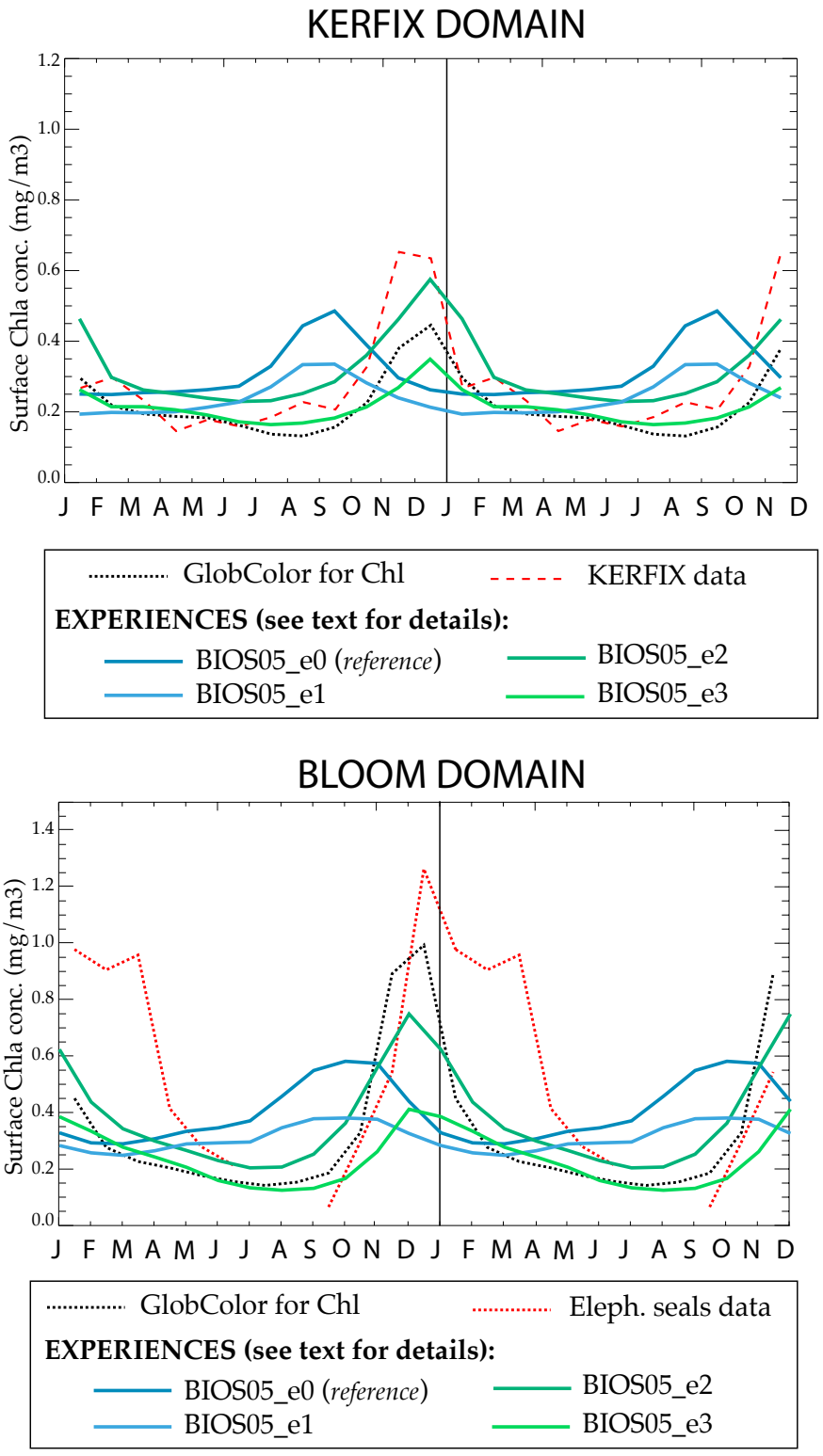

FIGURE 3.8: sChl seasonal cycles from the four BIOSINDIAN05 (or BIOS05) experiences compared to observational data at KERFIX (top) and BLOOM (bottom) domains. Only growth rate formulation changed between the 4 experiences: BIOS05_e0 corresponds to *oldpenal/oldprod*, BIOS05_e1 to *oldpenal/newprod*, BIOS05_e2 to *newpenal/oldprod* and BIOS05_e3 to *newpenal/newprod*.

than reference experience) in agreement with observations. In terms of sChl concentration neither of both experiences seemed to truly capture the correct phenology: while BIOS05_e2 was slightly overestimating sChl in winter, BIOS05_e3 underestimated sChl in summer. Our conclusion was that, globally the experience which best reproduced observations data was BIOS05_e2. Two reasons sustained this conclusion:

1. Observations confidence was much greater in summer than in winter. For the latter, very few pixels are actually sampled from satellite (thus, mean value can be biased), KERFIX time series contained very few data during winter for the 3 years and no data were available for elephant seals. On the contrary, in summer all 3 sources of observations were statistically rich and average values much more reliable. Therefore, a model closer to observations in summer would probably be better reproducing the whole seasonal cycle.

2. At the BLOOM domain, both sources of observations (ocean colour and elephant seals) presented higher sChl values than the ones produced by models. The model which gets closer to maximal concentrations (BIOS05_e2) seemed the best choice to us.

Growth rate formulation corresponding to BIOS05_e2 (i.e., *olprod/newpenal*) was implemented in a BIOPERIANT05 configuration: the GAA95b. The runs derived from GAA95b were then the "improved" version of HIST05. To compare both HIST05 and GAA95b, in figure 3.9 we represented the seasonal cycle of sChl and MLD together with the observational data at KERFIX and BLOOM domains. The comparison between the two modelled sChl seasonal cycles clearly shows an improvement of GAA95b with respect to HIST05: the winter values were very similar, GAA95b started increasing between 1 (at the BLOOM domain) to 2 month later than HIST05 and maximal bloom concentrations were higher (and closer to observations) for GAA95b than for HIST05. Even if the changes on growth rate formulation had an impact on these improvements, the MLD seasonal cycle was also significantly different between HIST05 and GAA95b. The latter simulated shallower MLD all through the year, getting closer to the observations climatology in winter but with too shallow minimal values during austral summer (December to February). Timing of the MLD also changed from HIST05 to GAA95b with longer deepening periods (February to October) and quicker stratification periods (October to December). As a consequence, maximal MLD values in GAA95b were attained slightly later than for HIST05. In this sense, the comparison with the observations was less clear; but an additional validation over larger domains showed a clear agreement of GAA95b with the observations.

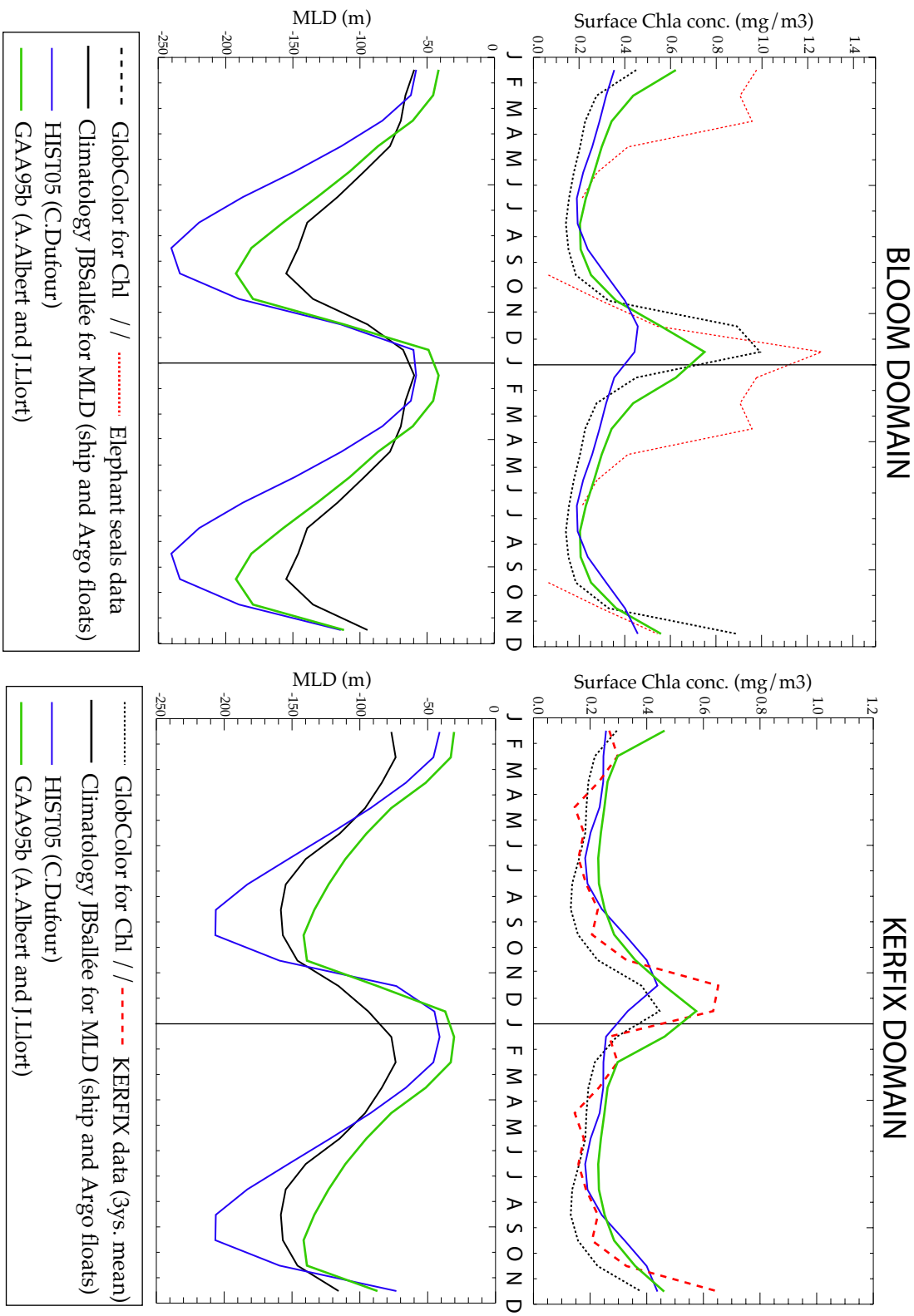

FIGURE 3.9: sChl and MLD seasonal cycle of the HIST05 and the GAA95b configurations compared to observational data at KERFIX (left) and BLOOM (right) domains

3.5 Water-column (1D) biogeochemical model

Configuration set up

In this section, I will describe the main features of the water column (i.e., 1D) PISCES configuration I developed during this PhD. This *offline* and 1D configuration was created to address how ocean physics controls Southern Ocean phytoplankton seasonal cycles (and hence, spring blooms at the ocean surface). The same question, generalized to any high-latitude region, is one of the longest and most explored questions on modern biogeochemical oceanography and has inspired a number of studies during the past decades (Sverdrup [1953], Siegel [2002], Behrenfeld [2010], Taylor and Ferrari [2011], Ferrari et al. [2014]). Most of these studies and theories are based on the North-Atlantic region and we wanted to contrast these theories to the very specific biogeochemical conditions of the Southern Ocean. A biogeochemical *offline* configuration was assumed to be a good approach to the bloom onset question because it allowed us to apply strict controls over the physical environment.

We aimed to answer this question via a sensitivity analysis approach, with the objective of defining clear links between physical oceanic features and phytoplankton dynamics throughout the seasonal cycle. The robustness of such an approach was based on taking into account a large number of runs from which statistical relationships between variables could be confidently established. Such a methodology required a modelling framework simple enough to identify the impact of an isolated physical variable over biogeochemistry, yet complex enough to reproduce observations under realistic physical scenarios and efficient enough (in terms of time and computing resources) to be repeated for a large number of times.

First of all, we defined an idealised seasonal cycle for the ocean physics. Our goal was to find the simplest physical framework able to reproduce a fairly realistic phytoplankton seasonal cycle. This physical framework was built as follows:

- Lateral advection was neglected. The biological seasonal cycle was assumed to be exclusively driven by vertical processes: light availability (from the surface to deep layers) and nutrient supply (from deep layers to the surface).
- The seasonal cycle of net downward shortwave solar radiation at the surface was represented by a sinusoidal function with minimal value centred at winter Austral solstice (21st June) and maximal at summer solstice (21st Dec). The amplitude corresponded to a solar cycle at the KERFIX station. We did not considered sub-seasonal variability (i.e., changes on cloudiness, sea surface albedo or aerosols) neither regions with the presence of (permanent or not) sea-ice. The seasonal cycle of surface solar radiation is represented in figure 3.10.A.

- The water column was roughly divided on two layers distinctive by its mixing: an upper actively mixed layer ($\kappa = 1m^2/s$) of depth Z_{mix}, and a bottom layer of low mixing ($\kappa = 10^{-5}m^2/s$). To avoid unrealistic responses we slightly modified this idealised κ vertical profile: the surface layer represents weaker mixing to account for friction with the atmosphere ($\kappa_{surface} = 10^{-4}m^2/s$) and transition between upper mixing layer and bottom waters at Z_{mix} was smoothed over 3 vertical levels (see figure 3.10.C).
- The seasonal cycle of the depth of mixing Zmix was divided into 3 phases: constant deepening (autumn-winter), constant shallowing (winter-spring) and stable (spring-summer) (see figure 3.10.B).

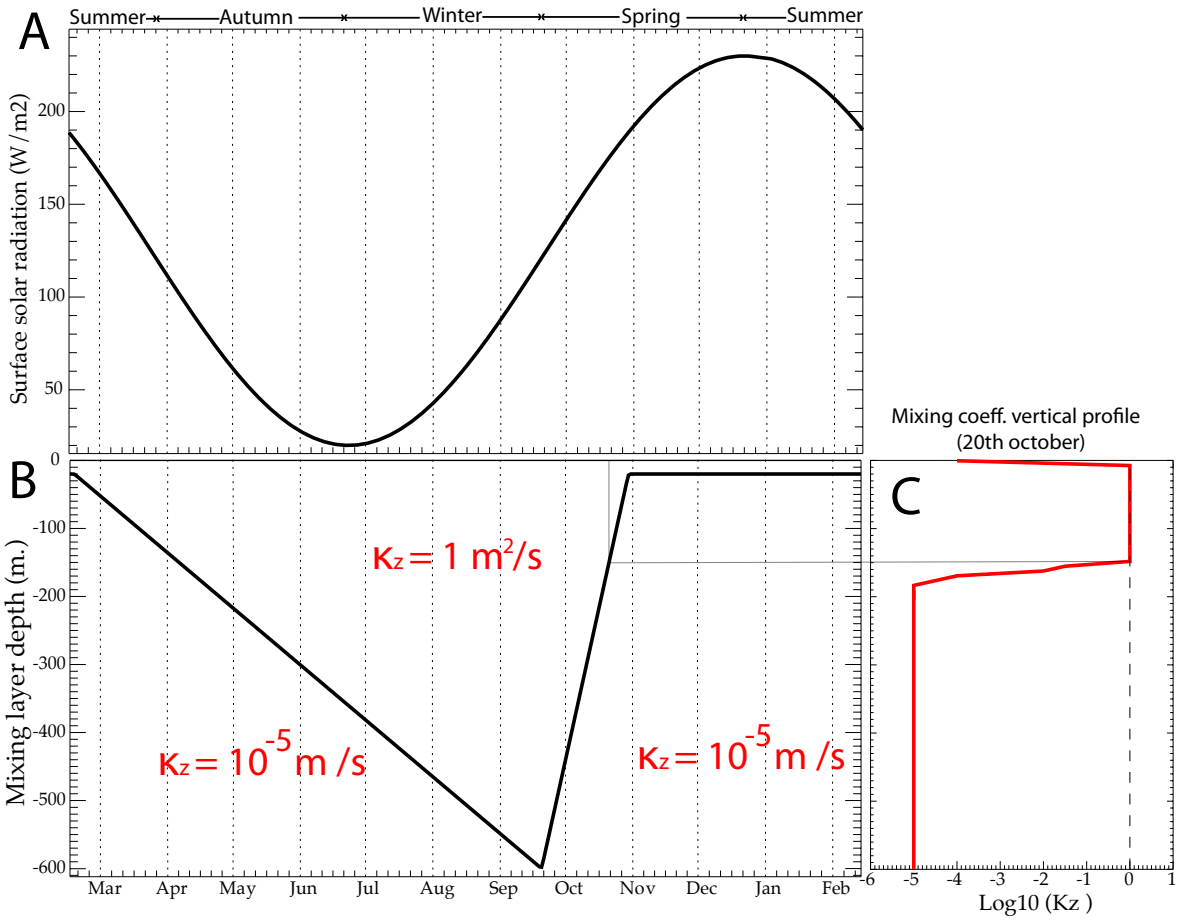

FIGURE 3.10: The physical idealised forcing. Surface solar radiation (A) and mixing layer depth seasonal cycle (B). Vertical profile of κ_z at the 20th October (C). The values of κ_z are also presented above and below mixing layer depth.

Seasonal variations on water temperature are known to influence specific phytoplankton growth rate (Eppley [1972]). However, after some sensitivity tests we concluded that, at the ranges of temperatures found in Southern Ocean (between 2 and 6°C), the temperature influence over phytoplankton seasonality was minor compared to the influence of mixing and Fe supply. A climatological temperature seasonal cycle extracted from a regional 3D configuration was used as reference cycle for the ensemble of runs.

Based on these assumptions, we created a frequency of 5 days for the physical forcing for a whole annual cycle coupled to the PISCES biogeochemical model. Coupling was done *offline* i.e., at each time-step (tuned to 6hours) a new set of values for those physical variables influencing the phytoplankton growth rate computation (light, turbulent mixing and temperature at each depth) was used as input for PISCES. Nutrient and plankton concentration was computed at each time-step based on the physical forcing and previous concentration.

Initial conditions

Runs started late austral summer (15th Feb). We assumed that at this date, mixing depth is the shallowest, iron is (mostly) depleted and grazing pressure is equilibrated to phytoplankton growth, maintaining a stable and low stock of biomass. To initialise the vertical nutrients profile (N, P and Si) we used mean profiles at the KERFIX station (on 15th Feb) from BIOPERIANT05-HIST05 configuraiton climatology (10-years mean). Silicate acid it is known to be a limiting factor for diatoms during strong bloom events in the Southern Ocean (Boyd [2002]) and PISCES accounts for this kind of limitation. However, we aimed to focus on the role of Fe input over phytoplankton growth and bloom dynamics. We re-defined Si initial profiles to an homogeneous concentration of 30μmol/l through water column and we tested the Si was not limiting during the blooming phase. Hereinafter, diatoms will be referred as microphytoplankton as we are not considering Si limitation.

In the Southern Ocean, Fe vertical supply is not fixed but results from the combination of two magnitudes: the maximal mixing penetration depth or maximal mixing depth (maxZ_{mix}) and the ferricline[8] depth (Z_{Fe}). These two magnitudes are, unlike nutrients stocks in other blooming regions, decoupled from each other (**?**) i.e., Z_{Fe} is usually deeper than winter mixing[9]. This decoupling creates an essential specificity of Southern Ocean biogeochemisty: some regions of the Southern Ocean have very deep winter mixing with year-long sustained Fe limitation. To ensure that our idealised model reproduces this Southern Ocean specificity (and associated phytoplankton seasonal cycle) in a realistic way, Fe supply resulted from the combination of Z_{Fe} and maxZ_{mix} (figure 3.11). Dissolved Fe initial profile was defined by assuming low concentrations (0.03 nMol/L) above a prescribed ferricline depth (Z_{Fe}), and larger concentrations (0.5 nMol/L) below (see central t-Z section in figure 3.12). This vertical distribution of iron is an idealised and extreme case that defines summer Z_{Fe} without ambiguity.

A simple *spin-up* procedure was set up: the model configuration was run for 3 years with Fe and macronutrients being forced to its their initial values at each summer, over the first 5 days

[8] Similarly to the nutricline, the ferricline is the depth at which the stock of iron becomes "important" (i.e., at least 0.5 nmolFe/L). It is usually defined as the depth of maximal $\frac{\partial Fe}{\partial z}$ (Tagliabue et al. [2011]).

[9] The reason for that is that Fe seems to be subjected to specific biochemical reactions that reduces concentration in upper layers.

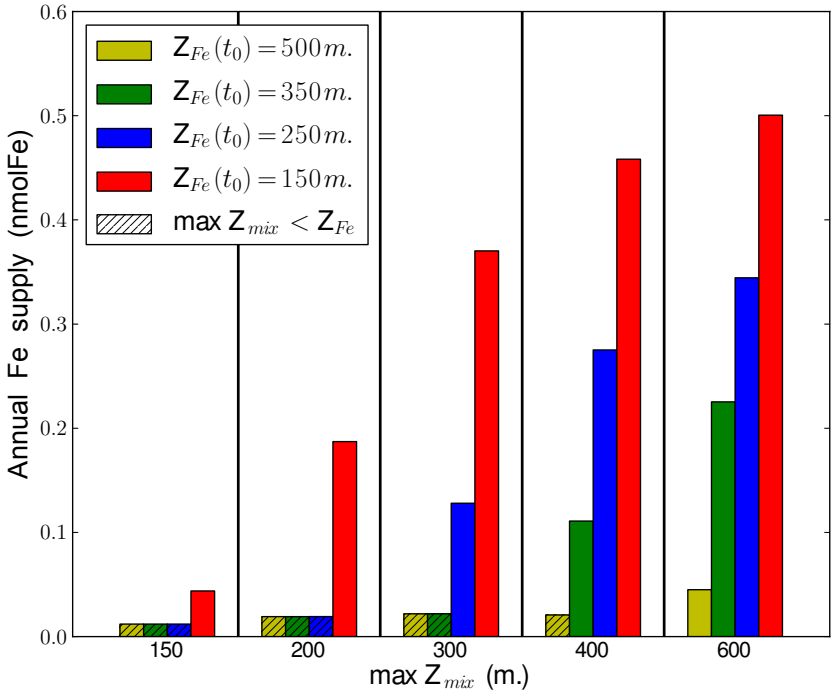

FIGURE 3.11: Histogram of the amount of Fe supplied to the first 50m. The distribution is obtained from the maxZ_{mix}/Fe-supply relationship for each of the 1,290 modelled scenarios. The bars for which winter mixing was shallower than ferricline are indicated with 45° black line pattern.

of the seasonal cycle. Initial conditions for the 4 plankton compartments (nanophytoplankton, diatoms, micro-zooplankton and meso-zooplankton) were set to low values for the first year and they achieved a stationary seasonal cycle after 2 years of running (figure 3.12). The results were based on the third year of simulation. Outputs were saved on a daily frequency. An example of the 3rd year daily outputs of mixing layer depth (forcing), surface Chl and integrated biomass (modelled) is presented in figure 3.13.

Multiple runs algorithm

As presented in introduction of this section, this configuration was set up to understand how the physical environment controls phytoplankton blooms by conducting a series of sensitivity tests. The 1D *offline* biogeochemical model has the advantage of reducing uncertainties derived from the physics model and, at same time, the possibility of tightly controlling the physical environment at the seasonal scale. With the aim to reproduce the physical conditions encountered around the Southern Ocean and study how they impact over phytoplankton seasonality; an algorithm was written to automatically create idealised physical *scenarios* and force the PISCES 1D configuration with them. Our hypothesis was that the bloom phenology diversity in Southern

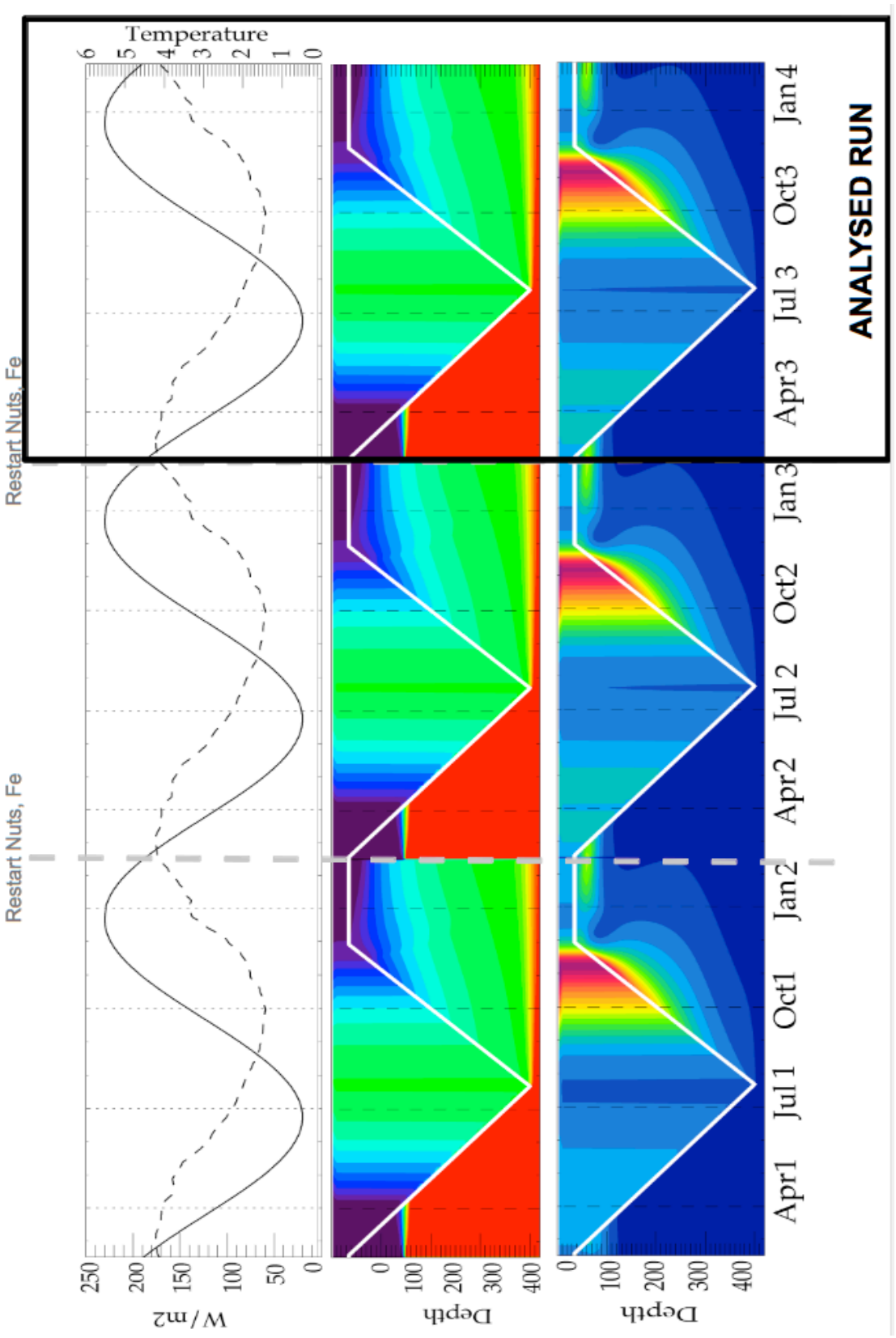

FIGURE 3.12: Procedure to obtain a stable seasonal cycle thanks to a 2-years spin-up. TOP: Surface solar radiation (solid black line) and temperature (dashed black line) seasonal cycle during 3-years. MIDDLE: Vertical section of the seasonal evolution of Fe concentration from 0 to 400m for the three years; Z_{mix} is represented by a white line. BOTTOM: Vertical section of the seasonal evolution of Chl concentration from 0 to 400m for the three years; Z_{mix} is represented by a white line. Dashed grey vertical lines indicate the dates of Fe(z) and nutrients re-initialisation.

A black box indicates the 3-year of the run, the only seasonal cycle used for the results.

Ocean open waters (as identified by Arrigo et al. [2008] and Thomalla et al. [2011]) is due to the combination of mixing seasonality (i.e., magnitude and timing) an iron supply.

To create a large number of Southern Ocean mixing-iron supply scenarios we decomposed mixing depth seasonal cycle in 4 descriptors (presented in figure 3.13)

i The winter maximal mixing depth (maxZ_{mix})

ii The summer minimal mixing depth (minZ_{mix})

iii The date at which maxZ_{mix} is reached ($t_{maxZ_{mix}}$)

iv The date at which minZ_{mix} is reached ($t_{minZ_{mix}}$)

and an additional descriptor for initial (i.e., summer) ferricline:

v The summer ferricline depth (Z_{Fe}).

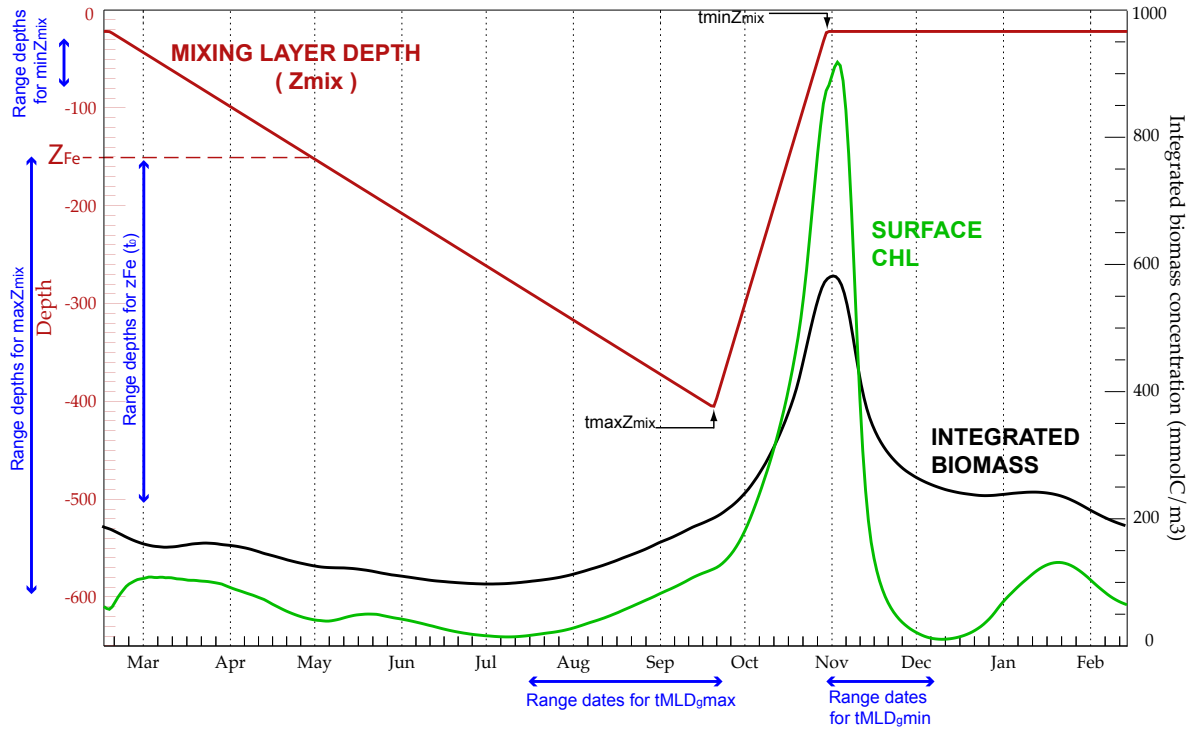

FIGURE 3.13: Seasonal cycle of Zmix (red line), Integrated phytoplankton biomass (black line) and surface chlorophyll (green line) for one of the modelled blooms. The red horizontal dashed line marks the depth of the summer ferricline (ZFe).

The discrete sampling of values for those 5 seasonal descriptors was aimed to cover the whole range of observed values. The range of maxZ_{mix} and minZ_{mix} values was based on over 500,000

density profiles sampled by Argo floats data (Sallée et al. [2010b]). The range of Z_{Fe} values was based on a recent compilation of dissolved iron measurements in the Southern Ocean, presented in Tagliabue et al. [2011]. The ranges covered by each of these descriptor are illustrated in 3.13 with blue arrows.

Based on these 5 seasonal descriptors and its values, the algorithm created an ensemble of more than 1,200 scenarios by repeating the following procedure:

0. The algorithm assign one of the sampled values to each of the corresponding descriptors.

1. A complete seasonal cycle of MLD and κ_z is defined in "pre-existing" forcing files[10] based on the values assigned to Z_{mix} in step 0.

2. An initial Fe profile is defined in a "pre-existing" *restart*[11] file (the reference *restart* file) is based on the value assigned to Z_{Fe} Fe profile in step 0.

3. The initial vertical profiles for all nutrients are forced in the reference *restart* file using pre-defined nutrient profiles (see text for details) and the Fe profile created in step 2.

4. A new loop is opened and following sub-steps are repeated twice:

4a. The model is run for 12 months initialised with the reference *restart* file of steps 2-3 and forced by forcing files of step 1.

4b. Initial vertical profiles for all nutrients are forced by the reference *restart* file using nutrient and Fe profiles created in step 2. Unlike step 3, the four biological compartments (phyto- and zooplankton groups) are let free to evolve: initial value of year n is equal to last value of year n-1.

5. The model is run for 12-months once more (3rd year) and the outputs are saved.

A consequence of the automatic sampling of values for each descriptor is that all values had the same probability to appear. Such an assumption can not be compared with the "real" (i.e., unattainable) distribution of values in the Southern Ocean. Instead, we compared the available distributions of MLD and ferricline data in the observations databases with the values sampled by the algorithm (figure 3.14). Modelled scenarios well reproduced (i.e., the 50% of cases around median value) ferricline depths in the main range of observations[12] (figure 3.14a). Mixing depth distribution in the modelled ensemble (in figure 3.14) is slightly biased with too deep maxZ_{mix} and too shallow minZ_{mix}. Such a bias is intentionally created: observations (even those based on Argo floats) tend to be smoother than "real" conditions and extreme values are very often

[10] The same forcing files are modified at each loop.

[11] *Restart* files are usually used to start a model configuration based on a precedent one. The state of the system in the last timestep of the "old" run is used as starting point for the "new" run. Here we used *restart* model feature to initialise a new run with a Fe profile defined by the algorithm instead of by a precedent run.

[12] These observation were compiled by Tagliabue et al. [2011]

under-sampled due to averaging or sensors resolution. Our aim was to explore the whole range of realistic physical environment but specially those extreme cases that are under-sampled due to its rareness.

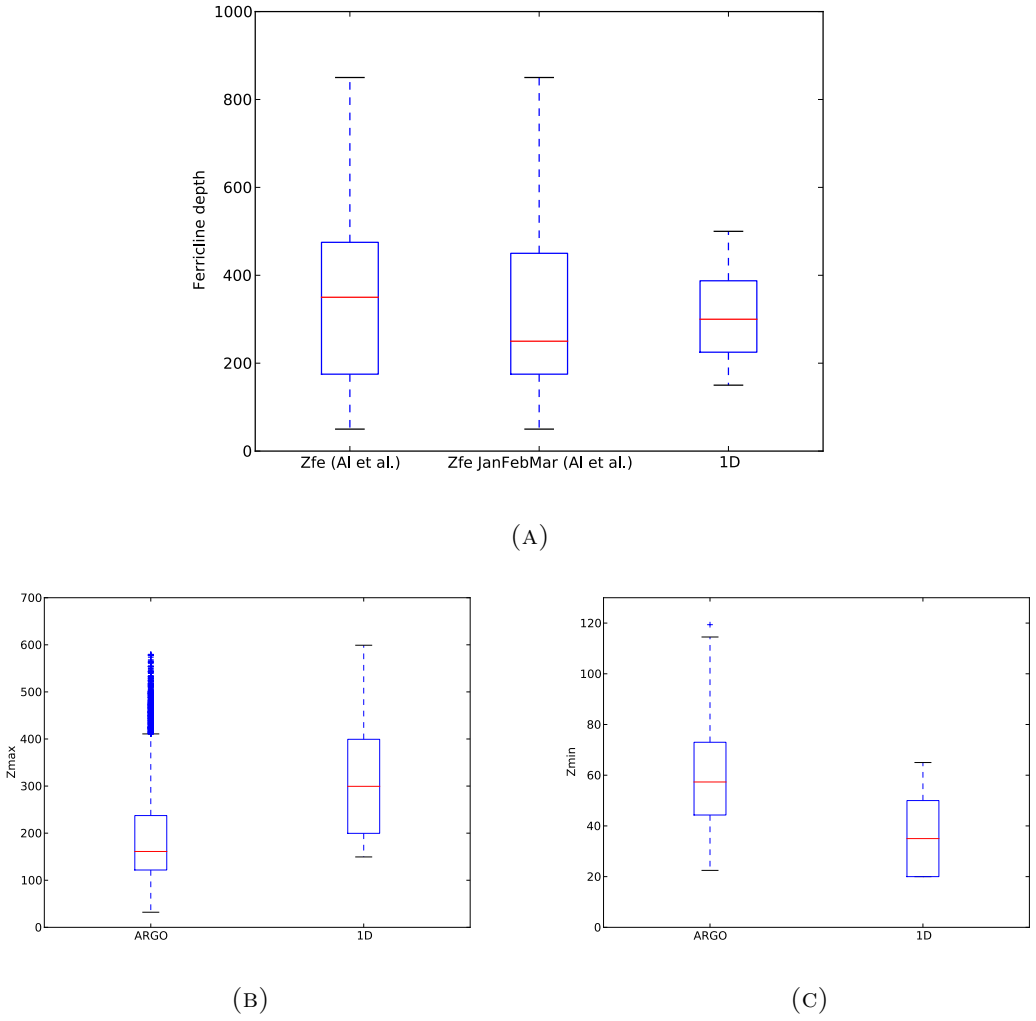

FIGURE 3.14: Box and whisker plots comparing the distribution for Z_{Fe} (year mean and in summer) and summer imposed Z_{Fe} in 1D configuration (A); observed MLD_{max} and modelled $maxZ_{mix}$ (B); observed MLD_{min} and modelled $minZ_{mix}$ (C). The size of the box represents the quartiles 1–3, with the vertical bar corresponding to the median and the whiskers representing 1.5 times the inter-quartile range.

The whole range sChl and MLD cycles reproduced in the ensemble of runs is represented by the grey surface in 3.15, where I compared it with observations data in the KERFIX station.

It must be reminded that modelled scenarios were not meant to reproduce the seasonal cycle of sChl in the KERFIX station, but to represent the diversity of seasonal cycles in the open waters of Southern Ocean. The comparison with KERFIX station 3-years timeseries was presented to show how *in-situ* data fits in the space of modelled blooms. However, this comparison it also suggested that, in average, modelled bloom tended to occur earlier than observed ones. Such a premature onset was related to the growth rate formulation chosen for the 1D model configuration. Amongst

the four options to compute the phytoplankton growth (see 3.2), we chosen the *oldprod*/*oldpenal* option (i.e., standard code version) for the 1D configuration. We decided to use the standard code version (instead of the *newpenal* option that improved bloom timing in the 3D configurations) because the strict winter penalisation was likely to influence bloom controls. Using *newpenal* option, production was strongly reduced in winter when MLD is deeper than euphotic layer. On the contrary, production raises in spring when the penalisation disappears and surface layers are rich in nutrients. Hence, a "Sverdrup's like" onset (bottom-up controlled) was likely to occur. The ensemble of 1D runs was mainly created to address the processes that govern bloom onset and phenology, and to compare the importance of both bottom-up (light, growth rate) and top-down (grazing) controls over the bloom, especially in winter. Dismissing the new winter penalisation we were not imposing a "preference" for any of the controls.

Exploiting outputs

The final phase of our methodology was to explore the large number of modelled scenarios. Each one of the outputs files contained more than 30 different physical and biogeochemical variables such as nutrients concentration, light and iron limitation for each phytoplankton group or grazing rates. Our aim was not to understand each of these scenarios in detail but to infer causality relationships between variables from the behaviour of the ensemble of scenarios. To do so in a efficient way, we defined a set of "bloom diagnostics" which described and quantified features of phytoplankton seasonal cycles. Some example of bloom diagnostics were the maximal Chl concentration, the date at which this maxima was attained, the amount of iron injected into upper layers or the total integrated PP.

A series of algorithms were then written to go through all outputs files, apply such diagnostics to each scenario and save resulting values into an ASCII file. In the same file several physical descriptors (such as maximal winter mixing depth, mixing layer date of max and min or initial Z_{Fe}) of each scenario were also saved. The ASCII file contained the same number of lines as the different scenarios and with several columns containing saved physical descriptors and bloom diagnostics values. Representing the scatter plots between a physical descriptor and a bloom diagnostics was possible to establish statistical links between the environment and the bloom dynamics. For instance, we found that the maximal concentration of surface Chl is mainly controlled by the amount of Fe supplied into the upper 50m. layer (figure 3.16). The Z_{mix} re-stratification speed was identified as a secondary control of the bloom magnitude (colors in figure 3.16). It is interesting to note that how both the re-stratification speed and the iron supply combine to drive sChl maxima.

These algorithms were continuously being improved and the set of bloom diagnostics developed while the study advanced, as we felt it necessary to focus on new variables. The ≈1,200 modelled

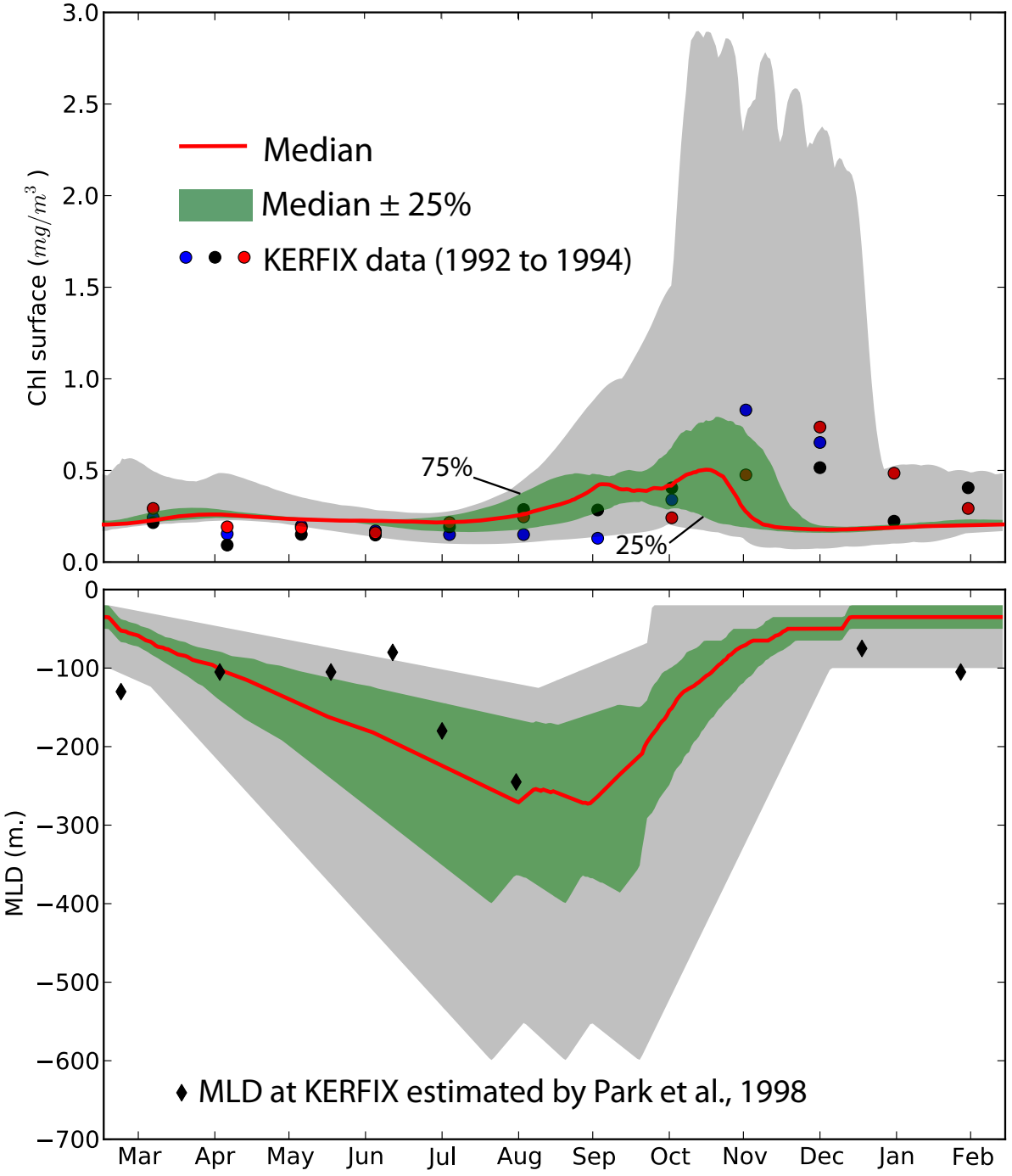

FIGURE 3.15: The sChl (TOP) and Z_{mix} (BOTTOM) seasonal cycles of all modelled scenarios. The median and the area covered by the 50% of runs around the median value (red line) is represented by the green area. 3-years sChl time-series and MLD (estimated from *in-situ* data by in Park et al. [1998]) at the KERFIX station are represented by dots (for sChl) and diamonds (for MLD). Dots color differentiate the year.

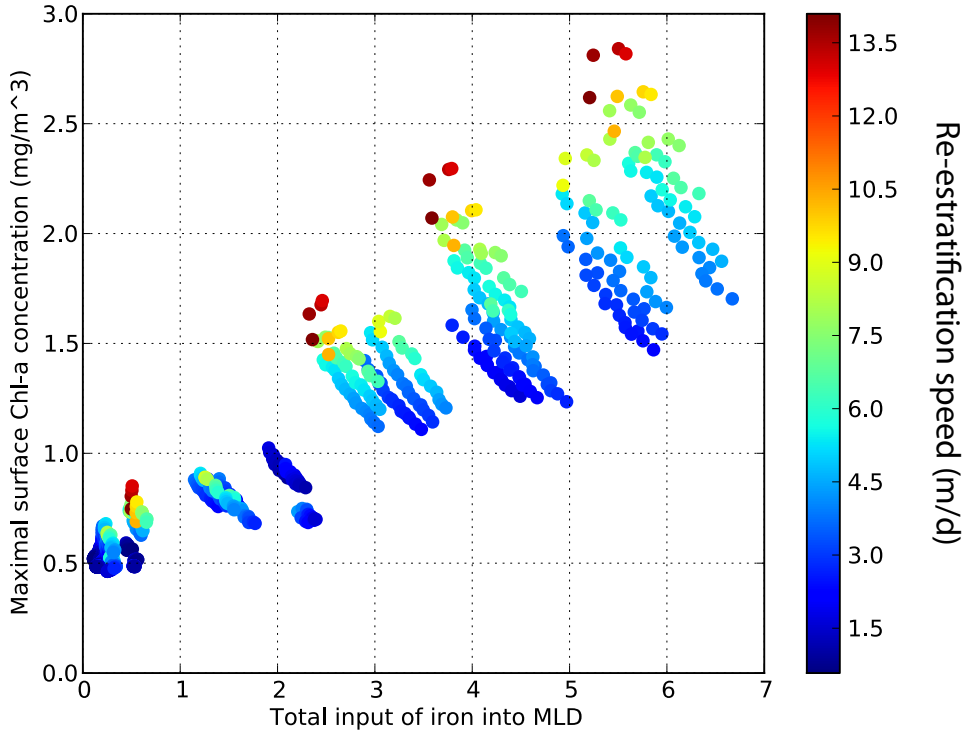

FIGURE 3.16: Maximal surface Chl concentration as a function of iron input into surface layer and Z_{mix} re-estratification speed (in color). Each circle stand for a modelled bloom.

scenarios were used as a huge database: a kind of a virtual Southern Ocean with "fully" resolved biogeochemical cycles (from surface to 2000m and for 365 days of the year) which could be easily sampled.

Results

Chapter 4

Bloom dynamics: mechanisms and phenology

4.1 Introduction

As presented in introduction, two different approaches were adopted to understand phytoplankton seasonal variability in the Southern Ocean. The first approach aimed to disentangle the elemental mechanisms underneath blooms dynamics and, once this mechanisms identified, to understand how they interact to produce bloom diversity observed in the Southern Ocean. In this chapter, I address the first aspect using a simple and idealised conceptual framework of the bloom evolution in an isolated water column.

Identifying the drivers that lead bloom dynamics is a long-time discussed question in biogeochemical oceanography. A number of authors have addressed it using theories (Sverdrup [1953], Huisman et al. [1999]), models (Taylor and Ferrari [2011], Behrenfeld et al. [2013a]) and data (Behrenfeld [2010],Chiswell [2011]); even if most of them focused on the North-Atlantic region. Here, we will try to extrapolate these theories to the specific case of the Southern Ocean using an idealised physical seasonal cycle to force a complex biogeochemical model. As argued in the bloom onset theories review by Behrenfeld and Boss [2014], biogeochemical models are an excellent tool to study phytoplankton blooms. The reason is that models do not presume any hypothesis for bloom formation: blooms emerge from the fundamental equations that describe plankton community and its dependency with physical environment.

Based on such premise, we aimed to understand how physical environment (through bottom-up controls: turbulent mixing, light, iron supply) and plankton ecosystem (through top-down controls: grazing and mortality) interact and influence bloom initiation, evolution and collapse. To reduce uncertainties we set up a novel 1D model configuration that recreated phytoplankton seasonal cycle under an idealised but "flexible" physical environment. Such configuration allowed us to create more than 1,000 different bloom scenarios that fairly reproduced the different environment encountered in Southern Ocean open waters. A statistical analysis of the ensemble of scenarios permitted to identify three major bloom phases: the onset, the climax and the apex. Moreover, we identified the dominant control for each of these bloom phases. Finally, using the complete set of data provided by the biogeochemical model, we tested different bloom detection methods commonly used in literature. Comparing these methods to the integrated bloom descriptors, we demonstrated how each bloom phase can be identified by a different detection criterion. In chapter 5 we will use these ideas to address bloom diversity observed by satellite data in the Southern Ocean.

4.2 *Onset, intensification and decline of phytoplankton blooms in the Southern Ocean* (Article)

Llort, J.; Sallée, J.B.; Lévy, M.; Tagliabue, A.

Article in minor revisions to ICES JMS special issue "60 years since Sverdrup's critical depth hypothesis"

Abstract

The seasonal cycle of phytoplankton biomass in the Southern Ocean (SO) is characterised by a period of rapid accumulation, known as bloom, that is typical of high-latitude regions. Recent studies have illustrated how spatial and temporal dynamics of blooms in the SO are more complex than in other oceans. This complexity is likely related to differences in vertical mixing and the depth of subsurface nutrient reserves, whose combination influences the bottom-up and top-down controls on biomass accumulation. In this work we examine the sensitivity of bloom dynamics to changes in mixing and depth of nutrient reserves using a biogeochemical model. Under idealized physical forcing, we produce seasonal cycles phytoplankton dynamics for an ensemble of SO scenarios and using our model, we describe the various blooms based on the rate of net biomass accumulation. Based on this metric, we define three crucial events in the evolution of phytoplankton blooms: the onset, when biomass first starts to accumulate; the climax, when this increase is the fastest; and the apex, when accumulation is maximal. We find that onsets, although always occurring in winter, can be bottom-up and top-down controlled. Climaxes are mostly found in spring and their magnitudes are bottom-up controlled by mixing and iron concentration. Apexes are always found in late spring and strongly top-down controlled. Using our model data to mimic the detection of blooms using ocean colour datasets, we find an appropriate biomass-based criteria is well suited to detecting onsets, while climaxes require a surface chlorophyll–based criteria. Our results also suggest that the Sverdrup critical depth criteria detects bloom climax rather than bloom onset. We suggest that the recent bloom onset debate may partly be due to a confusion between what is defined as the bloom onset and climax.

Introduction

The Southern Ocean (SO) is the largest High-Nutrient Low-Chlorophyll (HNLC) region in the world's ocean. Its relatively low productivity has been attributed to a combination of lack of iron (Martin et al. [1990]), elevated grazing and light limitation (Boyd and Ellwood [2010]). Despite these unfavourable biological growth conditions, large accumulations of phytoplankton biomass, or blooms, are observed in surface waters each spring over wide areas of the Southern Ocean (Thomalla et al. [2011]). The distribution of these blooms is very patchy in space and time.

Hot-spots of phytoplankton accumulation are mainly seen where sources of iron are significant, i.e., in the lee of Islands (Moore and Abbott [2000]; Arrigo et al. [2008]). Additionally, the bloom onset dates are rather spread in time, from October to January (Thomalla et al. [2011]), and do not show a clear latitudinal pattern. This is unlike the pattern for North Atlantic spring bloom which is zonal and propagates from South to North (Siegel [2002], Lévy et al. [2005]). The variability of bloom dynamics in the SO in terms of their amplitude, timing and location has been mainly documented for ocean colour observations (Moore and Abbott [2000], Arrigo et al. [2008], Thomalla et al. [2011]). However, the drivers of the observed variability remains unclear. We hypothesise that patchy environmental conditions, involving zonally asymmetric mixed-layer distributions (Sallée et al. [2010b]) combined with equally complex dissolved iron distributions (Tagliabue et al. [2011]; Tagliabue et al. [2014b]) are mostly responsible for the complex SO patterns.

Our current understanding of phytoplankton bloom dynamics mainly comes from work in the North Atlantic (NA), where the mixed-layer, nutrient and atmospheric environment are largely different than in the Southern Hemisphere. Historically, the emergence of blooms has been related to thinning of the layer of active vertical turbulence at ocean surface (hereafter referred to as 'mixing-layer', or Zmx, to be distinguished from the usual 'mixed-layer depth' or MLD), as this thinning implied an increase of averaged exposure of phytoplankton cells to light (Riley [1942]). Along with this bottom-up view, Sverdrup [1953] proposed that bloom would start when surface mixing-layer crosses a critical depth above which integrated phytoplankton growth would overcome phytoplankton losses (Siegel [2002]).

As an alternative to the bottom-up understanding of ocean blooms, a top-down view has also emerged. This view proposes that, in essence, the causes of phytoplankton concentrations can not be fully understood without considering the role of their main predator, zooplankton (Banse [1994]). The top-down hypothesis has gained interest recently via a series of papers that challenged the prevailing 'bottom up' paradigm (Behrenfeld and Boss [2013]). Using various tools (satellite data: Behrenfeld [2010]; float data: Boss and Behrenfeld [2010]; and model estimates: Behrenfeld et al. [2013a]), it has been suggested that the North Atlantic spring bloom does not initiate in spring alongside thinning mixing-layers, but rather in winter when mixing-layer is still expanding. This winter initiation is consistent with the hypothesis that dilution enables phytoplankton to better escape their predators and accumulate biomass (Evans and Parslow [1985]; Marra and Barber [2004]).

In this context, our primary objective is to examine the drivers of phytoplankton blooms over the full range of Southern Ocean environmental conditions. In particular, we examine how different environmental conditions (mixing-layer depth, ferricline, solar radiation) result in bottom-up or top-down control. To that end, we extend a framework in which the rate of net biomass accumulation (r) results from a competition between growth (μ) and loss (l) of phytoplankton:

$r = \mu - l = \frac{1}{P}\frac{dP}{dt}$, with P the total biomass of phytoplankton present in the water column (Riley [1942], Sverdrup [1953]; Behrenfeld [2010]). At equilibrium, phytoplankton growth and loss are in balance and phytoplankton population remains stable. This balance can be disturbed by a sudden change in iron supply, light conditions or stratification in isolation or in combination, which would then likely affect μ and l in different ways. Our overarching question is how such perturbations modify μ and l at seasonal scale, and which term is the most sensitive to a given perturbation and the most effective at driving variations in r (i.e. phytoplankton population fluctuations). One of the key aspects of our approach is that we examine three important steps in the annual cycle of blooms: the bloom onset, climax and apex. Using time evolution of r, we define these bloom steps as follows:

1. The bloom **onset** is when total biomass starts to accumulate.
2. The bloom **climax** occurs when the rate of biomass accumulation is maximal. After this instant, accumulation of phytoplankton continues but at a slower rate because ecosystem has yet started its way to readjustment (i.e.: to recoupling).
3. Finally, the bloom **apex** marks the peak in total biomass, i.e.: the time after which $l > \mu$ (recoupling is actually achieved) and accumulation starts decreasing.

Figure 4.1 illustrates the three steps associated with the time of minimum integrated biomass (onset), of maximum slope of integrated biomass (climax) and of maximum integrated biomass (apex). This distinction complements previous studies on bloom dynamics that focused either exclusively on onset (Sverdrup [1953]; Behrenfeld [2010]) or on climax (Ferrari et al. [2014]; Lozier et al. [2011]). We address the question of bloom drivers in the SO in the framework of a numerical model. This model uses a state of the art biogeochemical network (Aumont and Bopp [2006]) within a vertically discretized 1D water column configuration where vertical mixing is the main physical process. Aiming to examine the full range of Southern Ocean conditions, we perform statistical analyses using an ensemble of 1,200 model simulations with distinct seasonal cycles of mixing-layer depth, ferricline and solar radiation. Bloom onset, climax and apex dates are diagnosed for each run in the ensemble. Simultaneously, the distributions of variables such as iron supply, mixing-layer depth, light, phytoplankton growth and loss rates for each of the three bloom stages are attributed to drivers. Furthermore, we investigate when bottom-up or top-down controls prevailed. This model allows us to test existing theories on bloom onset in an idealized and comprehensive framework, and to discuss them in the context of the Southern Ocean.

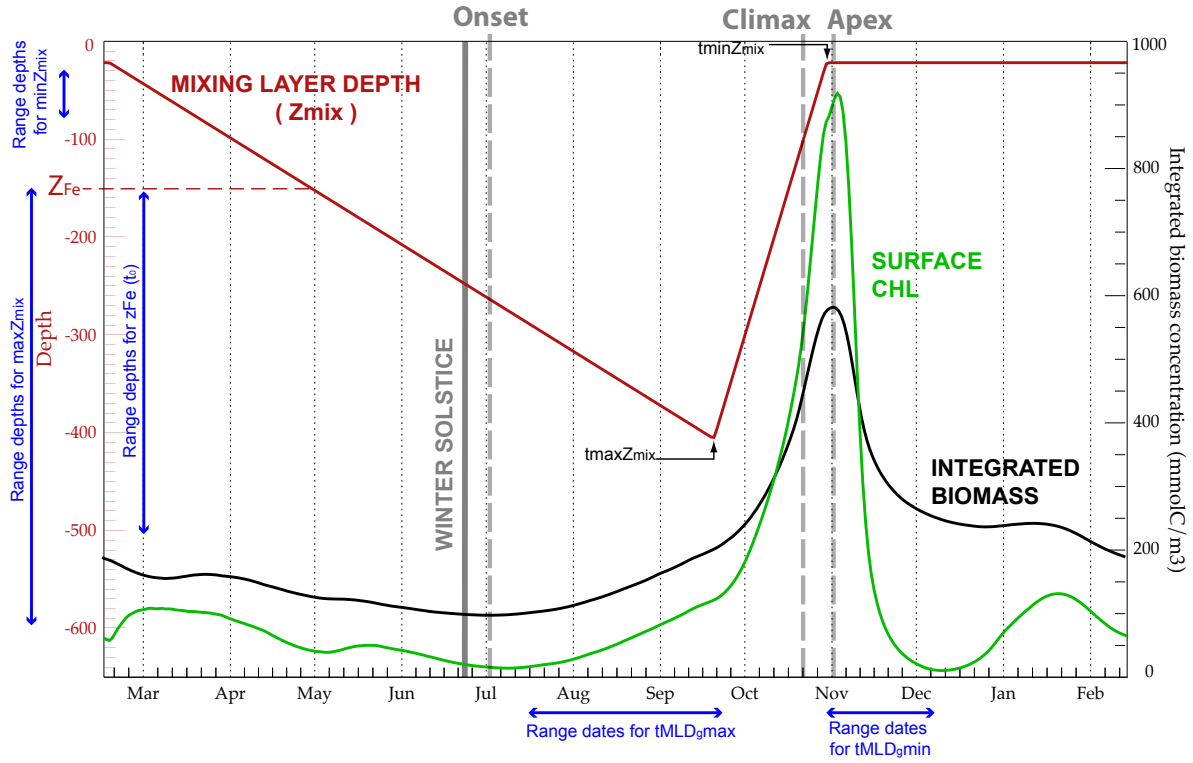

FIGURE 4.1: Seasonal cycle of Z_{mix} (red line), Integrated phytoplankton biomass (black line) and surface chlorophyll (green line) for one of the modelled blooms. The red horizontal dashed line marks the depth of the summer ferricline (Z_{Fe}). The vertical grey solid line indicate the date of the Winter solstice (21st June). Vertical grey dashed lines indicate the three bloom stages: onset, climax and apex. Blue arrows show the range of values tested in the ensemble of runs.

Methods

Biogeochemical model

The model was set up to represent the Permanent Open Ocean Zone (POOZ) of the Southern Ocean, away from ice formation and melting, where nitrate and silica do not limit productivity. Our goal in this study is to untangle how the different phases of a bloom (onset, climax, apex) are controlled by their physical and biogeochemical environment. As such, we deliberately chose to reduce the complexity of the problem by considering a 1D physical framework (e.g, lateral advection is neglected). Varying vertical diffusion reproduces seasonal cycle of the mixing-layer depth. Along with this idealised physical configuration, we model the associated biogeochemical activity with the model PISCES (Aumont and Bopp [2006]). PISCES contains 24 biogeochemical tracers with five nutrients able to limit phytoplankton growth: Nitrate, Phosphate, Ammonium, Iron and Silicate. The iron pool is explicitly modelled and controlled by a range of processes such as phytoplankton uptake, bacterial uptake, zooplankton and bacterial recycling, remineralisation and scavenging. In addition, four living pools are represented: two phytoplankton size classes (e.g.: small and large) and two zooplankton size classes (microzooplankton and mesozooplankton). Large phytoplankton differ from the small phytoplankton by higher requirements

in Fe and a greater iron half-saturation constant. Grazing pressure on each phytoplankton is also differentiated by size: microzooplankton (Z) preferentially grazes small phytoplankton while mesozooplankton (M) preferentially grazes the larger phytoplankton but also microzooplankton.

Prognostic equation for each phytoplankton group (i=1,2) is:

$$\frac{\delta P_i}{\delta t} = \mu_i P_i - g_i^Z(P_i)\ Z - g_i^M(P_i)\ M - m_i P_i + \frac{\delta}{\delta z}\left[\kappa_z \frac{\delta P_i}{\delta z}\right] \qquad i = 1,2 \tag{4.1}$$

where P_i is the biomass, μ_i is the growth rate, g_i represents the grazing rate and m_i the mortality rate. The last right hand side term is the effect of vertical diffusion over biomass due to vertical mixing of intensity κ_z. The growth rate (μ_i) was computed as follows:

$$\mu_i \ = \ \mu_{max}\ f_i(T)\ h(z) \left(1 \ - \ \exp \frac{-\alpha_i\ Q_i^{Chl}\ PAR_i}{\mu_{max}\ f_i(T)\ L_i} \right) L_i, \qquad i = 1,2 \tag{4.2}$$

where $f_i(T)$ is the dependency of the growth rate with temperature (Eppley [1972]), h(z) a penalisation term for deep mixing, PAR_i is function of the shortwave radiation at the surface, α_i is the initial slope of the P-I curve, Q_i^{Chl} the Chl:C quota for each phytoplankton and L_i is the nutrient limitation. Nutrients limitation in our set-up can only be due to Fe, so $L_i \equiv L_i^{Fe}$ where:

$$L_i^{Fe} \ = \ min\left(1,\ max\left(0,\ \frac{Q_i^{Fe} \ - \ Q_{i,min}^{Fe}}{Q_{i,opt}^{Fe}}\right)\right). \tag{4.3}$$

Iron limitation is formulated following a *Quota* approach (Droop [1983]) with the term $Q_{i,opt}^{Fe}$ allowing luxury uptake (as in Buitenhuis and Geider [2010]). The model equations were computed on a regular vertical grid of 74+1 vertical levels (constant spacing of 7m for the first 74 levels and a last one of 500m depth) and a time step of 20 minutes. The vertical mixing coefficient (κ_z), temperature and surface photosynthetic available radiation (PAR) were analytically prescribed every six hours. Vertical mixing coefficient were assumed to be constant and equal to 1 m^2s^{-1} within a surface mixing-layer of depth Zmx, and equal to 10^{-5} m^2s^{-1} below. We imposed an idealized seasonal cycle of the Zmx with three phases: a fall/winter phase associated with convection and progressive deepening of the Zmx; a spring phase where cessation of convection lead to the thinning of the Zmx; and a summer phase where Zmx is relatively shallow and constant (red curve in figure 4.1). To ensure that the timing of these phases and the magnitude of the Zmx were relatively realistic we used data estimates derived from Argo data (Sallée et al. [2010b]), which provided us with an estimate of the depth of the seasonal thermocline in the SO, which we assume reflects the mixing depth. Sub-seasonal variability in the Zmx was not accounted for. For temperature and surface PAR, we used a smoothed climatological seasonal cycle constructed from observations (DFS3-ERA40 Brodeau et al. [2010]) averaged over the 40-60°S latitudinal band.

The summer initial condition for dissolved Fe profile was constructed by assuming low concentrations (0.03 nMol/L) above a prescribed ferricline depth (Z_{Fe}), and larger concentrations (0.5 nMol/L) below. The depth of the ferricline for the initial condition iron profile is one of the parameters we vary in our set of simulations. It is generally understood that the summer Fe profile is set by a combination of remineralization, scavenging and physical supplies by lateral sources. While remineralization and scavenging are parameterised in PISCES, there remains a large degree of uncertainty in the parameterisation. Lateral supplies, on the other hand, were not explicitly accounted for. To overcome these issues and, at the same time, to allow the model to reach a repeating and stationary seasonal cycle, the dissolved iron profile was restored towards its initial value at the end of each summer. The restoring was done over 5 days. Initial vertical profiles for N, P and Si were constructed based on the winter mean profiles collected in KERFIX station (Jeandel et al. [1998]). As for Fe, macronutrients were restored to its their initial values at each summer over 3 years. Initial conditions for the four living compartments were set to low values for the first year. They achieved a stationary seasonal cycle after 2 years of run. The simulations were integrated for 3 years, starting in Austral summer (15th Feb), with outputs saved at daily frequency. Results are based on the third year of simulation. As an example, figure 4.1 shows a complete seasonal cycle of integrated biomass (black curve), surface Chl (green), Z_{mix} (red) and summer Z_{Fe}, for one of these runs.

Ensemble runs

An ensemble of runs was performed by varying the Z_{mix} and summer Z_{Fe} in the range of values found in the POOZ. Specifically:

i The winter maximal mixing depth (maxZ_{mix})

ii The summer minimal mixing depth (minZ_{mix})

iii The date at which maxZ_{mix} was reached ($t_{maxZ_{mix}}$)

iv The date at which minZ_{mix} was reached ($t_{minZ_{mix}}$)

v The summer Ferricline depth, Z_{Fe}

The variables i-v were set based on among a discrete set of observed values, with equal weight given to each discrete value (see ranges in figure 4.1, blue arrows). The ranges for Z_{Fe} were established on the basis of a recent compilation of dissolved iron measurements Tagliabue et al. [2011], the ranges of values used to set Z_{mix} is based on more than 500,000 density profiles sampled in SO by Argo floats data (Sallée et al. [2010b]). Our choice of variables led to an ensemble of almost 1,200 different scenarios that combine different values of the above parameters i-v that cover a wide range of Z_{mix}/Z_{Fe} observed in the SO.

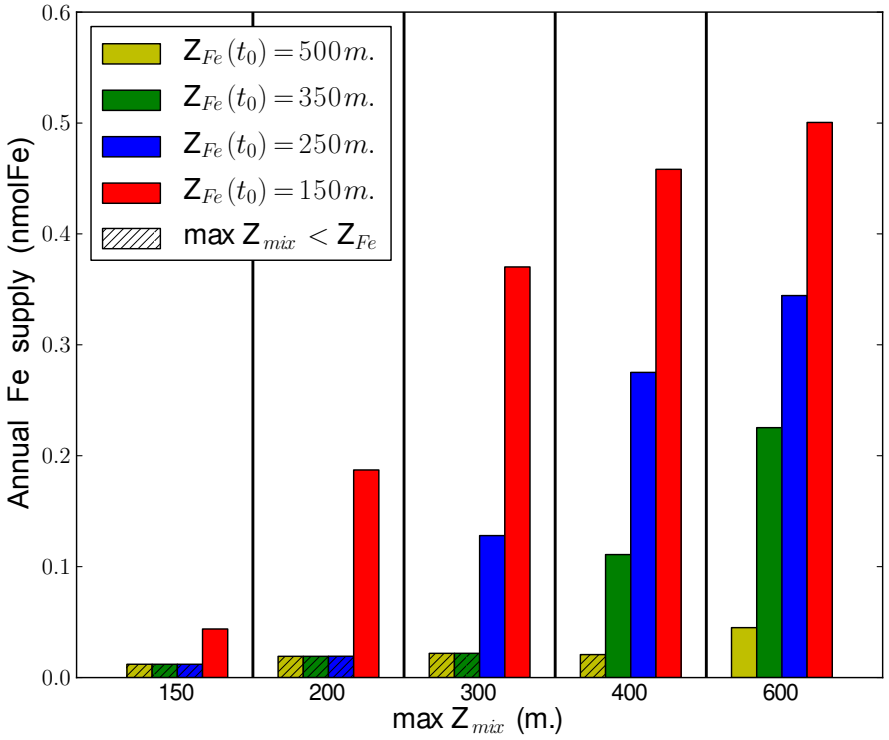

FIGURE 4.2: Histogram of the total amount of Fe supplied to the 0-50m. surface layer as a function of the maxZ_{mix} and the summer ferricline (colors).

In our model, the amount of Fe injected at the surface each year is not prescribed: Fe is entrained in the mixing layer durint the deepening phase. Thus, the Fe supply depends on the relative depths of the ferricline and maxZ_{mix} (Fig. 2). The relationship between both variables is however non linear, due to the effects of consumption/remineralisation by the biological community and the rate of stratification/destratification. A peculiarity of the SO is that the ferricline depth is often found below the maximum winter mixed layer depth (Tagliabue et al. [2014b]), implying some regions permanently Fe-limited despite strong and deep winter mixing. In our scenarios, this situation occurs when Z_{Fe} is greater than maxZ_{mix} (figure 4.2). Note that this is different from other high-latitude productive regions such as the NA, where nitrate is the main limiting nutrient. In the NA, the depth of winter mixing and the convective nitrate supplies are more tightly correlated than its SO counterpart (depth of winter mixing and convective Fe supplies).

Bloom onset, climax and apex

In this study, we decompose the bloom phenology in three main events based on the rate of net biomass accumulation (r), which writes as:

$$r = \frac{1}{P^{int}} \frac{dP^{int}}{dt}, \quad \text{whith} \quad P^{int} = \int_0^H P dz \tag{4.4}$$

with H the depth of the water column. For simplicity, hereinafter we will refer to P^{int} as P. From the seasonal evolution of r, we define the bloom onset (total biomass starts to increase: P_{min}, $r = 0$ and $r' > 0$; hereafter all temporal derivatives are marked by a prime, i.e., $r' = \delta r/\delta t$); the bloom climax (the rate of accumulation is maximum: $r = r_{max}$ and $r' = 0$); and the bloom apex (bloom peaks in total biomass: $P = P_{max}$, $r = 0$ and $r' < 0$). See figure 4.1 where the three steps are reported. We note here that r is computed in our study from a total water column integral, which slightly differs from what is done in Sverdrup [1953] or Behrenfeld [2010] where P was integrated down to the base of the mixing-layer. As Chiswell [2013] pointed out, mixing layer integration of P might be misleading when the mixing layer restratifies as plankton is not conserved in the Z_{mix}. Integrating over the whole water column overcomes the discontinuity issue pointed out by Chiswell [2013].

Integrating equation 4.1 and dividing all terms by P^{int}, r can be written as the integrated balance between phytoplankton source (i.e., growth rate, μ) and sinks (i.e., grazing and mortality rates, g and m respectively):

$$r = \mu - g - m \tag{4.5}$$

Hence, the evolution of modelled ecosystem in the column water can be synthesized as:

$$r = \mu - l \tag{4.6}$$

with μ as the mean growth rate of the total depth integrated phytoplankton community, and l as the sum of grazing and mortality.

Bloom timing

In our set of experiments, the time of the deepest convection ($t_{maxZ_{mix}}$) can vary by up to two months between experiments, and the time at which summer stratification is reached ($t_{minZ_{mix}}$) by one month. To account for this variability, the timing of the different bloom phases is not only measured relatively to the day of the year, but also relatively to the phase of the physical forcing, i.e. relative to the time of $t_{minZ_{mix}}$ and $t_{maxZ_{mix}}$. In this sense, bloom phases occurring before $t_{maxZ_{mix}}$ are occurring in "winter", when the mixing-layer is still deepening. On the other hand, bloom phases occurring between $t_{maxZ_{mix}}$ and $t_{minZ_{mix}}$ are occurring during the springtime thinning of the mixing-layer.

Bottom up versus top-down control

In this paper we aim at investigating whether the bloom seasonal cycle is controlled by bottom-up or top-down processes. Here, we detail how the relative intensity of μ' and l' can be used to link onset, climax and apex to its bottom-up or top-down controls.

Onset ($r = 0,\ r' > 0$) occurs when gains first overcomes losses. At onset phytoplankton biomass is minimal and losses are always decreasing. However, there exists two possible ecosystem configuration able to trigger the bloom (figure 4.3):

- Growth Regime: The growth rate has already started to increase while loss rate is still decreasing or stable. In such circumstances, growth will become larger than loss at some point leading to the initiation of net biomass accumulation in the column water (i.e., $r > 0$). The onset is controlled by the growth (i.e., light and nutrients) and therefore, bottom-up driven. Analytically, this regime can be expressed as:

$$\mu' > 0,\ l' \leq 0 \ \Rightarrow \ r' > 0 \tag{4.7}$$

- Dilution Regime: Growth and loss rate are decreasing due to nutrients depletion, low light conditions and Z_{mix} deepening. The latter causes the dilution of plankton (both, phyto- and grazers) when increasing the volume of water in the mixing layer. This process strongly decreases the prey-predator encounter probability causing a faster decrease on loss rate than on growth rate. The grazing pressure relaxation allows phytoplankton ecosystem to start increasing. This regime is top-down controlled and it corresponds to bloom onset scenario described in Marra and Barber [2004] and Behrenfeld [2010], Boss and Behrenfeld [2010]. It can be analytically expressed by:

$$l' < \mu' < 0 \ \Rightarrow \ r' > 0 \tag{4.8}$$

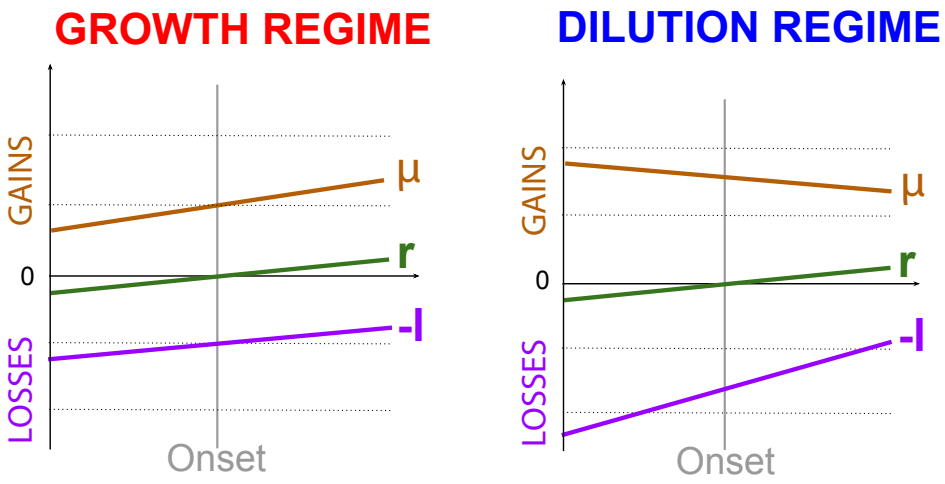

FIGURE 4.3: Diagram of the two mechanism able to trigger the bloom in winter. In growth (red), net accumulation (green) and losses (blue) rates are represented for the (a) Growth Regime and (b) the Dilution Regime. Losses rate is represented as negative (-l) to illustrate the balance $r = \mu - l$. The vertical grey line marks the date of onset at which r becomes greater than zero.

Climax ($r = r_{max}, r' = 0$) marks the instant of the fastest population increasing. Consequently, climax is the inflection point in the seasonal evolution of biomass:

$$r = r_{max} \Rightarrow r' = 0 \text{ where } P'' \propto r'. \tag{4.9}$$

From an ecosystem point of view, this means that trend in loss rates overcomes the trend in growth rate ($l' = \mu'$). Therefore, the bloom climax marks the beginning of the 'recoupling' process that leads to the re-equilibrium of the system. Full recoupling is reached later in the year at the date we refer to as the apex date. Climax can be achieved in two different ways: either μ' becoming negative due to nutrient limitation (bottom-up control) or l' becoming greater than μ' (top-down control).

Finally, **apex** ($r = 0, r' < 0$) marks the actual time of recoupling, when losses first overcome gains. At apex, losses are always increasing, $l' > 0$. Apex can be reached when growth is still increasing, and biomass accumulation is stopped by grazers (i.e. $l' > \mu'$ with $\mu' > 0$); we refer to this case as the top-down controlled. In the bottom-up case, the apex is mainly due to change on the growth rate trend, i.e., $\mu' < 0$. This situation is often caused by the nutrients depletion in the mixing layer. We note that both top-down and bottom-up controls can mutually act together. Our analysis only points out the dominant process at play.

Results

Abrupt and smooth blooms

Two types of bloom phenology emerge from our 1,200 ensemble: abrupt blooms, characterised by a sudden and very strong intensification of biomass accumulation, and smooth blooms, which display a smoother biomass accumulation. In fact, there is a continuous range of possible phenologies between these two bloom types and, hence, no objective criterion that distinguishes them. Nevertheless, as abrupt blooms reach, by definition, a higher value of r at climax, the 20% of blooms with the largest r_{max} were identified as abrupt, and the remaining 80% as smooth in the following analysis. Importantly, these two types of SO bloom phenologies are also identifiable from ocean colour observations (Sallée et al., 2014; in this issue).

For illustrative purpose, we will describe an example of an abrupt and smooth bloom taken from our results (figure 4.4). In the abrupt case example (figure 4.4 a-c), the Z_{mix} reaches 400m in winter and the summer ferricline is located at 150m. This deep winter mixing causes strong light limitation over 6 months of the year (from May to October). Simultaneously, Fe limitation declines as Z_{mix} becomes deeper than Z_{Fe}, and entrains Fe to the surface. The bloom onset occurs around 1st July and is followed by 2.5 months of a low and stable positive r during which the Z_{mix} continues to progressively deepen. We will refer to this period as the *plateau*. Then,

when $t_{maxZ_{mix}}$ is reached and the Z_{mix} starts shallowing, r rapidly increases until climax (r_{max}) is reached on 20th of October. In this scenario, the climax is an abrupt and strong peak that occurs during the period of Z_{mix} restratification. This date also marks the start of a large and rapid increase in both, integrated biomass (P) and surface chlorophyll (sChl) (black and green lines in 4.4 a). Apex is reached 10 days after the climax (1st November) associated to a rapid decline in r, which is driven by decreasing μ as Fe-limitation becomes important, as well as increasing losses ($l' >> 0$). Following apex, growth/loss equilibrium ($r \approx 0$) is re-established over the summer months (i.e., grazers-prey recoupling). This type of bloom is characteristic of high-latitude regions like the NA and iron rich waters of the SO (Waniek [2003]).

In the smooth bloom case example (figure 4.4 b-d) Z_{mix} reaches 200m in winter, with a long period of restratification (more than 2 months) and a relatively deep mixing during summer (65m). Z_{Fe} is deeper than maxZ_{mix}, so mixing does not reach the largest Fe stocks, which maintains a significant Fe limitation all year round (red surface in figure 4.4 d). As for abrupt bloom case, onset occurs in mid-June and is followed by a *plateau* phase which lasts during Z_{mix} deepening. In contrast to the abrupt bloom (4.4 a-c), the *plateau* has a much smoother shape and, instead of switching to a high r phase, is followed by a phase where r declines slowly. Climax is in late-July, in the midst of the *plateau* and just before $t_{maxZ_{mix}}$; the accumulation intensity at climax is almost four times lower than for the abrupt bloom case ($r_{max}^{smooth} = 0.02d^{-1}$ compared to $r_{max}^{abrupt} = 0.075d^{-1}$). Restratification is not associated with an increase in accumulation, which is likely due to prevailing Fe limitation. The climax lead to the beginning of recoupling and apex is reached after 2 months (around mid-September), associated to a strong grazing pressure that overcomes the steady increase in growth rate (at $r = 0$: $l' > \mu' > 0$, figure 4.4 b-d). Overall, the temporal changes in r are much less pronounced than for the abrupt case (figure 4.4 a-c) and the apex seems to arise from the long process of re-equilibrium that begins just after the onset, due to maintained top-down control. P and sChl display a weak seasonal cycle with maximal values between September and October. The maximal value of sChl is reached just before P_{max}, which in contrast to the abrupt bloom case, has a broader and lower peak.

Bloom seasonal cycle: onset, climax and apex

Onset

A remarkably consistent result over our 1,200 simulations is that in 100% of the situations that we have explored, the bloom onset always occurs in winter, when the mixing-layer is deepening (figure 4.5 a). The median value of the onset date is around 2 months before $t_{maxZ_{mix}}$ and 4 months before $t_{minZ_{mix}}$. Abrupt blooms tend to initiate earlier than smooth blooms, and the spread of the time of initiation is wider for smooth blooms than for abrupt blooms.

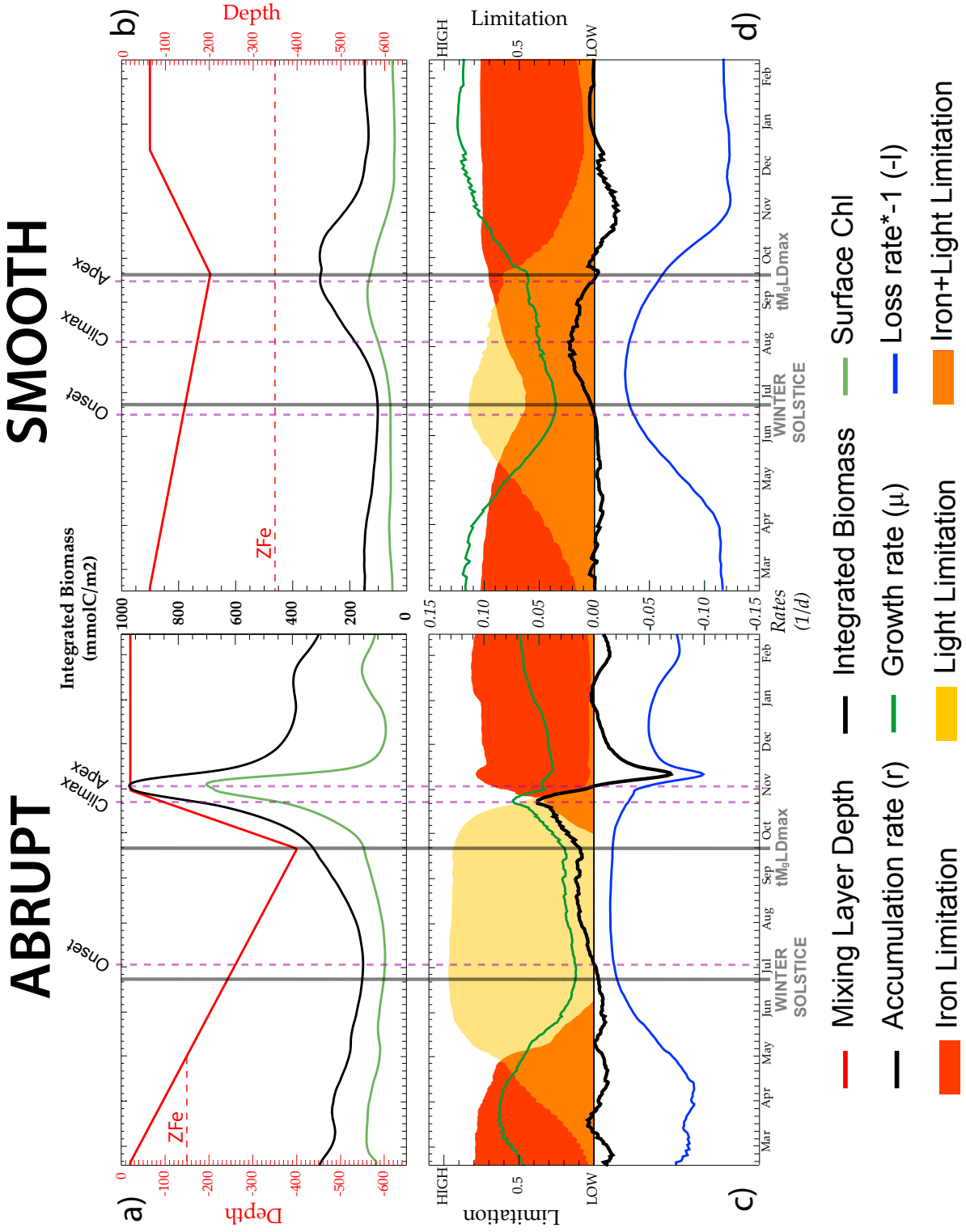

FIGURE 4.4: Seasonal cycle of the forcing Z_{mix} (red line) and model outputs of integrated biomass (black line) and surface Chlorophyll (green line) for (a) an abrupt Bloom and (b) a smooth Bloom. Summer Z_{Fe} is indicated by an horizontal red dashed line. The seasonal cycle of the accumulation rate (r, black line), the growth rate (μ, green line) and losses rate (l, blue line) for both runs are represented in panels (c) and (d). Losses rate is represented as negative (-l) to illustrate the balance $r = \mu - l$. Limitation due to Fe and Light are shaded in red and yellow areas; orange areas stands for the time at which both factors are limiting. Winter solstice date and maxZ_{mix} date are indicated by a vertical grey line. onset, climax and apex dates for each run are marked by a light blue dashed line.

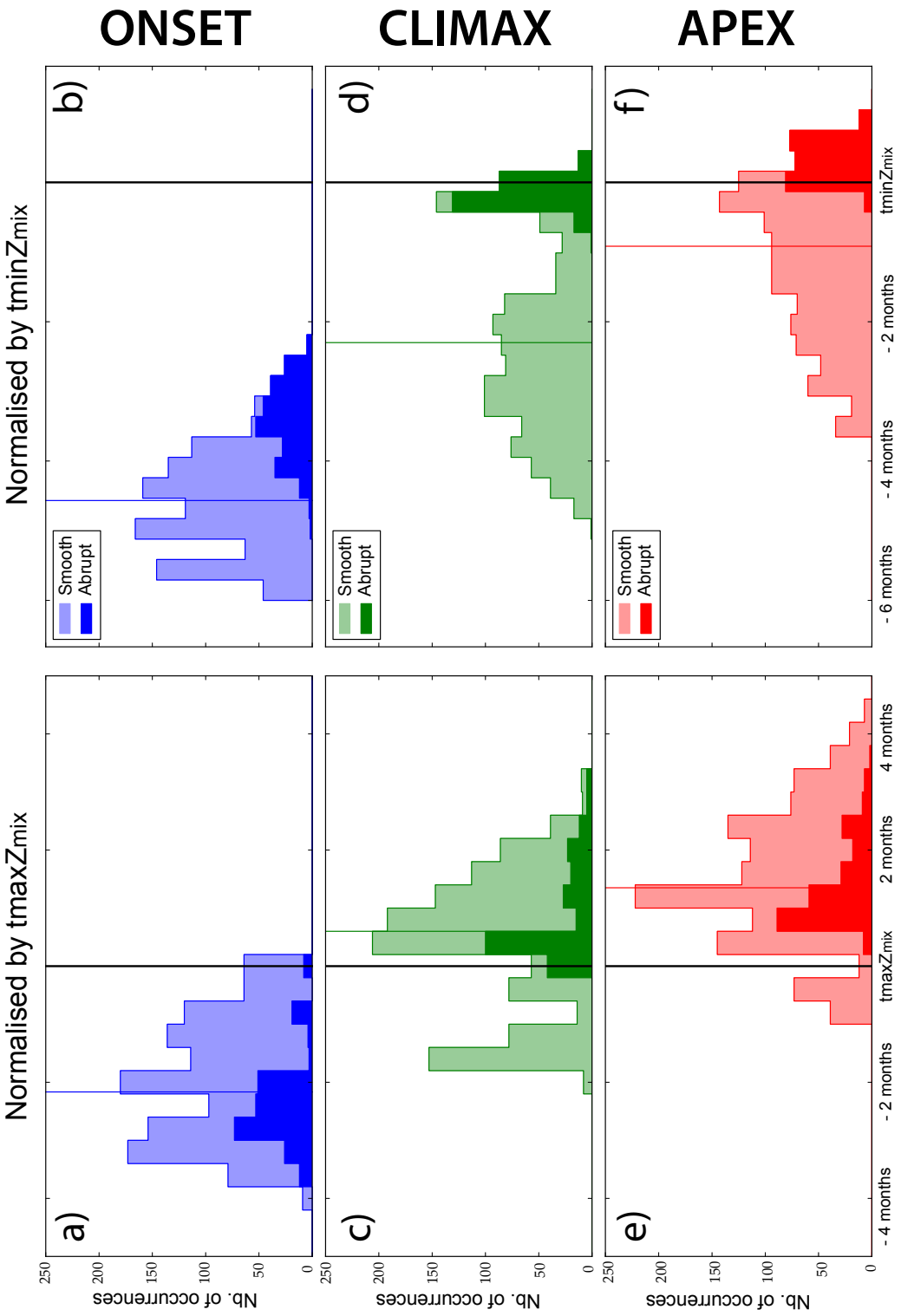

FIGURE 4.5: Bloom onset, climax and apex dates for each modelled bloom have been normalised by the corresponding $t_{maxZ_{mix}}$ (left column) and $t_{minZ_{mix}}$ (right column). In the figure, the histogram of the ensemble of modelled blooms representing: (a) the onset date normalised to the $t_{maxZ_{mix}}$ date, (b) the onset date normalised to the $t_{minZ_{mix}}$ date, (c) the climax date normalised to the $t_{maxZ_{mix}}$ date, (d) the climax date normalised to the $t_{minZ_{mix}}$ date, (e) the apex date normalised to the $t_{maxZ_{mix}}$ date and (f) the apex date normalised to the $t_{minZ_{mix}}$ date. Median value is represented by a vertical line. abrupt blooms distribution are in dark colour and smooth blooms distribution in light colour. Normalisation allows to identify the link the bloom phase with the dynamics of the Z_{mix}. For instance, independently of the absolute onset date, negative values represent onsets occurring before $t_{maxZ_{mix}}$ (i.e., before the start of stratification) while positive values indicate that bloom starts after $t_{minZ_{mix}}$ (i.e., during stratification).

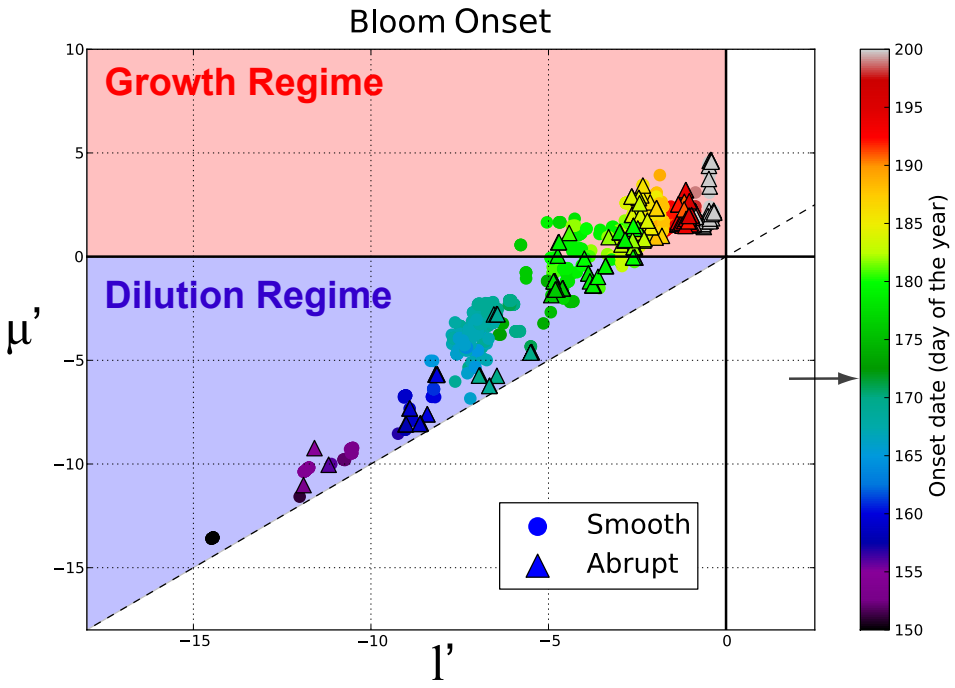

FIGURE 4.6: Growth and losses rate trends at the date of onset for the ensemble of modelled blooms. Circles stand for smooth blooms and triangles for abrupt blooms. Growth Regime quadrant (background red shade) and Dilution regime semi-quadrant (background blue shade). The absolute onset date (day of the year) is represented by symbols color. Austral winter solstice date (21st of June, day of the year 172) is marked with an arrow on the colorbar.

As introduced above, these winter onsets can either be growth- or dilution-driven. Here we assess each of the blooms in terms of the rate of change in losses and growth (l', μ', respectively) at the time of onset (figure 4.6). In this way we can discriminate between the bottom-up (increase in growth rate or Growth regime) and top-down (decrease in grazing or Dilution regime) control. Overall, across the 1,200 scenarios of our study we find an equal distribution between Growth regimes ($\mu' > 0$, red quadrant in figure 4.6) and Dilution regimes ($\mu' < 0$, blue semi-quadrant in figure 4.6). No significant differences in the onset regime are found for abrupt blooms (represented by triangles in figure 4.6).

In terms of absolute timing, all onsets occurring after the winter solstice are associated to Growth regimes and those occurring before the winter solstice, to the Dilution regime (see colorbar in figure 4.6). Thus, in our simulations (and unlike the results of Behrenfeld et al. [2013a] in a model of the North Atlantic) dilution is not always efficient enough to initiate the bloom. We found that the efficiency of dilution at initiating the bloom is related to the speed of destratification of the mixing-layer. Dilution is efficient when the destratification is strong enough to dilute predators, but weak enough to retain favourable light conditions for phytoplankton. In our simulations, we find a threshold between dilution and Growth regimes of at $\approx$ 2m/day (supplementary material figure 4.7). When the destratification rate is greater than $\approx$2m/day, the decrease in losses due to dilution are not strong enough to overcome the decrease in growth and to cause the bloom to

onset. In this case, the onset is delayed until light conditions become more favourable (i.e., after winter solstice), switching to a Growth regime. Alternatively, when the destratification rate is less than ≈ 2m/day the opposite occurs, favouring dilution regimes.

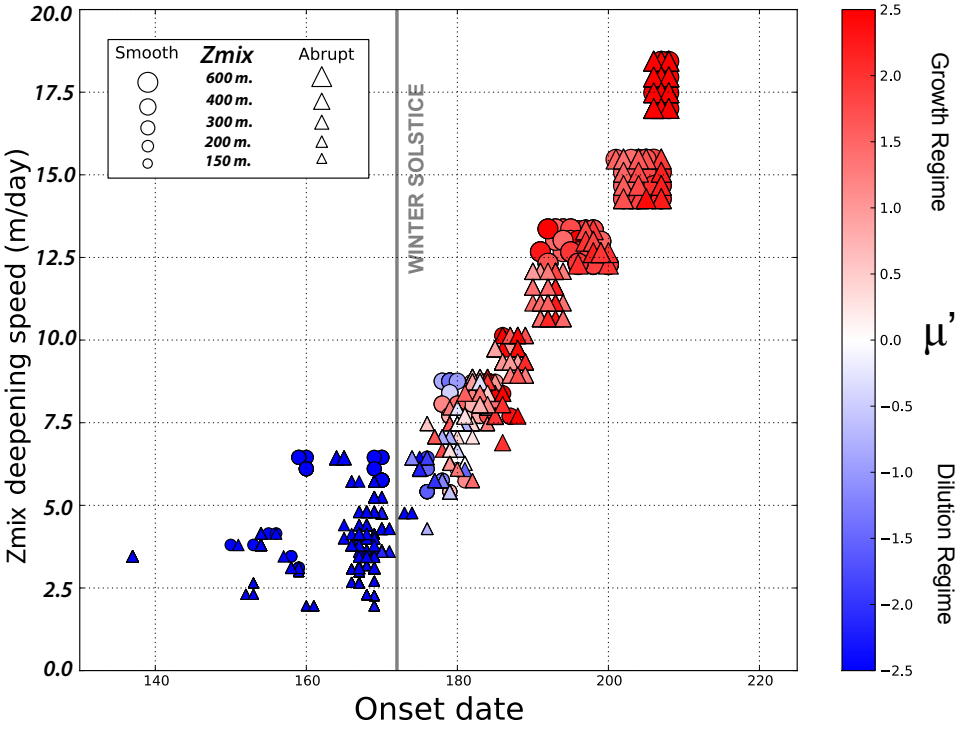

FIGURE 4.7: Growth rate at onset for each bloom is represented as a function of onset date and Zmix deepening speed. Red and blue colours stands for Grotwh or Dilution regime respectively. The size of symbols represent the maxZmix for each bloom. Circles stand for smooth blooms and triangles for abrupt blooms.

Climax

After the bloom onset, biomass accumulation increases until it reaches a maximum rate that we define as the climax (time of $r = r_{max}$). We note here that this date is different from the date of maximal biomass stock: accumulation continues until r switches back to a negative value. Instead, climax refers to the maximum increase rate of integrated biomass. In contrast to the bloom onset, for the large majority of blooms (≈ 80%), climax is reached during the phase of Z_{mix} retreat, i.e. after maxZ_{mix} (figure 4.5 c). The remaining 20% of blooms are characterized by a climax before or when the mixing-layer reaches its maximum depth. However, all of these blooms with a climax before maxZ_{mix} are smooth blooms. Abrupt blooms, associated with, by definition, a large (i.e., an "intense" climax) have their climax occurring after maxZ_{mix}.

Interestingly, for all seasonal cycles analysed, we found the accumulation reaches its maximum before the surface layer re-stratifies to its minimal value (figure 4.5 d). In summary, we find that in 80% of our simulation climax occur during spring stratification (i.e., before $t_{minZ_{mix}}$ and

after $t_{maxZ_{mix}}$). In addition, climax associated with all of the abrupt blooms occur at the time where the mixing layer reaches its minimal value (i.e. at $t_{minZ_{mix}}$ and after $t_{maxZ_{mix}}$; dark green in figure 4.6 c-d). These results suggest a relationship between climax date and intensity, and the surface layer re-stratification period, which in turns points out the possible importance of light on biomass accumulation rate. Accordingly, we find that the faster is the restratification of the surface layer, the larger is the maximum accumulation rate (figure 4.8), with the total Fe input playing a secondary role. We note that for a given restratification speed (except for the very low restratification, slower than $5m/d$), r_{max} is tightly linked to the total Fe input in the surface layer. We understand the tight relationship between r_{max} and the restratification as an indication of bottom-up control: a rapid improvement in light conditions leads to a parallel increase in growth rate (μ), which quickly translates into a rapid elevation of r, as grazers are not able to respond at the same rate. The amount of Fe available in winter thus works as a catalyst, allowing phytoplankton to take an optimal benefit of the increase in light conditions.

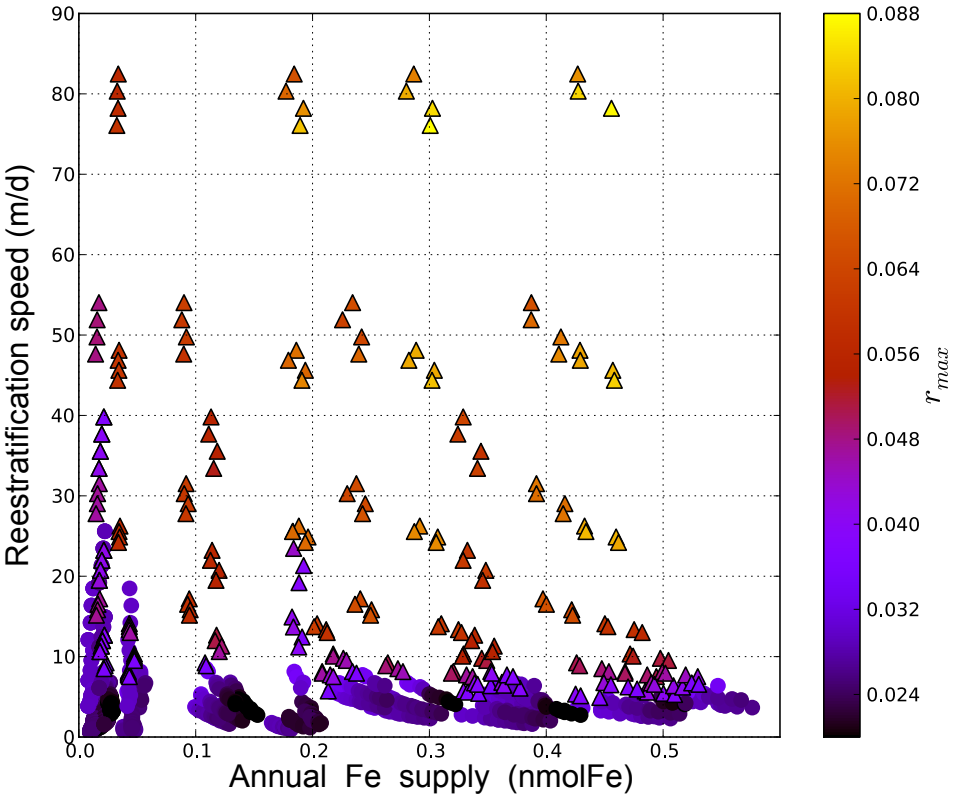

FIGURE 4.8: The climax intensity (or r_{max}; in d^{-1}) is represented in colour as a function of the vertical iron supply and the reestratification speed. Circles stand for smooth blooms and triangles for abrupt blooms.

Apex

The apex date is reached when loss rate first overcomes growth rate ($l = \mu$) causing biomass accumulation to arrest ($r = 0$). For 90% of the scenarios we analysed, apex occurs after the

mixing layer reaches its maximum (median value around 1.5 months later; figure 4.5 e). In addition, apex is reached, in more than 75% of bloom scenarios, before the date of minimum mixing depth (median value around 1 month before; figure 4.5 f). However, apex for abrupt blooms occurs after $t_{minZ_{mix}}$ (hence also after $t_{maxZ_{mix}}$; figure 4.5 e,f). Such blooms can be viewed as examples of 'bloom and bust' dynamics occurring during a rapid restratification that causes a sudden drop in r following the climax (compare figure 4.5 d and f; dark colours, or example of figure 4.4 b).

By assessing the state of the ecosystem at the apex date we can better understand the processes leading to this stage. At apex, l' is always positive (figure 4.9), which means grazing pressure is enhanced. In contrast, μ' can be either positive (but necessarily lower than l') or negative (figure 4.9). Over the ensemble of scenarios, 68% have an increase in growth ($\mu' > 0$) at the time of apex, and 32% have a decrease in growth ($\mu' < 0$) at the time of apex. However, l' is always grater than μ' (up to a factor 10 in some cases) indicating strong top-down control for our entire suite of scenarios. The earliest apex dates are always associated with $\mu' > 0$ (figure 4.9), while after around day 260 ($\sim$ mid-September), μ' can either be positive or negative at recoupling. The highest loss rates ($l' > 100$/day) are always associated to abrupt blooms (see triangles in figure 4.9).

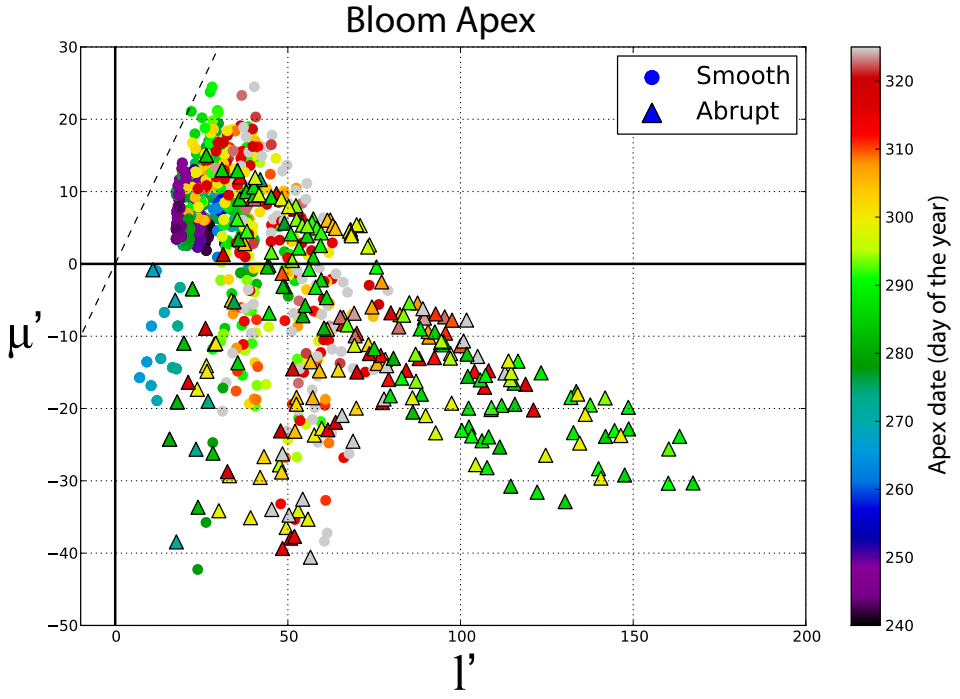

FIGURE 4.9: Growth and losses rate trends at the date of the apex for the ensemble of modelled blooms. Circles stand for smooth blooms and triangles for abrupt blooms. The absolute apex date (day of the year) is represented by symbols colour.

A comparison of bloom detection criteria

Many of the seasonal cycles generated by our model are characterized by a *plateau* phase, with positive, but weak and relatively constant accumulation between onset and climax (see section 4.2 and figure 4.4). While in terms of biomass accumulation, the bloom has definitely started (i.e., $r > 0$), there is little accumulation of chlorophyll at the ocean surface (sChl; see examples in figure 4.4, green curve). Clearly, detecting bloom onset from surface chlorophyll observations would be challenging in such cases. In this section, we aim to better understand what can be learned from surface observations of chlorophyll accumulation.

Surface chlorophyll (sChl) and surface biomass (sP) are extracted from the model runs and used as input for two bloom detection criteria (typically applied to surface observations, e.g. Behrenfeld [2010]; Brody and Lozier [2014], Brody et al. [2013]). By comparing this surface-derived information with the actual onset and climax we computed from the full vertical profile (presented in section 4.2) we can quantify potential uncertainties. The two surface criteria we use are:

1. P*-criterion: date at which P*' > 0 (Behrenfeld [2010]), where:

$$P \approx P^* = sP \times Z_{mix} \text{ while } t < t_{maxZ_{mix}} \tag{4.10}$$

2. sChl-criterion: Date of maximal sChl"

P*-criterion detects dates that coincides, for 85% of blooms, to the onset computed from the full vertical profile (figure 4.10 a). This result is not surprising given the model set up: in our model, the mixing layer is very strongly mixed, so we expect P to be relatively constant over Z_{mix} and very weak below the mixing layer (so, $P^* \approx P$). The accuracy of the P*-criterion is therefore strongly tied to the choice of the mixing depth with which P* is computed: it must be a strongly mixed surface layer which is not always well described by typical mixed-layer depth criterion (e.g. Taylor and Ferrari [2011]). Arguably, P*-criterion will work better during the convective phase of the surface layer, when mixed-layer actively mixes. The P*-criterion detects onset dates around 2 months before the climax (figure 4.10 b), in agreement with the typical time difference found between onset and climax (figure 4.5 a,c).

The sChl-criterion detects dates that are only very weakly related to the actual onsets in our model scenarios (figure 4.10 c). Onset dates derived from this criteria are 1 to 4 months later than the actual onset, with a median value of 2.5 months later. Interestingly, the dates detected by sChl-criterion are more closely related to the bloom climax (figure 4.10 d), with this bias even clearer for abrupt blooms (dark green on figure 4.10 d). We conclude that sChl-criterion (or criteria based on sChl"), that are often used in ocean colour studies, are more closely related to the strongest period of the bloom rather than to onset.

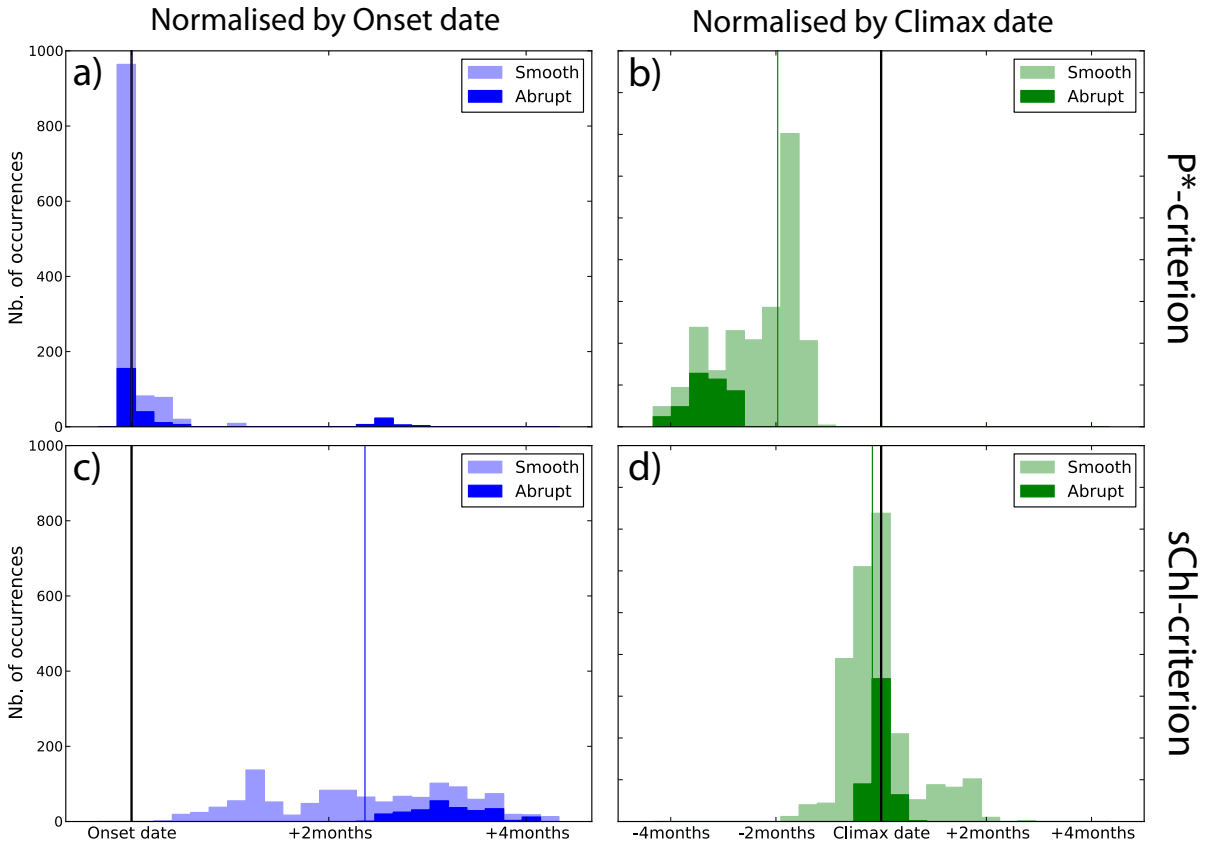

FIGURE 4.10: The histogram of the ensemble of modelled blooms representing: (a)bloom detection date using P*-criterion normalised to the actual onset date, (b) bloom detection date using sChl-criterion normalised to the actual onset date, (c) bloom detection date using P*-criterion normalised to the actual climax date, (d) bloom detection date using sChl-criterion normalised to the actual climax date. Median value is represented by a vertical line. abrupt blooms distribution are in dark colour and smooth blooms distribution in light colour.

Evaluating Sverdrup's bloom conditions

Sverdrup hypothesized that phytoplankton net accumulation can increase if mixed layer depth (MLD) is shallower than a critical depth (Z_c; defined as the euphotic layer) at which integrated gains balance integrated losses (Sverdrup [1953]). This critical depth can be mathematically expressed as (Siegel [2002]):

$$Z_c = \frac{1}{K}\frac{I_0}{I_c}, \tag{4.11}$$

where I_0 is the surface PAR, K the light attenuation coefficient (in m^{-1}), and I_c an empirical value ranging from 0.35 to 3.5 mol photon/m^2/d. Here, Z_c is computed at each timestep using SO adapted light attenuation coefficient proposed in Nelson and Smith [1991]. Different values of I_c were tested: 0.35, 1.5 and 3.5 mol photon/m^2/d. Since the highest two I_c values cause a shallow biased Z_c a high number of scenarios did not result in any date where $Z_{mix} = Z_c$. Results are therefore presented for the lowest I_c of 0.35 mol photon/m^2/d. We next investigate

whether Sverdrup's bloom conditions are satisfied using the two surface bloom detection methods presented above (P*-criterion and sChl-criterion).

P*-criterion detects dates 3-5 months before Sverdrup's conditions are satisfied (median value around 4 months before; figure 4.11 a). Similarly, close to 95% of the dates associated with sChl-criterion are before Z_{mix} becomes shallower than Z_c. However, for abrupt blooms, the sChl-criterion detects dates that are distributed around the date at which Sverdrup's conditions are satisfied. Given that we found the sChl-criterion to be a good approximation of bloom climax, our results suggest that Sverdrup's conditions are associated with bloom intensification (climax) rather than onset.

Discussion

During the last 20 years, numerous studies based on SO bloom dynamics have emerged. Most of them rely on satellite observations in this remote region (Moore et al. [1999]; Venables et al. [2007]; Fauchereau et al. [2011]) with the exception of specific locations where mooring observations have been sampled (Jeandel et al. [1998]; Abbott et al. [2000]; Weeding and Trull [2013]), occasional oceanographic surveys (Boyd et al. [2000]; Pollard et al. [2007]; Blain et al. [2007]) and recent datasets obtained by elephant seals equipped with CTD and fluorescence sensors (Blain et al. [2013]). While in situ observations usually offer water-column measurements, they are limited to specific regions and last for only a few weeks/months. In contrast, satellite-based chlorophyll data provide substantial spatial and temporal coverage. However, they are limited to interpret bloom dynamics solely based on its surface imprint.

Satellite-based analysis of high-latitude bloom onset often relate the increase of surface chlorophyll to the stratification of the mixed layer in spring. From this temporal correlation authors conclude that alleviation of light limitation in the MLD is the main bloom trigger (Nelson and Smith [1991]; Siegel [2002]). Such results are based on the seminal concepts of Gran and Braarud [1935] and Riley [1942] and theoretically supported by Sverdrup's hypothesis (Sverdrup [1953]). More recently, combined analyses of satellite and model data identified onset based on its "strict" definition: the date at which integrated gains overcome losses (Behrenfeld [2010]). In this case, onset is systematically found in winter presumably caused by a fast decrease on grazing pressure during MLD deepening. This apparent inconsistency between the two results is subject to much debate (Chiswell [2011]; Behrenfeld and Boss [2013]; Ferrari et al. [2014]).

Our results shed light on the current debate by describing the bloom as a sequence of three distinct phases: an onset, a climax, and an apex. While a "strict" onset definition is consistent with a winter onset (in agreement with Behrenfeld [2010], Behrenfeld et al. [2013a]) the surface spring bloom is associated with the climax of the integrated bloom, which is the rapid accumulation occurring after the winter onset. We therefore suggest that much of the debate regarding winter

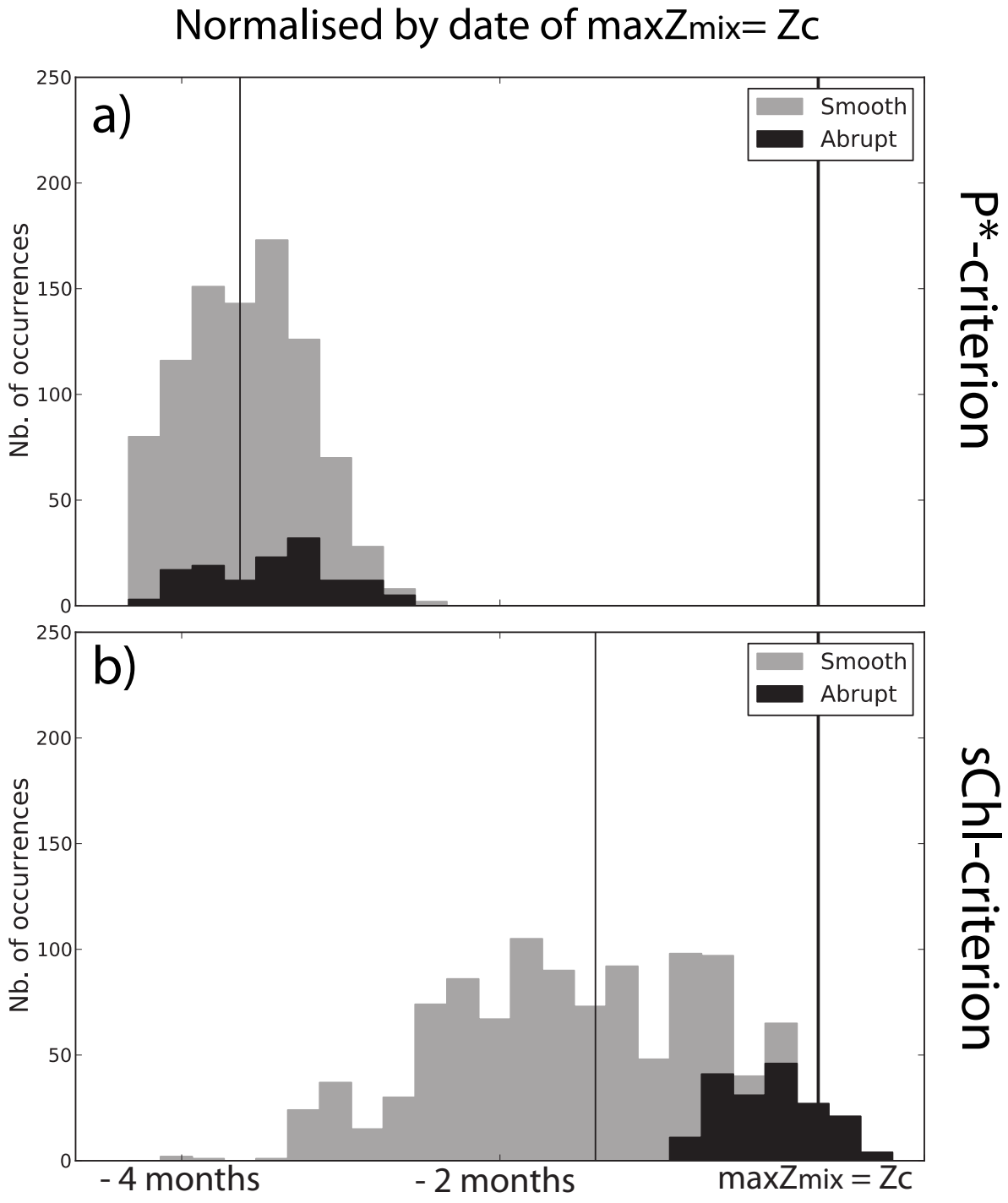

FIGURE 4.11: The histogram of the ensemble of modelled blooms representing: (a) bloom detection date using P*-criterion normalised by the date at which Sverdrup's conditions are satisfied, (b) bloom detection date using sChl-criterion normalised by the date at which Sverdrup's conditions are satisfied. Median value is represented by a vertical line. abrupt blooms distribution are in dark colour and smooth blooms distribution in light colour.

versus spring onset mostly results from confusions on the definition of the word "onset". It is important to note that what originally made blooms such an attractive phenomenon was "the sudden appearance of an enormous numbers of diatoms in early spring" (Bigelow [1926]). Hence, in our opinion, the most important phase of the bloom is perhaps the climax, not the onset. We demonstrate that is possible to differentiate both stages using surface satellite-based products thanks to existing methods able to detect bloom dynamics (figure 4.10 a-b). The method we have tested ($P^* = MLD \times sP$ and proposed in Behrenfeld [2010]) can be successfully applied during winter destratification if three conditions are satisfied: ocean colour satellite data is available in winter, the timing and magnitude of MLD can be accurately estimated, and the MLD is actively mixed (i.e., MLD $\approx Z_{mix}$).

One advantage of using a model approach is that allows us to investigate the mechanisms that drive the phenomena of winter onset. Interestingly, two possible winter bloom triggers have been identified: grazer-prey dilution and winter net growth (figure 4.6). In addition, we find that dilution is only efficient when the destratification of the mixing layer is not too fast. When destratification is rapid, grazers are diluted, but the phytoplankton growth is reduced even more strongly due to light limitation. In such cases, the winter onset is delayed to later in the season, when light conditions improve following the winter solstice.

The date at which net accumulation stops (i.e., the apex) is strongly top-down controlled (figure 4.9). The complete recoupling and the afterwards readjustment is influenced by numerous complex biogeochemical processes involving remineralisation, aggregation of particles or virus infection (Boyd et al. [2012b]). We want to stress here that any given model, even if containing a significant level of complexity, would be suspect in the representation of these processes, which are still poorly understood. This is particularly true in the Southern Ocean, where the complex cycle of iron is involved.

Our results and conclusions are based on an idealised model where strong assumptions where applied to minimise the degrees of freedom and ease results interpretation. This simplifications and assumptions must be taken into account when interpreting the results. First of all, the seasonal cycle is modelled in a 1D water-column where lateral advection is not considered. Even if this may have important consequences on nutrients/iron transport, our approach is supported by recent works on iron supply in the SO (Tagliabue et al. [2011]; Tagliabue et al. [2014b]). Second, in our model vertical mixing is assumed to be very strong an homogeneous from the surface to a depth level (Z_{mix}) and very low below. This highly turbulent mixing-layer is a reasonable assumption for the Southern Ocean where winds are generally strong and sustain efficient turbulent vertical mixing. However, we did not address the sources of vertical mixing and the possible subseasonal variations in mixing. We note here that in the present study we analysed bloom in relation to the mixing layer depth, which is not necessarily the same as the mixed-layer depth. While Sverdrup referred to the seasonal thermocline (classically associated

to the mixed-layer), recent studies have focused the interest on the upper-layer mixing (based on the critical turbulence hypothesis of Huisman et al. [1999]) and the mechanisms able to reduce it: positive heat fluxes (Taylor and Ferrari [2011] and Ferrari et al. [2014]), wind reduction (Chiswell [2011]) or submesoscale eddies (Lévy et al. [2001]; Mahadevan et al. [2012]). In our study, we avoided such controversy by imposing a very strong mixed upper-layer with no subseasonal variability. In the real ocean (and specially in the SO), the phytoplankton activity (and therefore, the bloom formation and evolution) is highly affected by atmospheric and oceanic physical events with day-to-week duration length (Waniek [2003]). Such events, are arguably an important source of variability when addressing the phytoplankton seasonal cycle with ocean-colour satellite data.

In our set of experiments, the limiting nutrient was always dissolved iron while is known that in Fe-rich water of the SO, diatoms can also be limited by silicic acid (Boyd and Ellwood [2010]). We therefore note that our results should not be extrapolated to any other location or SO regions where main iron supply is not winter mixing (e.g., South Georgia Is. or Kerguelen Is. and Plateau), where silicic acid is a limiting factor, nor to higher latitudes (>70°S) where the role of light and ice seasonal cycle can be critical on the phytoplankton bloom phenology.

Conclusions

Implementing an ensemble of more than 1,200 idealised physical scenarios for an isolated water column, a complex biogeochemical model has been forced with the aim to reproduce the plankton seasonal cycle for a collection of open waters/ice-free SO spots. Daily frequency model outputs covering a large spectra of the variables involved in the phytoplanktonic bloom allowed us to target the question of bloom formation mechanisms from different focus.

Three crucial stages on bloom seasonal evolution have been defined: onset, climax and apex date. All onsets occurred in winter and most of the climax, in spring. For the onset, upper-layer mixing (or Z_{mix}) appeared as a key component on tilting the system to be bottom-up or top-down controlled. In the case of climax, the amount of Fe (and thus the relative depth between mixing layer and ferricline) seemed to play a secondary but significant role on the intensity of accumulation. Concerning apex, permanent top-down control was identified.

Two bloom detection criteria were tested using model surface chlorophyll and mixed layer integrated biomass estimated from surface values. The biomass-based criterion appeared as a good proxy for detecting bloom onset while the criterion based on surface chlorophyll was reliable on detecting the climax. From an analytical formulation of Sverdrup's hypothesis we demonstrated that can be only satisfied, for some specific kind of blooms, during climax phase.

Our results suggests the existence of bottom-up as well as top-down drivers of the different phases of the blooms. It also enlightens the apparent controversy between onset/surface bloom detection and it shows how different criteria can be used to answer different questions.

Acknowledgments

The authors would like to thank J.LeSommer and L.Bopp for their suggestions, comments and discussions at several stages of this study. We are grateful to A.Albert, C.Ethé, S.Ayata and O.Aumont for its invaluable help on the technical aspects and setting up of model configuration.

4.3 Conclusions

Modelling study conclusions presented in this chapter high-lighted the complex link between bloom dynamics and its environment. We showed how bloom dynamics can not be simplified to an initiation and end date but that there was at least three important phases. We carefully defined the onset, climax and apex date together with the factors that control each of these phases. Amongst these controls, light and winter mixing (and its influence on diminishing grazing pressure) appeared important during the onset and climax (with a significant role of iron in the latter) while apex was mainly top-down controlled by grazing. The timing and intensity at which these phases occur determine bloom phenology (i.e., abrupt or smooth blooms).

Once each boom phase control was identified, we did a step forward to compare our integrated view of the bloom with the bloom surface expression that can be captured from satellite data. Interestingly, we found that common bloom detection methods using surface chlorophyll determine not the onset but the climax phase of the bloom. Nevertheless, we also shown that bloom onset is detectable using an estimation of the integrated biomass proposed in Behrenfeld [2010]. This results motived us to combine satellite and Argo data in the Southern Ocean with the aim to detect both onset and climax phases in a observational data base. By detecting these two bloom phases and comparing each relative timing, we were able to identify three different bloom regimes coherently distributed over the Southern Ocean. Synthesising the features of each of these regimes we proposed an organisation of Southern Ocean blooms into three different phenology regimes.

This observational work was realised in collaboration of J.B.Sallée, specialist on the exploitation of Argo floats database in the Southern Ocean. Our collaboration resulted in the production of the article that will be presented in the first part of this chapter. This article has also been submitted to ICES JMS Sverdrup's special issue. In the second part of this chapter, I will present a model-based complement of this work. In this second part, I used a biogeochemical model configuration of the Southern Ocean to test some of the assumptions applied in the observational study. Actually, using a similar logic of the one applied in the 1D study when testing satellite detection methods, here I re-test the surface estimation of integrated biomass using a 3D model which physical environment is much more realistic. Interestingly, from this comparison it was possible to identify some cases for which integrated biomass can not be estimated from surface.

Chapter 5

Bloom phenology in the Souhtern Ocean

5.1 Introduction

In the precedent chapter I presented an idealised study addressing the controls of phytoplankton blooms at the Southern Ocean. We distinguished three bloom phases: onset, climax and apex. Based on an ensemble of 1,200 idealised seasonal cycles, we related each of the three bloom phases to physical (bottom-up) or biological (top-down) controls. Lastly, we proposed different detection methods to detect each of these phases using satellite and ocean interior (i.e., turbulent mixing in the column water) estimations.

The results of this modelling work in chapter 4 are, however, based on a very idealised seasonal cycle of turbulent mixing. In the "real" ocean, the seasonal cycle of the physical processes that impact phytoplankton (mainly turbulent mixing and nutrient supply, in open waters) is much more complex. Mixing intensification (in magnitude and depth) during autumn and winter, and later weakening in spring, does not occur at a regular pace but results from the concatenation of atmospheric and oceanic events at different time and space scales.

In order to extrapolate the conclusions of the precedent study to a more realistic (and complex) framework, we decided to address Southern Ocean phytoplankton blooms using observational data. Ocean colour data was co-localised to *in-situ* estimations of the water column stratification to infer bloom evolution within the water column. The concepts and results from the modelling study were used to identify each bloom phase (i.e., onset, climax and apex) using the appropriate bloom detection method. Interestingly, most of the results obtained form the idealised model appeared to be coherent with the statistical results issued from observations. Furthermore, we were able to identify three distinct phenology regimes in the Southern Ocean and to propose

the drivers that originate this diversity. All this work was conducted in tight collaboration with J.B.Sallée (at BAS, Cambridge, when the collaboration started and later at LOCEAN, Paris) and resulted in the submission of the article *Characterisation of distinct bloom phenology regimes in the Southern Ocean* to ICES JMS special issue on Sverdrup's hypothesis. The full content of this scientific article will be presented in the first part of this chapter, section 5.2.

The second part will present a complementary work of this study[1]. Using the regional models configurations presented in chapter 3, I tested some of the hypotheses we assumed when addressing blooms based on observations. As we did in the 1D study, the model was used to look through the whole water column and to compare integrated biomass to estimations from surface. This approach allowed me to identify some cases not represented in our 1D simplified model, for which surface Chl and MLD information is not sufficient to estimate the integrated biomass. Incoherences between observation-based and the two model-based studies, shed some light on the intrinsic limitations of both large-scale observations and biogeochemical models.

5.2 *Characterisation of distinct bloom phenology regimes in the Southern ocean* (Article)

Sallée, J.B.; Llort, J.; Tagliabue, A, .Lévy, M.;
Submitted to ICES JMS special issue "60 years since Sverdrup's critical depth hypothesis"

Abstract

In this study we document the regional variations of bloom phenology in the Southern Ocean, based on a 13-year product of ocean color measurements collocated with observation-based estimates of the mixed-layer depth. One key aspect of our work is to discriminate between mixed-layer integrated bloom and surface bloom. By segregating blooms that occur before or after the winter solstice and blooms where integrated and surface biomass increase together or display a lag, we define three dominating Southern Ocean bloom regimes. While the regime definitions are solely based on bloom timing characteristics, the three regimes organize coherently in geographical space, and are associated with distinct dynamical regions of the Southern Ocean: the subtropics; the subantarctic; and the Antarctic Circumpolar Current region. All regimes have their mixed-layer integrated onset between autumn and winter, when the daylight length is short, and mixed-layer actively mixes and deepens. We discuss how these autumn-winter blooms are controlled by either nutrient entrainment and/or reduction of prey-grazer encounter rate. In

[1] not added in the submitted article

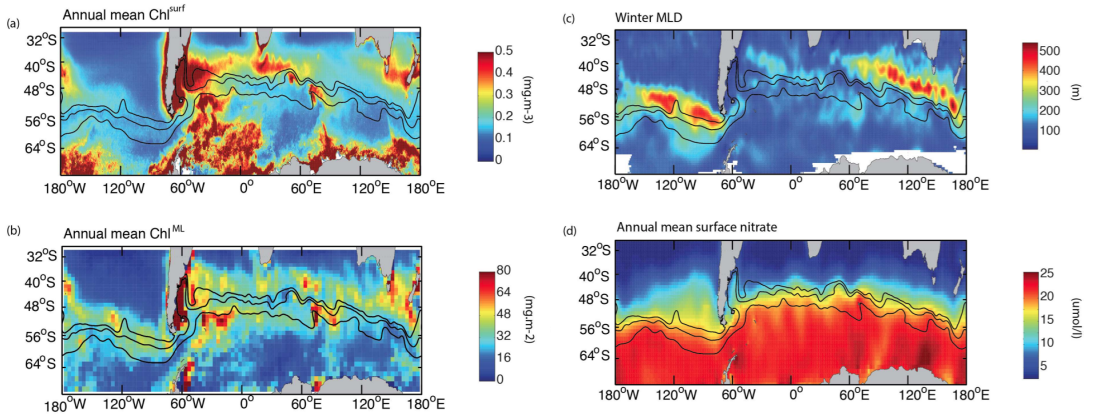

FIGURE 5.1: Climatological (a) annual mean of surface chlorophyll (Chl^{surf}; mg m^{-3}; (b) annual mean mixed-layer integrated chlorophyll (Chl^{ML}; mg m^{-2}; (c̃) winter (september) mixed-layer depth from estimated from the observational dataset; and (d) annual mean surface nutrient concentration (μ mol/l) from the World Ocean Atlas 2009. In panel (a-c) the three black lines represent the approximate climatological position of the three main ACC branches, from south to north: polar front, subantarctic front, and northern branch of the subantarctic front following Sallée et al. [2008].

addition to the autumn-winter biomass increase, the subantarctic regime has a significant spring-time biomass growth associated with the shutdown of turbulence when air°-sea heat flux switches from surface cooling to surface warming.

Introduction

Satellite observations and studies based on in situ observations have shown that phytoplankton distribution in the Southern Ocean displays patchy regional variability (5.1.a) and a wide range of distinct seasonal cycle regimes (e.g. Moore and Abbott [2002]; Arrigo et al. [2008]; Thomalla et al. [2011]; Chiswell et al. [2013]; Franks [2014]; Carranza and Gille [2014]). While phytoplankton biomass and the associated primary productivity fluctuate according to season (e.g. Arrigo et al. [2008]) and location, the environmental conditions that drive these patterns are poorly understood. These misunderstandings hamper our ability to apprehend how seasonality might be modified in the future (e.g. Henson et al. [2013]) and the associated implications for Southern Ocean food webs.

A unique aspect of the Southern Ocean circulation is the presence of a strong eastward, circumpolar current, the Antarctic Circumpolar Current (ACC). On the northern edge of the ACC, subtropical gyres flow counterclockwise, and their intense and energetic western boundary currents join the northern branches of the ACC in the western Atlantic, Indian, and Pacific basins. The ACC and the western boundary currents have a profound influence on the physical and geochemical characteristics of the Southern Ocean (Rintoul et al. [2010]). They form meridional dynamical barriers (Sallée et al. [2008]), which split the Southern Ocean into a number of distinct zones. Four main zones can be described, from north to south: the subtropical region, around

30° S, characterized by stratified surface layers (5.1.c), and relatively weak wind and buoyancy forcing; the subantarctic region, directly north of the ACC, which is characterized by very deep mixed-layers (5.1.c), intense winds, large buoyancy forcing, and the presence of the energetic western boundary currents; the ACC region, characterized by the top-to-bottom and large circumpolar current; and the subpolar region, south of the ACC, characterized by the seasonal presence of sea-ice, and a relatively stratified surface layer.

These dynamical zones of the Southern Ocean correspond to specific geochemical regions (e.g. Longhurst et al. [1995]). The surface layer of the subtropical region have low macronutrient concentrations (5.1.d), the subantarctic, ACC and subpolar regions are generally considered as macronutrient rich, iron limited regions (e.g. Martin et al. [1990]; Boyd et al. [2010]), although silicic acid is notably much lower in the subantarctic region than the ACC (e.g. Sarmiento et al. [2004]). Another notable aspect of the subantarctic zone is that it contains numerous continental sources of iron (Boyd and Ellwood [2010]), with the presence of continental plateau and many subantarctic islands, in the lee of the western boundary currents flowing eastward.

At present, it is not clear how the specific dynamical and geochemical regions of the Southern Ocean relate to the patchy phytoplankton distribution in the Southern Ocean (5.1; e.g. Thomalla et al. [2011]; Chiswell et al. [2013]). The aim of this study is to use a range of physical and biochemical observational products to shed light on the general chlorophyll bloom patterns in the Southern Ocean, and link these patterns to the distinct dynamical and geochemical regions of the Southern Ocean.

Our aim of describing regional variability of the Southern Ocean phytoplankton seasonal cycle falls within the more general context of the mechanisms associated with onset and duration of phytoplankton blooms. These mechanisms remain much debated despite decades of research (e.g. Sverdrup [1953]; Evans and Parslow [1985]; Townsend et al. [1992]; Huisman et al. [1999]; Behrenfeld [2010]; Mahadevan et al. [2012]; Taylor and Ferrari [2011]; Ferrari et al. [2014]). This debate arises from the wide diversity, and often inter-related, factors that control phytoplankton blooms, which range from physical (e.g. solar irradiance and the intensity of surface layer mixing), biological (e.g. growth or grazing rates) to chemical (e.g. availability or cycling of nutrients) factors.

The founding conceptual model of bloom dynamics, which arose in the first half of the last century, is the 'critical depth' theory (Gran and Braarud [1935]; Riley [1942]; Sverdrup [1953]), which proposes that blooms should commence when the ocean surface mixed-layer restratifies in spring. Recently, the extent to which the mixed-layer depth shallowing explains phytoplankton blooms has been questioned (e.g. Behrenfeld [2010]; Chiswell et al. [2013]; Taylor and Ferrari [2011]). For instance, several authors have proposed that surface layer turbulence (primarily driven by wind and air-sea buoyancy flux) is one of the key factors for bloom onset (e.g. Huisman et al. [1999]; Chiswell et al. [2013]; Taylor and Ferrari [2011]). Other works have proposed that

blooms do not occur in spring, but instead in autumn or early winter, which seems to invalidate the basis of the critical depth theory (Behrenfeld [2010]; Boss and Behrenfeld [2010]). Instead, a new framework, the "disturbance-recoupling" hypothesis, has been proposed, which focuses on the balance between phytoplankton growth and grazing (Behrenfeld [2010]). Finally, some of the confusion in our understanding of phytoplankton blooms might arise from whether blooms are examined from the standpoint of water-column integrated biomass, or from surface observations (Llort et al., submitted to this issue[2].

After presenting the datasets and methods in Section 5.2, we introduce examples of chlorophyll seasonal cycle in the Southern Ocean (Section 5.2). An important point in our study is that we seek to discriminate between water-column integrated chlorophyll and surface chlorophyll by co-locating surface chlorophyll observations with physical observations of the water-column. By doing so, we demonstrate that Southern Ocean blooms can be grouped into a number of distinct regimes based on their phenology (Section 5.2). We then discuss the seasonal cycle of each of these regimes (Section 5.2), before finishing with a discussion of our results (Section 5.2).

Data and Methods

Surface ocean colour product

Surface chlorophyll (Chl^{surf}) over the Southern Ocean is investigated in this study. We define the Southern Ocean as the region between the latitude 70°-30° S. Although remote sensing of Southern Ocean chlorophyll concentrations is effective in detecting large-scale chlorophyll bloom regime, the current algorithms for the Sea-viewing Wide Field-of-view Sensor (SeaWiFS, algorithm OC4v6), the Moderate Resolution Imaging Spectroradiometer (MODIS-Aqua, algorithm OC3M) and GlobColour significantly underestimate chlorophyll concentrations at high latitudes (Johnson et al. [2013]). Therefore, in this study, we use a new algorithm, specifically designed for the Southern Ocean that more accurately matches long-term in situ datasets (Johnson et al. [2013]). The new algorithm improves in situ versus satellite chlorophyll coefficients of determination (R2) from 0.27 to 0.46, 0.26 to 0.51 and 0.25 to 0.27, for OC4v6, OC3M and GlobColour, respectively, while also addressing the underestimation problem. We also compared our results to the Globcolour dataset and found the definition of the regimes and their characteristics to be very similar, giving us confidence in the broad reliability of our results. However, the absolute magnitudes of blooms are affected, and as the Johnson et al. [2013] algorithm best matches observations, we decided to present results using this algorithm. Overall, surface chlorophyll concentrations are available at a weekly resolution between the years 1998 to 2010, when cloud coverage allows.

[2]Chapter 4 of this manuscript.

Ocean interior

In order to investigate the role of ocean physics in driving phytoplankton blooms, we co-located ocean temperature and salinity observations with the satellite-derived estimates of Chl^{surf}. To do this we utilise two different ocean interior datasets, as described below.

First, defined as the "observational dataset", we use in-situ observations of temperature/salinity profiles from a combination of the Argo float database and the ship-based Southern Ocean Data Base (SODB; see http://woceSOatlas.tamu.edu for more information). The Argo project contributes about half of the Southern Ocean profiles, fills the center of ocean basins and provides complete sampling over the austral winter (Sallée et al. [2010b]). We use only profiles that have passed the Argo real-time quality control, containing information on their position, date, pressure, temperature (T) and salinity (S). Most Argo profiles sample T and S from the surface to 2000 m depth every 10 days. From this database we extract information regarding the mixed-layer depth. The advantage of this approach is that it provides ocean observations at the time and location of the Chl^{surf} concentration estimate from satelitte. However, as the satellite coverage is much greater than the in situ temperature/salinity coverage, this co-location procedure reduces the number of Chl^{surf} estimates available.

Second, defined as the "reanalysis dataset", we use a statistical reanalysis of ocean observation: the EN3 product produced by the UK Met-Office (http://www.metoffice.gov.uk/hadobs/en3/). The EN3 product consists of objective analyses formed from ship and Argo profile data. It provides monthly-analyzed fields of full-depth temperature and salinity profiles on a one-degree grid. While the data is provided from 1950, we only used data from the year 2002 onward, when the objective analysis is constrained by Argo observations in the Southern Ocean.

Mixed Layer Depth (MLD) was extracted from individual profiles of the observational dataset and the reanalysis dataset. We calculated the MLD with a surface-density-difference criterion of $\Delta\sigma \leq 0.03$ kg m^{-3} (Sallée et al. [2006]). Sallée et al. [2006] tested a number of methods and shows that this particular criterion is well adapted to localized the base of the seasonal mixed-layer in the Southern Ocean.

Everywhere possible we used the "observational dataset" to estimate mixed-layer depth. However, when the analysis requested the full length of the seasonal cycle (e.g., to reproduce the seasonal cycle of the mixed-layer integrated chlorophyll, or to compute the initiation date of the mixed-layer integrated chlorophyll), the "reanalysis dataset" was used.

Water-column integrated chlorophyll

Although no observations of water-column integrated chlorophyll exist at large scales, in this study we evaluate it via the combination of surface satellite estimates of Chl^{surf} and interior

ocean structure. We assume that chlorophyll is well mixed above the mixed-layer base, and that there is no chlorophyll below the mixed-layer base. Under such assumptions, we quanfity the water-column integrated chlorophyll, Chl^{ML}, as: $Chl^{ML} = H \cdot Chl^{surf}$, where H is the mixed-layer depth. We note that our assumptions may be questioned in spring when the MLD rapidly shallows, as under such conditions some chlorophyll may be left below the mixed-layer base (e.g. Chiswell, 2013; Lévy, submitted to this issue). One therefore needs to be cautious of the interpretation of Chl^{ML} in spring. In addition, Chl^{ML} is likely to be an underestimate of the actual water-column integrated chlorophyll.

We note that we assume here that Chl^{surf} and Chl^{ML} have the same seasonal pattern as respectively the surface biomass content and the mixed-layer integrated biomass content. In Section 5.2 we discuss the extent to this is true by attempting to compute the carbon concentration from Chl^{surf}, based on the chlorophyll-to-carbon ratio, Chl:C (Behrenfeld [2005]): Chl:C = $Chl:C_{min}$ + [$Chl:C_{max}$ - $Chl:C_{min}$] e^{-3Ig}, where Ig is the mixed-layer integrated irradiance (in moles photons m^{-2} h^{-1}), $Chl:C_{min}$ = 4 10^{-3} mg Chl (mg C)$^{-1}$, and $Chl:C_{max}$ = 0.013 mg Chl (mg C)$^{-1}$ (Behrenfeld [2010]). We show that Chl^{surf} and C have very similar seasonal pattern.

Onset detection method

In this Section, we describe the onset detection method that we apply to both Chl^{ML} and Chl^{surf} time series. Hereafter, Chl^{ML}-onset will refer to the date of onset detected on the Chl^{ML} time-series, and Chl^{surf} the date of onset detected on the Chl^{surf} time-series.

An important challenge is to identify the date of the start of intensification of chlorophyll (either Chl^{ML} or Chl^{surf}) in a manner that can be efficiently and accurately applied to a large datasets. Phenology studies currently use several methods to estimate the timing of a phytoplankton bloom. Ji et al. [2010] identify three broad categories of methods (see also Brody et al. [2013]): threshold method based on biomass; threshold method based on cumulative chlorophyll content; and rate of change methods. Threshold methods based on chlorophyll biomass define bloom initiation as the time at which a given threshold is reached (e.g. Siegel [2002]; Thomalla et al. [2011]; Cole et al. [2012]; Sapiano et al. [2012]). Threshold methods based on cumulative chlorophyll biomass identify a bloom as the time at which a cumulative summation of chlorophyll biomass crosses a threshold percentile of the total biomass. Finally, rate of change methods estimate bloom initiation from the point of most rapid increase on a chlorophyll time series or function fit to that time series.

Brody et al. [2013] investigated the differences between these bloom detection methods. Their conclusion was that the first group of methods (chlorophyll biomass threshold) can be strongly biased for specific time-series and are well suited to investigating the match or mismatch between phytoplankton and upper trophic levels. The second group of methods (cumulative chlorophyll

biomass threshold) is also very sensitive to the date used for the start of the time series and thus cannot be implemented at the basin scale using a globally fixed start date (Brody et al. [2013]). Finally the third group of methods (rate of change) identifies blooms when chlorophyll is increasing rapidly from the pre-bloom minimum, while absolute biomass levels may still remain low. These methods can be useful in examining the seasonal physical or biological mechanisms that create conditions in which a bloom can occur (Brody et al. [2013]).

Based on the analysis of Brody et al. [2013] we chose to apply a rate of change method that we designed and tuned for our dataset. At each grid-point of the chlorophyll dataset, a 13-year time-series (1998-2010) is extracted and linearly interpolated and a fast fourrier transform low-pass filter is applied to remove any high-frequency variability irrelevant to seasonal time-scale and bloom onset. The bloom onset of one particular year is defined as the maximum of the second derivative of Chl (Chl_{tt}) in the time window where the derivative of Chl (Chl_t) (i) is positive, and (ii) contains a local maximum (here Chl is either Chl^{ML} or Chl^{surf}). If the bloom peak is below 1.2 times the seasonal minimum of Chl, we do not consider a bloom to have occurred. Our definition ensures that each defined onset is robust and exists as a bloom in the dataset. Additional constraints are applied to avoid unrealistic bloom detection: (i) the largest data-gap within the 4 months centered on the defined onset must be smaller than 45 days; (ii) the integrated amount of chlorophyll accumulated within 6 months before the onset must be less than 25% of the total amount of chlorophyll summed over the year, centered on the time of onset.

We acknowledge that a definition "by eye" would produce in many instances a more robust definition of onset. However, our goal is to define an objective definition as robust as possible that can consistently treat more than 1 million seasonal cycles and investigate general basin-scale phenomena.

The Chl^{surf}-onset detection procedure nicely positions the Chl^{surf}-onset date at the start of the high Chl^{surf} season (5.2). We note however that in some instances the detected Chl^{surf}-onset seems to be a bit late (e.g. 5.2.a in 2006; 5.2.a in 2010) compare to other cases where Chl^{surf}-onset appears to be detected in the very early days of the increasing season (e.g. 5.2.b in 2008). All automatic detection methods will have such caveats and error associated with it (Cole et al. [2012]; Brody et al. [2013]). Cole et al. [2012] estimates the error on such automatic detection method to about 30 days in the Southern Ocean, which appears, by eyes, as a correct order of magnitude on the specific examples shown in 5.2. We acknowledge that a definition "by eye" would produce in many instances a more robust definition of onset. However, our goal is to define an objective definition as robust as possible that can consistently treat more than 1 million seasonal cycles and investigate general basin-scale phenomena. We applied the same detection method on the Chl^{ML} time-series as an estimate of the bloom Chl^{ML}-onset date. Similar to the Chl^{surf}-onset date, we found the method reliable in detecting Chl^{ML}-onset as the starting date of the increased Chl^{ML} season (5.2).

Atmospheric fluxes

Atmospheric winds, buoyancy, and short-wave forcings are obtained from NCEP Climate Forcing System Reanalysis (http://cfs.ncep.noaa.gov/cfsr/). We used atmospheric fields from this reanalysis for the year 1998-2010, consistent with surface chlorophyll dataset timeframe. The winds of the reanalysis product are strongly constrained by assimilation of satellite wind observation. However, we note that buoyancy flux fields remain poorly known in the Southern Ocean, and are only weakly constrained in atmospheric reanalysis efforts. These constraints are even weaker for freshwater fluxes. We therefore approximate the buoyancy flux to its heat component, which is less uncertain. Mixed-layer integrated irradiance, Ig, is computed from downward short wave flux: $\mathrm{Ig} = \int_0^H \mathrm{I}_0\ \mathrm{e}^{-kz}\ \mathrm{dz}$, where I_0 is the downward short wave flux at sea surface, k is the attenuation coefficient in the surface layer, and H is the mixed-layer depth. Attenuation coefficient depends on both water attenuation (k_w) and chlorophyll self-shading attenuation (k_{chl}). In this paper, we use $\mathrm{k}_w = 0.02\ \mathrm{m}^{-1}$ and $\mathrm{k}_{chl} = 0.0865\ \ \mathrm{m}^{-1}$ (e.g. Nelson and Smith, 1991).

Chlorophyll time series and bloom P-onset and Chl-onset characteristics

Southern Ocean bloom Chl^{ML}-onset and Chl^{surf}-onset dates are estimated by a systematic method on more than one million seasonal cycles based on satellite-derived surface Chl^{surf} co-located with estimates of mixed-layer depth (see Section 5.2). Two time-series of Chl^{ML} and Chl^{surf}, and associated Chl^{ML}-onset and Chl^{surf}-onset dates are presented on 5.2. These examples are chosen to represent two distinct regimes of blooms: one where Chl^{ML} is in phase with Chl^{surf} (5.2.a), and one where Chl^{ML} and Chl^{surf} are slightly out of phase (5.2.b).

The two time-series present a very marked seasonal cycle, with Chl^{surf} increasing by 3-5 times during the high activity season. The surface bloom clearly stands out as the period during which Chl^{surf} dramatically increases. Surface and mixed-layer integrated chlorophyll blooms have been described as tightly linked to the seasonal cycle of the mixed-layer depth (e.g. Sverdrup, 1953; Berhenfield, 2010). We therefore compare chlorophyll time-series to the collocated mixed-layer time-series (from the reanalysis dataset; see Section 5.2). The phasing between the mixed-layer and the chlorophyll seasonal cycles appears consistent for different years of a given location, but clearly varies depending on the location (5.2). For instance, in 5.2.a, the surface chlorophyll bloom is associated with a deepening of the mixed-layer, while in 5.2.b the surface bloom is associated with a shallowing of the mixed-layer. These two strikingly different regimes recalls the debate around autumn versus spring blooms (Lévy et al. [2005]; Chiswell et al. [2013]).

In the two example of 5.2 we find that Chl^{ML}-onset and Chl^{surf}-onset can either be almost instantaneous or separated by a few months. We note that Chl^{ML}-onset is, here, always found during the deepening phase of the mixed layer, i.e. when the mixed-layer actively convects, and where the assumption of a well-mixed chlorophyll profile in the mixed-layer is the most robust.

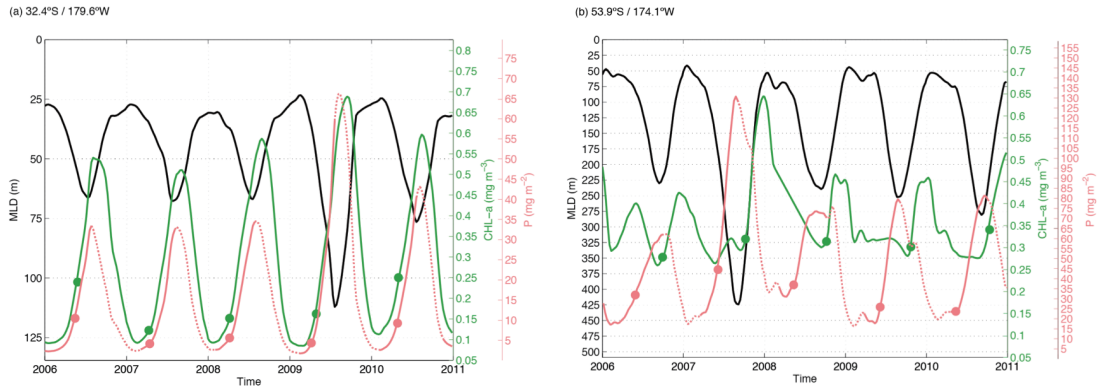

FIGURE 5.2: Two examples of time-series of (green) Chla in two distinct regions: (a) in a subtropical zone characterised by subtropical gyre circulation, at 33.4°S–179.6°W; and (b) in a subantarctic zone, influence by the ACC dynamics, at 53.9°S–174.1°W. Chla time- series is averaged over a region of 20x20 km centred on each location. For clarity, data are shown for 5 years, although the full time series are longer. Collocated (black) mixed-layer depth and (pink) mixed-layer integrated chlopohyll time-series are superimposed on each panel. For each seasonal cycles at each locations, green dots indicates the Chlsur f -onset date and pink dots the ChlML-onset date detected by our automatic procedure (see text for details). ChlML is shown as dated line during the mixed-layer restratification phase to remind the reader that our estimate of ChlML is questionable during this period (see text for details)

In the following section, we undertake a systematic analysis of bloom Chl^{ML}-onset and Chl^{surf}-onset on the entire dataset to investigate whether we can detect specific bloom regimes, as would suggest the examples in 5.2.

Southern Ocean regimes of surface bloom

Over the entire database of Southern Ocean, the Chl^{ML}-onset dates organize around two main modes (5.3.a). One mode, centered on May, is associated with autumn blooms that have a Chl^{ML}-onset before the winter solstice (21st June); the other mode, centered on July, is associated with winter blooms that have a Chl^{ML}-onset after the winter solstice. The winter solstice is a key date in the year as it corresponds to the date where incoming irradiance switches from declining to increasing (note, however, that one may argue that chlorophyll cares about the mixed-layer integrated irradiance, which can be distinct to incoming irradiance). The modal structure in Chl^{ML}-onset date could possibly be due to an unstable detection method picking very early Chl^{ML}-onsets in some instances and late Chl^{ML}-onsets in others (for instance, 5.2 suggests that some Chl^{ML}-onsets are detected slightly later than what we would have picked by eye). In order to test the 'stability' or 'sensitivity' of the Chl^{ML}-onset detection procedure, we investigate the amount of accumulated chlorophyll at Chl^{ML}-onset. If the modal structure in the Chl^{ML}-onset date histogram is due to an unstable detection procedure, a bimodal structure would arise in the percentage of accumulated chlorophyll at Chl^{ML}-onset: unrealistic early detection would be associated with low accumulated chlorophyll at Chl^{ML}-onset, while unrealistic late detection would be associated with high accumulation of chlorophyll at Chl^{ML}-onset. In contrast, we

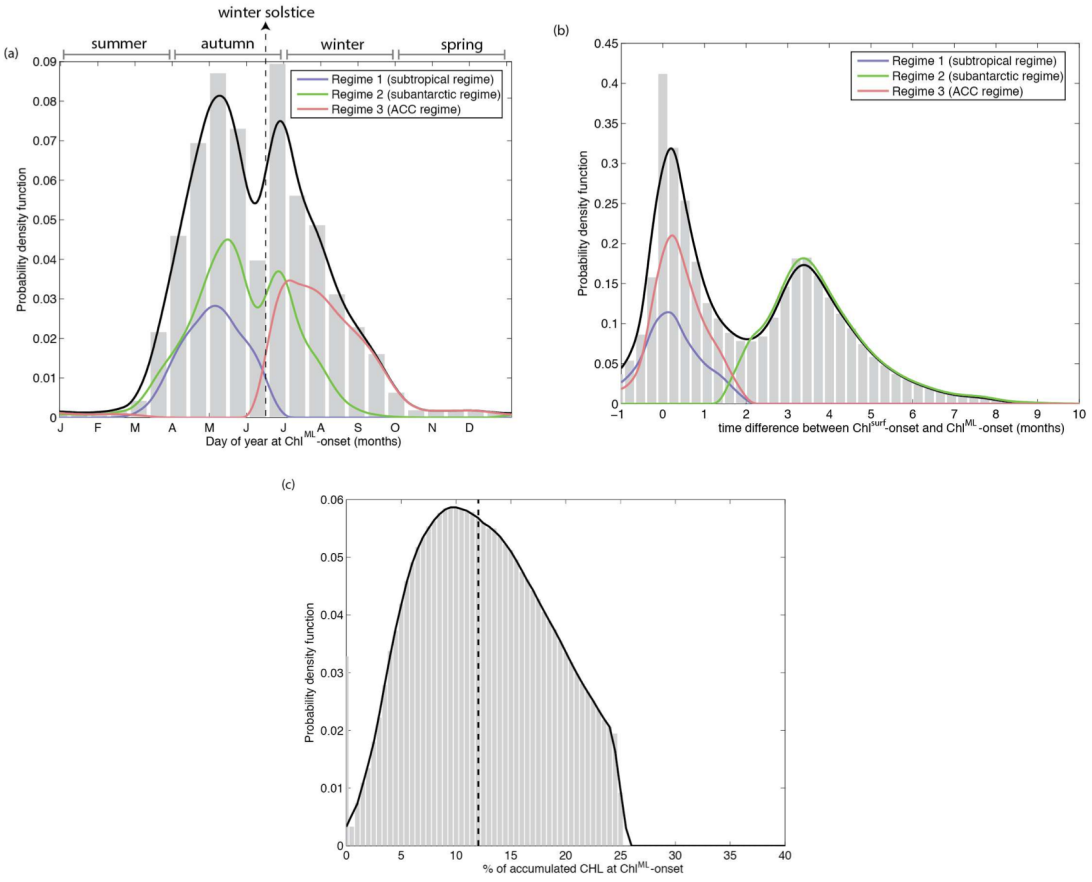

FIGURE 5.3: Probability density function (pdf) of the distribution of (a) the day of year of Chl^{ML}-onset; (b) the time difference between Chl^{ML}-onset and Chl^{surf}-onset; and (c) the percentage of accumulated chlorophyll at Chl^{ML}-onset. Gray bar show the pdf of the entire datasets. Smoothed pdf of (black) the entire dataset, and of (blue) regime 1, (green) regime 2, are (pink) regime 3 are superimposed on panel (a) and (b). Dashed line in panel (a) refers to the time of winter solstice. Dashed line in panel (c) denotes the median value of the distribution.

observe that the percentage of accumulated chlorophyll at Chl^{ML}-onset is consistent over the entire database, with a clear and unique mode centered on 12.6 % (5.3.b). This result gives us confidence that the Chl^{ML}-onset detection procedure is stable enough to investigate bloom regimes in the Southern Ocean.

We then turn to the time lag between Chl^{ML}-onset and Chl^{surf}-onset over the entire database. Two very clear modes stand out, with a group of blooms being characterized by almost parallel Chl^{ML}-onset and Chl^{surf}-onset, and a second group characterized by a lag of several months between Chl^{surf}-onset and Chl^{ML}-onset (5.3.c).

Based on these Chl^{ML}-onset and Chl^{surf}-onset histograms, we define four Southern Ocean regimes: (regime 1) blooms with Chl^{ML}-onset before the winter solstice, and nearly parallel Chl^{surf}-onset (within two months); (regime 2a) blooms with Chl^{ML}-onset before the winter solstice, and with a significant lag between Chl^{ML}-onset and Chl^{surf}-onset (greater than two months); (regime 2b) bloom with Chl^{ML}-onset after the winter solstice, and with a long time lag

between Chl^{ML}-onset and Chl^{surf}-onset (more than two months); and (regime 3) blooms with Chl^{ML}-onset after the winter solstice, and nearly parallel Chl^{surf}-onset (within two months). Ultimately, we seek to segregate blooms that occur before or after the winter solstice and blooms where integrated and surface biomass increase together or display a lag. For simplicity, in the remainder of this paper, we combine regime 2a and 2b, in a single "regime 2" since the regime 2a, and 2b did not show phenology different enough to be especially highlighted (not shown; regime 2 corresponds therefore to blooms with long time lag between Chl^{ML}-onset and Chl^{surf}-onset). We remind the reader that we have, so far, made no assumption regarding geographic location or mixed-layer structure, yet are able to group Southern Ocean chlorophyll blooms in three regimes. We now analyze the characteristics of each of these regimes.

We find that the three bloom regimes defined above display a coherent geographical organization (5.4). Blooms of regime 1 occur in a narrow zonal band between 30°-40° S in the subtropics (5.4.a) that are characterized by low surface nitrate concentrations (5.1.d). Blooms of regime 2 are concentrated in the subantarctic region of the Southern Ocean: south of the subtropical front region and directly north of the Antarctic Circumpolar Fronts (5.4.b). Finally blooms of regime 3 are primarily associated with the fronts of the Antarctic Circumpolar (ACC; 5.4.c). Given the coherent geographical distribution associated with the three regimes, for convenience, we hereafter refer to them as 'subtropical regime' for regime 1, 'subantarctic regime' for regime 2, and 'ACC regime' for regime 3. We note however that there are no clear geographical boundaries between the three regimes, which is consistent with the different blooms being driven by multiple processes (defined by a range of parameters, e.g. gyres, ACC, deep mixed-layers, iron inputs, etc.) rather than geographical bins.

The three regimes are associated with very distinct bloom characteristics. By definition, the subtropical regime has bloom Chl^{ML}-onsets centered in autumn (i.e. April°-June; 5.3.a). Similarly, the ACC regime has bloom Chl^{ML}-onsets centered in winter (i.e. July°-August; 5.3.a). Subantarctic regime Chl^{ML}-onset dates are mostly in autumn but some are in winter. All three regimes have their Chl^{ML}-onset during the period of convection, when air-sea heat fluxes are driving overturn of the surface layer (Air-sea heat flux $\sim$ -50°-100 W m^2 at Chl^{ML}-onset; 5.5.b). In addition, the subantarctic and ACC regimes have their Chl^{ML}-onset when surface irradiance is low (short wave $\sim$ 50 W m^2 at Chl^{ML}-onset; 5.5.c), and daylight length is short ($\sim$ 9 h per day; 5.5.a).

Before investigating the details of the seasonal cycles, it is instructive to discuss the typical physical and biogeochemical conditions of the regions where each regime falls. Subtropical regimes are located in the center of subtropical gyres, which are characterized by surface depleted macronutrients and shallow winter mixed-layers (averaged MLD_{max} of 86 m and average surface nitrate concentration of 0.7 μmol/kg; Table 5.1 and 5.1.c-d). Therefore, we anticipate the availability of macronutrients will be the major regulator of blooms in these regions. In contrast, subantarctic

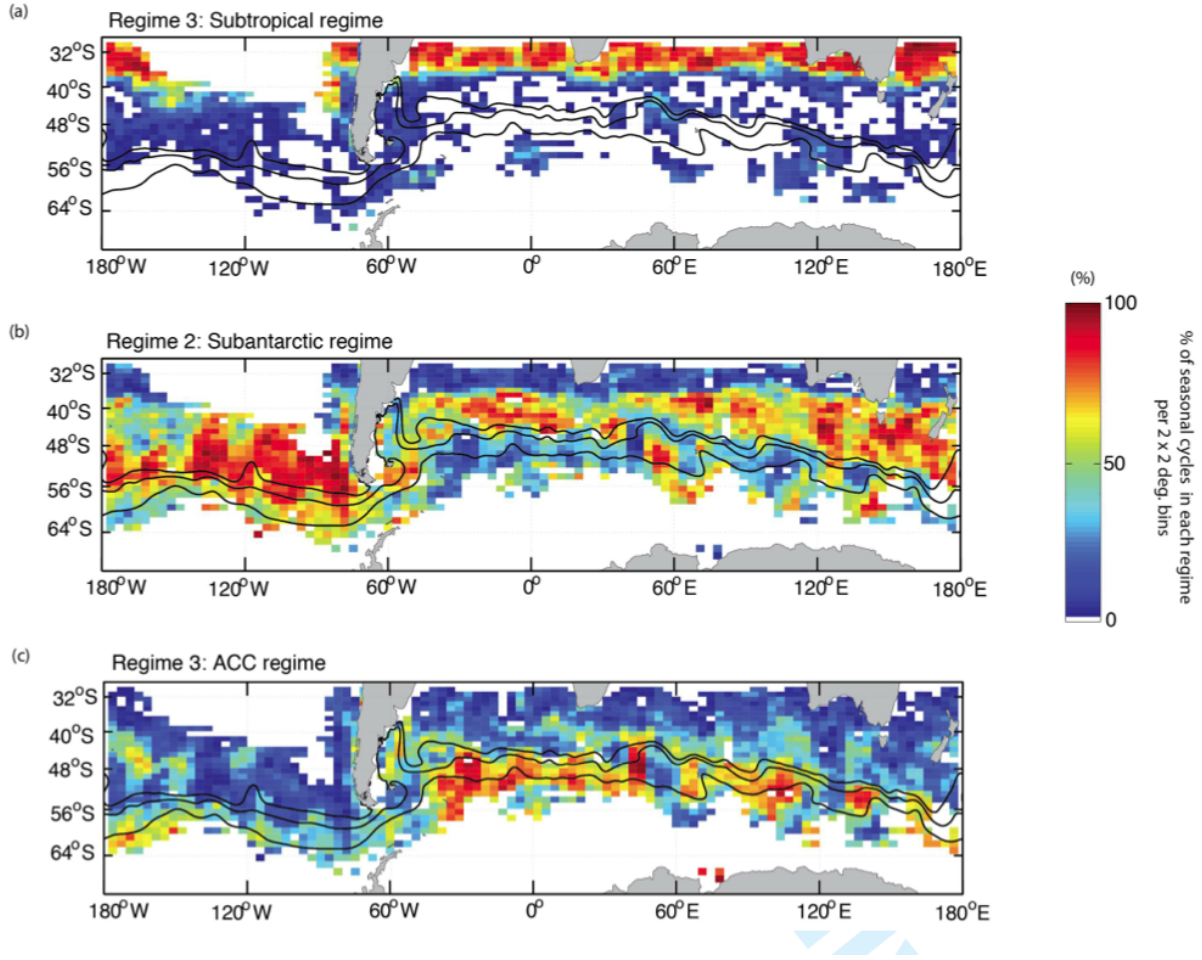

FIGURE 5.4: Geographical distribution of each bloom regime (see text for regime definition). The percentage of seasonal cycles associated with any given regime is gridded in 2 x 2°: (a) regime 1: subtropical blooms; (b) regime 2: subantarctic bloom; (c) regime3: ACC blooms. In panel (a-c) the three black lines represent the approximate climatological position of the three main ACC branches, from south to north: polar front, subantarctic front, and northern branch of the subantarctic front following Sallée et al. [2008].

and ACC regimes are located in region of very deep winter mixed-layer, much deeper than typical euphotic layer, and in regions richer in macronutrients (averaged MLD_{max} of 258 and 246 m respectively, and average surface nitrate concentration of 11.8 and 11.9 μmol/kg; Table 5.1 and 5.1.c-d). Subantarctic and ACC regions are also known as HNLC region. We therefore anticipate that these blooms will be governed by light and iron availability.

Seasonal cycles

For each of the three bloom regimes, we compute the median seasonal cycle of mixed-layer, Chl^{ML} and Chl^{surf} (5.6). In order to prevent the median from blurring Chl^{ML}-onset and the different phases of the bloom, we reference all seasonal cycles to their Chl^{ML}-onset date before averaging.

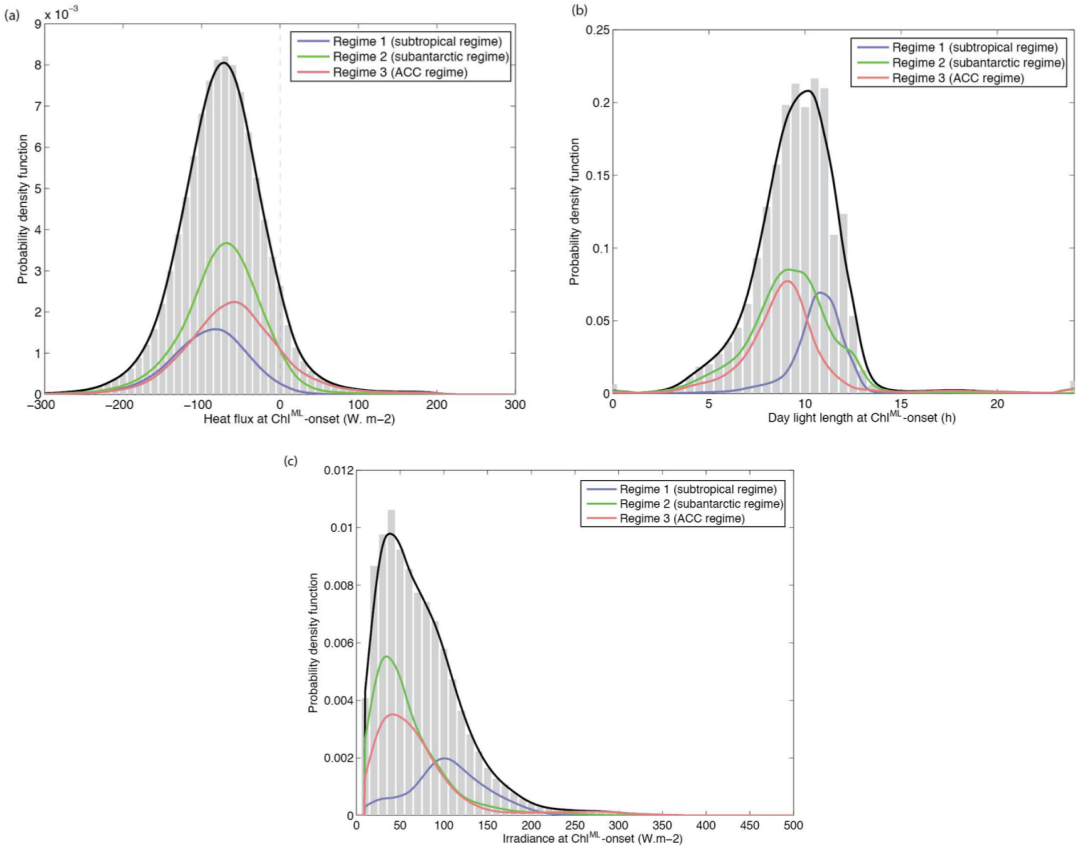

FIGURE 5.5: Probability density function (pdf) of the distribution of (a) the intensity of air-sea heat flux at P-onset (negative denotes an ocean cooling; W m^{-2}); (b) daylight length at the time of Chl^{ML}-onset (hours); and (c) surface irradiance at Chl^{ML}-onset ($W.m^{-2}$). Gray bar show the pdf of the entire datasets. Smoothed pdf of (black) the entire dataset, and of (blue) regime 1, (green) regime 2, are (pink) regime 3 are superimposed.

Similarly, we compute the mean seasonal cycle of air-sea heat flux, wind-stress, and downward short wave at ocean surface. We discuss the median seasonal cycle of each regime in turn, below.

	Subtropical regime	**Subantarctic regime**	**ACC regime**
MLD_{max} (m)	85.77 ± 27.71	257.80 ± 104.86	245.62 ± 105.67
Nitrate (μmol/kg)	0.71 ± 0.77	11.79 ± 6.44	11.91 ± 7.22
Silicate* (μmol/kg)	1.78 ± 1.17	-7.26 ± 5.02	-7.26 ± 5.7

TABLE 5.1: Climatological mean biogeochemical and physical surface characteristics values in each of the three regimes. MLD_{max} refers to the climatological winter depth of mixed-layer (from Argo; Sallée et al. [2010b]). Nitrate and Silicate* are climatological mean surface values from World Ocean Atlas. Averages are weighted by the geographical distribution of the number of profiles for each regime

The subtropical regime is marked by a Chl^{ML}-onset in autumn when the mixed-layer deepens (5.6.a). In this region the Chl^{ML}-onset is parallel to the Chl^{surf}-onset. Chl^{ML}-onset occurs in a convective mixed-layer (negative heat flux; 5.6.d) and when cycle of surface winds begins its seasonal increase. These characteristics rule out any control of Chl^{ML}-onset by a critical depth

or critical stratification and points to control by the entrainment of macronutrients in the surface layer associated with the deepening of the mixed layer. We note that the subtropical region is characterized by very low macronutrient concentrations in the surface layer (Table 5.1; 5.1.d), which supports the argument that the bloom herein is limited by the availability of nutrients. In addition, we note that the subtropical region is characterized by relatively shallow mixed-layers (MLD_{max} of 91 $\pm$ 21 m; Table 5.1; 5.1.c), so light availability is likely to play a minor role in regulating blooms in this region. Although the Chl^{ML}-onset occurs at the seasonal minimum of mixed-layer integrated irradiance, the irradiance at this time is notably much larger than for subantarctic and ACC regimes (yellow lines in 5.6.d-f). The bloom in the subtropical regime continues for the entire mixed-layer deepening period, and weakens when the mixed-layer reaches its maximum depth. Overall, the bloom seen at surface remains in phase with the integrated bloom over the year.

In contrast to the subtropical regime, the subantarctic regime is not in regions of low surface nitrate (Table 5.1; 5.1.d). The subantarctic regime Chl^{ML}-onset occurs in autumn, when the mixed-layer starts destratifying (5.6.b). Interestingly, the autumn-winter increase of Chl^{ML} is not seen at surface (i.e. on Chl^{surf}), which suggests that the actual increase of chlorophyll biomass is diluted in the increasing volume of the surface layer associated with mixed-layer deepening. Chl^{ML}-onsets in the subantarctic regime occur at low irradiance and in convective mixed-layers (5.6.e-f). When the mixed-layer layer reaches its maximum depth in winter, the increase of Chl^{ML} stops (see in August in 5.6.b), and a second increase phase starts in early spring (star on 5.6.b). This second phase of the bloom is associated with a large surface signal (i.e. on Chl^{surf}) and is associated to Chl^{surf}-onset. It occurs during the restratification phase of the mixed-layer (5.6.b) and when light conditions rapidly increase (5.6.e). The springtime increase of Chl^{ML} in the subantarctic regime is therefore consistent with a light control of the bloom. However, this springtime increase of Chl^{ML}, possibly light controlled, can begin in very deep mixed-layers (up to 400°-600 m, 5.7.a), which should rule out control by critical depth. Interestingly, we find that subantarctic Chl^{surf}-onsets are associated with air°-sea heat fluxes switching from surface cooling to surface warming (5.6.e and 5.7.b).

Similar to the two other regimes, the ACC regime Chl^{ML}-onset occurs during the destratification phase of the mixed-layer (5.6.c). However, ACC regime blooms have their Chl^{ML}-onset in winter, later in the year compared to the other regimes. We note however that Chl^{ML}-onset of the ACC regime might be biased too late in the year, due to a weak bloom initiation. As such, one might say that Chl^{ML}-onset of ACC regime actually occurs in autumn (as the other regimes). However, the important point we wish to highlight is that the increase in integrated chlorophyll in autumn/winter in the ACC regime is, if anything, very low (5.6.b-c). Chl^{surf} even decreases during the autumn months (5.6.b), suggesting that the automnal growth is so low that it cannot compensate for the dilution associated with the deepening of the mixed-layer base. Then, in winter, when the mixed-layer depth reaches its seasonal maximum, a very large and sudden

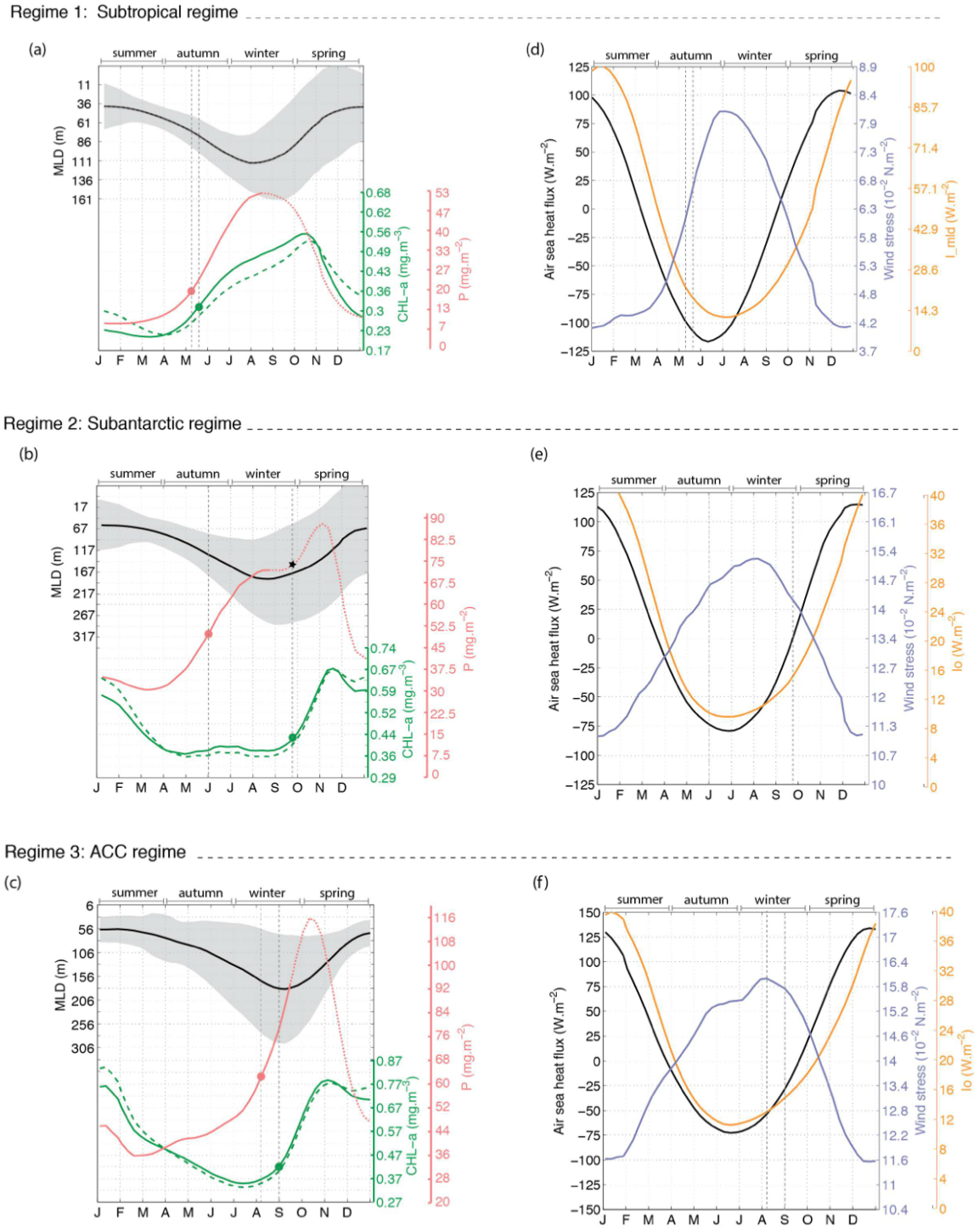

FIGURE 5.6: Mean of all seasonal cycle falling in (a-d) subtropical regime; (b-e) subantarctic regime; (c-f) ACC regime. Before taking the mean, all seasonal cycle are centred on their date of Chl^{ML}-onset. Panel (a-c) show the seasonal cycle of: (plain green) surface Chl_a (mg m^{-3}); (dashed green) associated surface carbon biomass (mg C); (pink) mixed-layer integrated chlorophyll, Chl^{ML} (mg m^{-2}); (black) mixed-layer depth from collocated in situ observation (m). Surface carbon biomass reads on the surface Chl_a axis, and has been multiplied by the following values to scale with chl_a: (a) 0.0124; (b) 0.0122; (c) 0.0098. Panel (d-f) show the seasonal cycle of: (black) air-sea heat flux (W m^{-2}); (purple) wind-stress (N m^{-2}); and (yellow) mixed-layer averaged irradiance (W m^{-2}). In panel (a-c) green dots indicates the median Chl^{surf}-onset date and pink dots the median Chl^{ML}-onset date detected by our automatic procedure (see text for details). Chl^{ML} is shown as as a doted line during the mixed-layer restratification phase to remind the reader that our estimate of Chl^{ML} is questionable during this period (see text for details). In panel (b), the black star on the Chl^{ML} curves denotes the time of Chl^{surf}-onset.

Chl^{surf}-onset and Chl^{ML}-onset are reported on all panels by the vertical gray dashed lines

increase of Chl^{ML} starts. In contrast to the subantarctic regime, the autumn-winter increase of Chl^{ML} happens at the end of the mixed-layer depth deepening season so the increase of integrated chlorophyll is not diluted in increasing volume of the surface layer. The chlorophyll increase signal translates therefore very clearly on Chl^{surf} (5.6.b). This winter increase of Chl^{ML} and Chl^{surf} starts at low irradiance, in convective mixed-layers (5.6.f and 5.7.b) and in deep mixed-layers (up to 200°-300 m; 5.7.a). The bloom continues over in spring when mixed-layer re-stratifies and light condition improves.

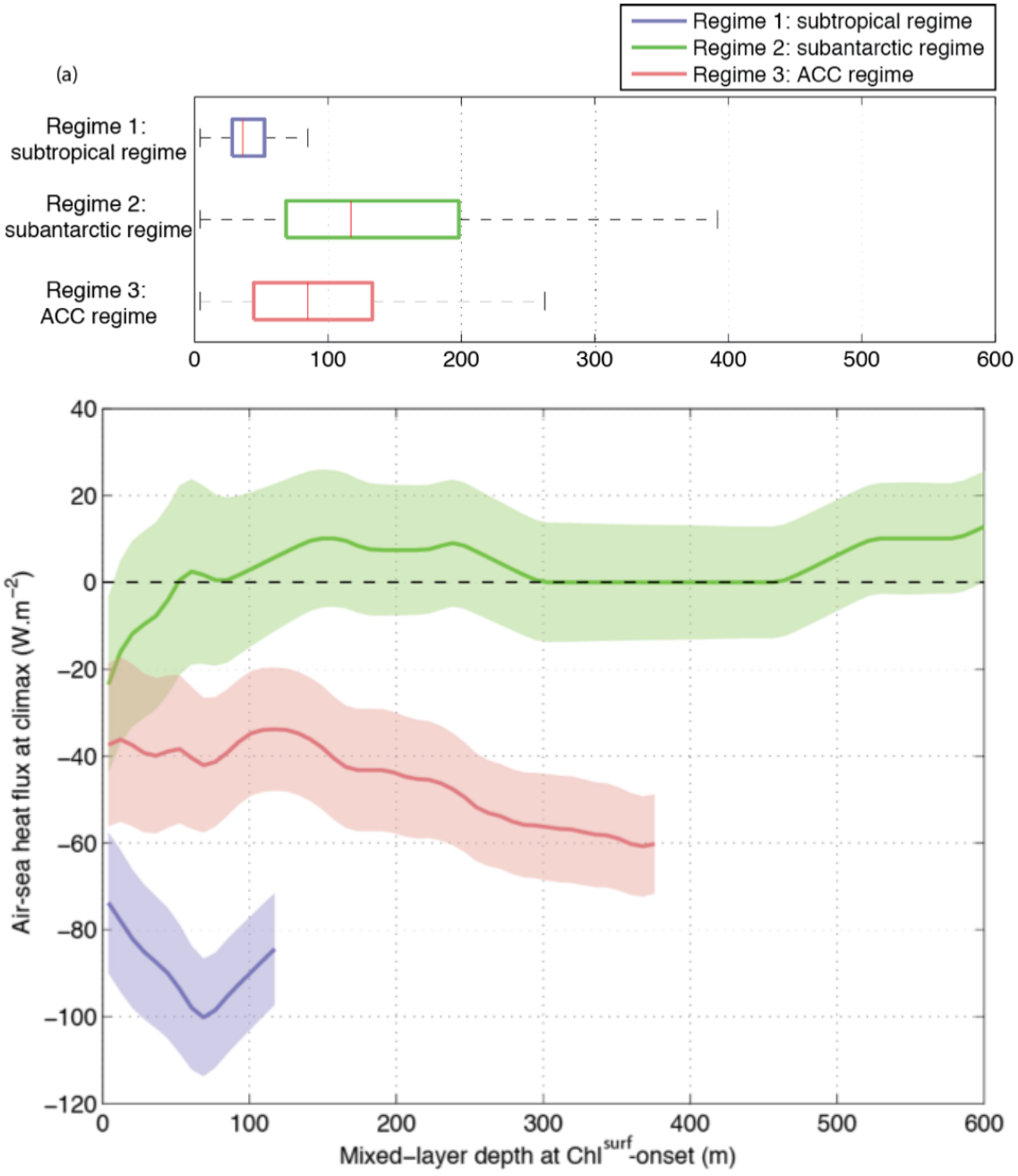

FIGURE 5.7: (a) Box plot of the mixed layer depth at Chl^{surf}-onset for each regime. (b) Air-sea heat flux at Chl^{surf}-onset versus mixed-layer depth at Chl^{surf}-onset: (plain curve) mean and (shading) standard deviation are shown for each regime. In both panels, the color refers to bloom regime: (blue) subtropical regime; (green) subantarctic regime; and (pink) ACC regime.

Discussion and conclusion

The bloom Chl^{ML}-onset and Chl^{surf}-onset in the Southern Ocean have been estimated from satellite-derived products and observation-based estimates of mixed-layer depth. Our automatic procedure was applied systematically over a large dataset, which allows us to illustrate basin scale regimes of bloom dynamics. The phenology of phytoplankton blooms appears to be organised into three distinct regimes when analyzing Chl^{ML}-onset and Chl^{surf}-onset dates. These regimes are associated with three specific geographic locations: 1) autumn Chl^{ML}-onset (i.e. before winter solstice) blooms in a single phase (i.e. almost parallel Chl^{surf}-onset and Chl^{ML}-onset) are found in the subtropics, 2) autumn-winter blooms with a second increase in spring (i.e. Chl^{surf}-onset and Chl^{ML}-onset separated by a few months) are found in the subantarctic zone (between the ACC and the subtropics), and 3) winter Chl^{ML}-onset (i.e. after winter solstice) blooms in a single phase (i.e. almost parallel Chl^{surf}-onset and Chl^{ML}-onset) are found in the ACC region. It is notable that these three regimes organize themselves coherently in geographical space that is mostly zonal (except the central Pacific basin, 80°-160° W, that appears as an exception for the subtropical regime, with almost no bloom in the region; 5.4). However, the subantarctic and ACC regimes clearly follow the known meridional deviations and standing meanders of the Antarctic Circumpolar Current. Our findings suggest that the three regimes are fundamentally controlled by distinct mixed-layer and nutrient characteristics.

Llort et al. (submitted to this issue) found that onset identified from Chl^{ML} corresponded in more than 85% of cases to the bloom onset detected from the actual water-column integrated biomass of their model (see also Sverdrup [1953]; Behrenfeld [2010]). In addition, they found that Chl^{surf}-onset is associated with the climax of the bloom, which corresponds to the date of maximum integrated chlorophyll increase. Chl^{ML}-onset and Chl^{surf}-onset, which we use to describe bloom regimes are therefore associated with two distinct key dates of bloom phenology. As noted by Llort et al. (submitted to this issue), some confusion in our understanding of chlorophyll bloom might have arisen from the use of the same word "onset" to refer to either Chl^{ML}-onset (e.g. Sverdrup [1953]; Behrenfeld [2010]) or Chl^{surf}-onset (e.g. Ferrari et al. [2014]; Lozier et al. [2011]). Indeed, our results clearly indicate that Chl^{ML}-onset and Chl^{surf}-onset refer to different phases of the bloom with arguably distinct controlling controlling factors (see also Llort et al., submitted to this issue).

Overall we find that all three regimes found in the present study have their Chl^{ML}-onset in autumn-winter when the solar irradiance is at its seasonal minimum, when daylight length is short, and when mixed-layer actively mixes. While the phenological differences between the three regimes clearly standout from our observational dataset, linking these differences to biological and physical control is challenging from the available observations. The year-round biogeochemical water-column observations necessary to determine the factors that control the different phases of

the bloom are presently not available. Nevertheless, we can speculate on the distinct controlling factors of each regime.

The subtropical regime is specific since it is located in a region of much stronger nitrate limitation (Table 5.1; 5.1.d) and relatively higher year-round light levels than the wider Southern Ocean. We find that the Chl^{ML}-onset in the subtropical regime occurs as soon as the mixed-layer deepens in fall and entrains sub-surface nitrate. The bloom then reaches its apex (i.e. date of maximum Chl^{ML}) when the mixed-layer depth is maximal. While we cannot disentangle the potential roles of dilution and nutrients with our dataset, the strong degree of nitrate limitation in this region implies this is most likely to be a bloom controlled by nitrate entrainment. In that sense, the subtropical regime bloom Chl^{ML}-onsets can be considered to be in a bottom-up regime.

In the subantarctic regime, the deepening of the mixed-layer in autumn-winter dilutes the surface layer, which must then reduce the prey-grazer encounter rate. However, for a bloom to be efficiently initiated by the reduction of the prey-grazer encounter rate, the system must at least be supporting some low levels of growth, or the growth must reduce slower than the reduction of loss associated with the reduction of the prey-grazer encounter rate (e.g. Llort et al., submitted to this issue). Again, this is difficult to assess, but we do observe a significant autumnal accumulation of integrated chlorophyll, which suggests some growth is occurring at the time of mixed layer deepening, or that loss is reducing faster than growth. In addition, Chl^{surf} remains constant in autumn (5.6.b), while we know that the mixed-layer is deepening at this seasons, which is an evidence that some growth must occur to balance the increase of the surface-layer volume. Accordingly, it is possible that dilution, lowering prey-grazer encounter rate, may stimulate this bloom and that the autumn-winter subantarctic regime bloom Chl^{ML}-onsets are a top-down controlled regime.

The subantarctic regime is also noteworthy in that in contains a springtime increase of Chl^{ML} after the autumn-winter increase. This springtime increase translates into a large surface signal, and is therefore associated to Chl^{surf}-onset. Interestingly, this springtime increase of Chl^{ML} can start in either deep or shallow mixed-layers (5.7.a). However, it consistently starts when air°-sea heat fluxes switch from cooling the surface layer to warming (5.7.b). Taylor and Ferrari [2011] proposed that the date at which air°-sea heat flux switches from cooling to warming would be a good proxy for the date at which turbulence in the mixed-layer would drop. Indeed, as mixed-layer turbulence ceases the degree of light limitation reduces (e.g. Huisman et al. [1999]). This improvement of the light environment associated with a more stable mixed layer can explain the springtime Chl^{ML} increase in this region.

The ACC regime is in stark contrast to the autumn-winter subantarctic blooms as autumnal dilution is not able to initiate the bloom. Instead, there is very little chlorophyll accumulation in autumn, suggestive of chronic limitation of growth and ruling out a strong role for dilution (Llort et al., submitted to this issue). A large integrated chlorophyll accumulation only starts when the

mixed-layer reaches its winter maximum. In the absence of dilution a plausible explanation is that strong iron limitation in the ACC regime prevents the autumnal dilution from triggering the bloom. It is only when the mixed-layers reach deep iron reservoir in winter that iron limitation is alleviated (e.g. Tagliabue et al. [2014a]). In parallel, light conditions start to improve and we therefore speculate that the combination of light and iron initiates a short and intense bottom-up controlled bloom in the ACC regime.

In summary, we find that autumn-winter blooms in the subtropical and ACC regimes are bottom-up controlled, associated with entrainment of nutrient (nitrate for the subtropical regime, and iron for the ACC regime). The autumn bloom in the subantarctic regime is top-down controlled, associated with a reduction of prey-grazer encounter when the mixed-layer destratifies. This subantarctic regime autumn bloom is followed by a bottom-up controlled springtime bloom, associated with rapid light improvement in the surface layer, which is caused by a reduction of surface-layer turbulence.

An implication of our interpretation is that the subantarctic regime is assumed to be less iron-governed than the ACC regime, which allows for some autumnal growth (permitting therefore the top-down controlled autumn-winter bloom) and permits the springtime secondary bloom not seen in the ACC. This may manifest itself due to differences between the two regions in total iron inputs or in iron recycling (Boyd et al. [2012a]; Tagliabue et al. [2014a]). At present, we do not have enough observations of dissolved iron, particularly at the times of seasonal transitions (Tagliabue et al. [2011]), nor do we have a broad enough understanding of the seasonal patterns of iron limitation (e.g. Moore et al. [2013]; Tagliabue et al. [2014a]) to address this at basin scale and over the full length of seasonal cycle. However, it is notable that the subantarctic regime contains the largest number of continental sources of iron in the Southern Ocean (e.g. South America, Falkland Islands, South Africa, Crozet Island, Tasmania, New Zealand; the only notable exception being Kerguelen Island). This consistently translates into the presence of large blooms and maximum iron utilization in the subantarctic region, downstream of the major western boundary currents flowing on the northern edge of the ACC, as estimated from satellite imagery (5.1.a; e.g. Thomalla et al. [2011]; Sokolov and Rintoul [2007]; Boyd et al. [2012a]).

One potential caveat in studying chlorophyll blooms from surface estimate of Chl^{surf} is that an increase of Chl^{surf} can be produced by photoadaptation rather than an increase of biomass. In order to test this, we computed the carbon concentration from Chl^{surf} based on the chlorophyll-to-carbon ratio, Chl:C (e.g. Behrenfeld [2005]; see methods). We find that in all three regimes, the increased in surface chlorophyll does coincide with the increase in carbon biomass (5.6.a-c). Another important assumption in our study is that chlorophyll is well mixed in the mixed-layer. We note that the three regimes described in this paper do not rely only on P, but are also clearly identified as three distinct patterns on surface chlorophyll (5.6.a-c). In addition, Chl^{ML}-onsets are detected in the deepening phase of the mixed-layer, when active convection occurs

and where we are confident that phytoplankton are actively mixed over the mixed-layer depth. Subsurface chlorophyll directly under the base of the surface layer when the mixed-layer is shallow in summer has been observed in the ocean (e.g. Sharples et al. [2006]), which would invalidate our assumption on the vertical structure of chlorophyll. Although the presence of such subsurface chlorophyll would affect our results, we note that summer mixed-layer in the subantarctic and ACC regions are of order of 50°-100 m (e.g. Sallée et al. [2010b]), so we are confident that light limitation in these regions would prevent chlorophyll to be maintain year-round under the base the mixed-layer. Making these assumptions has allowed us to identify three main bloom regimes of the Southern Ocean, as well as their distinct phenologies (autumn, winter and spring blooms). Future work will however need to be dedicated to the study of these regimes from in situ datasets. The growing bio-argo programme that reports concomitant biological and physical observations, year-round, will no doubt be of great help in assessing the details of the three main regimes identified in this paper.

Acknowledgement

We thank R. Johnson for kindly providing his reprocessed ocean color dataset, specifically treated for the Southern Ocean. R. Johnson originally used satellite data provided by NASA Goddard Space Flight Centre and the ESA GlobColour Project. We also thank J. Le Sommer and L. Bopp for the interesting discussions that partly motivated this work. The Argo float data were collected and made freely available by the International Argo Program (http://www.argo.ucsd.edu). J.B.S. received support from Agence Nationale de la Recherche (ANR), ANR-12-PDOC-0001, as well as from the British Antarctic Survey as a BAS Fellow.

5.3 Integrated view of bloom phenology regimes using a regional model

The use of ocean colour data together with water column information extracted from the Argo floats database allowed us to identify three distinct bloom regimes in the Southern Ocean. A subtropical regime distributed north of 40°S where the bloom appears early in the year coinciding with the resupply of nutrients in autumn. A sub-antarctic regime characterised by deep MLD, an early increase in chl through the water column and a bloom climax associated to positive air-sea fluxes. And the ACC regime, which is characterised by a late bloom onset (in spring) and short duration in time (likely due to the tight iron control).

These three regimes were, in part, differentiated by the time lag between the integrated and the surface bloom initiation. In chapter 4 we demonstrated how each of these two events are characteristics of different bloom phases. When working with observations, however, information on the biomass distribution through the water column is unattainable; only surface projections of integrated biomass can be observed. We overcame this obstacle by estimating integrated biomass (P) as the surface biomass multiplied by the mixed layer depth (i.e., $P \approx Chl^{ML} = sChl \times MLD$). Such an approximation has repeatedly been used in literature (Behrenfeld [2010]; Behrenfeld et al. [2013a]) even if some authors (see comment letter Chiswell [2013] and response Behrenfeld et al. [2013b]) proved that its reliability was limited to the winter period when the MLD actively mixes biomass all through the upper layers. The limitation was not a problem in identifying the integrated bloom onset as we showed that the integrated onsets are always in winter (chapter 4).

After this observational study, we decided to approach the same question (i.e., bloom phenology in the Southern Ocean) using a 3D regional forced model: the BIOPERIANT05-GAA95b presented in chapter 3. The main objectives were to provide an integrated (i.e., vertical and horizontal) view of the bloom dynamics, to detect potential weaknesses in the Chl^{ML} approximation and to test GAA95b's ability to reproduce observed bloom diversity.

Experience GAA95b was produced from a BIOPERIANT05 configuration with a horizontal resolution of 0.5 over the periantarctic domain from 30°S to 70°S. After a three years of spin-up this configuration was run for the period of 1992 to 2011 with ERAinterim atmospheric forcing. The dynamical compartment was fully coupled to the biogeochemical (PISCES), which the phytoplankton growth rate was computed with the options of *oldprod*/*newpenal* (see chapter 3 for details on these options).

GAA95b broadly reproduced spatial patterns of summer and winter MLD (figure 5.8.a that can be compared to 5.1.a) and the distribution and magnitude of surface blooms (figure 5.8.b). However, iron concentration downstream continental platforms was biased to be too high resulting in an

excessive amount of primary production in winter at low latitudes ($\leq$ 40°S). As discussed in chapter 3, and thanks to some changes on the growth rate formulation, bloom timing was in phase with the observations.

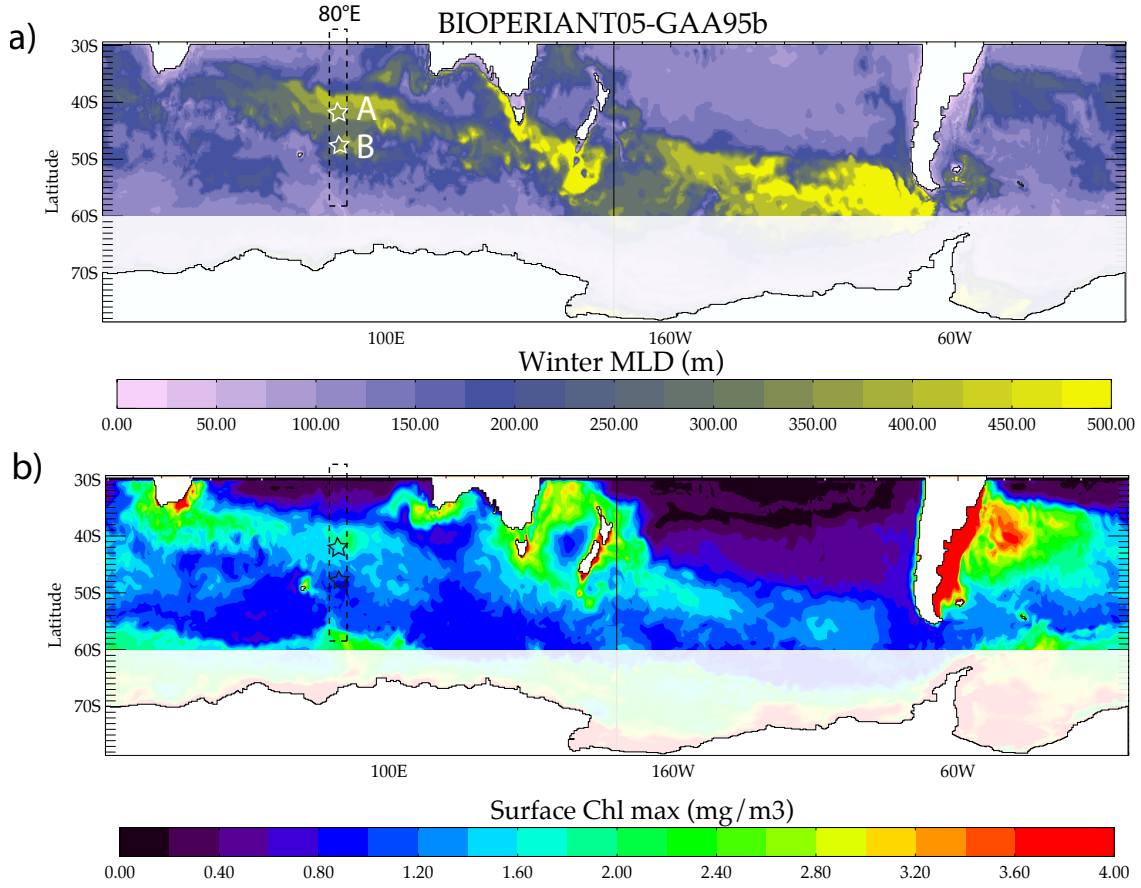

FIGURE 5.8: Spatial distribution of the maximal winter MLD, or MLD_{max}, (a) and maximal surface Chl concentration (b) for 1998 of GAA95b experience. The white area south of 60°S indicates the region which data was ignored in this study to mimic average satellite coverage. Stars indicate the 2 locations where integrated bloom was addressed in detail (see next paragraphs).

With the aim of obtaining comparable quantities between the observational study and the model results, we ignored the model data from 60°S to 70°S (overlapped in white in figure 5.8). Such data rejection was intended to mimic the average cloud coverage that blocks surface chlorophyll measurement from space. In winter, important cloud coverage produces data gaps that strongly limit the number of observations over an important extent of the Southern Ocean. As discussed in chapter 2 and in precedent section of this chapter, we applied a strict criteria over satellite data timeseries to ensure that blooms were properly detected. As a result of these criteria, the bloom regime study was limited to 60°S, in average.

We used the abundance of model data to detect bloom onset using three different magnitudes: Chl^{ML} to mimic the observations-based detection, integrated biomass from 0 to 600m (P) and the rate of net biomass accumulation (r). Using Chl^{ML} and P, onsets (hereinafter, Chl^{ML}-onset

and P-onset respectively) were detected with the same methodology applied for observations; as a reminder:

> *At each grid-point of the chlorophyll dataset, a 13-year time-series (1998-2010) is extracted and linearly interpolated and a fast fourrier transform low- pass filter is applied to remove any high-frequency variability irrelevant to seasonal time-scale and bloom onset. The bloom onset of one particular year is defined as the maximum of the second derivative of Chl (Chltt) in the time window where the derivative of Chl (Chlt) (i) is positive, and (ii) contains a local maximum (here Chl is either ChlML or Chlsurf). If the bloom peak is below 1.2 times the seasonal minimum of Chl, we do not consider a bloom to have occurred. Our definition ensures that each defined onset is robust and exists as a bloom in the dataset. Additional constraints are applied to avoid unrealistic bloom detection: (i) the largest data-gap within the 4 months centered on the defined onset must be smaller than 45 days; (ii) the integrated amount of chlorophyll accumulated within 6 months before the onset must be less than 25% of the total amount of chlorophyll summed over the year, centred on the time of onset.*

Bloom onset detection based on r (i.e., r-onset) is, without ambiguity, the latest date at which r becomes positive before maximal accumulation is attained (refer to chapter 4 for the details of this detection method). Hence, r-onset was considered the most reliable method as represented by the analytical formulation of the bloom onset definition (i.e., the date at which phytoplankton gains overcome the losses).

Discordances between integrated and surface inferred onsets.

The distribution of the blooms onsets detected through Chl^{ML}, P and r during 13-years (from 1998 to 2010, the same period as observations) are represented in figure 5.9); similarly as have done with the observations in figure 5.3. In this representation, Chl^{ML}-onset presented a clear bimodal distribution with a dominant mode of onsets detected before the winter solstice and a second mode after the winter solstice (figure 5.9.a). Such a distribution was very similar to the bimodal probability density function of figure 5.3.a obtained from observations. Surprisingly, the P-onset histogram strongly differed from Chl^{ML}-onset: all onsets were organised around a single mode after winter solstice (figure 5.9.b). The r-onset distribution also showed a single mode slightly earlier than for the P-onset (figure 5.9.c).

While the P and r-onset resemblance proved that P-onset detection was reliable; disparity between the Chl^{ML} and P-onset suggested a detection bias likely produced by Chl^{ML} approximation. It seemed obvious that, for an important number of cases, Chl^{ML} was not a proper estimation of the integrated biomass and, in consequence, Chl^{ML} failed in the detection of the bloom onset.

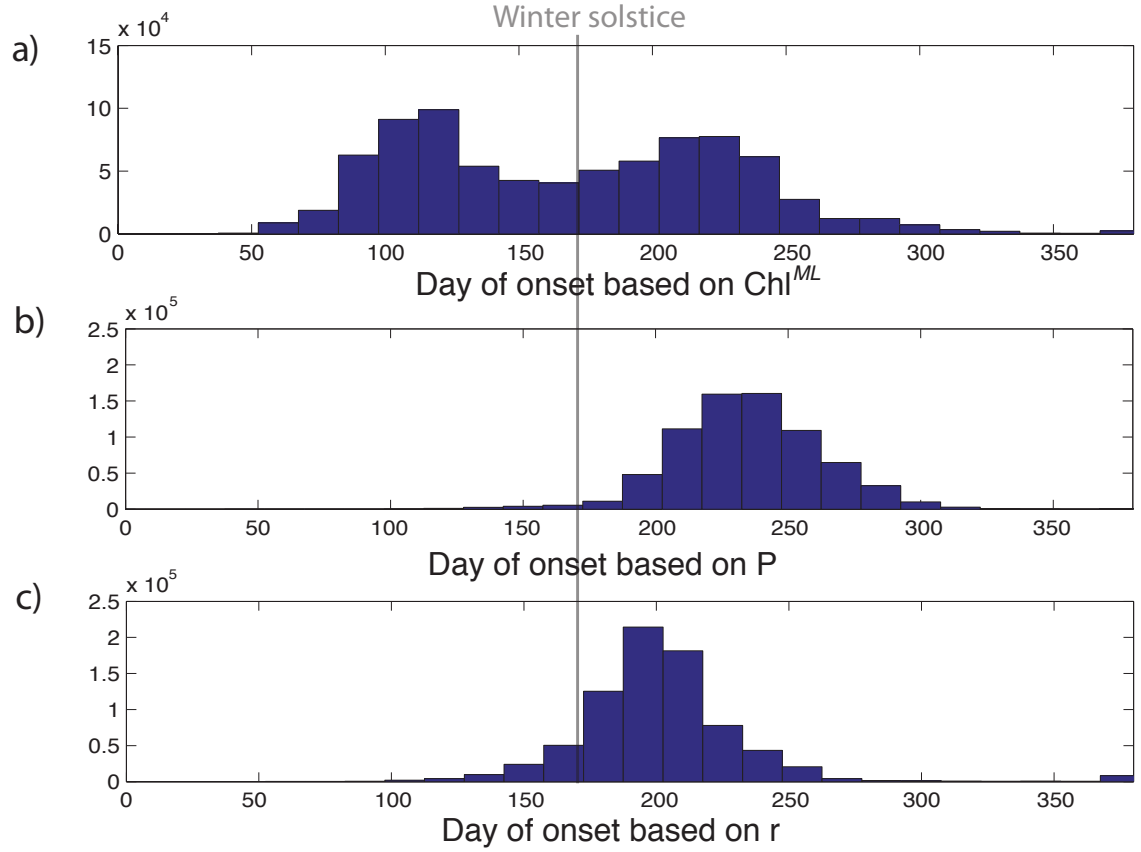

FIGURE 5.9: Histograms of the detected bloom onset dates in model GAA95b for year 1998-2011. Three detection criterion were used: maximal rate of change of Chl^{ML} (TOP), maximal rate of change of P (MIDDLE) and $r > 0$ (BOTTOM). Vertical grey line indicate the winter solstice day.

However, for a significant number of cases Chl^{ML} approximation seemed to work. This raises several questions: Under which circumstances P could be estimated using Chl^{ML}? For which vertical distributions of biomass were the Chl^{ML} approximation invalid? Were they realistic or caused by our model?

These questions were first addressed by representing the geographical distribution of Chl^{ML} and P-onset difference. Defining a threshold of detection mismatch of 100 days (i.e., we considered that if Chl^{ML}-onset was attributed earlier than 100 days from P-onset, Chl^{ML} approximation was unable to detect the "real" onset) we observed a coherent geographical distribution of "failed detections" (figure 5.10). Interestingly, locations where more than 75% of the blooms were detected too early by Chl^{ML} were distributed all along the sub-antarctic region. The geographical pattern was strongly similar to the geographical distribution of the sub-antarctic regime identified in the observations (figure 5.4.b) and also similar to the spatial MLD_{max} distribution in GAA95b (figure 5.8). Such a clear spatial agreement suggested a possible role of very deep MLD_{max} on failed detections. Moreover, it questioned the existence of the sub-antarctic regime as it could be caused by a detection artefact.

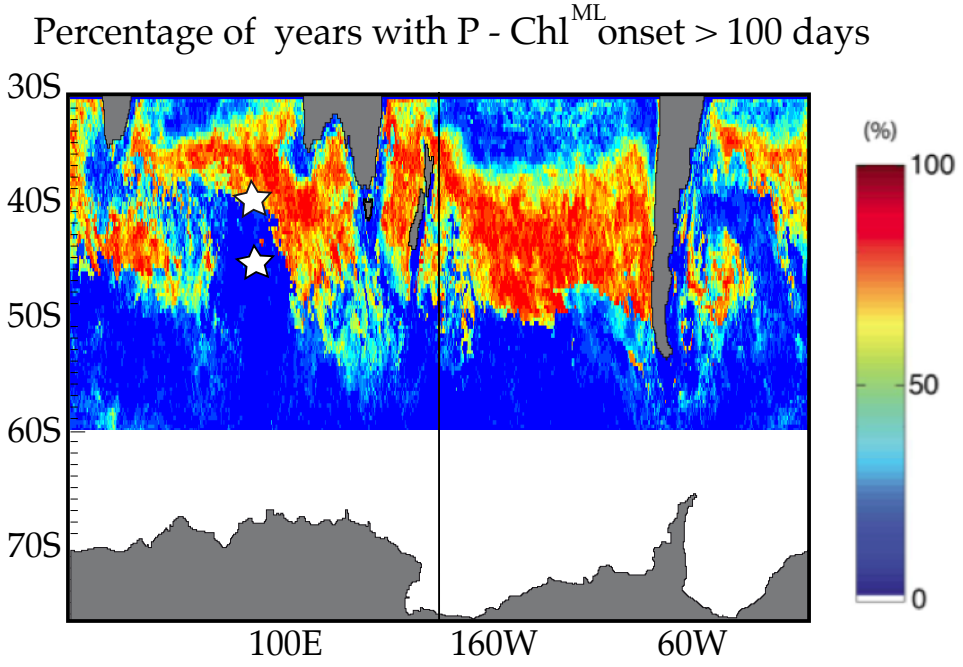

FIGURE 5.10: Map of the Southern Ocean with the percentage of years for which P and Chl^{ML} onsets presented a more than 100 days of mismatch. White stars indicate the two cell grids studied in detail: A at 80°E-41°S, B at 80°E-48°S.

To further investigate the "failed detection" we considered only two grids cells (one with a correct detection and one with a failed detection) to study a one-year timeseries in detail. We selected two grids cells at 80°E longitude with latitudes which were close enough to be considered as having similar solar forcing (these two locations are marked by stars in figure 5.10 and 5.8).

Chl^{ML} and P timeseries, for the first 3 years of the experience, are presented in figure 5.11. The raw and filtered signal, from which detection is based, are represented (blue and red thin lines, respectively) as well as the date at which onset was detected (vertical thin black lines). For simplicity, Chl^{ML} and P-onset dates are represented in color only for 1998. The northern location, referred to as A, (80°E-41°S, figures 5.11 a1 and a2) illustrated a mismatch between the detection methods of more than a 100 days. Filtered pattern of Chl^{ML} in this location (red line in figures 5.11.a1) presented an early increase at the same time that P was diminishing. The instant at which P-onset was attained, Chl^{ML} was already increasing and the integrated bloom onset (i.e., the P-onset) caused a slight slope change over Chl^{ML} curve, not strong enough to overcome a precedent perturbation (at which Chl^{ML}-onset was incorrectly attributed).

At the southern location, or B, (80°E-48°S, figures 5.11 b1 and b2) things were largely different. Chl^{ML} filtered curve (red line in b1) evolved quasi-parallel to P (red line in b2) and the two onsets coincide. Despite of similar latitudes and similar P timing and magnitude (thus, similar iron supply?), Chl^{ML} recreated two completely different, even opposite, seasonal cycles.

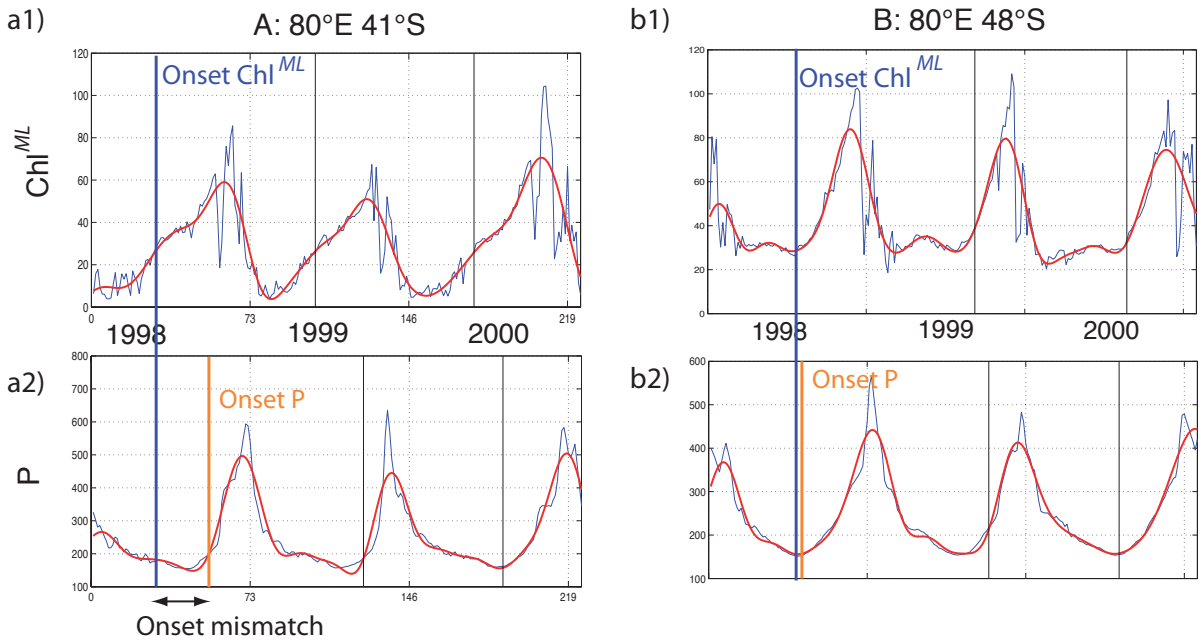

FIGURE 5.11: Timeseries of the Chl^{ML} (surface estimation of integrated biomass) and P (integrated biomass) for the years 1998 to 2000 at the locations A and B. Blue curves represent the raw data; red curves represent the filtered signal. Blue vertical lines indicate the detection of the Chl^{ML}-onset; orange vertical lines indicate the detection of the P-onset for year 1998

Thankfully, the model provided enough data to explore the vertical dimension at the locations A and B (figure 5.12). At first sight, the most appealing between A and B was the significant concentration of the subsurface (i.e., deeper than MLD) biomass: in A, the summer MLD oscillated around 30m (black thin line in figure 5.12.A1) but the biomass was quite high until 100m and weak concentration of biomass was diagnosed deeper than 350m (figure 5.12.A1, background colour), despite the surface Chl low concentrations (green line in figure 5.12.A2). This vertical distribution of biomass violated the fundamental assumption over which Chl^{ML} relied: the assumption that all the biomass in the water column is contained between the surface and the MLD. A straight consequence of this unaccounted biomass distribution wass the difference between P and Chl^{ML} during the first months of the year (figure 5.12.A2). While P slightly decreased (the black solid line), the very shallow MLD and the low surface Chl (green line) resulted in a low Chl^{ML} (black dashed line) that increased in autumn. Such an increase continued in early winter, dominated by a fast and irregular MLD deepening. The abrupt MLD deepening events were directly translated to Chl^{ML} and interpreted as potential onsets by the detection method: a sudden change in the increase rate of Chl^{ML} between a (false) minimal and the (false) maximal value. The resulting Chl^{ML} cycle is completely out of phase with respect to P (which onset was not attained until late winter-spring, when the MLD started to shallow).

At the location B (figure 5.12.B) the P and Chl^{ML}-onsets are coincident, despite of an apparent similarity to A in terms of iron supply (red line in figures A1 and B1), surface Chl and MLD_{max}. The comparison between A and B seasonal cycles (figure 5.12) however, allowed us to identify

two important differences that may cause Chl^{ML} to properly reproduce P cycle (at least from autumn to spring). First, the summer MLD in B was considerably deeper and the surface Chl stronger than in location A. Both factors played together to bring Chl^{ML} closer to the P, as the biomass left under MLD was insignificant with respect to the biomass within the MLD. Thanks to this, Chl^{ML} cycle started from a correct estimation and captured the autumn decrease in P. The second important difference with respect to location A, was evolution of the MLD during the deepening phase: in location B, the MLD deepened in a regular way with a weak deepening slope. Abrupt deepening events in winter were also observed and they also caused abrupt changes in Chl^{ML}. However, the bloom onset was not attributed to such changes because the Chl^{ML} cycle started from a high concentration and, when such an event occurred, Chl^{ML} was diminishing (exactly as P).

The conclusion from this integrated analysis was that there exists at least two elements able to invalidate the Chl^{ML} approximation:

- Low but significant subsurface stocks of biomass during summer. The existence of this biomass can be due to shallow summer MLDs in regions where the surface light reaches deep ocean layers (i.e., low latitudes) or to biomass detrained during the shallowing of the MLD.
- Vigorous, irregular and very deep MLD cycles which are likely to dominate Chl^{ML} signal and bring it out of phase with respect to P. This element is tightly related to the detection criteria we chosen, as the maximal double derivative is strongly sensitive to abrupt changes. However, as discussed in the first part of this chapter, all bloom detection criteria contain potential sources of error, thus we have carefully chosen the appropriate method for our case (see section 5.2 and Brody et al. [2013]).

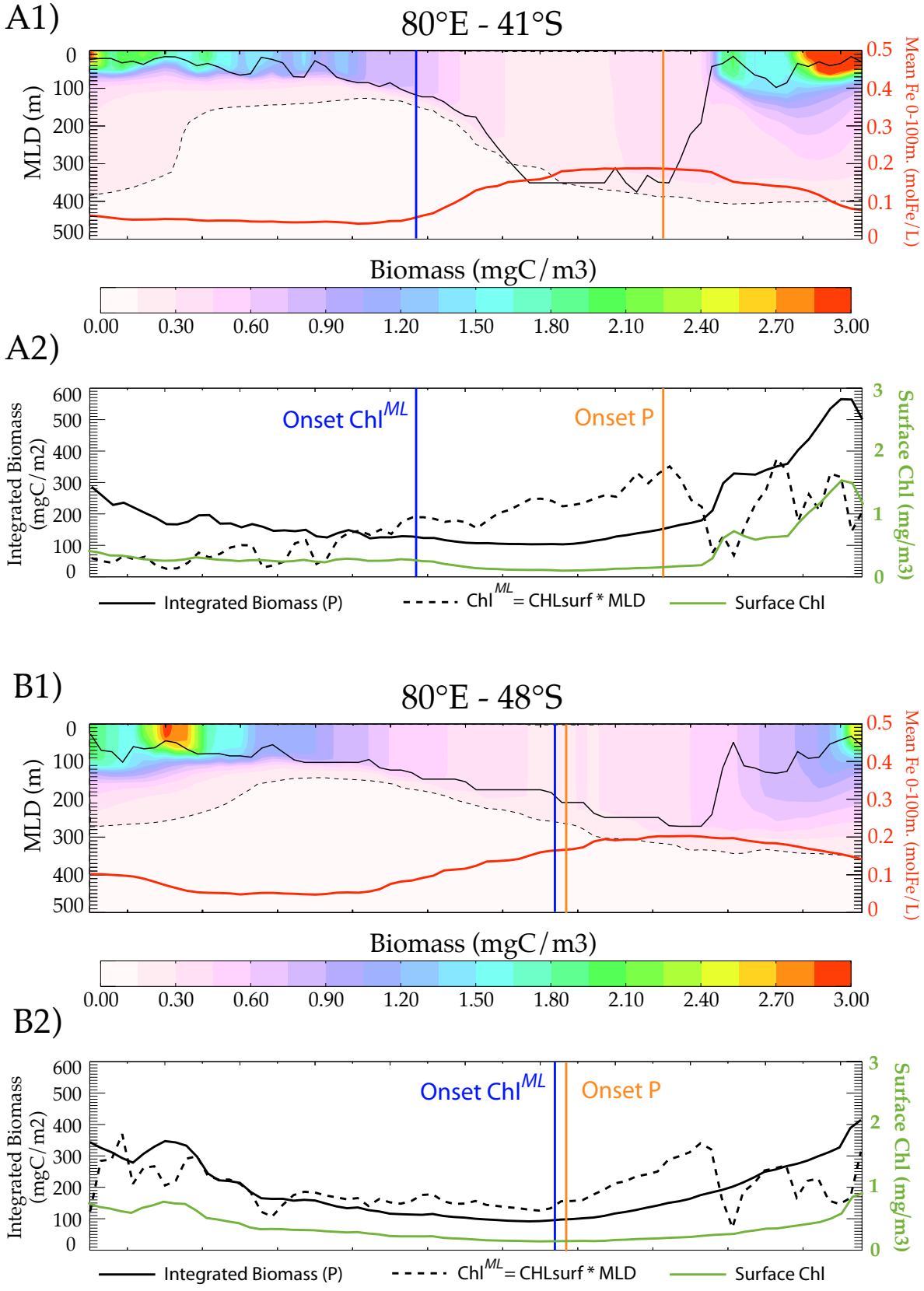

FIGURE 5.12: A1, B1: Vertical sections of the biomass during the year 1998 at locations A and B. Black solid line represents the MLD (left axis); red line represent the mean Fe concentration in the first 100m (right axis). Black thin dashed line indicate the iso-line of 0.15 mg/m^3 of biomass concentration. A2, B2: Seasonal cycles of Chl^{ML}, P and surface Chl. Black solid line represents the P (left axis); black dashed line represents Chl^{ML} and green solid line represents surface Chl (right axis). Blue and orange vertical lines indicate Chl^{ML}-onset and P-onset respectively.

5.4 Conclusions

The model results presented in the second part of this chapter suggested that Chl^{ML}-approximation used in our observation study may be flawed in some cases. The geographical distribution of points where Chl^{ML}-onsets appeared earlier than P-onsets coincided fairly well with the distribution of the sub-antarctic regime identified from observations (5.10). Such spatial coincidences questioned the robustness of the sub-antarctic regime. However, there are two points to be take into account that, in our opinion, justify the existence of such a intermediate-regime:

- In first place, model configuration GAA95b was set up using the strong winter penalisation for phytoplankton growth (i.e., *newpenal*). This new formulation contained a factor of penalisation proportional to the MLD that heavily diminishes growth when the MLD > Z_{euph} (see chapter 3 for details). GAA95b configuration was then likely to reduce deep production in winter (when the MLD is the deepest and Z_{euph} is the shallowest). This would enlarge the gap between P and Chl^{ML}, especially at lower latitudes where the summer MLDs are shallower and, consequently, the solar radiation can easily access subsurface waters[3].

- The second point concerns the fact that sub-antarctic bloom regime identified using satellite and Argo data presents features that differentiate it from both the ACC and the subtropical regime (not considering the geographical distribution which is tightly related to MLD). In particular, we shown (figure 5.7) how the surface Chl onsets in subantarctic blooms were correlated to the date that the air-sea heat fluxes switch to surface warming (i.e., actively convection shutdown; Taylor and Ferrari [2011]). Such surface Chl onsets occurred despite very deep MLD, which seemed to not occur with the model used here, for which the vertical distribution of Chl was highly homogeneous throughout MLD all year long.

***

Integrated annual primary production and carbon export (as resulting products of the whole phytoplankton seasonal cycle) are strongly related to bloom dynamics and thus they will depend on the integrated effect of both, bottom-up and top-down controls for the whole seasonal cycle. This is especially true in the real ocean where, as seen in this chapter, the bloom dynamics drivers are much subtle and complex: the vertical distribution and evolution of primary production is highly sensitive to latitude, iron supply and mixing.

[3]This point was planned to be addressed in a series of works during the last period of my PhD however due to an unexpected technical shut-down of JADE (in CINES supercomputer) from summer 2014 until now, we had been unable to carry this out. Our plan is to do the same test on bloom detection with the four regional experiences presented in chapter 3. We expect to quantify at which degree phytoplankton growth formulations modify the summer and winter biomass vertical distribution and thus, bloom regimes.

Recent works high-lighted how Climate Change may alter these different drivers and how these changes may impact on bloom phenology (Henson et al. [2013]) and primary production. Bopp et al. [2013] addressed how global ocean primary production was projectd to change in the CMIP5 models. They identified a zonal pattern of change for the primary production in the Southern Ocean which causes were not addressed. In the next chapter we will try to understand the CMIP5 projections in the Southern Ocean comparing the primary production trends to the projected trends for MLD, Fe, SST and solar surface radiation.

Chapter 6

Sensitivity of Southern Ocean primary production to Climate Change

6.1 Introduction

Climate Change (CC) is likely to induce significant alterations to the physics and biogeochemistry of the Southern Ocean (SO) (Bopp et al. [2001]; Dehairs et al. [2006]). The SO plays an integral role in the global climate. This is primarily due to its connectivity between three major ocean basins, its richness and redistribution of macronutrients (i.e., Nitrate, Phosphate) and the formation of mode waters which propagate northwards and resurface at lower latitudes (Sarmiento et al. [2004]; Sallée et al. [2006]). Therefore, our understanding of the response of the SO to Climate Change is vital, not only for the SO itself, but also to correctly address the global carbon budget for decades to come.

At the atmospheric scale, a persistent trend towards a positive phase of the Southern Annular Mode (SAM, the dominant mode of Southern Hemisphere climate variability) has been detected over the last decades (Thompson et al., 2000; Gillett and Thompson, 2003). Two opposing factors altering the SAM have been identified: the increase in greenhouse gases (causing a positive SAM) and the depletion of the ozone layer (causing a negative SAM trend in winter) (Thompson et al. [2011]). Climate Change is thus likely to be linked to the observed SAM positive trend. This tendency has important implications on the wind surface patterns that force SO circulation (Cai et al. [2005]); and consequently, it is expected to have an impact (albeit, still uncertain) on the PP and CO_2 uptake (Lovenduski and Gruber [2005]; Lenton and Matear [2007]).

The results in the most recent Coupled Model Intercomparison Project (CMIP5) clearly show a trend in the intensification and poleward shift of the westerly winds over the entire Southern Ocean for the end of the 21st century, which is related to a positive trend of the SAM (Meijers [2014]; Gillett and Fyfe [2013]). Such patterns are already significant in the RCP4.5 scenario and amplified in the RCP85. However, in the CMIP5 models, the sign and magnitude of change in PP are much more uncertain than with the dynamics (Henson et al. [2013]; Bopp et al. [2013]). These contributors are tightly linked to and are able influence bloom dynamics in a wide range of ways: changes on bloom phenology, export efficiency, community structure, specific growth rate and many others (Boyd and Ellwood [2010]; Behrenfeld et al. [2006]; Behrenfeld [2014]).

In this chapter, I shall first analyse the mean PP trends and its correlation to changes in MLD, using eight of the CMIP5 models under the RCP8.5 scenario at the end of the current century. This study will be extended with the design of a 1-D modelling approach which explores the multiple ways production (and community structure) can be related to change in stratification and iron supply. Here, we will demonstrate that the altered stratification is not enough to explain projected PP trends. Using one of the CMIP5 models (IPSL-CM5A-MR) we point out the change in surface solar radiation as PP stressor in the models.

6.2 CMIP5 projections in the Southern Ocean

6.2.1 Projected trends on primary production

Among the 21 Earth System Models (ESMs) used for the CMIP5 exercise (Taylor et al. [2012]), eight have been selected to address the effects of Climate Change on SO production. This selection was based on the selection of availability of outputs for new primary production, Fe and MLD. Furthermore, as stated in Bopp et al. [2013] (precursor of the current work): (the eight models) *They were also selected on the requirements that at least one representative concentration pathway (RCP) was performed up to 2099. We used historical simulations from 1870 to 2005, all climate change scenarios (RCPs) from 2006 to 2099, and pre-industrial control simulations.* Although, Bopp et al. [2013] used two more models in their study, here we neglected the two CESM models (i.e., CESM1-BGC and CMClimate Change-CESM) which MLD projections were completely opposed to mean trends (Sallée et al. [2013]).

These eight CMIP5 selected models are diverse in terms of their biogeochemical complexity (table 6.1). Firstly, the number of phytoplankton groups represented varies from one to three. Secondly, each model represents phytoplankton growth limitations due to iron supplies but the formulation of the Fe-related processes governing the supply strongly differs between models. However, all of these models present values of SO annual production within the wide range of satellite based PP estimates (table 6.2).

Model	Ocean	Biogeochemistry	Reference
GFDL-ESM2G	63lev. 0.3 °- 1°	30tr., 3PG N, P, Si, Fe	Dunne et al. (2012)
GFDL-ESM2M	63lev. 0.3 °- 1°	30tr., 3PG N, P, Si, Fe	Dunne et al. (2012)
HadGEM2-ES	40lev. 0.3 °- 1°	NPZD, 2PG N, Si, Fe	Palmer and Totterdell (2000)
IPSL-CM5A-LR	31lev. 0.5 °- 2°	24tr., 2PG NO3, NH4, P, Si, Fe	Dufresne et al. (2013) Aumont and Bopp (2006)
IPSL-CM5A-MR	31lev. 0.5 °- 2°	24tr., 2PG NO3, NH4, P, Si, Fe	Dufresne et al. (2013) Aumont and Bopp (2006)
NorESM1-ME	53lev. 1°	1PG -	Bentsel et al. (2012) Assmann et al. (2010)
MPI-ESM-LR	40lev. 1.5°	NPZD, 1PG N, P, Si, Fe	Giorgietta et al. (2013) Ilyina et al. (2013)
MPI-ESM-MR	40lev. 0.4 °	NPZD, 1PG N, P, Si, Fe	Giorgietta et al. (2013) Ilyina et al. (2013)

TABLE 6.1: lev. = levels, tr. = tracers, PG= Phytoplankton Groups. Adapted from Vancoppenolle et al. [2013] and Bopp et al. [2013]

CMIP5 Multi-model mean Hist. (1990-1999)	1500.08 (420.55)
OBS. [Arrigo et al., 2008]	1900.00
OBS. Carr et al. [2006]	1100.00-4900.00

TABLE 6.2: Mean annual primary production (in TgC) in the eight CMIP5 and estimated by two observation-based works.

In this chapter, we will study the models projections for the most extreme CMIP5 scenario (RCP85), corresponding to an additional radiative forcing level of 8.5 during the last decade of 21st century (2090-2099). A visual comparison of the historical and RCP85 multi-model mean integrated PP suggests a narrowing and minor poleward shift of the 'high' productivity band centred at 40°S (figure 6.1). Subtropical gyres progress southwards (particularly in Indian and Pacific sectors) and the Antartic waters become slightly more productive.

On average, the difference in annual PP (ΔPP) between the historical decade and the 2090-2099 period (ΔPP), varies from -140 TgC to +60 TgC depending on the model. Multi-model mean and standard deviation are -9.81 TgC and 41.44 TgC respectively. As stated in Bopp et al. [2013], such uncertain results on the magnitude and sign of ΔPP do not allow a solid conclusion. However, the spatial distribution of ΔPP seems to be coherent and robust. At first sight, the most remarkable feature is the strong zonal pattern of ΔPP over the entire Southern Ocean (figure 6.2.a). Subtropical bands presented much lower PP values ($\Delta PP \approx$ -25 gC/m^2/yr) while, in the 40°S-50°S band and in the Antarctic waters, the projected PP increased from 20 to 40 gC/m^2/yr, in average. The relative increase (with respect to the historical decade; in 6.2.b) is the strongest in coastal Antarctic waters (i.e., north of Ross and Weddel Seas) where projected

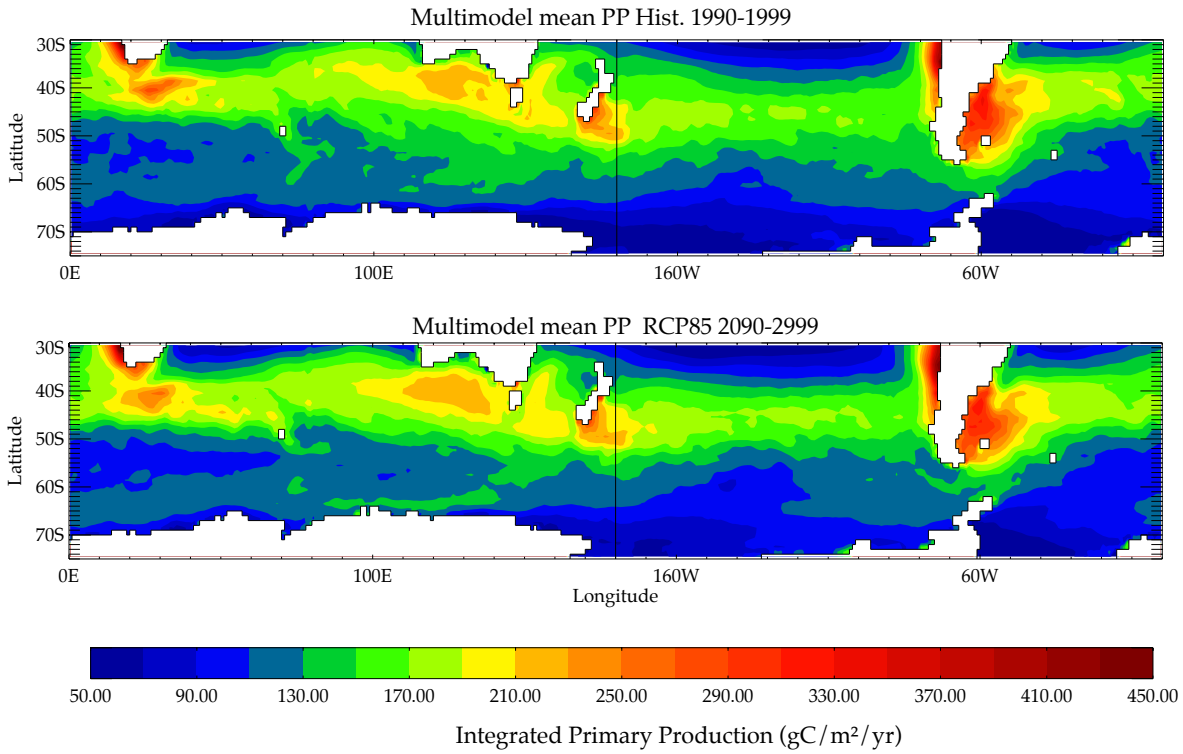

FIGURE 6.1: Spatial distribution of the eight CMIP5 multi-model mean integrated PP in the Southern Ocean. TOP: mean over the 'historical' decade (1990-1999). BOTTOM: mean over the last decade of the XXth century under RCP8.5 scenario.

productivity increases more than 40%. On the contrary, the region of highest relative decrease is the western subtropical Pacific, where the decrease is -40%.

With the aim to visualise inter-model agreement, ΔPP meridional mean for each zonal band has been represented for each of the 8 models (figure 6.3[1]):

30°-40°S: ΔPP presents a clear and strong negative mean trend (-20gC/m2/yr) over the three basins. Except GFDL, the rest of models agree in the sign ΔPP in this region.

40°-50°S: ΔPP is projected weak and low for the ensemble of model (except for the MPI-ESM-LR in some specific regions). The sign is fairly robust in the Atlantic and Indian sectors (4-5 over 8 models agree) but much less in the Pacific.

50°-60°S: ΔPP is negative or close to 0 for the majority of models over the three sectors. However, at some meridians (p.e., 100E or 160W) the magnitude of the multi-model mean seems to be influenced by the two MPI models. Such bias is partly compensated in some regions by NorESM-1-ME model, the only one projecting a clear positive trend.

[1]Caption of figure 6.3: Zonal sections of the ΔPP. Black line represents the multimodel mean and each of the models used is represented by grey lines. Grey vertical rectangles stands for continents.

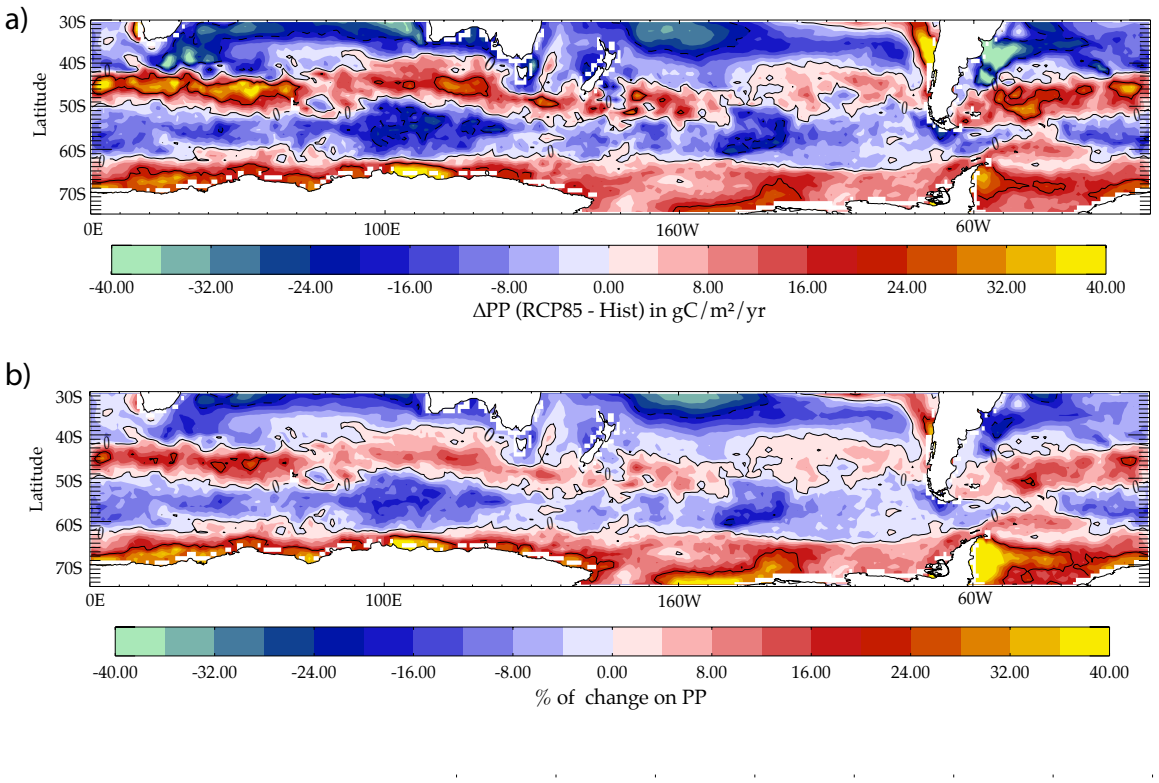

FIGURE 6.2: Mutlimodel $\Delta intPP$ (RCP85 - HIST) over the Southern Ocean (a). Multimodel mean percentage of change in PP with the respect to 1990-1999 (b)

60°-70°S: ΔPP is positive with low inter-model agreement on the magnitude but significantly good agreement on the sign (only 2 models project decrease of PP in the Atlantic). Again, inter-model agreement is the lowest in the Pacific sector.

6.2.2 Projected changes in the MLD and its influence on ΔPP

The analysis of the CMIP5 model for the physical component of the Southern Hemisphere showed that surface wind may intensify and shift poleward for about 1.5° at the end of the XX$^t h$ (Meijers [2014]). Such poleward shift is likely related to the observed persistent positive phase of the SAM. In CMIP5 models[2], these changes drive in turn the whole frontal and upper-ocean mixing structures to higher latitudes (Sallée et al. [2013]).

MLD seasonal dynamics are highly dependent on the upper-mixing and frontal structure in the Southern Ocean (Sallée et al. [2010b]). MLD, in turn, plays an important (but complex) control on primary production at the seasonal scale (see chapter 4). In winter, active mixing re-supplies

[2]The response of the ocean to the poleward and intensification of surface winds is currently under debate in the community. High-resolution modelling studies suggested an increase in eddy activity and an important role of the bathymetry as a resistance to an eventual poleward shift of the frontal system

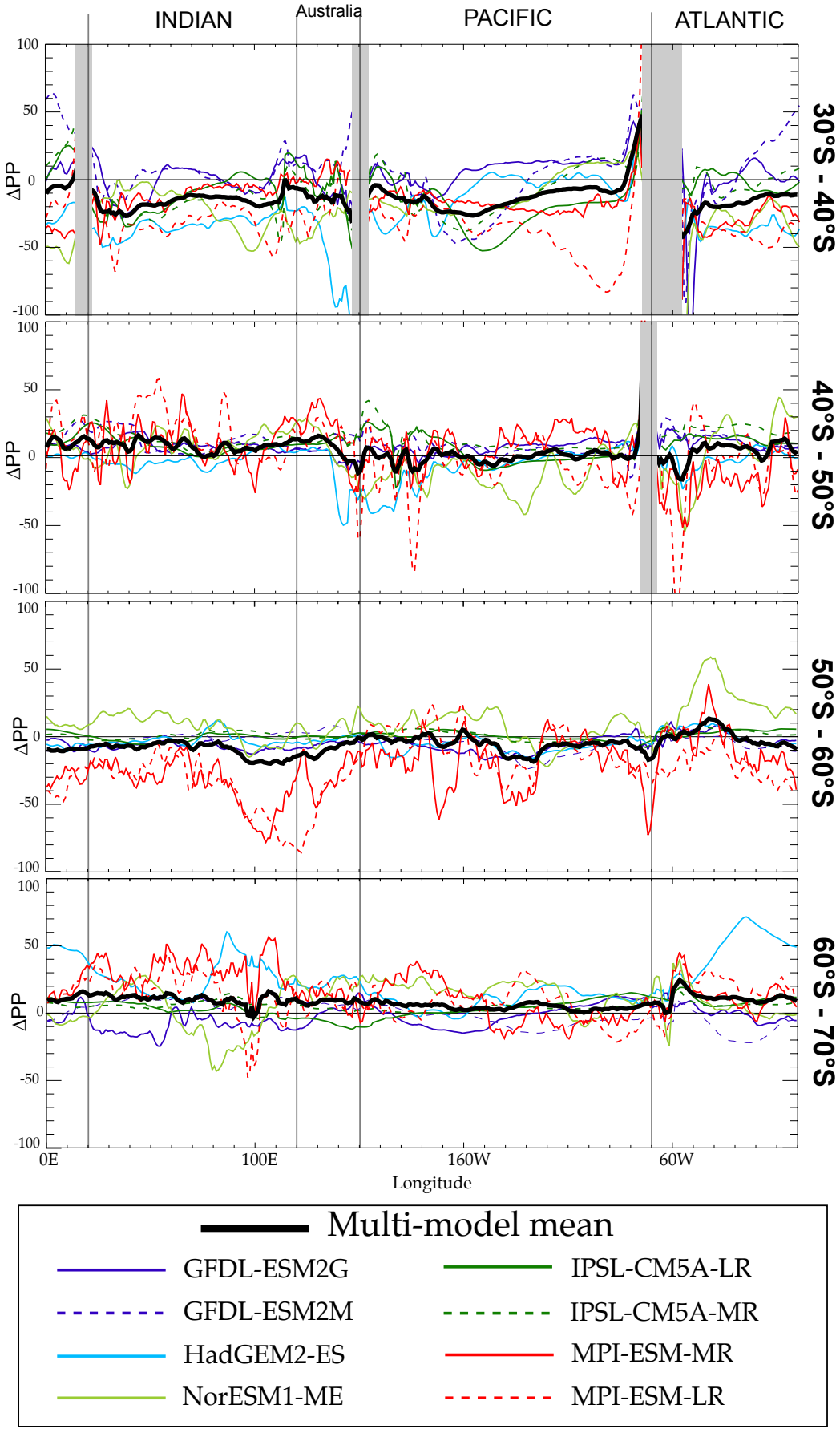

FIGURE 6.3: See footnote

upper ocean layers with nutrients, controls the amount of light captured by the phytoplankton and dilutes biomass concentration with subsurface (and plankton-free) waters. In summer, mixing influences primary production in opposed ways:

- In the regions where the summer MLD's are significantly deep (≥100m), phytoplankton are light limited during some part of the summer. Hence, a more stratified ocean in summer would lead to an increase in PP.
- In the regions where summer production is not limited by light but by nutrients depletion (Fe or Si), a deeper summer mixing could eventually enhance PP by continuously bringing nutrients to the euphotic layer.

To examine whether or not the projected MLD changes were, in the eight CMIP5 models, associated to ΔPP, we will firstly analyse the results for the projected change on the maximum (i.e.: winter; ΔMLD_{max}) and minimum (i.e.: summer; ΔMLD_{min}) MLD. Secondly, these results will be compared to the trends in ΔPP. Future trends on MLD are defined as $\Delta MLD = MLD_{RCP8.5} - MLD_{Hist}$; consequently $\Delta MLD > 0$ indicates a projected future deepening (i.e., less stratified waters) and $\Delta MLD < 0$ a projected future shallowing (i.e., more stratified waters).

The distribution of mean ΔMLD_{max} (colours in figure 6.4.A) is not zonal and varies between sectors. The Pacific sector shows a large area of winter MLD shallowing (between 60 and 90 meters) and a very good agreement between models except in the south-east Pacific. In the Atlantic and Indian sectors the multimodel agreement is lower (with the exception of the Indian subtropical band where a strong shallowing is projected) but a fairly consistent band of deepening emerges, going from the 70°E-35°S to 170°E-55°S. South of this band (around 50°S-60°S of the Atlantic and Indian sectors) ΔMLD_{max} not present any robust sign of change. Finally, all the models project a ΔMLD_{max} shallowing on Antarctic waters excepting the Amundsen Sea (only two models disagree with sign). On the other hand, mean ΔMLD_{min} spatial distribution is much more zonal. There is a significant multi-model agreement from 30°S to 50°S where a 10-20m shallower MLD is projected. South of 50°S, most of models simulate a zonal band of deeper ΔMLD_{min}, but sign and magnitude of change is uncertain for the Antarctic waters ($>$ 65°S).

Such zonal structure in ΔMLD_{min} strongly resembles the projected response on ΔPP presented previously. In fact, the mean spatial patterns of ΔPP coincide well with ΔMLD_{min}, much more than that of ΔMLD_{max} (figure 6.5). ΔMLD_{max} has some correlation in the eastern Indian and Pacific oceans, with an increase in PP where the MLD deepens (Indian, south of Australia) and decrease where the MLD shallows (between 50°S and 60°S in the Pacific). The sign of this correlation may suggest an altered PP due to changes in iron supply (deeper MLD_{max} implying more Fe). However, this is not true for the subtropics in the Indian sector nor for the whole

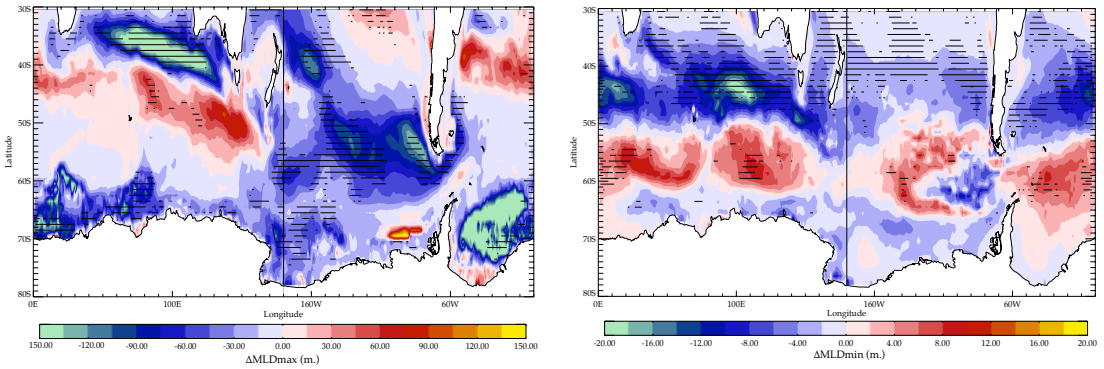

FIGURE 6.4: Multimodel mean change in MLDmax (a) and MLDmin (b) between RCP85 scenario and the historical decade. Horizontal black lines indicate where all models agree on the sign of change.

Antarctic waters. On the contrary, the spatial correspondence between ΔMLD_{min} and ΔPP hold over the entire Southern Ocean. Over the Atlantic and Indian sectors both variables are perfectly correlated showing an increase on PP where MLD_{min} stratifies and a decrease where it deepens. In the Pacific, the correlation is weaker partly due to a patch of stratification in the south-eastern part (in blue) where multimodel agreement is very low (see figure 6.4.B).

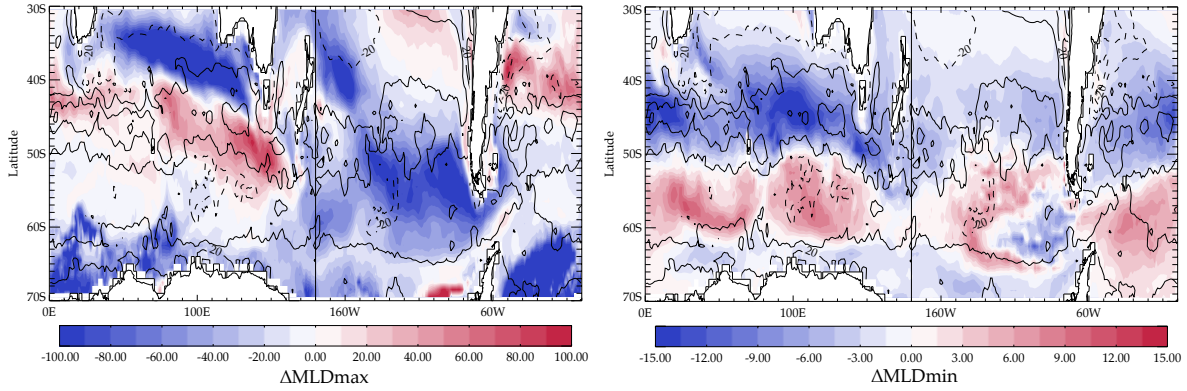

FIGURE 6.5: Multimodel mean change in ΔMLD_{max} (a) and ΔMLD_{max} (b) between RCP85 scenario and the historical decade. Multimodel mean ΔPP is represented by the black contours where solid/dashed traits correspond to future increase/decrease on PP

A straight and simplistic interpretation of this result would be that the possible light limitations on PP in the historical decade are alleviated when summer mixing weakens. However, conclusions from a multi-model mean must be handled with care. Indeed, the emerging signal from the ensemble of models can be caused by an effect of the "amplification" of those PP drivers common amongst all models. For instance, the apparent strong PP light dependence could eventually be due to the fact that in all models phytoplankton growth light limitation is similarly represented, while other limiting factors (as iron) are represented with different grades of complexity between

models. Thus, the good multi-model agreement on projecting MLD_{min} can eventually amplify the influence of the light limitation over PP.

This "averaging" effect argument seems to be reinforced when representing the ΔPP-MLD_{min} relationship model by model (figure 6.6). At first , the ensemble of figures shows how the magnitude of ΔMLD_{min} strongly varies amongst models, which can cause the mean to be 'biased' by the most extreme projections. Furthermore, even if negative ΔPP-ΔMLD_{min} correlation is visible for the majority of models in specific locations, many regions where this correlation is inverted are clearly identifiable. This fact weakens the potential conclusions based on the mean signal and suggest the existence of other mechanisms influencing ΔPP.

6.3 Mechanics of mixing and iron supply control over primary production

To better understand how ΔMLD_{min} and ΔMLD_{max} may impact PP in the Southern Ocean, we have conducted an ensemble of modelling experiments with a simplified physical framework used to force a complex biogeochemical model (PISCES model, which constitutes the biogeochemical component of IPSL models and others). The simplified physical framework allowed us to apply a tight control on the PP stressors (i.e., summer and winter mixing depth, iron supply, etc.) and quantify the influence of each stressor over annual PP. This methodology is based on the multiple run algorithm detailed in chapter **??**.

Four example cases of modelled seasonal cycles are represented in figure 6.7. They have been chosen among the ensemble of 1,200 runs because they represent four extreme cases that can be found in Southern Ocean waters. In these four examples, two stressors are aClimate Changeounted for: depth of mixing (MLD_{max}) and ferricline summer depth (Z_{Fe}). The amount of iron vertically supplied to productive surface layers (which is the only source of Fe considered here) results from the coupling between MLD_{max} and Z_{Fe}. Combining two different values for MLD_{max} (deep and shallow) and two for Z_{Fe} we have obtained the four cases of figure 6.7. Deep mixing cases present production reduced to 0 from June to Sept, likely due to light limitation. On the contrary, the cases of shallow winter mixing present a low but maintained winter productivity. The two MLD extreme cases present similar values of total PP (66.8 gC/m2/yr for the low Fe, shallow mixing (A) and 69.3 gC/m2/yr for the high Fe, deep mixing (D)), what suggest that, for case A, winter productivity may compensate for low spring-summer production due to Fe depletion. From this result we can infer that the "optimal" scenario (in terms of productivity) would be something similar to case B: winter mixing is shallow enough to allow production during winter and deep enough to bring a considerable amount of Fe to surface layers that maintains production during spring. Case B also illustrates a secondary but important consequence of a strong Fe supply: under high Fe conditions microphytoplankton significantly contributed to total

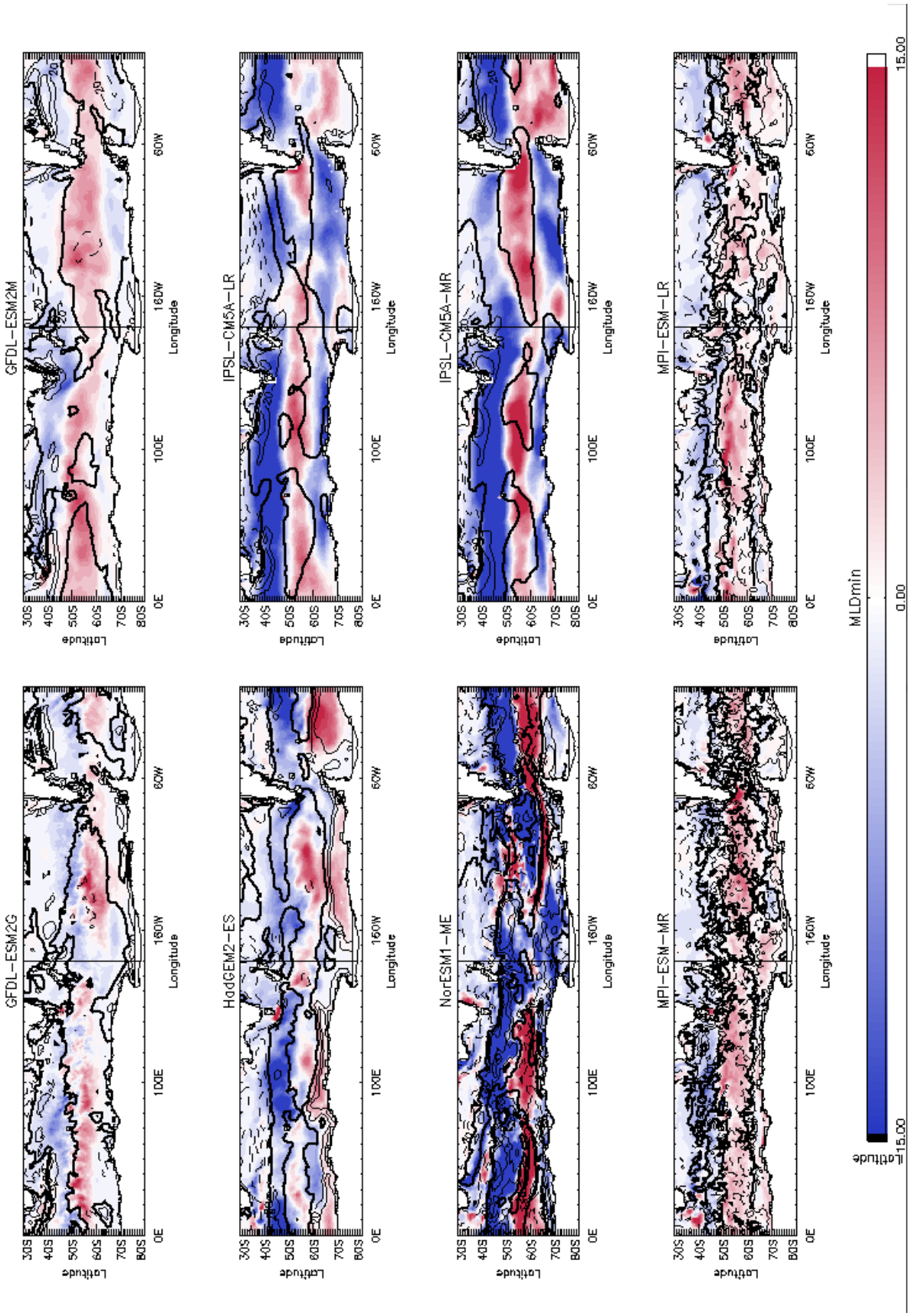

FIGURE 6.6: ΔMLD_{min} (in color) and ΔPP (countours) for each of the eight models used. Solid countours represent ΔPP=0; dashed contours represent negative ΔPP and thin contours represent positive ΔPP

PP. The role of microphytoplankton in rich environments is clearly visible comparing A and B panels (shallow mixing cases). For these two cases, the increase on PP under high Fe conditions is mainly due to an increase in microphytoplankton production. Case D (deep mixing and high Fe supply) presents a more complex situation: the production in peak of the two phytoplankton types is shifted in time and summer production (from December to January) is mainly due to microphytoplankton contribution.

6.3.1 Winter and summer stratification influence on primary production

The four examples above illustrate that both, mixing depth and iron supply had an impact on total production. These drivers are not independent from one another: winter mixing depth is expected to be proportional to vertical Fe supply (even if in the "real" ocean the large variety of Z_{Fe} do not always ensures a linear relationship Tagliabue et al. [2011]).

To isolate the influence of altered stratification on productivity to the influence of Fe supply, we have selected two subsets from opposed scenarios: shallow ferricline $Z_{Fe} = 150m$ (i.e. Fe is easily transported to surface), and deep ferricline, $Z_{Fe} = 500m$ (i.e., very deep mixing is necessary to bring iron to surface layers). For each of these subsets, we have averaged the production depending on its $MLD_{max} - MLD_{min}$ values (figure 6.8). The total integrated PP corresponding to $MLD_{min} = 50m$ and $MLD_{max} = 400m$ is used as reference (or "Historical") value to normalise the ensemble and quantify the ΔPP due to altered stratification in terms of percentages of change (figure 6.8). Tracing idealistic trajectories over this image (an example is

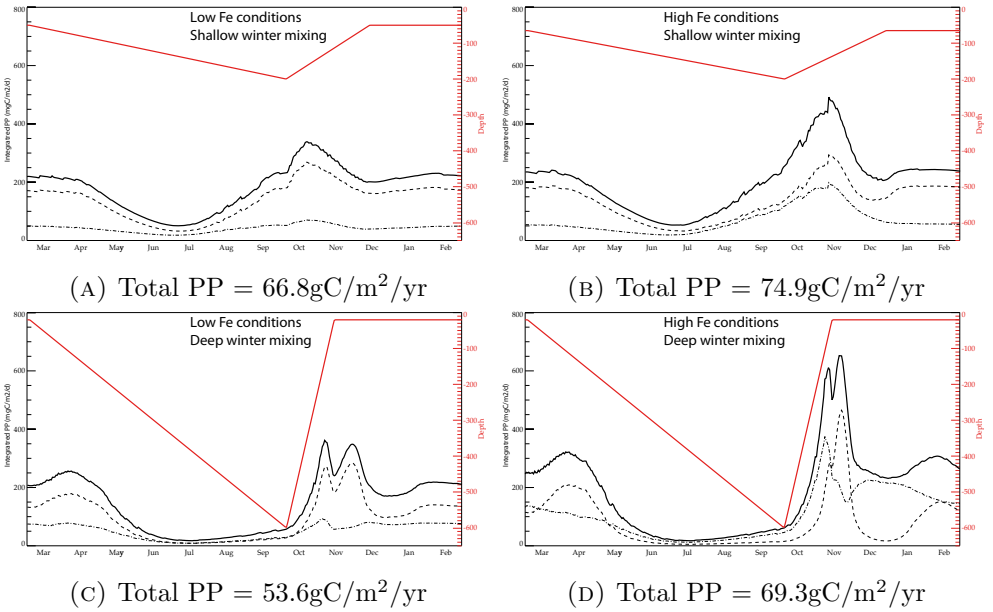

(A) Total PP = 66.8gC/m^2/yr (B) Total PP = 74.9gC/m^2/yr

(C) Total PP = 53.6gC/m^2/yr (D) Total PP = 69.3gC/m^2/yr

FIGURE 6.7: High and low iron conditions extreme scenarios. Seasonal cylce of the MLD, integrated PP and biomass for nanophytoplankton (solid lines) and microphytoplankton group (dashed lines)

represented in figure 6.8 by dashed black lines) is equivalent to analysing the projected PP in a single Southern Ocean spot, in a kind of Eulerian approach. For instance, let us assume an initial state (i.e., 1990-1999 mean) of $MLD_{max} = 400m$, $MLD_{min} = 50m$ and $Z_{Fe} = 500m$ (white circle in figure 6.8.I). If winter and summer mixing are projected to change $\Delta MLD_{max} = -100m$ and $\Delta MLD_{min} = -15m$ respectively, the model predicts an increase on productivity of $\Delta PP \approx +5\%$ (only due to stratification changes). Compared to the high Fe environment (in panel 6.8.II), an identical change in stratification caused to an opposed impact: decrease on productivity of around -5%. This differentiated response is likely due to the dominant phytoplankton group (PG) at each region. In low Fe environments (6.8.I, like cases A and C in figure 6.7), the main (an almost only) contributor is nanophytoplankton which is easily limited by light but has low iron requirements. Therefore, for this ecosystem, more stratification (i.e.: more light within the MLD) implies more production. On the contrary, under high Fe conditions (6.8.II, like cases B and D in figure 6.7), microphytoplankton contribute to total PP as much as nanophytoplankton and, consequently, total production to is much more iron-dependent. Under these circumstances, the reduction in Fe supply (due to stronger winter stratification; ΔMLD_{max} <0) decreases PP. It is interesting to note that this statement becomes false when the range on MLD_{max} is deeper than 400m. The observed decrease on productivity when deepening from 400 to 700m (figure 6.8.II) suggests a dominant effect of light limitation regardless of an increased iron supply.

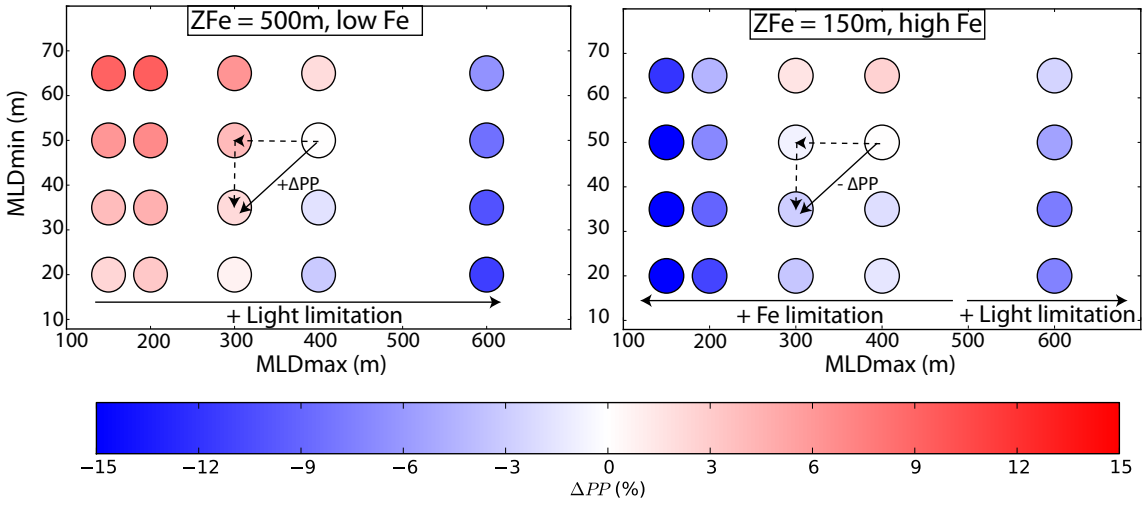

FIGURE 6.8: Impact of altered stratification on the integrated PP for a group of 'Low Fe' (Z_{Fe}=500m) conditions 1D scenarios (left) and a group of 'High Fe' (Z_{Fe}=150m) conditions 1D scenarios (right). Circles represent the average ΔPP (in color) of the 1D scenarios with the same MLD_{max} and MLD_{min} in the group. An example of combined alteration on winter and summer stratification is indicated by the dashed and solid arrows. At bottom, black arrows indicate the main controls of change in PP due to altered stratification.

Changes in summer stratification seem to have a much a simpler influence over PP: ΔMLD_{min} is proportional to ΔPP. For any MLD_{max}, and regardless of Fe conditions, an increase of summer stratification ($\Delta MLD_{min} < 0$) leads to lower PP values ($\Delta MLD_{min} < 0 \implies \Delta PP < 0$) (and

the opposite is equally true). We can already note that this result is completely opposed to the apparent ΔMLD_{min} - ΔPP relationship identified in the previous section (figure 6.5). This discrepancy will be addressed in next section using a set of summer specific 1D runs.

6.3.2 How vertical iron supply controls community structure?

In preceding sections it has been shown that total primary production it is proportional to vertical iron supply. However, this enhancement of production does not occurs in a trivial way due to the specificities of the different phytoplankton groups constituting the producers community. In order to quantify how iron supply alters a (simple) community structure, and thus total production, we represented the annual PP for each PG as a function of the iron supply (figure 6.9). Results are presented grouped by the corresponding winter mixing depth.

Microphytoplankton production (solid lines) was proportional to iron supply but hardly dependent on MLD_{max} (in color). Winter mixing however controlled nanophytoplankton production (dashed lines) as seen from the separation between MLD_{max} lines. The shallower the winter mixing, the higher the productivity, suggesting that the winter growth limitation was the main control for nanophytoplankton. Last but not least, the inversely proportional relationship between nanophytoplankton PP and Fe_{supply} reveals a strong interspecies competition for Fe. In Fe-rich and well-mixed waters, microphytoplankton take up an important part of the micronutrient available leading to a decrease on nanophytoplankton production. This result can be clearly stated by comparing a solid and dashed line of the same color. Under exactly the same winter mixing (i.e. almost identical $PA\bar{R}_{MLD}$) nanophytoplankton production decreased with Fe. This apparent paradox can only be justified by the fact that macrophytoplankton enhanced Fe-uptake caused Fe-limitation on nanophytoplankton. However, it is important to note that, even under the optimal conditions, microphytoplankton productivity hardly surpassed nanophytoplankton contribution (red lines in figure 6.9 and example case D in figure 6.7 are representative of such situation). The global result of such interplay is an annual production directly proportional to iron supply but in a lower degree that one would expect.

6.3.3 Winter mixing and vertical iron supply as coupled drivers

To analyse how the identified mechanisms interact with each other to drive total PP, we represented total PP as a function of MLD_{max} and summer Ferricline depth (Z_{Fe}), interpolated using the whole ensemble of runs; i.e. the 1,190 different 1D scenarios (figure 6.10). This representation illustrates a an interesting and complex pattern for total production that, for clarity, we will comment in two parts:

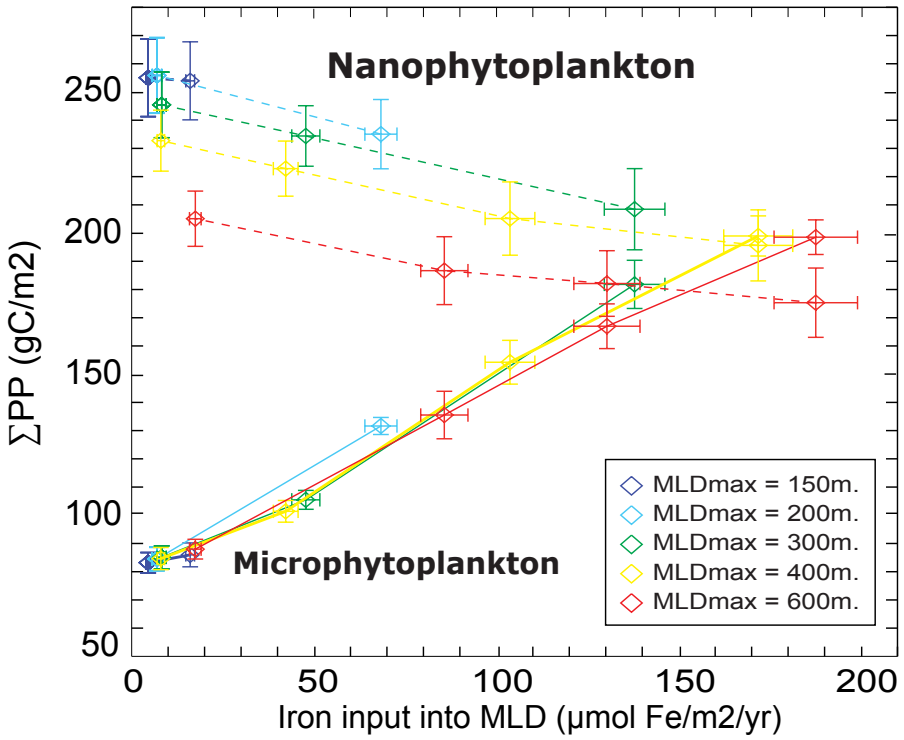

FIGURE 6.9: Integrated PP for nanophytoplankton and microphytiplankton as a function of iron supply and MLD_{max} (in colour) from the ensemble of 1D scenarios. Results have been averaged in clusters of similar MLD_{max}/Fe_{supply} and its values represented by diamonds with the corresponding standard deviations represented by vertical/horizontal bars

ZFe $<$ 350m.: When Z_{Fe} was relatively close to surface, winter mixing was able to alleviate nutrient limitation entraining iron to upper layers. Moreover, mixing has a double role: deeper mixing enhances both iron supply (for a given Z_{Fe}) and light limitation. Thus the resulting PP emerges from the balance between iron alleviation and light limitation. Such a double role seemed to be decoupled depending on the magnitude of the mixing depth. For $MLD_{max} < 400m$, PP increased with winter depth thanks to a greater supply of Fe; but beyond $MLD_{max} = 400m$, light limitation over the year was strong enough to reduce productivity in high-Fe waters. Furthermore, based on 6.3.2 results, in all these cases both PGs equally contribute to annual production.

ZFe $>$ 350m.: In contrast to the previous case, this scenarios were strongly Fe-limited due to deep ferriclines. Production was consequently weak (less than 65 $gC/m^2/yr$) with a (low) maxima around 225m, where light-Fe balance was optimal. For these scenarios the ecosystem was dominated by nanophytoplankton. Low nutrient-requirements allowed nanophytoplankton to be productive under Fe-stressed conditions if enough light was available (between 200 to 250 meters). The square in grey in figure 6.10 identifies an environment

of strong mixing and low production (due to scarce iron supply), specific to the Southern Ocean.

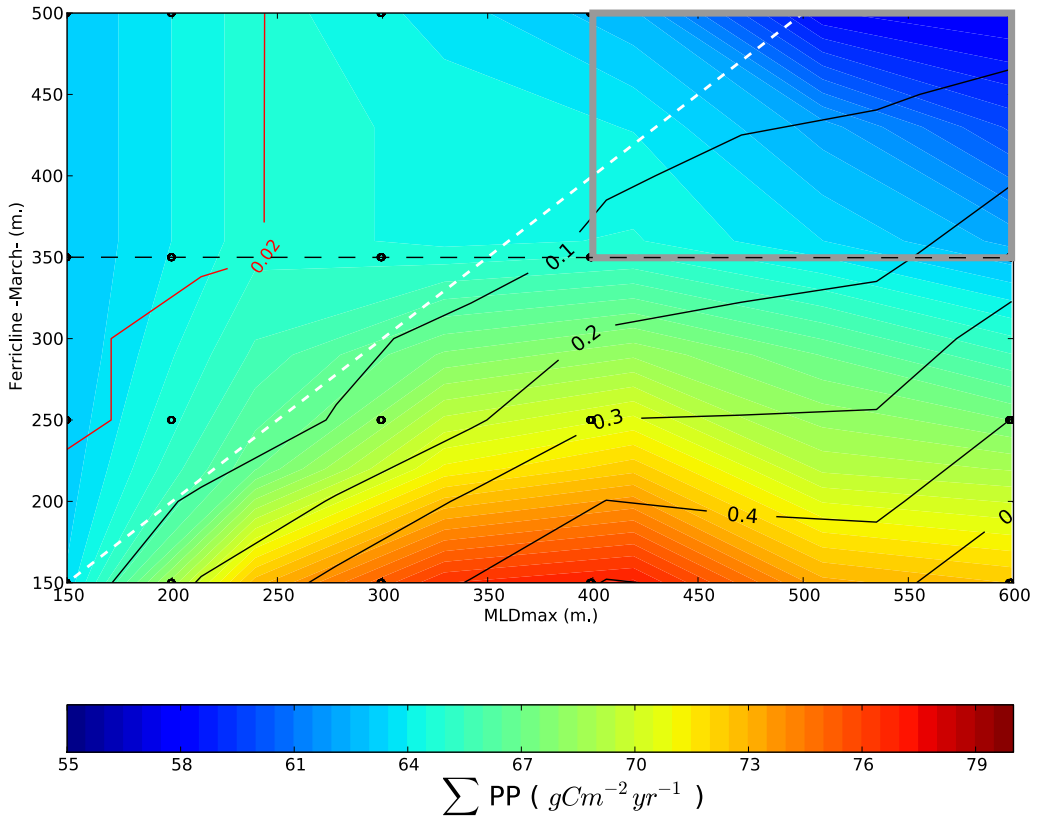

FIGURE 6.10: PP (in color) as a function of MLDmax and summer Ferricline depth (ZFe) interpolated using the whole ensemble of runs (>1,100 different scenarios). Black lines indicate the amount of iron input into the MLD over the year and the white-dashed line is a 1:1 relationship to indicate those areas at which winter mixing reach and penetrate below Ferricline depth (right side of the white line)

6.3.4 What is the net effect of summer stratification?

Here, we focus on understanding how a change in summer mixing affects PP in the particular case of our 1D model. To do so, I adapted the multiple run algorithm for a new experiment where only summer stratification conditions were modified. As shown in previous paragraphs, PP response to mixing was also dependent on the Fe concentration. To take the latter into aClimate Changeount I repeated the same "summer mixing experiment" only for two extreme cases very similar to A and D cases in 6.8; i.e. one with shallow winter mixing and deep Z_{Fe} and a second one with deep winter mixing and shallow Z_{Fe}. For each of these cases, summer Z_{Fe} and winter MLD (in timing and magnitude) were fixed and only summer MLD varied: from 20 to 100m at a 20 meters interval (i.e.: 5 "summer scenarios" per case). From the two sets of outputs,

each phytoplankton group integrated PP was computed not for the whole seasonal cycle but only for the summer period (December, January and February).

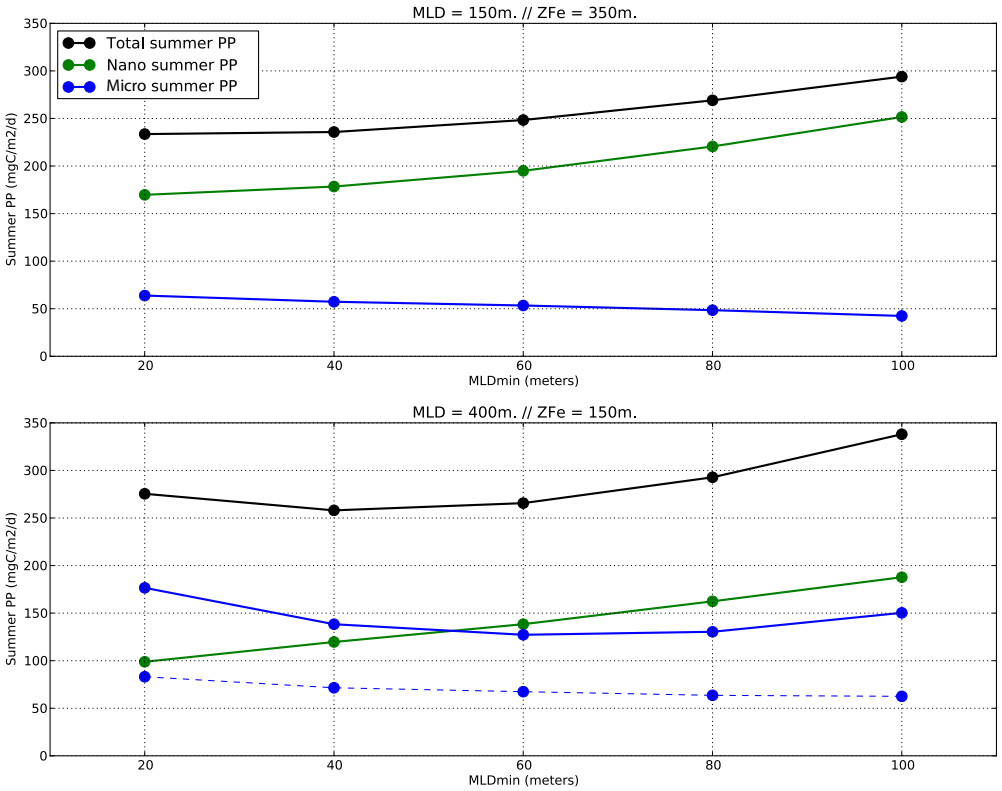

FIGURE 6.11: Mean integrated PP during austral summer (December January and February) as a function of MLD_{min} as diagnosed in the 1D model. Results are presented for a high-Fe/deep MLD_{max} case (TOP) and for a low-Fe/shallow MLD_{max} case (BOTTOM). Total integrated PP is represented by the black line, nanophytoplankton contribution to the total PP is represented by the green line, microphytoplankton contribution to the total PP is represented by the blue line

For both cases, is clearly seen that deeper summer mixing enhanced summer production (figure 6.11). This relationship agrees with the results presented in figure 6.8 stressing the fact that the increase on productivity occurred (mainly) in summer. When assessing the contribution of each phytoplankton group, the opposing slopes of nano- and microphytoplankton contribution stands out (green and blue lines in figure 6.8). While nanophytoplankton production decreased when summer mixing shallowed, microphytoplankton did the opposite: production increased. For the deep mixing high-Fe scenario and between 20 to 60m, microphytoplankton were able to surpass nanophytoplankton production. Also in this scenario, for MLD_{min} deeper than 60m, microphytoplankton trend was reversed and production increased with deeper mixing. We argued that this increment was due to an increase on summer iron resupply as MLD_{min} got close to Z_{Fe}.

An identical set of runs but with Z_{Fe} at 400m confirmed this hypothesis as microphytoplankton PP curve presented a constant decreasing PP with MLD_{min} (blue dashed line in figure 6.11.B).

Three possible mechanisms were identified to explain these trends:

- Grazing pressure over nanophytoplankton was enhanced by shallower mixing, due to a reduction on the grazer-prey encounter time.
- Nanophytoplankton took advantage of deep summer mixing layers, as these layers were richer in nutrients. Such an increase on nutrients could eventually be compensated by the decrease on mean PAR_{MLD}. However, the strong turbulent mixing in our model ($\kappa = 1m^2/s$) guaranteed an active vertical transport hence, a weak impact on light limitation.
- The competition for nutrients (specially for Fe) between the two PG caused that, when one was disadvantaged (p.e. nanophytoplankton in shallow mixing), more resources were available for the other one.

These three mechanisms would be interconnected and occurring simultaneously.

In this section, we have addressed the factors controlling the primary production in the Southern Ocean. We have seen that, over the year, total PP emerges from a complex combination of Fe-supply, ecosystem diversity and mixing depth (figure 6.10). In addition, we set up a specific set of 1D runs to understand the statistical result found in CMIP5 models: the PP increase due to more stratified waters in summer. Surprisingly, the study of the mechanisms controlling summer PP based on 1D runs suggested that, except for ecosystems dominated by microphytoplankton, an increase on summer stratification causes a decrease on PP.

The lack of coherence between the 1D and the CMIP5 models, motivated us to enlarge our view and to look for new players that could drive CMIP5 PP projected trends. To do so in an efficient way, we decided to work with only one of the CMIP5 models: the IPSL medium resolution model or IPSL-CM5A-MR. The results concerning future projected changes in iron concentration, solar surface flux and temperature are presented in next section.

6.4 Shedding light on hidden future drivers

The most likely additional stressors able to alter PP are iron availability and surface solar flux. Water temperature of the euphotic layer could also have an eventual impact through the increase of phytoplankton specific growth rate in warmer waters (as defined by the Eppley curve, Eppley [1972]).

The predicted trends under RCP85 scenario for each of these variables[3] by the IPSL-CM5A-MR are represented in figure 6.12:

- The change in Fe concentration (averaged from 0 to 50 meters) was extremely weak for most of the Southern Ocean: a low decrease (ΔFe $<$ 0.01 nmolFe/m ^{3}) was identified east of the Pacific and Indian sectors while most of coastal waters (unless South-American) presented a strong increase (ΔFe $>$ 0.2 nmolFe/m^3). No trace of zonal band or ΔPP-like pattern.
- The change in SST presented a near-zonal structure with positive trends over all the Southern Ocean. The range of magnitude change was large, with local strong warming (south of GoodHope Cape and along Agulhas return current ΔSST $>$7°C), an average change of ΔSST $\approx$4.2°C north of 50°S and a much weaker alteration south of this latitude (1°C $<$ ΔSST$<$2°C). Such an increase may primarily be due to the atmospheric and oceanic warming but probably also influenced by the poleward shift of the whole frontal system. However, SST trends presented a generalised warming over the whole Southern Ocean that could eventually influenced a PP increase but not explained the zonal band of negative ΔPP around 60°S.
- The third stressor considered, the projected change in sea surface solar flux, presented an interesting spatial structure (figure 6.12 c): surface light radiation increased almost a 10% north of 50°S and over Antarctic coastal waters. Conversely, it decreased in a band constrained between 50°-60°S in the Atlantic and Indian sectors, slightly southwards in the Pacific (55°-65°S). Such a pattern is likely related to the poleward shift in atmospheric circulation and the strengthening of winds enhancing sea spray aerosol emissions and therefore the mean cloud coverage (Korhonen et al. [2010]) and had been observed in other CMIP5 models (Chepfer et al. [2014]). An alteration of the solar radiation reaching sea surface can significantly impact PP in the Southern Ocean, specially south of 50°S, where light is the dominant limiting factor for a large part of the year (from late-autumn to winter; Boyd and Ellwood [2010]).

Interestingly, the projected ΔPP patterns in the IPSL model (represented in figure 6.6) coincides with the trends in surface radiation: the production increase from 40° to 50°S, with little decrease between 50° to 60°S and an increase south of 60°C. However, such a coherence was not diagnosed in the Pacific Sector nor in the subtropical band. In conclusion, surface solar flux seemed to be a significant, but not exclusive, driver of change.

Poleward shift on Primary Production patterns

As presented in Meijers [2014], in CMIP5 models, the oceanic resposne to intensification and poleward shift of surface winds (caused by the persistent positive phase of SAM), is a poleward

[3]We assumed the change in sea surface temperature (SST) could be used as a proxy of the mean upper-ocean temperature.

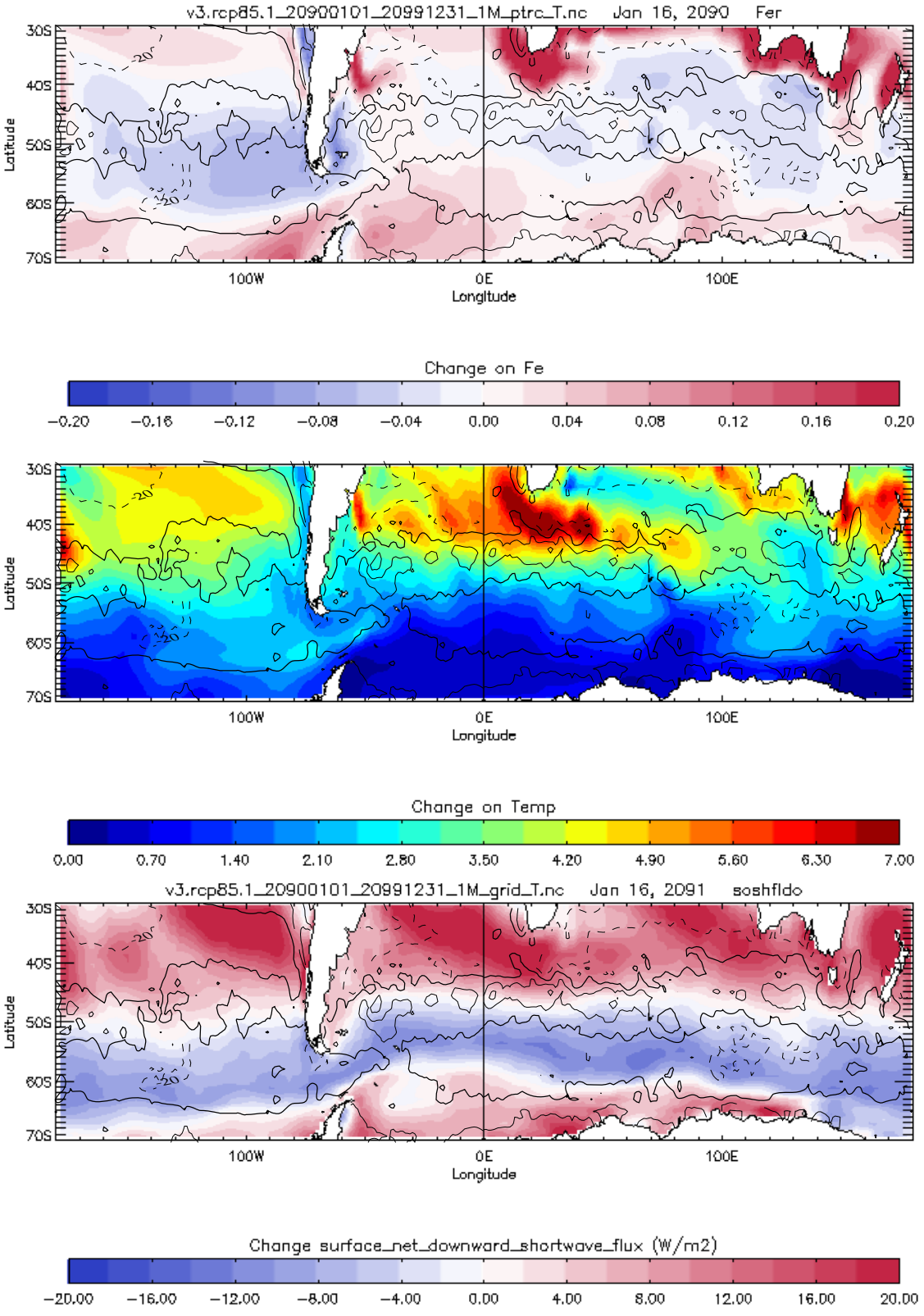

FIGURE 6.12: RCP85 to Historical decade mean change for [0,50] mean Fe concentration (TOP), SST (CENTER) and surface net shortwave solar flux (BOTTOM) for the IPSL-CM5A-MR model

1.5° shift of the whole Southern Ocean frontal dynamics. Based on this statement, we hypothesised that the mean ΔPP pattern projected by CMIP5 models (see figure 6.2) resulted from a shift of the PP historical mean pattern added to changes in surface PAR. A qualitative justification of such hypothesis is presented in figure 6.13: the meridional section of $PP_{RCP8.5}$ for each of the three Southern Ocean basins was represented in the upper panel (black lines) together with the PP_{HIST} shifted 1.5° southwards, in dashed black. Shifted-PP_{HIST} correctly fitted the curve of $PP_{RCP8.5}$ to certain latitudes (∼47°S at Indian, ∼50°S at Pacific and ∼52°C at Atlantic) with very small differences in magnitude. This coincidence suggested that, from 30°S to ∼50°S, PP was not altered in magnitude but only a shifted in latitude, as a consequence of the poleward shift of all physical and biogeochemical conditions. At latitudes higher than 50°S (and until 60°-65°S), PP_{RCP85} decreased over the three sectors. Such decrease seems to fit reasonably well with the projected decrease of surface PAR (black line in bottom panels). For the Indian and Pacific sectors, the band of $\Delta PP < 0$ coincided with the band of decreased surface PAR; for the Atlantic however, PP did not experienced any change until 52°S despite a light reduction starting around 46°S. Southern of 65°S, PP_{RCP85} increased everywhere together with a strong augmentation of the surface solar flux. An interesting conclusion from this representation is that, in absolute terms, PP_{RCP85} only increases in the Antarctic waters: PP increase identified at 40°S-50°S (figure 6.2) may be an artefact due to poleward shift, balanced by the decrease in subtropics.

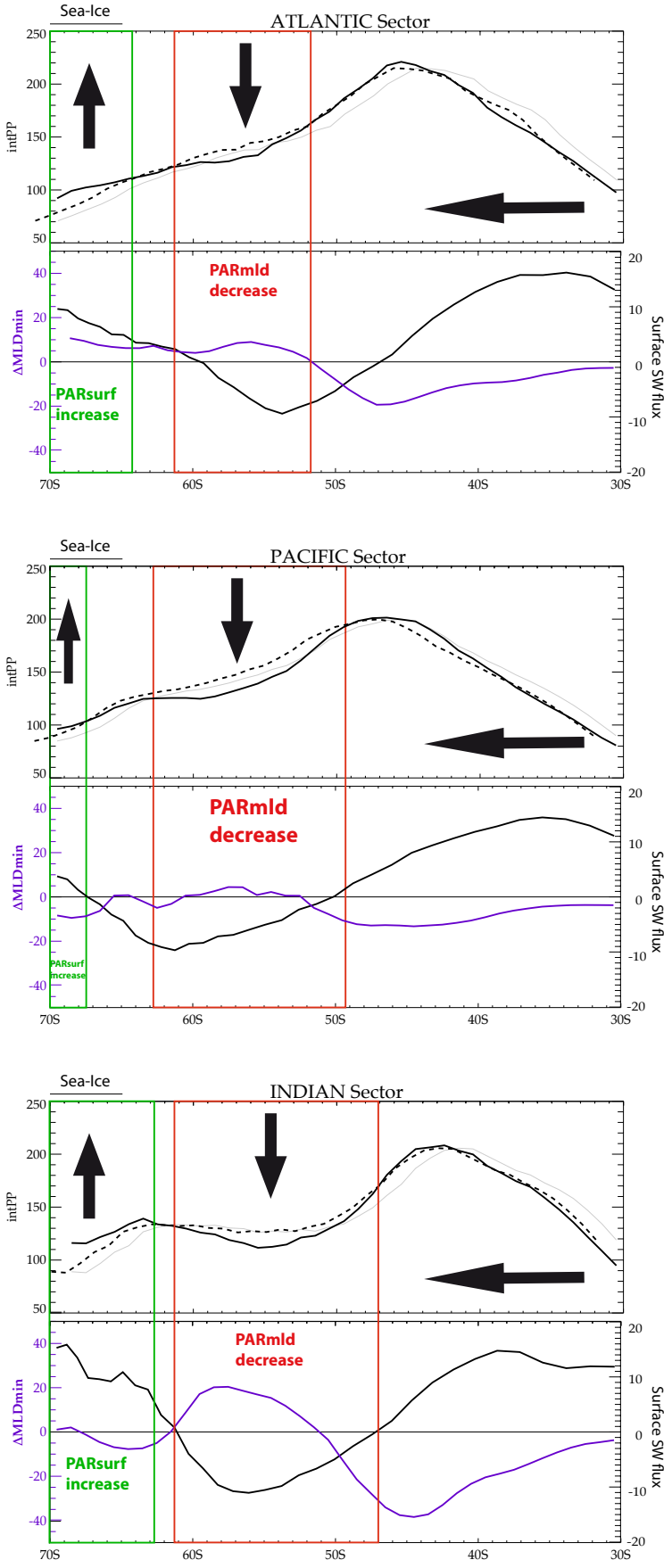

FIGURE 6.13: Upper panels: Zonal mean sections for the PP_{Hist} (in grey), PP_{Hist} shifted 1.5° southwards (dashed black), PP_{RCP85} (black). Arrows indicate the dominant PP trend (horizontal=shift, downwards=decrease, upwards=increase. Bottom panels: ΔMLD_{min} (blue) and $\Delta SW_{surface}$. Increase and decrease on PP is highlighted with green and red boxes respectively, to stress the concordance between PP trends and solar flux anomalies.

6.5 Summary and Conclusions

In this chapter, I addressed how Primary Production is influenced by physical processes in the Southern Ocean and, more specifically, how an alteration of the physical ocean environment due to Climate Change can impact productivity. I analysed projected change in PP and MLD for the end of the current century produced by eight CMIP5 models, under the most extreme radiative scenario (RCP85). The patterns of change in annual PP (ΔPP) presented a clear zonal band structure with alternate phases of increase and decrease on production. Such a spatial structure appeared to be strongly correlated to the trends in summer MLD (or ΔMLD_{min}). However, this correlation was much stronger over the multi-model mean than for each of the models. Surprisingly, the correspondence of ΔPP to winter mixing (MLD_{max}) was very low.

We then compared CMIP5 results with a simple 1D ocean model coupled to the biogeochemical PISCES module. This approach allowed us to test the sensitivity of the total PP and community structure to changes in winter and summer MLD. We showed how MLD_{max} applied a complex control over annual PP: on one hand, linked to the vertical supply of iron while, on the other hand, limiting winter production through the reduction of the light received by phytoplankton. The high sensitivity of total PP to slight changes in winter MLD, Fe concentration or plankton diversity found in our 1D runs, justifies the lack of robustness between CMIP5 models, which strongly differ on the representation of these three magnitudes. Therefore, our first conclusion is that even if an impact of the altered winter MLD on PP existed, such an impact cannot be identified from a multi-model mean signal. But then, what shaped the clear band-structured PP trends in CMIP5 outputs?

A possible answer to this question (and based on figure 6.5) could be the change in summer MLD. The effect of summer MLD on primary production has already been pointed out by several authors as a potential factor of stress for Southern Ocean PP (Bopp et al. [2013]). The effect of a more stratified ocean on PP is still unclear as stratification, improves summer light conditions for phytoplankton and, yet reduces the amount of nutrients available from late spring to autumn. The clear correspondence between ΔMLD_{min} and ΔPP found for the averaged CMIP5 models suggested that more stratification enhances production. With the aim to address these question properly and from an approach "external" to CMIP5 results, we set up an specific ensemble of 1D runs with all physical parameters fixed, except MLD_{min}. At first sight, results were completely opposed to CMIP5 ones: more stratified summer MLD reduced summer PP. However, when looking only to the contribution of microphytoplankton, 1D model agreed with CMIP5 showing a dependency of microphytoplankton production to MLD_{min} in accord with the ΔMLD_{min} - ΔPP relationship in CMIP5 (figure 6.11). Therefore, PP trends on CMIP5 models could be explained by an enhancement of the production driven mainly by microphytoplankton, specially where waters were rich in iron. Even if theoretically true, we identified three arguments that strongly weakened this explanation:

1. ΔMLD_{min} - ΔPP correspondence was rarely found inside each of the 8 models and it was likely biased by models projecting strong changes (as NorESM and MPI; see figure 6.6).

2. The "dominant" models (the one contributing the most to the averaged trends) had a lack of representation of phytoplankton diversity (only 1 PG for NorESM and MPI, see table 6.1) and thus, the expression of diatom-like behaviour was highly improbable.

3. Assuming that the PP trends in CMIP5 were exclusively due to the enhancement of microphytoplankton summer production, the rate of this enhancement would be more than twice the rate obtained in 1D runs (+1.2% "per stratified meter" in CMIP5 against a +0.5%/m in the 1D).

We decided to look for an alternative explanation of the trends of PP as projected in CMIP5 models.

To do so, we focused on only one of the ESM models of the CMIP5 ensemble, the IPSL-CM5A-MR, which we used to address the projected trends on three addtional stressors: dissolved Fe, sea surface temperature and surface solar flux (figure 6.12). Among the three, the surface solar flux was the only stressor to agree with a PP decrease over the 50°-60° band. Such decrease on productivity would then be due to a reduction of the amount of solar radiation reaching ocean surface. There was, however, a piece missing in this puzzle: solar surface radiation seemed to increase everywhere north of 45°S thus, the projected decrease on productivity in the subtropics could not be justified. In these medium latitude regions light control is much lower and it was very likely that the dominant stressor was not the change in solar flux. We had finally resolved the question by the addition of two processes: an annular poleward shift of the zonal features of primary production (caused by of the large-scale shift of the whole Southern Ocean atmosphere and ocean dynamics Meijers [2014]); added to a change in surface solar radiance that drove trends over high latitudes (decrease over 50°-60°S and increase 60°-70°S). We have illustrated such results in figure 6.13 by shifting the zonal PP average and comparing it to its historical values.

Even if the ensemble of CMIP5 models constitutes a unique tool to estimate future ocean trends, its results must be carefully analysed and interpreted. Some features seemed to be highlighted (for instance, light dependence) while others were under-represented due to lack of agreement and complex responses (e.g. impact of winter mixing and its coupling with iron supply). Furthermore, recent studies based on high-resolution coupled models do not project such a clear southward shift of the frontal dynamics. Thus, it is possible that important dynamical processes are not being fully represented in CMIP5.

The Southern Ocean presents a strong regional variability in terms of PP that influences the spatial, seasonal and interannual variability of the air-sea CO_2 flux (Metzl et al. [1999]). Given

the significant role of this ocean on the global carbon cycle, we think that is essential to further investigate the Southern Ocean primary production with specific approaches that complement CMIP5 outputs. Such approaches must be based on medium to high resolution (sub-)regional models and higher data coverage in time (i.e., during winter) and in space (i.e., accurately vertical iron and mixing distribution); along with a deeper understanding of the intricate biogeochemical processes that control phytoplankton community dynamics (in particular, those concerning regenerated production and export).

CONCLUSIONS

Conclusions and perspectives

Conclusions

The main objective of my thesis works was to investigate the mechanisms that control primary production in the Southern Ocean. This general question was split up into three specific questions. My thesis works provided a series of results and conclusions for each one of these questions which I will briefly summarise here.

What are the mechanisms driving phytoplankton bloom dynamics in the Southern Ocean?

The study I carried out using more than 1,200 modelled Southern Ocean blooms allowed us to identify three crucial phase of the bloom evolution: the onset, the climax and the apex. The model outputs, on a daily frequency, for the specific phytoplankton growth, mortality and grazing rates were used to identify the dominant controls at each bloom phase.

All onsets occurred around the winter solstice and two different controls were identified: a top-down control (dilution of grazers) for the earliest onsets and a bottom-up control (light) for onsets occurring after the winter solstice. Bloom climaxes occurred during spring due to the shallowing of the mixing layer and the improvement of light conditions. Interestingly, the amount of Fe seemed to play a secondary but significant role in the intensity of phytoplankton accumulation during climax. Apexes were identified in early summer which was controlled by grazing.

The magnitude of the climax was used to classify blooms in two types of phenology: abrupt and smooth. I showed how abrupt blooms were typical of iron-rich and fast shallowing waters. On the contrary, smooth blooms occurred in nutrient limited waters or in environments with a weak seasonal cycle (lower latitudes). This link between the bloom phenology and the environment could be used to address the diversity of bloom phenology observed in the Southern Ocean. Unfortunately, the definition of the climax phase requires an accurate measurement of the integrated biomass rate of change, which is impossible to obtain from ocean colour data. I proposed however,

a solution to this issue. Using the outputs of the 1D model, I demonstrated that commonly used satellite surface bloom detection criteria (Cole et al. [2012]; Brody et al. [2013]) do not detect the onset, but the climax of the bloom. Intense bloom climaxes have a strong surface Chl imprints that are tipically misled as the bloom onset by satellite based studies. The 1D diagnostics also showed that is possible to detect the proper onset from satellite data if the information on the MLD is available.

How these mechanisms combine to produce the bloom diversity observed in the Southern Ocean?

Using satellite-derived products and observation-based estimates of mixed-layer depth we were able to estimate the onset and climax of blooms (i.e., Chl^{ML}-onsets as referred in the article) and climaxes (i.e., Chl^{surf}-onsets as referred in the article) for 13 years of observations in the Southern Ocean. Both onsets and climaxes were detected using the methods tested in our 1D study. The determination of these two bloom phases allowed us to address the bloom phenology diversity in the Southern Ocean. Interestingly, the bloom diversity appeared to be organised into three distinct regimes associated with three specific geographic locations: subtropical region, sub-antarctic region and ACC region. Based on the results of the 1D study we could infer the drivers of the phenology diversity from the distribution of onset-to-climax time duration and the geographical position of the blooms.

Amongst the three bloom regimes, sub-antarctic regime had the most complex dynamics. Only this regime presented a climax occurring more than three months after the onset. In addition, climax dates were concomitant to the date at which air-sea heat fluxes switched from cooling to warming, even for very deep of the MLDs (i.e., more than 400m). Such a mechanism has been identified as trigger of surface blooms in the North-Atlantic by Taylor and Ferrari [2011] and Ferrari et al. [2014].

This work was complemented with a model-based study with the aim to contrast the detection methodology applied. Using a 3D biogeochemical configuration, I used surface and MLD model data to mimic the observation-based bloom detection methods. In parallel, I detected the bloom onset from the integrated biomass data of the model. The comparison between the two methods shown how, for certain type of blooms and MLD dynamics, Chl^{ML} approximation failed to detect integrated onset blooms. In particular, the stocks of subsurface (i.e., below the MLD) biomass in late summer caused Chl^{ML} approximation to be underestimated. Such an incorrect initial estimation had repercussions throughout the entire seasonal cycle, and thus the detection of bloom onset.

The studies that allowed me to answer these two questions, models were used to both understand the underpinnings of phytoplankton blooms and to evaluate different techniques applied to satellite observations. Interestingly, the disagreements we encountered between the different

models and between models and observation pointed out some limits of the models to reproduce fine-scale physical processes. Thus, the combination of models and observations created a beneficial symbiosis for both parts. This demonstrates, in my opinion, the importance of combine and compare observations and models.

How Southern Ocean primary production is likely to be influenced by a Climate Change's altered environment?

In the last results chapter of this manuscript I adopted an integrated view to study the primary production in the Southern Ocean. The objective was to identify the drivers of the annual primary production (PP) in the present and in the future ocean. My aim was to understand the zonal pattern of future PP trends diagnosed in eight CMIP5 models by Bopp et al. [2013]. Analysis of changes in multi-model winter and summer MLDs showed a spatial correspondence between trends of PP and summer MLDs. A process study investigating the influence of summer stratification on PP on individual model trends put the PP-MLD relationship into question. Moreover, using one of the CMIP5 models (the IPSL-CM5A) I highlighted that surface solar radiation could be a potential driver of PP. To fully explain the CMIP5's PP trends, I proposed a combination of two Climate Change impacts: a large-scale poleward shift of frontal dynamics in the Southern Ocean (Meijers [2014]) together with a decrease of solar radiation in a 10°-zonal band around 60°S. As a part of the works planned for the next months, I will continue complete this study to be synthesised in an article (in collaboration with L.Bopp and M.Lévy). Amongst the diagnoses we would like to add there is an analysis of surface Fe and solar radiation for the eight CMIP5 models.

The causes of the PP trends projected by eight CMIP5 models in the Southern Ocean has also been a subject of study. It is important to note that these trends (and the proposed causes) have not yet been contrasted with observations or other modelling approaches. For instance, some studies have shown that the poleward shift of the ocean dynamics due to the positive phase of the SAM is not reproduced in high resolution Southern Ocean models. Concerning the decrease on solar surface radiation around 60°S : it is still not clear what drives this in the model and there are no direct observations that support these results. There are however, some hints in recent literature that suggest that the trend in solar radiation is robust in the models (Ceppi et al. [2014] and Chepfer et al. [2014]).

Perspectives

My works focused on different aspects of the primary production in the Southern Ocean. The ensemble of presented results allowed me to conclude with some new insights on the relationship

between phytoplankton blooms and the environment where these blooms take place. Several results showed the importance of bottom-up controls on bloom dynamics during the intense phase of the bloom (i.e., the climax). Most of the bloom studies in literature focus on this crucial phase of the bloom. The "Disturbance-recovery hypothesis" (DRH; Behrenfeld and Boss [2014]) proposes a much wider view and addresses the whole seasonal cycle of the plankton ecosystem. This hypothesis describes the high-latitude blooms as expressions of disturbances on the equilibrium (or coupling) between phytoplankton and grazers. The DRH generalises the bloom theories to any ecosystem in the global ocean, stressing the role of top-down controls. Although I mainly focused on the winter and spring period of the bloom, the biogeochemical model configurations I used fully resolved the ecosystem evolution throughout the entire seasonal cycle. These models could be used to address the phytoplankton seasonal cycle from a 'DRH point of view': analysing the prey-grazers coupling during the entire seasonal cycle and all over the global ocean. These studies may modify our perception of the hotspots of primary production (as proposed by Behrenfeld [2014]) because, as showed, the surface Chl signal it is not enough to correctly estimate the amount of integrated biomass and primary production. Another challenging perspective is the plankton ecosystem evolution during summer, when the coupling between phytoplankton and grazers is maximal. During this period, a number of complex biogeochemical processes take place and new factors come into play (e.g., viral activity, phytoplankton species succession, remineralisation). Although most of these processes are represented in PISCES model, we did not addressed these questions. To properly resolve the mechanisms controlling plankton community in summer it is necessary to joint *in-situ* and laboratory studies with models studies, to profit of beneficial symbioses as the applied here using satellite, *in-situ* and model data. In the Southern Ocean such a multi-disciplinary approach would allow to improve the understanding on the complex iron recycling cycle (i.e., the *ferrous wheel* Boyd and Ellwood [2010]).

The conclusions of the 1D model configuration shaped our vision of Southern Ocean blooms and were later used to interpret the different bloom regimes estimated from observations. However, this novel model configuration was based on very strong physical simplifications. Amongst the assumptions we used to set-up the 1D model, at least one is worth further investigation. In the model, a very strong turbulent mixing was imposed: $\kappa_z = 10^{-5}$ m^2/s from the surface to a certain depth (Z_{mix}). Such an actively mixed layer (called the mixing layer) presented a very simple seasonal cycle: regular deepening in winter, regular shallowing in spring and constant summer value. In the real ocean, the evolution of such a mixing layer is very different. Research using high-resolution models (Taylor and Ferrari [2011]) and in-situ data (Mahadevan et al. [2012]; Ferrari et al. [2014]; Swart et al. [2014]; K. Johnson[4]) have stated the large sensitivity of mixing layer to atmospheric and sub-mesoscale events. All of these works related rapid stratification events of the mixing layer to sudden increases in surface Chl. From my point of view, these intra-seasonal events occurring in late winter are the triggers of bloom climax, but they do not have any influence

[4]http://soccom.princeton.edu/content/deep-mixing-southern-ocean-and-spring-bloom-seen-soccom-profiling-floats

on the bloom onset[5], which usually occurred a few months prior to the climax. Nonetheless, these near-surface stratification events may have important consequences on the primary production as they are characterised by periods of very high rates of biomass accumulation. With the aim to quantify the importance of intra-seasonal stratification events over primary production in the sub-antarctic region, I started a collaboration with the PhD student S.Nicholson (UPMC, France and UCT, South-Africa). S.Nicholson is using a new version of my 1D configuration to study the impact of different κ_z vertical profiles on the bloom dynamics and to estimate the impact of summer intra-seasonal mixing events on primary production. This modelling study is being created in parallel to the analysis of high-resolution observations in the sub-antarctic zone (Swart et al. [2014]).

A general motivation for phytoplankton bloom studies is to understand the processes which influence the biological pump of carbon at higher latitudes. In this study we addressed the first part of this issue; the bloom dynamics. However, further work is necessary to understand how bloom dynamics relates to the carbon cycle. For instance, it would be interesting to address at which phases of the bloom carbon export is enhanced and how bloom dynamics influences the air-sea flux variability of CO_2. During my participation in KEOPS2 I actively worked on the acquisition of pCO_2 sea-surface measurements during the formation phase of Kerguelen's bloom. One of the main results of the study produced from this data (in Appendice A) was the rapid establishment of CO_2 sinks due to the biological activity. This result stresses the importance of blooms on the sign of CO_2 air-sea flux.

The ensemble of works presented here bring new insights on the primary production at high-latitudes. My results illustrate the complexity of the bloom dynamics: several controls are in constant competition throughout the seasonal cycle and is impossible to reduce the whole bloom dynamics to an isolated control. We demonstrated however, that Southern Ocean blooms mechanisms are very similar to the North-Atlantic blooms except for the role of iron, that enhances the bloom phenology diversity. Iron is also a source of uncertainty for climate models. The future trends of change on primary production in the Southern Ocean are highly sensitive to both the iron supply and the phytoplankton diversity, but any of these two elements is properly resolved in CMIP5 models.

In conclusion, an accurate estimation of the mutual influence between the Southern Ocean and the Climate Change requires future efforts to represent Southern Ocean specificities in the Earth System models and an integrated understanding of the plankton ecosystem dynamics.

[5] A similar conclusion is presented in Ferrari et al. [2014], which authors refer to the surface Chl imprint of the climax as the "surface spring bloom".

APPENDICE

Appendix A

Rapid establishment of the CO2 sink associated with Kerguelen's 2 bloom observed during the KEOPS2/OISO20 cruise. (Article)

Rapid establishment of the CO_2 sink associated with Kerguelen's bloom observed during the KEOPS2/OISO20 cruise.

C. Lo Monaco, N. Metzl, F. D'Ovidio, J. Llort, C. Ridame

Sorbonne Universités (UPMC, Univ Paris 06)-CNRS-IRD-MNHN, LOCEAN Laboratory, 4 place Jussieu, F-75005 Paris, France

Contact: claire.lomonaco@locean-ipsl.upmc.fr

Draft, 20 October 2014

Abstract

Iron and light are the main factors limiting the biological pump of CO_2 in the Southern Ocean. Iron fertilization experiments have demonstrated the potential for increased uptake of atmospheric CO_2, but little is known about the evolution of fertilized environnements. This paper presents observations collected in one of the largest phytoplankton bloom of the Southern Ocean sustained by iron originating from the Kerguelen Plateau. We first complement previous studies by investigating the mechanisms that control air-sea CO_2 fluxes over and downstream of the Kerguelen Plateau at the onset of the bloom based on measurements obtained in October-November 2011. These new observations show the rapid establishment of a strong CO_2 sink in waters fertilized with iron as soon as vertical mixing is reduced. The magnitude of the CO_2 sink was closely related to chlorophyll-a and iron concentrations. Because iron concentration strongly depends on the distance from the iron source and the mode of delivery, we identified lateral advection as the main mechanism controlling air-sea CO_2 fluxes downtream the Kerguelen Plateau during the growing season. In the southern part of the bloom, situated over the Plateau (iron source), the CO_2 sink was stronger and spatially more homogeneous than in the plume offshore. However, we also witnessed a substantial reduction in the uptake of atmospheric CO_2 over the Plateau following a strong winds event. Next, we used all the data available in this region in order to draw the seasonal evolution of air-sea CO_2 fluxes. The CO_2 sink is rapidly reduced during the course of the growing season, which we attribute to iron and silicic acid depletion. South of the Polar Front, where nutrients depletion is delayed, we suggest that the amplitude and duration of the CO_2 sink is mainly controlled by vertical mixing. The impact of iron fertilization on air-sea CO_2 fluxes is revealed by comparing the uptake of CO_2 integrated over the productive season in the bloom, between 1 and 1.5 molC/m^2/yr, and in the iron-poor HNLC waters, where we found a typical value of 0.4 molC/m^2/yr. Extrapolating our results to the ice-free Southern Ocean (~50°S-60°S) suggests that iron fertilization of the whole area would increase the contemporay oceanic uptake of CO_2 by less than 0.1 PgC/yr, i.e., less than 1% of the current anthropogenic CO_2 emissions.

1. Introduction

The Southern Ocean plays a major role in moderating global warming by absorbing annually around 1 Pg (10^{15} g) of carbon (Takahashi et al., 2009; Lenton et al., 2013). Although this number amounts to about 10% of the CO_2 currently released to the atmosphere by human activities (mostly fossil fuel burning and land use change; Le Quéré et al., 2014), it hides a much larger potential because of iron limitation (Martin et al., 1990). Indeed, most of the CO_2 uptake occurs in the frontal region between 40°S and 50°S where iron is available to sustain primary production, whereas south of the Polar Front (~50°S) stands the largest High Nutrient Low Chlorophyll (HNLC) area (Tagliabue et al., 2012). Iron enrichment experiments conducted in the HNLC region have demonstrated the role of iron in controlling primary production and the potential for increased uptake of atmospheric CO_2 when photosynthesis is stimulated (Boyd et al., 2007). However, due to the limited area and the short time-scales involved in these studies, the long-term efficiency and the consequences of artificial iron fertilization are still very uncertain.

An alternative to assess the impact of iron fertilization on the uptake of atmospheric CO_2 is offered by naturally fertilized environments, notably over and downstream of the Kerguelen Plateau in the Southern Ocean, where a large phytoplankton bloom is observed every summer (e.g., Mongin et al., 2008). A previous study conducted in this region in February 2005 (KEOPS/OISO12 cruise) confirmed that natural iron fertilization enhances the biological uptake of CO_2 over the Plateau compared to the surrounding HNLC waters (Blain et al., 2007). These observations, however, were limited to the declining phase of the bloom in its southern part. Kerguelen's bloom covers hundreds of thousands km^2, and since spatial heterogeneity can be anticipated, more observations were needed to accurately assess the impact of iron fertilization on air-sea CO_2 fluxes.

The KEOPS project was designed to achieve a better understanding of the mechanisms at play over and downstream of the Kerguelen Plateau, in order to assess the impact of iron fertilization on biogeochemical cycles and ecosystems. The KEOPS2 survey was conducted at the start of the productive season, in October-November 2011, and coupled with the 20th OISO cruise, with the objective of monitoring the establishment of the CO_2 sink associated with Kerguelen's bloom and investigating the mechanisms responsible for spatial and temporal variations in air-sea CO_2 fluxes in different regions of the bloom. In this paper, we

first present underway measurements of CO_2 and related parameters collected during the KEOPS2/OISO20 cruise. This allows to evaluate and understand the evolution of air-sea CO_2 fluxes over the Plateau and in the plume offshore during the transition from winter conditions to the growing season. These new observations are discussed with regard to iron and other nutrients availability, lateral transport and vertical mixing. Next, we used all available observations from the Surface Ocean CO_2 Atlas (SOCAT, Bakker et al., 2014), merged with KEOPS and more recent OISO data, in order to evaluate the seasonal evolution of air-sea CO_2 fluxes in and out of Kerguelen's bloom, and thus quantify the impact of iron fertilization on the uptake of atmospheric CO_2.

2. Material and methods

This work is primarily based on *in situ* measurements collected during the KEOPS2/OISO20 cruise. Sampling and measurement techniques are described below. In order to push our analysis further, we also evaluated the seasonal evolution of air-sea CO_2 fluxes using all the OISO/KEOPS data available to date (1998-2013), complemented by observations from four previous cruises (1991-1993) obtained from the SOCAT database (version 2.0; Bakker et al., 2014), as well as measurements obtained from the CARIOCA buoy launched during the KEOPS2 survey. Underway measurements of the fugacity of CO_2 (fCO_2) obtained during all OISO cruises (including the two KEOPS surveys), are or will soon be available at the Carbon Dioxide Information Analysis Center (CDIAC, http://cdiac.ornl.gov/oceans) and in the SOCAT database (http://www.socat.info). In addition to *in situ* measurements, we used satellite data to map chlorophyll-a concentration (Fig.1 produced with the Giovanni online data system, available at http://disc.sci.gsfc.nasa.gov/), and to compute climatological winds for air-sea CO_2 flux calculation (see Sect.2.2).

2.1. Sampling strategy and measurement techniques

The study site is defined around the Kerguelen Plateau, from 64°E to 75°E, and between 47°S and 51°S (Figs. 1 and 2). This region includes various biogeochemical systems, from the typical High Nutrients Low Chlorophyll (HNLC) waters generally found south of the Polar Front (PF), to the highly productive waters over and downstream of the Plateau (Fig. 1). The most extensive survey dedicated to understanding the functioning of this iron fertilized environment was conducted during the KEOPS2/OISO20 cruise, when physicists,

107 biogeochemists and biologists were brought together to investigate the mechanisms at play in
108 different regions of the bloom. The previous KEOPS/OISO12 cruise, conducted in January-
109 February 2005, involved as much expertise, but it was limited to the southern part of the
110 bloom situated over the Plateau. Below we describe the sampling and measurement
111 techniques followed during the KEOPS2/OISO20 cruise, which are very similar to those
112 followed during the first KEOPS survey (Jouandet et al., 2008), and during all OISO cruises
113 (Metzl et al., 1999; Jabaud-Jan et al., 2004; Metzl, 2009; Lourantou and Metzl, 2011).
114
115 The KEOPS2 survey was conducted onboard *R.R.V. Marion Dufresne* in 2011, from the 17th
116 of October, when the ship approached the Kerguelen Plateau on its western side, to the 21st of
117 November, when the ship headed north of Kerguelen Island (see cruise track in Figs. 1 and 2).
118 Our work is mostly based on hydrological and biogeochemical properties measured underway
119 in surface waters (~5m depth). Underway surface measurements include the fugacity of CO_2
120 (fCO_2), sea surface temperature (SST), sea surface salinity (SSS) and fluorescence. In
121 addition, atmospheric CO_2 was measured every 4 hours, and surface water samples were
122 colleted every 4 hours for total CO_2 (TCO_2), total alkalinity (TA), chlorophyll-a and nutrients
123 concentrations and every 8 hours for salinity.
124
125 The technique for fCO_2 measurements was described in details by Poisson et al. (1993), Metzl
126 et al. (1995, 1999) and Jabaud-Jan et al. (2004). In short, sea surface water is continuously
127 equilibrated using a 'thin film' type equilibrator thermostated with surface seawater. The CO_2
128 in the dried gas is measured with a non-dispersive infrared analyser (Siemens). The analysis
129 of standard gases used for calibration indicated an accuracy to ±0.7 µatm. All fCO_2 values
130 presented here are normalized to 1013 hPa. TCO_2 and TA were measured onboard, using a
131 potentiometric method with a closed cell, and Certified Referenced Materials (CRMs, batch
132 111, provided by Dr. A. Dickson, SIO, University of California). Accuracy estimated from the
133 CRMs analysis was ±4 µmol/kg for both TA and TCO_2. SST and SSS were obtained from
134 two Sea-Bird thermosalinographs. SSS was checked against measurements performed
135 onboard using a salinometer (Park et al., 2014). Accuracy for SSS was evaluated to ±0.005.
136 Nutrients were also measured directly onboard using a Skalar auto-analyzer (Blain et al.,
137 2014). Accuracy was determined by measuring certified standards (CERTIPUR, Merck): it
138 was 3.5% for nitrate and 2.2% for silicic acid ($Si(OH)_4$) for concentrations around 35
139 µmol/kg. Underway chlorophyll-a measurements were obtained by filtering between 1L and

2L of seawater on 25mm GF/F Whatman filters (pressure <200 mbar). Filters were stored at -80°C until measurements were performed at LOCEAN using a Hitaschi F-4500 spectrofluorometer, after extraction of the filters in 90% acetone, following the method described by Neveux and Lantoine (1993). The precision of chlorophyll-a measurements is typically around 5%. We used chlorophyll-a measurements to calibrate underway fluorescence data, but due to the poor correlation obtained (r^2=0.5), calibrated fluorescence data must be considered with care.

Water samples were also collected at depth using a rosette equipped with 22 Niskin bottles and a Seabird CTD (Conductivity-Temperature-Depth) sensors. We used the data obtained between 0 and 20m to complement underway measurements, with the exception of chlorophyll-a data as it was not obtained using the same technique (high performance liquid chromatography) as for underway surface data. CTD (Conductivity-Temperature-Depth) profiles were also obtained at all stations, allowing to evaluate the mixed layer depth. Most of the stations are situated along the north-south and east-west transects (along ~72°E and ~48.5°S), that cover the southern and eastern sides of the Plateau and the plume offshore (Fig. 1). Here we present measurements collected at the station A3 situated over the Plateau in the core of the southern bloom investigated during the first KEOPS survey, and which was revisited twice during the KEOPS2 survey and again during the following OISO cruises.

2.2. Air-sea CO_2 flux calculation

The net flux of CO_2 across the air-sea interface (FCO_2) was calculated according to the following equation:

$$FCO_2 = k \,.\, s \,.\, \Delta fCO_2 \quad (1)$$

k is the piston velocity evaluated as a function of wind speed (Wanninkhof, 1992), s is the solubility of CO_2 in seawater calculated from *in situ* temperature and salinity after Weiss (1974), and ΔfCO_2 is the difference between the fugacity of CO_2 in surface waters and in the marine air above (ΔfCO_2 = fCO_2sea - fCO_2air). Positive values of ΔfCO_2 indicate an outgassing of CO_2 to the atmosphere (CO_2 source), and negative values indicate an uptake of CO_2 by the ocean (CO_2 sink). We used the mean fCO_2air value of 388 µatm based on measurements obtained at ~15m above the sea surface during the KEOPS2 survey, and the mean temperature and salinity values of 3°C and 33.8, respectively. The mean CO_2 molar fraction xCO_2 measured onboard was 391.3±0.6 ppm during the survey around Kerguelen,

and 389.5±2 ppm between 25°S and 50°S. The latter compares well with the mean xCO_2 of 389.0±0.6 ppm measured in October/November 2011 at the nearest atmospheric monitoring station situated on Amsterdam Island at 77.5°E 38.3°S (M. Ramonet, pers. com.). We evaluated FCO_2 using either wind speed measurements made onboard or climatological monthly winds computed from QuikScat satellite data (Level 3 surface wind speed obtained from the Physical Oceanography Distributed Active Archive Center at the NASA Jet Propulsion Laboratory, Pasadena, CA, http://podaac.jpl.nasa.gov).

3. Results

3.1. Distribution of surface fCO_2 observed in October and November

The KEOPS2 survey started in October, when surface chlorophyll-a concentrations were still low in most of the studied area due to light limitation (Fig. 1a). As a consequence, surface fCO_2 was close to equilibrium with atmospheric CO_2 (388 µatm) or higher, with the exception of shallow coastal waters that acted as a large sink for atmospheric CO_2, with surface fCO_2 values as low as 300 µatm (Figs. 2a and 3a). South-east of Kerguelen Island, where the plateau deepens to more than 500m, we observed a large region of CO_2 outgassing (ΔfCO_2 around +20 µatm) associated with high surface salinity (Fig. 2e). High surface fCO_2 values are representative of winter conditions in the Southern Ocean when vertical mixing maintains high concentrations of TCO_2 in surface waters, therefore acting against the effect of cooling (e.g. Metzl et al. 2006). A smaller area of CO_2 outgassing was also observed on the warm side of the Polar Front (PF) zone before the onset of the bloom. On the contrary, surface fCO_2 measured in October on the cold side of (within) the PF meander was close to equilibrium with atmospheric CO_2.

Weekly satellite images of chlorophyll-a show an early phytoplankton bloom in the warm waters of the PF zone east of 73°E at end of October. It was rapidly followed by an increase in chlorophyll-a concentration in the cold waters over and downstream of the Plateau, such that early in November most of the study region acted as a sink for atmospheric CO_2, with surface fCO_2 values ranging from 275 µatm to 390 µatm. The minimum and maximum fCO_2 values were obtained in shallow waters (<500m). Very low fCO_2 values, down to 100 µatm below the atmospheric level, were also measured on the warm side of the PF zone (east of 73.5°E), whereas within the PF meander (71°E-73.5°E) the mean ΔfCO_2 was around -30

205 µatm. The region over the Plateau south of Kerguelen Island, that acted as a source of CO_2 in
206 October, also turned into a relatively large sink in November, with ΔfCO_2 values ranging
207 from -80 µatm to -30 µatm (Figs. 2a and 3a).
208
209 In order to identify the mechanisms responsible for the evolution of surface fCO_2 observed at
210 the onset of the phytoplankton bloom, we analyzed in more details the underway surface
211 measurements of fCO_2 and other relevant parameters collected in different regions of the
212 bloom. Below, we first present observations collected offshore (bathymetry >1000m)
213 downstream of the Kerguelen Plateau, a region referred to as the Plume, and which includes
214 the cold waters within the PF meander (71°E-73.5°E, hereafter the Middle zone), as well as
215 the warmer waters found in the PF zone (north of 47.4°S and east of 73.5°E). Next we present
216 observations collected over the Plateau (iron source) south of the PF (>49°5.S). We conclude
217 the section by discussing the mean air-sea CO_2 fluxes calculated in the different regions in
218 October and November.
219
220 *3.2. Evolution of surface fCO_2 in the Plume*
221 The survey downstream of the Kerguelen Plateau started on the 21st of October, when
222 chlorophyll-a concentrations were still low and surface fCO_2 was close to equilibrium with
223 atmospheric CO_2 (Figs. 1a and 2a, Table 1). Surface and water column measurements were
224 collected along the north-south transect at ~72°E, starting over the Plateau (station A3),
225 covering the western part of the Plume (north of 49.5°S), and crossing the Polar Front at his
226 northernmost position (47.4°S, Fig. 2). Surface fCO_2 measurements obtained in the Plume
227 show fluctuations around the equilibrium value with a maximum amplitude of 45 µatm (Fig.
228 3a). Because of low chlorophyll-a concentrations, surface fCO_2 is expected to vary with
229 temperature and mixing. It is clear from Fig. 3 that the high surface fCO_2 (small outgassing)
230 observed between 48°S and 49°S is related to high SST. However, less than half of the spatial
231 variability in surface fCO_2 can be explained by the effect of temperature alone (~15 µatm/°C
232 according to Takahashi et al., 1993). Consequently, more than half of the observed variability
233 is due to the higher TCO_2 concentrations measured in the area of CO_2 outgassing compared to
234 the surrounding surface waters, which must be explained by lateral and/or vertical mixing.
235 The rapid variations in SST observed within the PF meander reflect the re-circulation of
236 southern (cold) and northern (warm) surface waters (Park et al., 2014). However, since the
237 contribution of northern waters is expected to reduce surface TCO_2 concentrations in the

238 Plume compared to the cold southern waters, we conclude that lateral advection has a minor
239 impact on surface fCO_2 (due to the opposite effects of temperature and TCO_2). Instead, our
240 observations point to vertical mixing as the main driver for the observed spatial variations in
241 surface fCO_2. Indeed, the CO_2 outgassing observed between 48°S and 49°S is related to
242 relatively deep layers (80-110m), while the small uptake of CO_2 observed in the colder waters
243 around 49°S (Fig. 3) can be attributed to the combined effect of reduced mixing (60-70m) and
244 low but significant chlorophyll-a concentrations (Table 1).
245
246 The passage of the PF was marked by a rapid change in surface temperature from ~2.5°C to
247 3.9°C between 47.5°S and 47.4°S (Figs. 2 and 3). This resulted in a rapid increase in surface
248 fCO_2 from near-equilibrium values south of the PF (387±7 µatm) to a small source of CO_2
249 north of the PF (406±12 µatm), which can be explained by the temperature effect alone (+22
250 µatm). In the warm waters of the PF zone, we recorded the maximum fCO_2 value of 430 µatm
251 at 47.3°S, followed by a sudden decrease down to near-equilibrium, and a second fCO_2
252 maximum at 46.8°S (Fig. 3a). Such rapid changes in surface fCO_2 reflected the impact of
253 eddies associated with the frontal structure (Park et al., 2014).
254
255 The second visit of the Middle zone occurred 10 days later (Oct., 31 to Nov., 2) when both
256 surface and water column measurements were collected along the east-west transect along
257 ~48.5°S. At that time the whole region had turned into a small sink for atmospheric CO_2 of
258 the order of 10 to 20 µatm (Fig. 4a). This decrease in fCO_2 resulted from the opposite effects
259 of surface warming by ~0.7°C (+11 µatm) and a decrease in TCO_2 concentrations by ~10
260 µmol/kg (Table 1). The latter could partly be due to a small increase in chlorophyll-a
261 concentration observed over the 10-days period. Both the changes in TCO_2 and chlorophyll-a
262 concentrations are likely related to the reduction in vertical mixing revealed by reduced mixed
263 layer depths (40-90m) and a decrease in surface salinity (Table 1). We observed a larger CO_2
264 sink in the western (cold) part of the Plume (~20 µatm) compared to its eastern (warm) part
265 (~10 µatm), which is explained by both temperature and TCO_2 concentrations. The low
266 surface fCO_2 and TCO_2 measured in cold waters were associated with high surface salinity
267 and low $Si(OH)_4$ concentrations, which could reflect an increased biological activity in the
268 waters of southern origin (consistent with observations over the Plateau, see Sect. 3.3).
269

In the warm waters of the PF zone, the mixed layer was already relatively shallow at the end of October (<80m, Table 2). Ten days later it was less than 40m deep east of 73.5°E, and a large area of intense biological uptake of CO_2 was observed, with surface fCO_2 values as low as 290 µatm (Fig. 4a) and chlorophyll-a concentrations between 2 and 6 µg/l (Table 1). The reason for the early onset of an intense bloom in this area is not yet fully understood. One mechanism likely involved is the fast delivery of iron from the Plateau north of Kerguelen Island thanks to the strong jets associated with the frontal structure in this region (e.g., Lourantou and Metzl, 2011 ; Park et al., 2014), since we can expect that the amount of iron lost during the transit (due to biological and physical processes) is reduced. In the Middle region, the first important drawdown of fCO_2 (down to 350 µatm) was observed on the 3rd of November over a small area (72.8°E-73°E). Two days later, we measured a very similar CO_2 sink at the same latitude, but covering a larger area (72.9°E-73.4°E). This area was characterized by warmer SST (~3.5°C) than the surrounding waters (~3.0°C, Fig. 4), which may reflect reduced vertical mixing and/or the incursion of warm waters from the PF zone.

By the 8th of November most of the area investigated downstream of the Plateau acted as a moderate to large sink for atmospheric CO_2. In the Middle zone, the mean CO_2 sink was of the order of 30 µatm, and was associated with a doubling in chlorophyll-a concentrations since the last visit three days before (Table 1). The effect of enhanced photosynthesis on surface fCO_2 was partly compensated by a warming by ~0.3°C on the eastern part of the Middle zone (72.5°E-73.6°E). The concomitance of surface warming and increased biological uptake of CO_2 is attributed to reduced vertical mixing (<80m). In the eastern part of the Plume, surface fCO_2 remained low until the end of the survey, whereas large and rapid spatial variations were observed in surface fCO_2 measured in the western part (71°E-72.5°E, Fig. 4a). In the region between 72°E and 72.3°E, where temperature remained relatively low all through November (around 3°C), we observed an increase in surface fCO_2 to near-equilibrium with atmospheric CO_2 on the 10th of November, followed by the re-establishment of the CO_2 sink, and a second increase to near-equilibrium four days later. Similar changes in surface fCO_2 were observed west of 72°E, but the driving mechanisms were somewhat different. Indeed, the increase to near-equilibrium observed on the 18th of November was due to the combined effect of surface warming by ~0.5°C (delayed by ~10 days compared to the eastern part of the Plume) and reduced chlorophyll-a concentrations (Table 1).

303 Low fCO_2 values (down to 320 µatm) were measured at the end of November where the PF
304 reaches its northernmost position. These extreme values, however, were very localized. The
305 mean fCO_2 in the PF zone at the end of November was 360 µatm, with maximum values of
306 380 µatm.
307
308 *3.3. Evolution of surface CO_2 over the Kerguelen Plateau*
309 The southern part of the bloom, observed to the south-east of Kerguelen Island, where the
310 Plateau deepens to 500-1000m, was investigated in details during the first KEOPS cruise in
311 January-February 2005. These previous measurements, obtained during the declining phase of
312 the bloom, showed a core of maximum chlorophyll-a concentrations (>1 µg/l) between 50°S
313 and 51°S at ~72°E (station A3), associated with minimum surface fCO_2 values (58±11 µatm
314 lower than in the surrounding HNLC waters, Blain et al., 2007). This area was revisited three
315 times during the KEOPS2 survey (Table 1, Fig. 3).
316
317 In October, we measured high surface fCO_2 in the Plateau region (50°S-51°S, 70°E-72°E),
318 about 25 µatm above atmospheric CO_2, whereas in HNLC waters upstream of the Plateau,
319 surface fCO_2 was near-equilibrium (Fig. 2a, Table 1). The CO_2 outgassing observed over the
320 Plateau is clearly related to the deep mixing observed in this area (MLD >140m, Fig. 2)
321 compared to HNLC waters upstream (Table 2), leading to higher TCO_2 and nutrients
322 concentrations over the Plateau (Table 1). Surface temperature was slightly lower over the
323 Plateau than in the waters upstream, and chlorophyll-a concentration was slightly higher. This
324 suggests that both temperature and primary production partly compensate for mixing with the
325 CO_2-rich subsurface waters.
326
327 The combined effect of vertical mixing, temperature and photosynthesis on surface fCO_2 was
328 also observed between the first visit over the Plateau on the 18th of October and the second
329 visit on the following day, when the mean surface fCO_2 was reduced by 13 µatm and surface
330 waters were cooler by ~0.2°C (Fig. 3, Table 1). Sea surface cooling likely resulted from the
331 low air temperature, combined with reduced vertical mixing, as suggested by water column
332 measurements collected on the 20th of October that showed an increase in temperature from
333 the surface to the base of the mixed layer (by ~0.4°C, Fig. 5). According to Takahashi et al.
334 (1993), the temperature effect explains about 25% of the sudden decrease in surface fCO_2.
335 The remaining 75% is attributed to enhanced photosynthesis. Indeed, water column

336 measurements revealed that TCO_2 concentrations were about 15 µmol/kg lower at the surface
337 than in the Winter Water layer found between 175m and 200m (subsurface temperature
338 minimum, Fig. 5). This signal supports the idea that the biological pump of CO_2 was already
339 active at the end of October, despite the deep mixed layer. This is further supported by a small
340 increase in surface chlorophyll-a concentrations observed between the 18th and the 21st of
341 October (Table 1), which may hide a larger increase in subsurface waters (chlorophyll
342 maximum).
343
344 Surface measurements were collected three weeks later (Nov., 8-9) in the northern part of the
345 Plateau region (49.5°S-50°S, Fig. 3, Table 1). SST was higher than during the first visit
346 (+0.5°C) due to warming in the atmosphere, and SSS was slightly lower, both suggesting
347 reduced vertical mixing. Surface fCO_2 decreased by ~90 µatm over the 3-weeks period, in
348 response to an increase in chlorophyll-a concentrations by a factor 10 (>2 µg/l) and possibly
349 reduced mixing with subsurface waters. This resulted in a strong CO_2 sink (~60 µatm) and
350 minimum values in surface TCO_2 and nutrients. At this time, when the bloom was growing,
351 surface chlorophyll-a concentrations were twice as large over the Plateau than in the Plume
352 offshore, and the CO_2 sink was twice as strong.
353
354 One week later (Nov., 15-17), the last visit over the Plateau revealed an increase in surface
355 fCO_2 by ~25 µatm and reduced spatial variability (Fig. 3a), associated with sea surface
356 cooling and mixed layers as deep as during the first occupation in October (~150m, Table 2).
357 The salinity profile was also very similar, while temperature increased by ~0.5°C in the mixed
358 layer due to warming in the atmosphere (Fig. 5). The concentration in chlorophyll-a was quite
359 homogeneous in the mixed layer, reflecting an effective mixing at the time of observation.
360 This is supported by strong winds measured on the 15th of November (15-20 m/s), and a rapid
361 slow down on the following day (~10 m/s). Our observations suggest that this short event of
362 strong winds induced an increase in surface fCO_2 of the order of 30 µatm, followed by a
363 decrease of about 10 µatm when winds are reduced (although SST increased by ~0.2°C).
364 Despite this deep mixing event, the Plateau region acted as a substantial sink for atmospheric
365 CO_2, relatively steady at the end of the survey (39±6 µatm), whereas in the Plume
366 downstream of the Plateau, we observed large and rapid spatial and temporal variations in
367 surface fCO_2 resulting in a moderate CO_2 sink at the end of the survey (26±10 µatm).
368

3.4. Mean air-sea CO_2 fluxes in and out of Kerguelen's bloom

Air-sea CO_2 fluxes were generally small in October (Table 2). The largest flux was an outgassing of CO_2 observed over the Plateau south of Kerguelen Island, which we attributed to deep mixing (140-180m). Based on our observations, we can expect substantial variations in air-sea CO_2 fluxes in this region due to rapid changes in winds and the subsequent stratification/destratification of the upper ocean. In the HNLC region upstream of the Plateau, we calculated a mean CO_2 flux close to zero, associated with shallower mixed layer (80-150m). In the Middle zone, where the mixed layer was even shallower (60-110m), the mean CO_2 flux was also close to zero before the onset of the bloom. This resulted from the combined effects of lateral and vertical mixing on SST and TCO_2 leading to a small outgassing of CO_2 in the warm waters, and low but significant biological activity that induced a small CO_2 sink in the cold waters of southern origin. In the PF zone, north of the plume, we estimated a small outgassing of CO_2 at the end of October, mainly explained by the temperature effect (warm waters). In shallow waters (<500m), our observations indicate a mean air-sea CO_2 flux close to zero in October, mostly due to small ΔfCO_2 values and the combination of CO_2 source (salty waters) and CO_2 sink areas. In the few places where we measured low fCO_2, notably inside the Morbihan Gulf (SSS< 33.5, Figure 2), the uptake of CO_2 was of the order of 30 mmolC/m^2/day for observed winds around 15 m/s.

In November, the fertilized region over and downstream of the Plateau was globally a large sink for atmospheric CO_2, as can be expected from chlorophyll-a concentrations (Fig. 1). The largest uptake of atmospheric CO_2 was observed in the PF zone (~20 mmolC/m^2/day) and was associated with maximum chlorophyll-a concentrations (Table 1). The mean CO_2 uptake estimated over the Plateau was twice as low than in the PF zone, but slighlty larger than in the Middle zone (Table 2). However, the mean fCO_2 drawdown observed from October to November was three times larger over the Plateau (60 µatm) than in the Middle zone (20 µatm). We do not have observation in the PF zone east of 73.5°E before the onset of the bloom, but we can expect that surface fCO_2 was close to equilibrium with atmospheric CO_2 (similarly as what we observed in the PF zone north-east of Kerguelen Island and in the eastern part of the Middle zone). This would give a mean fCO_2 drawdown around 80 µatm, i.e., four times larger than in the Middle zone.

In shallow waters (bathymetry <500m), air-sea CO_2 fluxes were highly variable in November due to the large variability in surface fCO_2. In coastal waters, the mean CO_2 uptake was as large as in the PF zone (~20 mmolC/m^2/day).

4. Discussion

Observations collected during the KEOPS2/OISO20 cruise have revealed differences in the mechanisms that control air-sea CO_2 fluxes in different regions of Kerguelen's phytoplankton bloom. Over the southern Plateau, south of the PF, we observed rapid changes in surface fCO_2 due to changes in vertical mixing, both at the end of winter and during the productive season when strong winds events destratified the water column. Spatial variability, on the contrary, was reduced over the Plateau compared to the Middle zone. Due to the PF meander, the Middle zone could be seen as an incursion northward of cold waters enriched with TCO_2 and nutrients. The analysis of CTD, drifter and satellite data indeed suggests that cold waters are advected from the Plateau south of Kerguelen Island to the western (cold) part of the Middle region following the path of the PF (Park et al., 2014). North-East of Kerguelen Island, the PF meets the strong jets associated with the Subantarctic Front and turns eastward then southward. This allows mixing between warm waters enriched with iron (from their passage over the Plateau north of Kerguelen) and cold southern waters transported northward along the PF. The analysis of satellite data showed that the cold waters then get trapped in the cyclonic eddy observed around 72°E between 48°S and 48.5°S. This structure is characterized by a minimum in chlorophyll-a concentration within the bloom (Fig. 1b) and relatively low iron concentrations (Quéroué et al., 2014). The latter can be explained by the two circulation characteristics mentioned above: firstly the Middle region receive an inflow of HNLC waters from the passage in between the Kerguelen and Heard plateaus, and therefore not enriched by the iron sources located on shallow regions; secondly, part of the iron rich waters coming from the Plateau stagnates in the Middle zone for long times (~30 days or longer) so that their originally high iron content is depleted by biotic and abiotic scavenging mechanisms. On the contrary, the rapid transport of the waters from the Plateau North of Kerguelen, along the PF, allows for a larger input of iron in the northern and eastern parts of the Plume. This circulation pattern resulted in large spatial gradients in the Plume for most surface properties, including temperature and chlorophyll-a, hence fCO_2.

433 Due to light limitation, primary production was generally low in October despite the
434 availability of nutrients, including iron over and downstream of the Plateau (Quéroué et al.,
435 2014). Consequently, surface fCO_2 was mainly controlled by temperature and mixing. Figure
436 6a shows the relationship between surface fCO_2 and temperature. In October we observed
437 similar surface fCO_2 values in the cold waters over the Plateau and in the warmest waters
438 found in the PF zone to the north. Given the mean temperature difference, one could expect
439 surface fCO_2 to be 30 µatm lower over the Plateau. This highlights the important contribution
440 of vertical mixing in the control of winter air-sea CO_2 fluxes. During the transport of cold
441 waters from the Plateau to the Middle zone, surface fCO_2 is reduced because of reduced
442 vertical mixing and low primary production. Surface fCO_2 is also slightly reduced when the
443 warm waters of the PF zone are injected in the Middle zone (cooling effect). It follows that
444 surface fCO_2 was lower in the Middle zone than over the Plateau or in the PF zone, which
445 illustrates the important role of re-circulation within the PF meander to generate a small
446 uptake of atmospheric CO_2 at the end of winter.
447
448 Our observations suggest that the start of the CO_2 sink largely depends on vertical mixing due
449 to both light limitation and mixing with subsurface waters The stratification of the water
450 column occurred between the end of October and the beginning of November. Over the
451 Plateau, this first resulted in sea surface cooling (due to low air temperature) and a decrease in
452 surface fCO_2 by ~13 µatm due to the combined effects of cooling, reduced vertical mixing
453 and photosynthesis. In the cold waters of the Middle zone, stratification was associated with
454 sea surface warming, whose effect on surface fCO_2 (+10 µatm) played against the impact of
455 reduced vertical mixing and photosynthesis, resulting in a small decrease in surface fCO_2 (by
456 ~10 µatm), whereas in the warm waters of the Middle zone, SST did not change much, and
457 surface fCO_2 was thus reduced by ~20 µatm.
458
459 As soon as the mixed layer was reduced, we observed a significant increase in chlorophyll-a
460 concentrations over and downstream of the Plateau. The biological control on air-sea CO_2
461 fluxes can be appreciated through the relationship observed between surface fCO_2 and
462 chlorophyll-a concentrations, showing a good anti-correlation (both spatially and temporally)
463 as soon as the bloom started to grow (Fig. 6b). We found differences in the magnitude of the
464 CO_2 uptake in different regions of the bloom, which we attributed to biological activity and
465 the availability of iron (small temperature effect). In the Middle zone (steady CO_2 sink of the

466 order of -15 µatm at the end of winter), the onset of the bloom resulted in a mean fCO_2
467 drawdown of ~30 µatm in the eastern (warm) part and ~20 µatm in the western (cold) part.
468 The latter was characterized by lower iron and chlorophyll-a concentrations (hence higher
469 surface fCO_2) and rapid spatial and temporal variations in most surface properties due to
470 movements of the cyclonic eddy observed around 72°E. The strongest CO_2 sink was observed
471 in the PF zone east of Kerguelen Plateau, where the early stratification of the water colum
472 (probably at the end of October) led to an early and strong bloom. Assuming that surface
473 fCO_2 was near equilibrium before the onset of the bloom, we estimated a mean fCO_2
474 drawdown of 80 µatm for chlorophyll-a concentrations exceeding 2 µg/l (Fig. 6b), and
475 attributed this large biological signal to the fast delivery of iron from the Plateau north of
476 Kerguelen (strong jets). Our results thus suggest that once the ocean is stratified, the main
477 mechanism controlling the magnitude of the CO_2 sink in the Plume offshore is lateral
478 transport (pathway and speed).
479
480 Over the Plateau to the south, we observed a mean fCO_2 drawdown around 60 µatm in
481 response to the onset of the bloom for chlorophyll-a concentrations between 2 and 3 µg/l (Fig.
482 6b). Correcting for the increase in temperature that occurred after the stratification of the
483 water column gives a mean biological signal around 70 µatm. This number, obtained above
484 the iron source, is fairly close to the biological signal estimated in the PF zone east of
485 Kerguelen, two regions where iron was largely available at the beginning of the growing
486 season (Quéroué et al., 2014). However, observations obtained at the end of the survey
487 showed that the magnitude of the CO_2 sink over the Plateau can be substantially reduced (by
488 ~25 µatm) when the mixed layer deepens due to increased surface TCO_2 concentrations
489 (slightly counterbalanced by sea surface cooling). It is not clear whether reduced
490 photosynthesis (light limitation) also contributed to enhance surface TCO_2 because
491 chlorophyll-a concentration remained high (Fig. 6b). These results suggest that changes in
492 winds and the following stratification/destratification of the upper ocean is another important
493 factor (in addition to iron availability) in the control of air-sea CO_2 fluxes over the Plateau
494 (south of the PF).
495
496 As discussed before, the onset of the CO_2 sink associated with Kerguelen's blooms seems to
497 depend essentially on vertical mixing. The rapid fCO_2 drawdown observed early in November
498 (as soon as surface waters became isolated from the deep ocean) was clearly related to a

499 decrease in surface TCO_2 and nutrients concentrations due to both biological consumption in
500 the upper layer and limited exchanges with the underlying deep reservoir. For this reason, we
501 observed good relationships between surface fCO_2 and the concentrations of major nutrients
502 (Figure 6c,d, Table 1). The largest reduction in surface nutrients was observed in the warm
503 waters of the PF zone and over the Plateau to the south, where the biological uptake of CO_2
504 was the largest. At the end of the survey, nitrate concentrations were still relatively high in all
505 the regions investigated here (20-25 µmol/kg), whereas silicic acid ($Si(OH)_4$) concentrations
506 were of the order of 10 µmol/kg, with the exception of the Plateau region where the
507 deepening of the mixed layer refilled surface waters with nutrients (Table 1). In the course of
508 the growing season, it is thus likely that $Si(OH)_4$ becomes rapidly depleted in the warm waters
509 of the Plume, whereas $Si(OH)_4$ limitation is probably delayed in the cold waters over the
510 Plateau thanks to higher winter concentrations and deep mixing events during summer. This
511 hypothesis was supported by underway measurements collected three months later along the
512 same east-west transect revisited during the next OISO cruise, and again one year later during
513 the OISO22 cruise (Feb. 2013). These re-occupations conducted later in the productive season
514 showed a large reduction in chlorophyll-a concentrations in the Plume offshore, which we
515 attribute to the reduction in $Si(OH)_4$ concentrations. Indeed, maximum chlorophyll-a
516 concentrations (~1 µg/l) were observed in the cold waters transported northward along the PF
517 (~71°E) where $Si(OH)_4$ concentrations were the highest (~7 µmol/kg), whereas in the Plume
518 to the east (71.6°E-83°E) chlorophyll-a and $Si(OH)_4$ concentrations did not exceed 0.2 µg/l
519 and 2 µmol/kg respectively.
520
521 Our results show that the magnitude of the CO_2 sink at the start of the productive season
522 mostly depends on iron availability. Because the Plateau is a source of iron, we estimated that
523 the biological drawdown of CO_2 was three times larger there than in the Middle (re-
524 circulation) zone. As nutrients are consumed during the growing season, we propose that
525 $Si(OH)_4$ eventually becomes depleted, thus replacing iron as limiting factor in regions where
526 the upper ocean remains isolated from the underlying deep waters. Based on our observations,
527 and assuming a delayed $Si(OH)_4$ depletion in cold waters, one might expect that the uptake of
528 CO_2 integrated over the whole productive season would be larger over the southern Plateau
529 than in the Plume advected east of Kerguelen. In order to investigate this issue, we used the
530 SOCAT database to draw the seasonal evolution of air-sea CO_2 fluxes in the different regions
531 of the bloom (Fig. 7). Surprisingly, the CO_2 uptake integrated from October to March was

similar over the Plateau and in the Middle zone (~1 molC/m^2, Table 3), despite the large difference in the biological signal observed at the start of the productive season. The CO_2 sink generally starts earlier in the Plume offshore (in October) than over the Plateau to the south (early in November, with only a few exception, for example in 2005 when a small CO_2 sink was observed in October over the Plateau). The strongest CO_2 uptake in the whole dataset is found in the PF zone at the onset of the bloom. However, observations obtained later in the season suggest that the CO_2 sink is rapidly reduced by half, likely due to iron and/or $Si(OH)_4$ depletion. In the Middle zone and over the Plateau to the south, the decline of the CO_2 sink is delayed by one or two months, likely due to the delayed nutrients depletion that can be explained by a lower biological consumption in the Middle zone and the refill of surface waters during deep mixing events over the Plateau. The data collected during the declining phase of the bloom (from January to March) show a faster decrease in the CO_2 uptake over the Plateau than in the Middle zone, which can be explained by vertical mixing, similarly as for the onset of the CO_2 sink in October/November.

In contrast to the bloom region, air-sea CO_2 fluxes show no clear seasonal cycle in HNLC waters (Fig. 7). The mean flux calculated in January agrees well with the value of -1.1 mmolC/m^2/day estimated by Metzl et al. (2006) based on data collected upstream of the Kerguelen Plateau (~65°E, 50°S-58°S). In August, they reported a small CO_2 outgasing in this region (+2.5 mmolC/m^2/day), whereas we estimated a small CO_2 sink. Consequently, their estimate of the annual CO_2 uptake (0.5 mmolC/m^2) is lower than ours (0.8 mmolC/m^2).

5. Conclusions

The KEOPS2/OISO20 cruise allowed to monitor the establishment of the CO_2 sink associated with Kerguelen phytoplankton bloom, and to investigate the mechanisms that control air-sea CO_2 fluxes at the start of the productive season. Observations obtained in October support the idea that winter deep mixing plays a key role in limiting the uptake of atmospheric CO_2 in the Southern Ocean, both because of light limitation and mixing with the CO_2-rich subsurface waters. We found that the temperature effect on fCO_2 is generally small south of the PF, while in the PF zone, reduced mixing at the end of winter is associated with sea surface warming that would maintain high surface fCO_2 if primary production did not increase. Stratification of the upper ocean marks the start of the growing season and is rapidly followed by the

564 establishment of a strong CO_2 sink over and dowstream the Kerguelen Plateau. Our results
565 show that the magnitude of the CO_2 sink at the start of the productive season is closely related
566 to chlorophyll-a concentration and iron availability. In the Plume, iron availability strongly
567 depends on lateral advection that transports iron from the remote sources: either from north of
568 the island to the eastern part of the Plume (fast delivery due to the strong jets), or from the
569 south to the western part of the Plume (mixing with HNLC waters, re-circulation). Lateral
570 transport is thus identifed as the main mechanism explaining the moderate uptake of
571 atmospheric CO_2 observed in the Plume in November. Over the Plateau (iron source), we
572 observed a larger and spatially more homogeneous CO_2 sink. Nevertheless, we also observed
573 an episode of deep mixing (~150m) over the Plateau after the onset of the bloom, which
574 resulted in a substantial reduction in the uptake of atmospheric CO_2 due to increased surface
575 TCO_2 concentrations. Such episodic destratification of the water column could explain why
576 the uptake of CO_2 integrated over the productive season was similar over the Plateau and in
577 the Plume offshore, despite the delayed depletion in $Si(OH)_4$ and iron over the Plateau. Using
578 all available information, we estimated an uptake of CO_2 between 1 and 1.5 molC/m^2 in the
579 bloom area when integrated over the productive season (October to March), which is between
580 2.5 and 4 times larger than value estimated in HNLC waters. Extrapolating our results to the
581 whole Permanent Open Ocean Zone between 50°S and 60°S (~ 9.10^6 km^2, Metzl et al., 2006)
582 suggests that if this region was fertilized with iron in the same manner as what we observed
583 around Kerguelen, the annual uptake of atmospheric CO_2 would increase by less than 0.1 Pg
584 of carbon. We thus conclude that although iron fertilization in the Southern Ocean rapidly
585 activates the biological uptake of CO_2, its impact on the global carbon budget is very likely
586 negligible compared to the 10 Pg of anthropogenic carbon released every year to the
587 atmosphere (Le Quéré et al., 2014).
588

589 ***Acknowledgements***

590 We thank S. Blain, project leader, and B. Quéguiner, chief scientist, as well as the captain and
591 crew of *R.R.V. Marion Dufresne* and the staff at the French Polar Institute (IPEV) for their
592 important contribution to the success of the cruise. We are also very grateful to all technicians
593 and scientists who helped to obtain and interpret our data, in particular J. Capparos, L.
594 Chirurgien, C. De La Vega, I. Durand, A. Guéneuguès, F. Kaczmar, D. Lefevre, L. Merlivat,
595 L. Oriol, and F. Perrault. The KEOPS2 project was funded by the French institutes INSU

596 (Institut National des Sciences de l'Univers), IPEV (Institut Paul Emile Victor) and ANR
597 (Agence Nationale de la Recherche). The OISO program is supported by the French institutes
598 INSU, IPEV and IPSL (Institut Pierre Simon Laplace), and the European project
599 FP7/CARBOCHANGE (grant 264879).
600

601 ## *References*

602 Bakker, D.C.E., M.C. Nielsdottir, P.J. Morris, H.J. Venables, and A.J. Watson, (2007), The
603 island mass effect and biological carbon uptake for the subantarctic Crozet Archipelago,
604 *Deep-Sea Research II 54*, 2174-2190.

605 Bakker, D. C. E., et al. (2014), An update to the Surface Ocean CO_2 Atlas (SOCAT version
606 2), *Earth Syst. Sci. Data, 6*, 69-90, doi:10.5194/essd-6-69-2014, 2014.

607 Blain, S., et al., (2007), Effect of natural iron fertilization on carbon sequestration in the
608 Southern Ocean, *Nature 446*, 1070-1074, doi:10.1038/nature05700.

609 S. Blain, S., J. Capparos, A. Guéneuguès, I. Obernosterer, and L. Oriol (2014). Distributions
610 and stoichiometry of dissolved nitrogen and phosphorus in the iron fertilized region near
611 Kerguelen (Southern Ocean) . *Biogeosciences Discuss., 11*, 9949-9977.

612 Boyd, P. W., et al., (2007), Mesoscale iron enrichment experiments 1993-2005: Synthesis and
613 future directions, *Science, 315*, 612–617, doi:10.1126/science.1131669.

614 Jabaud-Jan A., N. Metzl, C. Brunet, A. Poisson and B. Schauer, 2004. Variability of the
615 Carbon Dioxide System in the Southern Indian Ocean (20°S-60°S): the impact of a warm
616 anomaly in austral summer 1998. *Global Biogeochem. Cycles, 18 (1)*, GB1042,
617 doi:10.1029/2002GB002017.

618 Jouandet, M.P., Blain, S., Metzl, N., Brunet, C., Trull, T.W., and Obernosterer, I., 2008. A
619 seasonal carbon budget for a naturally iron-fertilized bloom over the Kerguelen Plateau in
620 the Southern Ocean, *Deep-Sea Res. II, 55*, 856–867, doi:10.1016/j.dsr2.2007.12.037.

621 Le Quéré, C., et al., (2014), Global Carbon Budget 2013, Earth Syst. Sci. Data, 6, 235-263.

622 Lenton, A., et al. (2013), Sea-air CO_2 fluxes in the Southern Ocean for the period 1990-2009,
623 *Biogeosciences, 10*, 4037-4054, doi:10.5194/bg-10-4037-2013.

624 Lourantou, A., and N. Metzl, (2011). Decadal evolution of carbon sink within a strong bloom
625 area in the subantarctic zone. *Geophys. Res. Lett., 38*, L23608, doi:10.1029/2011GL049614.

626 Martin, J. H., R. M. Gordon, and S. E. Fitzwater (1990), Iron in Antarctic waters, *Nature, 345*,
627 156–158.

628 Metzl, N., A.Poisson, F. Louanchi, C. Brunet, B. Schauer, B. Brès, 1995. Spatio-temporal
629 distributions of air-sea fluxes of CO_2 in the Indian and Antarctic Oceans: a first step. *Tellus*,
630 *47B*, 56-69.

631 Metzl, N., B.Tilbrook and A. Poisson, 1999. The annual fCO_2 cycle and the air-sea CO_2 flux
632 in the sub-Antarctic Ocean. *Tellus, 51B*, 4, 849-861.

633 Metzl, N., C. Brunet, A. Jabaud-Jan, A. Poisson, and B. Schauer (2006). Summer and winter
634 air-sea CO_2 fluxes in the Southern Ocean. *Deep-Sea Research I, 53*, 1548-1563, doi:
635 10.1016/j.dsr.2006.07.006.

636 Metzl, N., (2009). Decadal increase of oceanic carbon dioxide in Southern Indian Ocean
637 surface waters (1991–2007). *Deep-Sea Res. II, 56*, 607–619.

638 Mongin, M., Molina, E., and Trull, T. W., (2008). Seasonality and scale of the Kerguelen
639 plateau phytoplankton bloom: A remote sensing and modeling analysis of the influence of
640 natural iron fertilization in the Southern Ocean, *Deep-Sea Res. II, 55*, 880–892,
641 doi:10.1016/j.dsr2.2007.12.039.

642 Neveux, J., and F. Lantoine, (1993). Spectrofluorometric assay of chlorophylls and
643 phaeopigments using the least squares approximation technique, *Deep-Sea Res. I, 40(9)*,
644 1747-1765, 1993.

645 Park, Y.-H., I. Durand, E. Kestenare, G. Rougier, M. Zhou, F. d'Ovidio, C. Cotté, and J.-H.
646 Lee (2014). Polar Front around the Kerguelen Islands: An up-to-date determination and
647 associated circulation of surface/subsurface waters, J. Geophys. Res. Oceans, 119,
648 doi:10.1002/2014JC010061.

649 Poisson, A., N. Metzl, C. Brunet, B. Schauer, B. Brès, D. Ruiz-Pino and F. Louanchi, 1993.
650 Variability of sources and sinks of CO_2 and in the western Indian and Southern Oceans
651 during the year 1991. *J. Geophys. Res., 98 (C12)*, 22759-22778.

652 Quéroué, F., G. Sarthou, F. Chever, P. van der Merwe, D. Lannuzel, A. Townsend, E.
653 Bucciarelli, H. Planquette, M. Cheize, S. Blain, F. D'Ovidio, and A. Bowie (2014). A new

study of natural Fe fertilization processes in the vicinity of the Kerguelen Islands (KEOPS2 experiment). *Biogeosciences Discuss*.

Schlitzer, R., (2014), Ocean Data View, http://odv.awi.de.

Tagliabue, A., Mtshali, T., Aumont, O., Bowie, A. R., Klunder, M. B., Roychoudhury, A. N., and Swart, S., (2012). A global compilation dissolved iron measurements: focus on distributions and processes in the Southern Ocean. *Biogeosciences, 9*, 2333-2349, doi:10.5194/bg-9-2333-2012.

Takahashi, T., Olafsson, J., Goddard, J., Chipman, D.W., and Sutherland, S.C., (1993). Seasonal variation of CO_2 and nutrients in the high-latitude surface oceans: a comparative study. *Global Biogeochem. Cycles, 7*, 843–878.

Takahashi, T. et al. (2009). Climatological mean and decadal change in surface ocean pCO_2, and net sea-air CO_2 flux over the global oceans. *Deep-Sea Res. II, 56*, 554-577. doi:10.1016/j.dsr2.2008.12.009.

Wanninkhof, R. (1992), Relationship between wind speed and gas exchange over the ocean, J. *Geophys. Res., 97(C5)*, 7373–7382, doi:10.1029/92JC00188.

Weiss, R. F. (1974), Carbon dioxide in water and seawater: The solubility of a non-ideal gas, *Mar. Chem., 2*, 203–215, doi:10.1016/0304-4203(74)90015-2.

672 ## *Tables*

673 Table 1 : Mean and standard deviation of surface measurements in October-November 2011.

	Lon. (°E) range	Lat. (°S) range	fCO_2 µatm	SST °C	SSS	Chla µg/l	TCO_2 µmol/kg	Alk µmol/kg	Nitrate µmol/kg	$Si(OH)_4$ µmol/kg
Upstream (HNLC)										
Oct., 17-18	64.1-69.9	49.8-50.7	393±7	2.2±0.3	33.72±0.10	0.1±0.1	2137±4	2287±7	26.6±0.7	12.8±2.3
Oct., 25-27	66.5-68.6	50.1-50.4	380±11	2.2±0.1	33.74±0.01	0.2±0.0	2139±3	2279±6	25.3±0.5	13.0±0.9
Plateau (500-1000m)										
Oct., 18	69.9-72.1	50.0-50.7	412±6	2.1±0.2	33.85±0.01	0.2±0.1	2147±8	2284±2	29.0±0.2	22.6±0.4
Oct., 19-21	71.0-72.2	50.0-50.6	399±5	1.9±0.2	33.86±0.01	0.3±0.1	2156±7	2294±7	27.8±0.6	22.7±0.4
Nov., 8-9	71.6-72.2	49.7-49.9	322±7	2.5±0.1	33.84±0.01	2.4[a]	2121[a]	2289[a]	22.5±0.2	9.7±0.3
Nov., 15-17	71.8-72.2	49.6-50.7	349±6	2.3±0.1	33.87±0.01	2.3±0.7	2137±2	2295±5	24.9±0.8	15.3±2.4
Middle zone										
Oct., 21-22	72.0-72.3	48.1-49.9	387±7	2.4±0.3	33.82±0.02	0.3±0.1	2145±6	2288±8	26.1±0.8	16.6±1.0
Oct, 31-Nov, 2	71.4-73.5	48.5-48.7	371±7	3.1±0.2	33.81±0.01	0.4±0.1	2136±7	2282±2	25.5±0.8	14.6±0.7
Nov., 3-5	71.8-73.7	48.6-48.7	372±8	3.0±0.1	33.80±0.01	0.5±0.2	2134±1	2289±2	25.1±0.1	14.5±0.3
Nov., 8	72.3-73.7	48.7-49.6	347±8	3.3±0.2	33.78±0.01	1.3[a]	2127[a]	2298[a]	23.4[a]	11.8[a]
Nov., 10-14	71.4-72.6	48.7-49.0	357±10	3.0±0.3	33.82±0.03	1.4±0.5	2136±9	2294±5	24.5±0.5	12.4±3.5
Nov., 18-20	71.4-72.9	48.4-48.9	362±10	3.4±0.1	33.79±0.01	1.0±0.5	2130±6	2288±4	23.0±0.4	8.9±0.4
PF zone										
Oct., 23	71.5-71.7	46.8-47.4	406±12	4.0±0.2	33.66±0.02	0.5[b]	2123[a]	2271[a]	23.2[a]	7.3[a]
Nov., 2-3	73.6-75.0	48.5-48.5	319±23	4.2±0.2	33.73±0.01	2.4±0.5	2091±7	2277±3	18.4±0.1	5.9±0.2
Nov., 5-8	73.8-74.9	48.5-48.6	309±11	4.2±0.2	33.71±0.01	3.9±1.5	2100±11	2288±9	19.4±0.4	8.6±1.3
Nov., 21	69.4-69.6	46.8-47.2	363±19	4.6±0.1	33.66±0.00	0.4[a]	2121[a]	2283[a]	22.9[a]	11.1[a]
Shallow Plateau (<500m)										
Oct., 18-19[c]	70.2-71.1	49.5-50.0	401±27	2.4±0.3	33.75±0.17	0.1[a]	2143[a]	2303[a]	27.6[a]	18.9[a]
Oct., 23	71.7-71.9	47.3-47.8	393±15	2.9±0.7	33.77±0.09	0.6[b]	2140±10	2278±9	25.8±0.5	16.4±2.1
Oct., 23-25	68.6-71.7	47.2-50.1	389±7	2.4±0.6	33.77±0.06	0.5±0.4	2140±6	2291±9	25.8±0.5	16.6±2.2
Oct., 31	66.6-71.1	48.8-50.2	388±8	2.9±0.4	33.75±0.10	0.3±0.1	2147±4	2285±5	24.5±1.4	14.4±3.4
Nov., 9[c]	70.6-71.5	48.9-49.6	346±32	3.1±0.4	33.70±0.11	1.3±0.6	2129±7	2297±7	24.3±2.4	16.7±4.6
Nov., 20-21[c]	69.6-71.3	47.3-49.5	360±32	3.5±0.5	33.66±0.09	1.2[a]	2134±5	2286±7	19.7[a]	8.9[a]

674 [a]only one measurement available; [b]calibrated fluorescence; [c]includes coastal waters

675

676 Table 2: Mean ΔfCO_2 (sea – air), wind speed, air-sea CO_2 fluxes and range of the mixed layer
677 depth (MLD) observed in October and November 2011 around Kerguelen.

	Month	ΔfCO_2 (µatm)	Wind speed (m/s)	CO_2 flux (mmol/m^2/d) obs.wind[(a)]	CO_2 flux (mmol/m^2/d) clim.wind[(a)]	MLD range (m)
Upstream (HNLC)	Oct.	-3±12	7±4	-0.3	-0.8	80-150
Plateau (500-1000m)	Oct.	17±9	14±3	+7.2	+4.8	140-180
Plateau (500-1000m)	Nov.	-44±13	10±4	-9.5	-12.4	40-170
Middle zone	Oct.	-7±11	11±4	-1.8	-2.1	60-110
Middle zone	Nov.	-27±11	13±4	-9.6	-7.4	20-90
PF zone (~47°S)	Oct.	18±12	4±1	+0.7	+4.9	40-80
PF zone (>73.5°E)	Nov.	-77±23	11±5	-17.9	-21.2	20-40
Shallow Plateau (<500m)	Oct.	4±15	9±5	+0.7	+1.0	20-40
Shallow Plateau (<500m)	Nov.	-33±33	17±3	-19.3	-9.2	25

678 [(a)]CO_2 fluxes are calculated using either observed winds or the climatological value of 11.5 m/s.
679

680 Table 3: Climatological wind speed and air-sea CO_2 fluxes

	Winds (m/s)	Air-sea CO_2 fluxes (monthly means in mmolC/m^2/day)			
		HNLC (0-160°E)	Plateau	Middle zone	PF zone
August	12.5±1.1	-0.7±3.0	6.3±2.6	N.D.[(a)]	2.8±3.2
September	12.1±0.5	-2.1±2.1	5.4±3.1	3.1±1.0	4.4±2.4
October	11.5±0.7	-2.2±2.5	3.5±2.9	-0.3±2.0	-0.3±2.9
November	10.8±0.8	-2.2±1.2	-9.5±1.5	-7.2±4.5	-18.7±3.6
December	10.2±0.9	-2.8±2.4	N.D.[(a)]	-10[(b)]	-8±5.7
January	10.6±0.8	-2.3±2.8	-12±5.4	-8.8±2.1	-7.9±5.6
February	10.3±0.7	-1.3±2.6	-7.9±5.2	-7.5±3.3	-8.6±5.8
March	10.6±0.7	-2.1±1.6	3.0±2.9	-2.6±0.7	N.D.[(a)]
April	11.2±0.8	-4.1±2.8	N.D.[(a)]	N.D.[(a)]	-8±2.8
May	11.8±1.0	-4.0±2.3	N.D.[(a)]	N.D.[(a)]	-0.7±1.3
June	11.3±1.2	-0.8±0.5	N.D.[(a)]	N.D.[(a)]	1.4±0.9
July	12.3±0.7	-1.6±1.3	N.D.[(a)]	N.D.[(a)]	-0.9±3
		Integrated air-sea CO_2 fluxes (mmolC/m^2)			
October to March		-394	-1008[(c)]	-1095	-1550[(d)]
Annual uptake		-798			-1581[(d)]

681 [(a)]No Data; [(b)]calculated from CARIOCA buoy fCO_2 data; [(c)]calculated assuming a mean flux
682 of -10.7 mmolC/m^2/day in December; [(d)]calculated assuming a mean flux of -8.3
683 mmolC/m^2/day in March.

684

685

Figure captions

Figure 1: Satellite images of chlorophyll-a (µg/l) for a) October 2011 and b) November 2011 (MODIS, monthly mean). Dotted lines indicates the cruise track (the triangle locates station A3). The dashed line shows the mean position of the Polar Front (from Park et al., 2014).

Figure 2: Underway surface measurements of a-b) ΔfCO_2 (sea-air, in µatm), c-d) temperature (°C) and e-f) salinity obtained during the winter to summer transition in 2011. Left panels show observations collected in October and early November (17/10-5/11), while right panels show observations obtained exclusively in November (5-21/11). Thin dotted lines indicates the cruise track (the triangle locates station A3). The dashed line shows the mean position of the Polar Front (from Park et al., 2014). Bathymetry is indicated as shades of grey (every 500m).

Figure 3: North-South distribution of a) surface fCO_2 and b) sea surface temperature measured in October-November 2011 over and downstream of the Kerguelen Plateau (66.6°E-75°E). Symbols and color coding are used to indicate the time of observation: blue colors indicate end-winter conditions; purple symbols show the onset of the bloom; orange and red symbols are for mid-November. Green squares show measurements collected in shallow waters (bathymetry <500m) in October and November. The black horizontal line indicates the mean atmospheric fCO_2 value of 388 µatm. The position of station A3 is indicated (see profiles in Fig. 5).

Figure 4: East-West distribution of a) surface fCO_2 and b) sea surface temperature measured in October-November 2011 in the Plume offshore (47.8°S-49.5°S, bathymetry >1000m). Symbols and color coding are used to indicate the time of observation (same coding as for Fig. 3): blue dots indicate end-winter conditions; purple symbols show the onset of the bloom; orange and red symbols are for mid-November. The black horizontal line indicates the mean atmospheric fCO_2 value of 388 µatm.

Figure 5: Vertical profiles of a) potential temperature, b) salinity and c) total CO_2 measured at station A3 during the KEOPS2 survey in 2011 (black) before the onset of the bloom (20/10, triangles, with a zoom between 0 and 300m) and during the growing season (16/11, squares),

718 compared to the mean and standard deviation of measurements collected during the
719 KEOPS/OISO12 survey in 2005 when the bloom declined (19/01-12/02, gray dots, Jouandet
720 et al., 2008).
721
722 Figure 6: Relationships observed in October-November 2011 in surface waters between a)
723 fCO_2 and temperature, b) fCO_2 and chlorophyll-a, c) fCO_2 and nitrate and d) fCO_2 and
724 $Si(OH)_4$. The mean values were calculated over a few days (see Table 1). Color coding
725 indicates the different regions investigated around Kerguelen: the Middle zone (orange), the
726 Plateau south of 50°S (light blue), the Polar Front zone (red), the shallow Plateau (<500m,
727 green) and HNLC waters upstream of the Kerguelen Plateau (dark blue, end of October).
728
729 Figure 7: a) Evolution of the mean air-sea CO_2 fluxes estimated in different regions of
730 Kerguelen's bloom (data shown in panel b): the Middle zone (orange), the Plateau south of
731 50°S (light blue) and the Polar Front zone (red), and compared to HNLC waters found
732 upstream and downstream of the Kerguelen Plateau (dark blue, data shown in panel c). The
733 square symbol in panel a shows the mean value measured in December by the CARIOCA
734 buoy launched during the KEOPS2 survey (L. Merlivat, pers. com.). Diamonds show the
735 monthly means obtained from the SOCAT-v2 database (1991-2008) completed with the
736 recent OISO data (2010-2014, including the KEOPS2 survey).

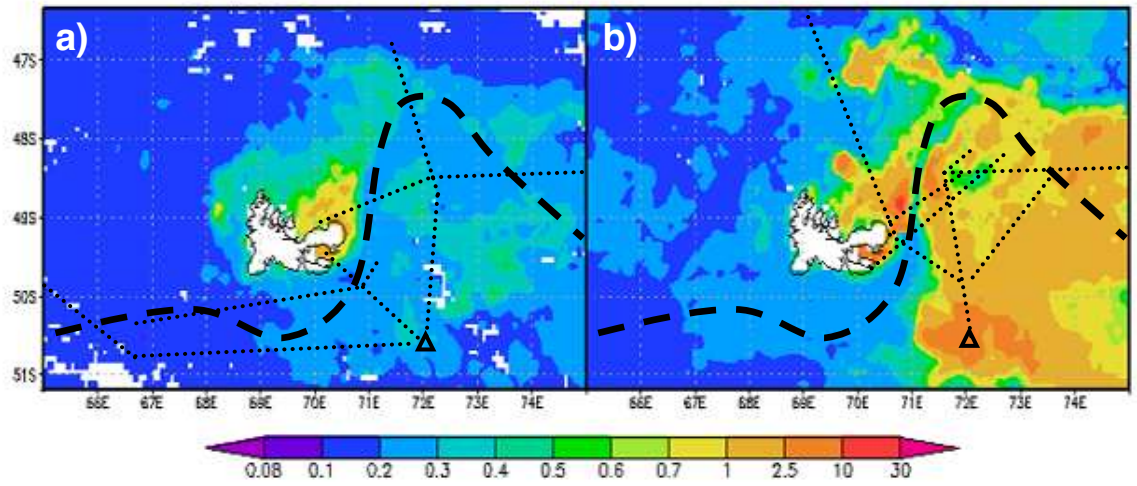

Figure 1: Satellite images of chlorophyll-a (µg/l) for a) October 2011 and b) November 2011 (MODIS, monthly mean). Dotted lines indicates the cruise track (the triangle locates station A3). The dashed line shows the mean position of the Polar Front (from Park et al., 2014).

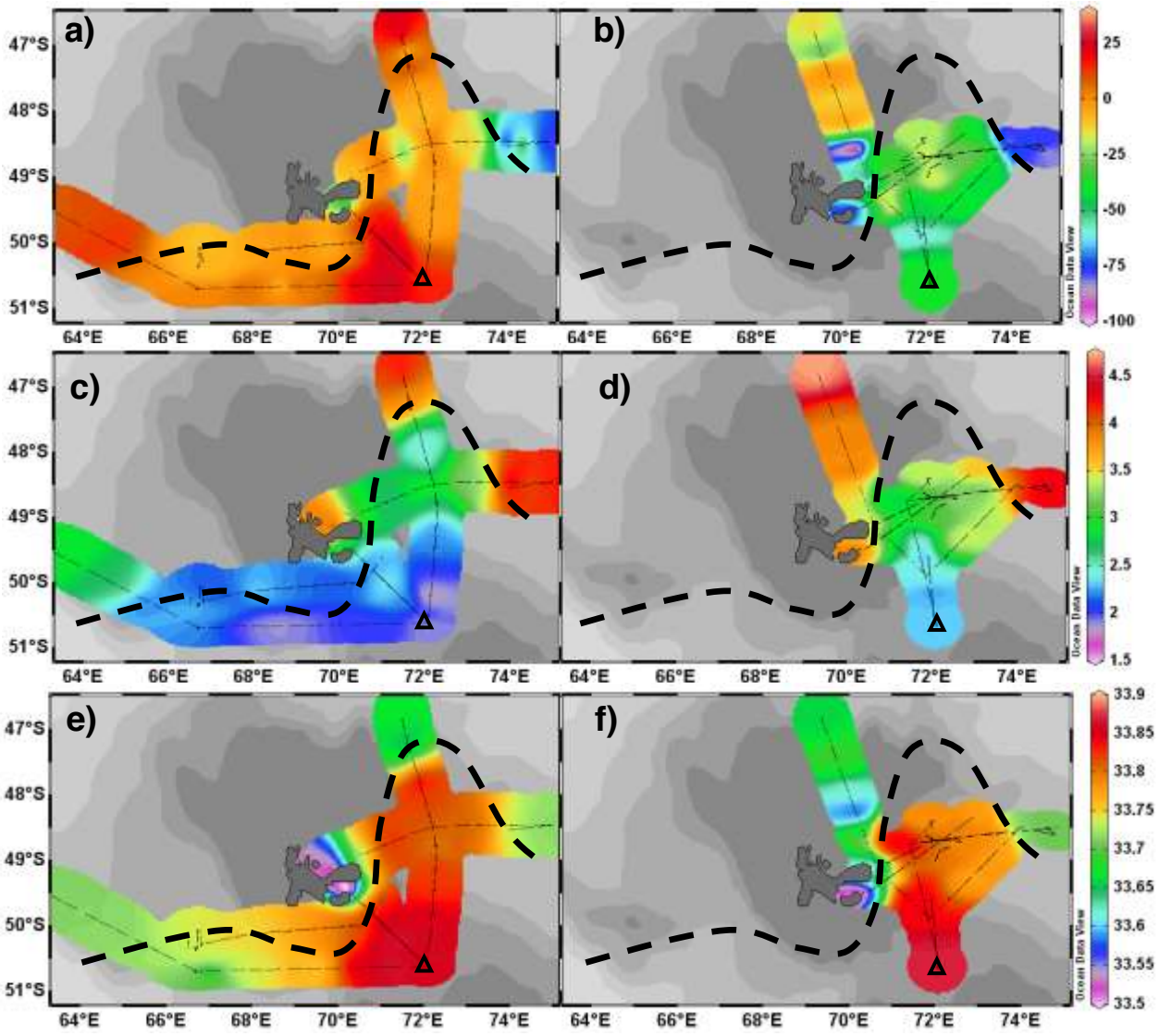

Figure 2: Underway surface measurements of a-b) ΔfCO_2 (sea-air, in µatm), c-d) temperature (°C) and e-f) salinity obtained during the winter to summer transition in 2011. Left panels show observations collected in October and early November (17/10-5/11), while right panels show observations obtained exclusively in November (5-21/11). Thin dotted lines indicates the cruise track (the triangle locates station A3). The dashed line shows the mean position of the Polar Front (from Park et al., 2014). Bathymetry is indicated as shades of grey (every 500m).

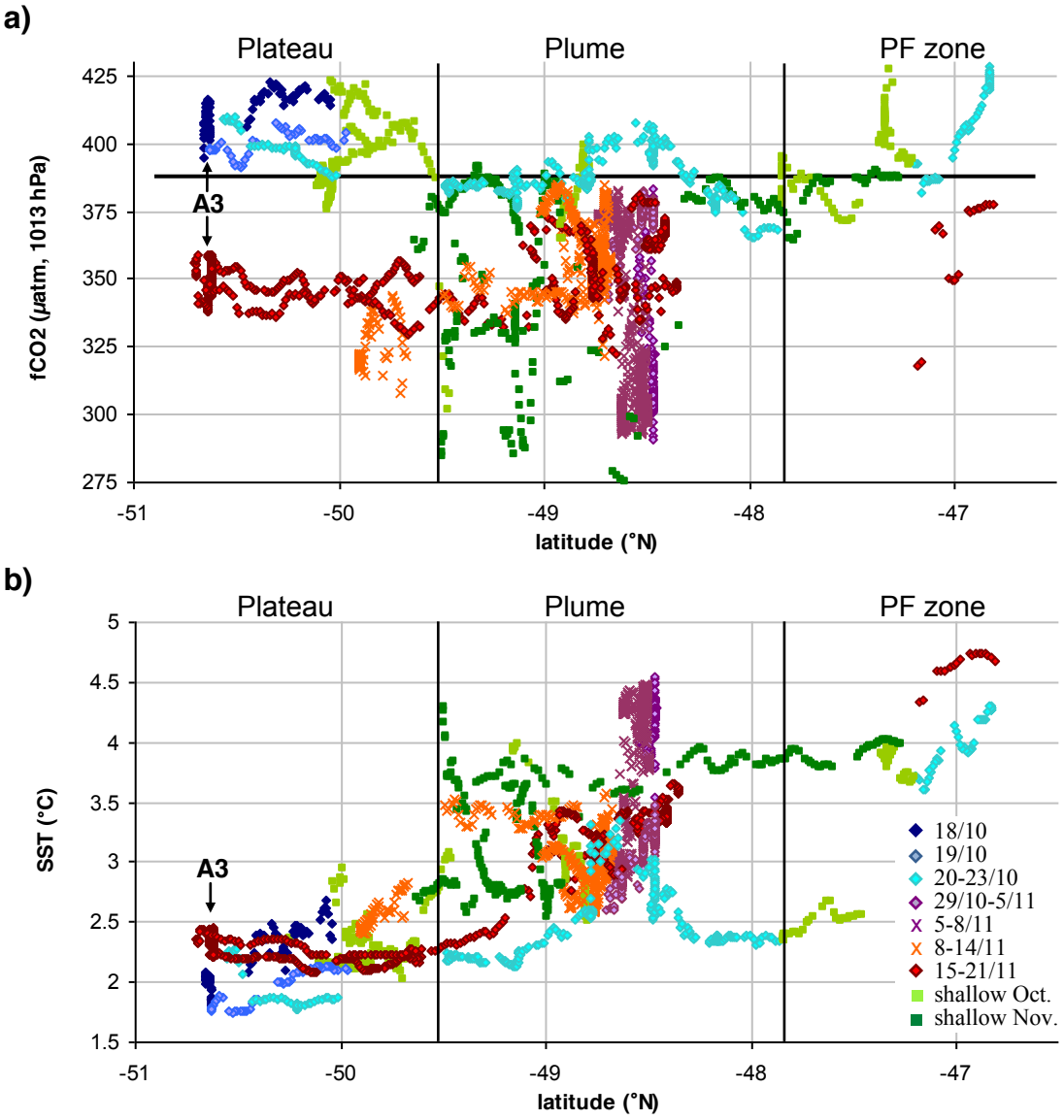

Figure 3: North-South distribution of a) surface fCO_2 and b) sea surface temperature measured in October-November 2011 over and downstream of the Kerguelen Plateau (66.6°E-75°E). Symbols and color coding are used to indicate the time of observation: blue colors indicate end-winter conditions; purple symbols show the onset of the bloom; orange and red symbols are for mid-November. Green squares show measurements collected in shallow waters (bathymetry <500m) in October and November. The black horizontal line indicates the mean atmospheric fCO_2 value of 388 µatm. The position of station A3 is indicated (see profiles in Fig. 5).

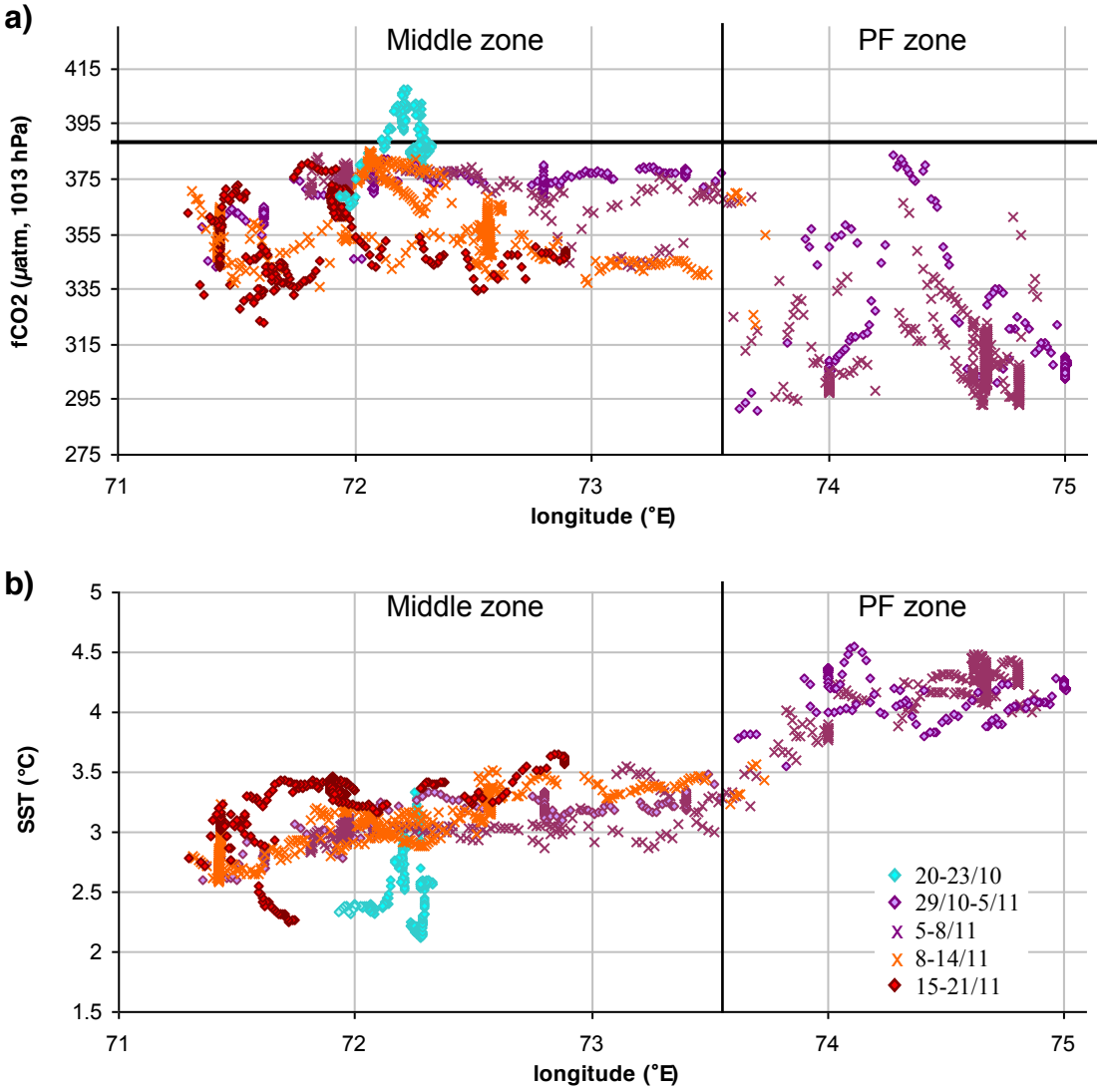

Figure 4: East-West distribution of a) surface fCO_2 and b) sea surface temperature measured in October-November 2011 in the Plume offshore (47.8°S-49.5°S, bathymetry >1000m). Symbols and color coding are used to indicate the time of observation (same coding as for Fig. 3): blue dots indicate end-winter conditions; purple symbols show the onset of the bloom; orange and red symbols are for mid-November. The black horizontal line indicates the mean atmospheric fCO_2 value of 388 µatm.

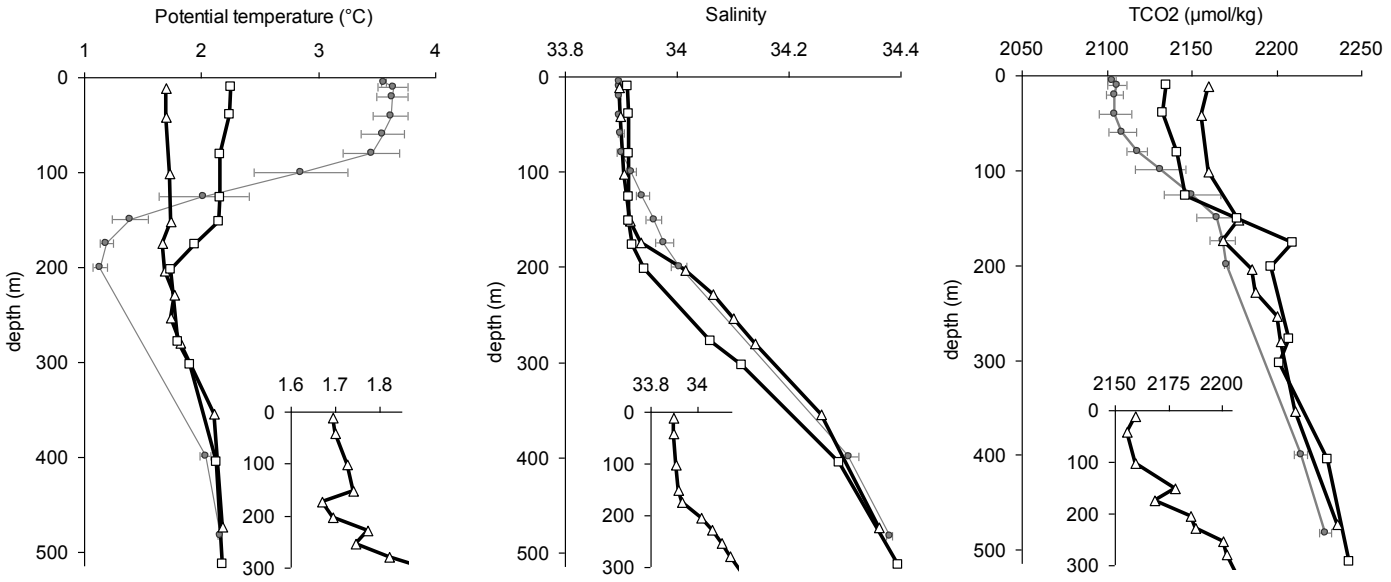

Figure 5: Vertical profiles of a) potential temperature, b) salinity and c) total CO_2 measured at station A3 during the KEOPS2 survey in 2011 (black) before the onset of the bloom (20/10, triangles, with a zoom between 0 and 300m) and during the growing season (16/11, squares), compared to the mean and standard deviation of measurements collected during the KEOPS/OISO12 survey in 2005 when the bloom declined (19/01-12/02, gray dots, Jouandet et al., 2008).

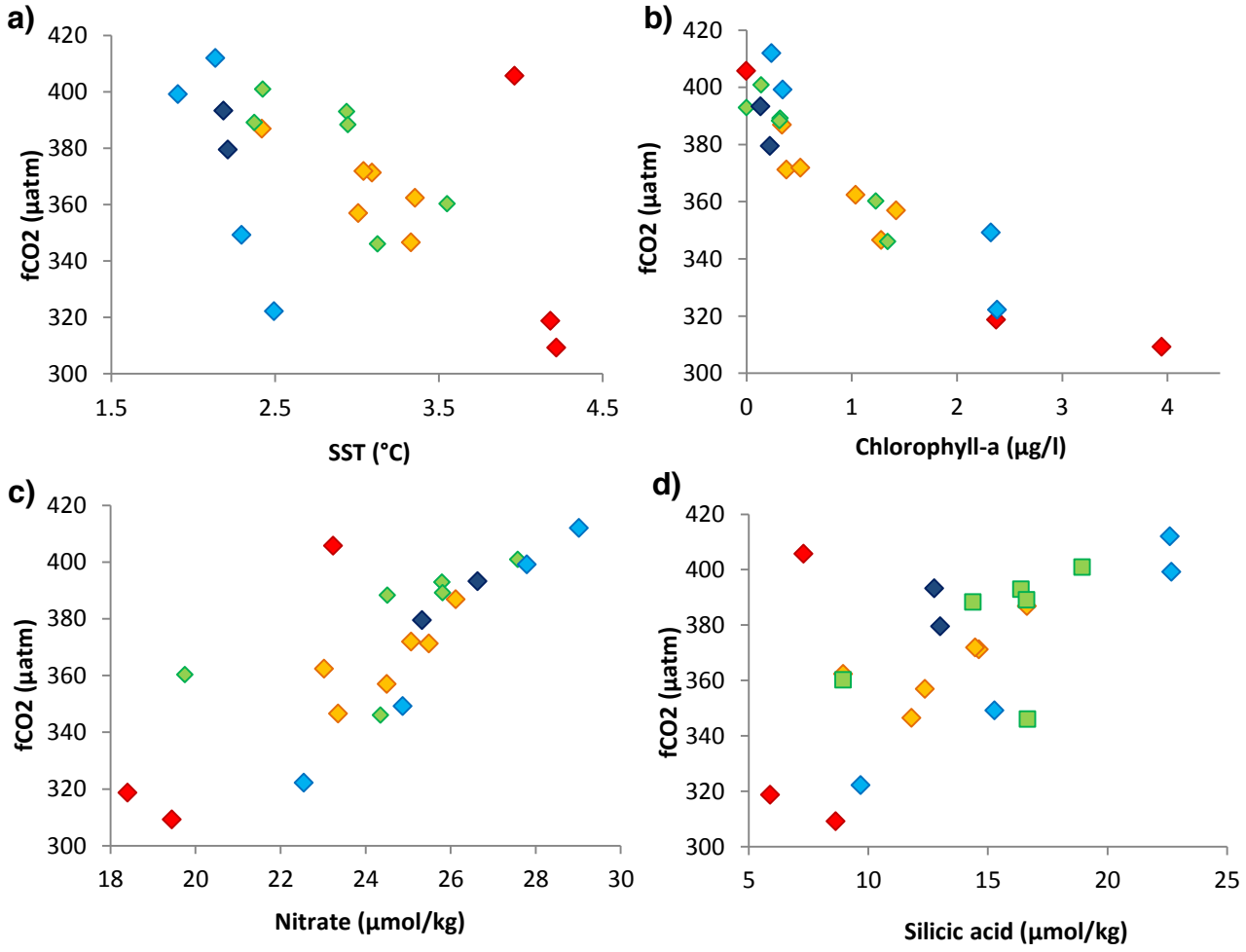

Figure 6: Relationships observed in October-November 2011 in surface waters between a) fCO_2 and temperature, b) fCO_2 and chlorophyll-a, c) fCO_2 and nitrate and d) fCO_2 and $Si(OH)_4$. The mean values were calculated over a few days (see Table 1). Color coding indicates the different regions investigated around Kerguelen: the Middle zone (orange), the Plateau south of 50°S (light blue), the Polar Front zone (red), the shallow Plateau (<500m, green) and HNLC waters upstream of the Kerguelen Plateau (dark blue, end of October).

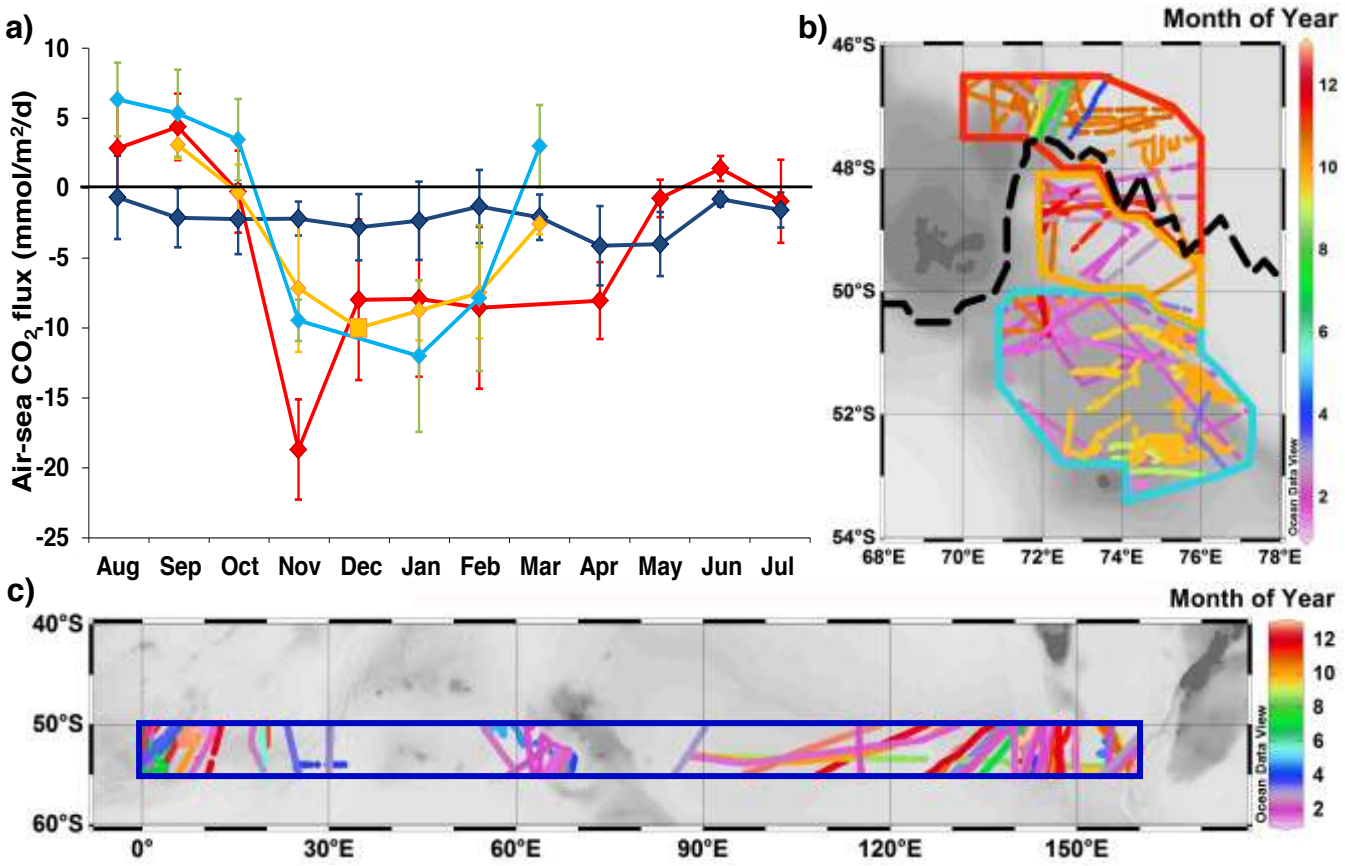

Figure 7: a) Evolution of the mean air-sea CO_2 fluxes estimated in different regions of Kerguelen's bloom (data shown in panel b): the Middle zone (orange), the Plateau south of 50°S (light blue) and the Polar Front zone (red), and compared to HNLC waters found upstream and downstream of the Kerguelen Plateau (dark blue, data shown in panel c). The square symbol in panel a shows the mean value measured in December by the CARIOCA buoy launched during the KEOPS2 survey (L. Merlivat, pers. com.). Diamonds show the monthly means obtained from the SOCAT-v2 database (1991-2008) completed with the recent OISO data (2010-2014, including the KEOPS2 survey).

Bibliography

Bibliography

Mark R Abbott, James G Richman, Ricardo M Letelier, and Jasmine S Bartlett. The spring bloom in the antarctic polar frontal zone as observed from a mesoscale array of bio-optical sensors. *Deep Sea Research Part II: Topical Studies in Oceanography*, 47(15–16):3285–3314, 2000. ISSN 0967-0645. doi: 10.1016/S0967-0645(00)00069-2. URL http://www.sciencedirect.com/science/article/pii/S0967064500000692.

Kevin R. Arrigo, Gert L. van Dijken, and Seth Bushinsky. Primary production in the southern ocean, 1997–2006. *Journal of Geophysical Research*, 113(C8), August 2008. ISSN 0148-0227. doi: 10.1029/2007JC004551. URL http://www.agu.org/pubs/crossref/2008/2007JC004551.shtml.

O. Aumont. Pisces biogeochemical model, 2012, pisces technical documentation. 2012.

O. Aumont and L. Bopp. Globalizing results from ocean in situ iron fertilization studies. *Global Biogeochemical Cycles*, 20(2), 2006. ISSN 0886-6236. doi: 10.1029/2005GB002591. URL http://www.agu.org/pubs/crossref/2006/2005GB002591.shtml.

Karl Banse. Grazing, temporal changes of phytoplankton concentrations, and the microbial loop in the open sea. In Paul G. Falkowski, Avril D. Woodhead, and Katherine Vivirito, editors, *Primary Productivity and Biogeochemical Cycles in the Sea*, number 43 in Environmental Science Research, pages 409–440. Springer US, January 1992. ISBN 978-1-4899-0764-6, 978-1-4899-0762-2. URL http://link.springer.com/chapter/10.1007/978-1-4899-0762-2_22.

Karl Banse. Grazing and zooplankton production as key controls of phytoplankton production in the open ocean. *Oceanography*, 7(1):13–20, 1994. URL http://www.tos.org/oceanography/archive/7-1_banse.pdf.

M. J. Behrenfeld. Abandoning sverdrup's critical depth hypothesis on phytoplankton blooms. *Ecology*, 91(4):977–989, 2010. URL http://www.esajournals.org/doi/abs/10.1890/09-1207.1.

Michael J. Behrenfeld. Carbon-based ocean productivity and phytoplankton physiology from space. *Global Biogeochemical Cycles*, 19(1), 2005. ISSN 0886-6236. doi: 10.1029/2004GB002299. URL http://www.agu.org/pubs/crossref/2005/2004GB002299.shtml.

Michael J. Behrenfeld. Climate-mediated dance of the plankton. *Nature Clim. Change*, 4(10): 880–887, October 2014. ISSN 1758-678X. doi: 10.1038/nclimate2349. URL http://www.nature.com/nclimate/journal/v4/n10/full/nclimate2349.html.

Michael J. Behrenfeld and Emmanuel S. Boss. Resurrecting the ecological underpinnings of ocean plankton blooms. *Annual Review of Marine Science*, 6(1):130930121936006, June 2013. ISSN 1941-1405, 1941-0611. doi: 10.1146/annurev-marine-052913-021325. URL http://www.annualreviews.org/doi/abs/10.1146/annurev-marine-052913-021325.

Michael J. Behrenfeld and Emmanuel S. Boss. Resurrecting the ecological underpinnings of ocean plankton blooms. *Annual Review of Marine Science*, 6(1):167–194, 2014. doi: 10.1146/annurev-marine-052913-021325. URL http://dx.doi.org/10.1146/annurev-marine-052913-021325.

Michael J. Behrenfeld, Robert T. O'Malley, David A. Siegel, Charles R. McClain, Jorge L. Sarmiento, Gene C. Feldman, Allen J. Milligan, Paul G. Falkowski, Ricardo M. Letelier, and Emmanuel S. Boss. Climate-driven trends in contemporary ocean productivity. *Nature*, 444 (7120):752–755, December 2006. ISSN 0028-0836, 1476-4687. doi: 10.1038/nature05317. URL http://www.nature.com/doifinder/10.1038/nature05317.

Michael J. Behrenfeld, Scott C. Doney, Ivan Lima, Emmanuel S. Boss, and David A. Siegel. Annual cycles of ecological disturbance and recovery underlying the subarctic atlantic spring plankton bloom: PHYTOPLANKTON BLOOMS. *Global Biogeochemical Cycles*, 27(2):526–540, April 2013a. ISSN 08866236. doi: 10.1002/gbc.20050. URL http://doi.wiley.com/10.1002/gbc.20050.

Michael J. Behrenfeld, Scott C. Doney, Ivan Lima, Emmanuel S. Boss, and David A. Siegel. Response to comment by s. chiswell: COMMENTARY. *Global Biogeochemical Cycles*, pages n/a–n/a, November 2013b. ISSN 08866236. doi: 10.1002/2013GB004720. URL http://doi.wiley.com/10.1002/2013GB004720.

Henry Bryant Bigelow. *Plankton of the offshore waters of the Gulf of Maine*. US Government Printing Office, 1926. URL http://fishbull.noaa.gov/40-2/contents.pdf.

S. Blain, C. Guieu, H. Claustre, K. Leblanc, T. Moutin, B. Quéguiner, J. Ras, and G. Sarthou. Availability of iron and major nutrients for phytoplankton in the northeast atlantic ocean. *Limnology and oceanography*, pages 2095–2104, 2004.

Stéphane Blain, Bernard Quéguiner, Leanne Armand, Sauveur Belviso, Bruno Bombled, Laurent Bopp, Andrew Bowie, Christian Brunet, Corina Brussaard, François Carlotti, Urania Christaki, Antoine Corbière, Isabelle Durand, Frederike Ebersbach, Jean-Luc Fuda, Nicole Garcia, Loes Gerringa, Brian Griffiths, Catherine Guigue, Christophe Guillerm, Stéphanie

Jacquet, Catherine Jeandel, Patrick Laan, Dominique Lefèvre, Claire Lo Monaco, Andrea Malits, Julie Mosseri, Ingrid Obernosterer, Young-Hyang Park, Marc Picheral, Philippe Pondaven, Thomas Remenyi, Valérie Sandroni, Géraldine Sarthou, Nicolas Savoye, Lionel Scouarnec, Marc Souhaut, Doris Thuiller, Klaas Timmermans, Thomas Trull, Julia Uitz, Pieter van Beek, Marcel Veldhuis, Dorothée Vincent, Eric Viollier, Lilita Vong, and Thibaut Wagener. Effect of natural iron fertilization on carbon sequestration in the southern ocean. *Nature*, 446 (7139):1070–1074, April 2007. ISSN 0028-0836, 1476-4687. doi: 10.1038/nature05700. URL http://www.nature.com/doifinder/10.1038/nature05700.

Stéphane Blain, Renaut Sophie, Xing Xiaogang, Claustre Hervé, and Guinet Christophe. Instrumented elephant seals reveal the seasonality in chlorophyll and light-mixing regime in the iron fertilized southern ocean.: CHLOROPHYLL AND LIGHT IN SOUTHERN OCEAN. *Geophysical Research Letters*, pages n/a–n/a, December 2013. ISSN 00948276. doi: 10.1002/2013GL058065. URL http://doi.wiley.com/10.1002/2013GL058065.

L. Bopp, L. Resplandy, J. C. Orr, S. C. Doney, J. P. Dunne, M. Gehlen, P. Halloran, C. Heinze, T. Ilyina, R. Séférian, J. Tjiputra, and M. Vichi. Multiple stressors of ocean ecosystems in the 21st century: projections with CMIP5 models. *Biogeosciences Discussions*, 10(2):3627–3676, February 2013. ISSN 1810-6285. doi: 10.5194/bgd-10-3627-2013. URL http://www.biogeosciences-discuss.net/10/3627/2013/.

Laurent Bopp, Patrick Monfray, Olivier Aumont, Jean-Louis Dufresne, Hervé Le Treut, Gurvan Madec, Laurent Terray, and James C. Orr. Potential impact of climate change on marine export production. *Global Biogeochemical Cycles*, 15(1):81–99, 2001. ISSN 1944-9224. doi: 10.1029/1999GB001256. URL http://onlinelibrary.wiley.com/doi/10.1029/1999GB001256/abstract.

I. Borrione and R. Schlitzer. Distribution and recurrence of phytoplankton blooms around south georgia, southern ocean. *Biogeosciences*, 10(1):217–231, January 2013. ISSN 1726-4189. doi: 10.5194/bg-10-217-2013. URL http://www.biogeosciences.net/10/217/2013/.

E. Boss and M. Behrenfeld. In situ evaluation of the initiation of the north atlantic phytoplankton bloom. *Geophysical Research Letters*, 37(18), September 2010. ISSN 0094-8276. doi: 10.1029/2010GL044174. URL http://www.agu.org/pubs/crossref/2010/2010GL044174.shtml.

P. W. Boyd. ENVIRONMENTAL FACTORS CONTROLLING PHYTOPLANKTON PROCESSES IN THE SOUTHERN OCEAN. *Journal of Phycology*, 38(5):844–861, 2002.

P. W. Boyd and M. J. Ellwood. The biogeochemical cycle of iron in the ocean. *Nature Geoscience*, 3(10):675–682, September 2010. ISSN 1752-0894, 1752-0908. doi: 10.1038/ngeo964. URL http://www.nature.com/doifinder/10.1038/ngeo964.

P. W. Boyd, K. R. Arrigo, R. Strzepek, and G. L. van Dijken. Mapping phytoplankton iron utilization: Insights into southern ocean supply mechanisms. *J. Geophys. Res.*, 117:18 PP., June 2012a. doi: 201210.1029/2011JC007726. URL http://www.agu.org.biblioplanets.gate.inist.fr/pubs/crossref/2012/2011JC007726.shtml.

Philip W. Boyd, Robert Strzepek, Feixue Fu, and David A. Hutchins. Environmental control of open-ocean phytoplankton groups: Now and in the future. *Limnology and Oceanography*, 55 (3):1353–1376, 2010. ISSN 00243590. doi: 10.4319/lo.2010.55.3.1353. URL http://www.aslo.org/lo/toc/vol_55/issue_3/1353.html.

Philip W. Boyd, Robert Strzepek, Steve Chiswell, Hoe Chang, Jennifer M. DeBruyn, Michael Ellwood, Sean Keenan, Andrew L. King, Elisabeth W. Maas, Scott Nodder, Sylvia G. Sander, Philip Sutton, Benjamin S. Twining, Steven W. Wilhelm, and David A. Hutchins. Microbial control of diatom bloom dynamics in the open ocean. *Geophysical Research Letters*, 39(18): n/a–n/a, 2012b. ISSN 1944-8007. doi: 10.1029/2012GL053448. URL http://onlinelibrary.wiley.com/doi/10.1029/2012GL053448/abstract.

P.W. Boyd, A.J. Watson, C.S. Law, E.R. Abraham, T. Trull, R. Murdoch, D.C.E. Bakker, A.R. Bowie, KO Buesseler, H. Chang, et al. A mesoscale phytoplankton bloom in the polar southern ocean stimulated by iron fertilization. *Nature*, 407(6805):695–702, 2000.

Keith E. Brainerd and Michael C. Gregg. Surface mixed and mixing layer depths. *Deep Sea Research Part I: Oceanographic Research Papers*, 42(9):1521–1543, 1995. URL http://www.sciencedirect.com/science/article/pii/096706379500068H.

Laurent Brodeau, Bernard Barnier, Anne-Marie Treguier, Thierry Penduff, and Sergei Gulev. An ERA40-based atmospheric forcing for global ocean circulation models. *Ocean Modelling*, 31 (3–4):88–104, 2010. ISSN 1463-5003. doi: 10.1016/j.ocemod.2009.10.005. URL http://www.sciencedirect.com/science/article/pii/S1463500309002017.

Sarah R. Brody and M. Susan Lozier. Changes in dominant mixing length scales as a driver of subpolar phytoplankton bloom initiation in the north atlantic. *Geophys. Res. Lett.*, page 2014GL059707, April 2014. ISSN 1944-8007. doi: 10.1002/2014GL059707. URL http://onlinelibrary.wiley.com/doi/10.1002/2014GL059707/abstract.

Sarah R. Brody, M. Susan Lozier, and John P. Dunne. A comparison of methods to determine phytoplankton bloom initiation: METHODS TO DETERMINE BLOOM INITIATION. *Journal of Geophysical Research: Oceans*, 118(5):2345–2357, May 2013. ISSN 21699275. doi: 10.1002/jgrc.20167. URL http://doi.wiley.com/10.1002/jgrc.20167.

Erik T. Buitenhuis and Richard J. Geider. A model of phytoplankton acclimation to iron-light colimitation. *Limnology and Oceanography*, 55(2):714, 2010. URL http://aslo.net/lo/toc/vol_55/issue_2/0714.pdf.

W. Cai, G. Shi, T. Cowan, D. Bi, and J. Ribbe. The response of the southern annular mode, the east australian current, and the southern mid-latitude ocean circulation to global warming. *Geophys. Res. Lett.*, 32(23):L23706, December 2005. ISSN 1944-8007. doi: 10.1029/2005GL024701. URL http://onlinelibrary.wiley.com/doi/10.1029/2005GL024701/abstract.

Mary-Elena Carr, Marjorie A.M. Friedrichs, Marjorie Schmeltz, Maki Noguchi Aita, David Antoine, Kevin R. Arrigo, Ichio Asanuma, Olivier Aumont, Richard Barber, Michael Behrenfeld, Robert Bidigare, Erik T. Buitenhuis, Janet Campbell, Aurea Ciotti, Heidi Dierssen, Mark Dowell, John Dunne, Wayne Esaias, Bernard Gentili, Watson Gregg, Steve Groom, Nicolas Hoepffner, Joji Ishizaka, Takahiko Kameda, Corinne Le Quéré, Steven Lohrenz, John Marra, Frédéric Mélin, Keith Moore, André Morel, Tasha E. Reddy, John Ryan, Michele Scardi, Tim Smyth, Kevin Turpie, Gavin Tilstone, Kirk Waters, and Yasuhiro Yamanaka. A comparison of global estimates of marine primary production from ocean color. *Deep Sea Research Part II: Topical Studies in Oceanography*, 53(5-7):741–770, March 2006. ISSN 09670645. doi: 10.1016/j.dsr2.2006.01.028. URL http://linkinghub.elsevier.com/retrieve/pii/S0967064506000555.

Magdalena M Carranza and Sarah T Gille. Southern ocean wind-driven entrainment enhances satellite chlorophyll-a through the summer. *Journal of Geophysical Research: Oceans*, 2014.

Paulo Ceppi, Mark D. Zelinka, and Dennis L. Hartmann. The response of the southern hemispheric eddy-driven jet to future changes in shortwave radiation in CMIP5: CEPPI ET AL. *Geophysical Research Letters*, 41(9):3244–3250, May 2014. ISSN 00948276. doi: 10.1002/2014GL060043. URL http://doi.wiley.com/10.1002/2014GL060043.

H Chepfer, V Noel, D Winker, and M Chiriaco. Where and when will we observe cloud changes due to climate warming? *Geophysical Research Letters*, 2014.

Sm Chiswell. Annual cycles and spring blooms in phytoplankton: don't abandon sverdrup completely. *Marine Ecology Progress Series*, 443:39–50, December 2011. ISSN 0171-8630, 1616-1599. doi: 10.3354/meps09453. URL http://www.int-res.com/abstracts/meps/v443/p39-50/.

Stephen M. Chiswell. Comment on "annual cycles of ecological disturbance and recovery underlying the subarctic atlantic spring plankton bloom": COMMENTARY. *Global Biogeochemical Cycles*, pages n/a–n/a, November 2013. ISSN 08866236. doi: 10.1002/2013GB004681. URL http://doi.wiley.com/10.1002/2013GB004681.

Stephen M. Chiswell, Janet Bradford-Grieve, Mark G. Hadfield, and Sean C. Kennan. Climatology of surface chlorophyll a, autumn-winter and spring blooms in the south–west pacific ocean. *Journal of Geophysical Research: Oceans*, pages n/a–n/a, 2013. ISSN 2169-9291. doi: 10.1002/jgrc.20088. URL http://onlinelibrary.wiley.com/doi/10.1002/jgrc.20088/abstract.

Harriet Cole, Stephanie Henson, Adrian Martin, and Andrew Yool. Mind the gap: The impact of missing data on the calculation of phytoplankton phenology metrics. *Journal of Geophysical Research: Oceans*, 117(C8):n/a–n/a, 2012. ISSN 2156-2202. doi: 10.1029/2012JC008249. URL http://onlinelibrary.wiley.com/doi/10.1029/2012JC008249/abstract.

D. H. Cushing. An alternative method of estimating the critical depth. *ICES Journal of Marine Science*, 27(2):131–140, May 1962. ISSN 1054-3139, 1095-9289. doi: 10.1093/icesjms/27.2.131. URL http://icesjms.oxfordjournals.org/content/27/2/131.full.pdf+html?hwshib2=authn%3A1398785273%3A20140428%253A426135b2-a12e-4635-8b87-a749e1161459%3A0%3A0%3A0%3Azhg7uyICKxCuCofNd3yWBQ%3D%3D.

Trine Dale, Francisco Rey, and B. Heimdal. Seasonal development of phytoplankton at a high latitude oceanic site. *SARSIA-BERGEN-*, 84(5/6):419–436, 1999. URL http://www.vliz.be/imisdocs/publications/32227.pdf.

F. A. Dehairs, C. Lancelot, L. André, H. Goosse, M. Frankignoulle, S. Becquevort, A. Borges, D. Cardinal, A. de Montety, B. Delille, M. Elskens, S. Jacquet, W. Lefebvre, B. Pasquer, N. Savoye, and V. Schoemann. Assessing the sensitivity of the southern ocean's biological carbon pump to climate change (BELCANTO II): final report. 2006. URL http://www.vliz.be/imis/imis.php?module=ref&refid=109766.

Shenfu Dong, Janet Sprintall, Sarah T. Gille, and Lynne Talley. Southern ocean mixed-layer depth from argo float profiles. *J. Geophys. Res.*, 113:12 PP., June 2008. doi: 200810.1029/2006JC004051. URL http://www.agu.org.biblioplanets.gate.inist.fr/pubs/crossref/2008/2006JC004051.shtml.

A.C. Dragon, P. Monestiez, A. Bar-Hen, and C. Guinet. Linking foraging behaviour to physical oceanographic structures: Southern elephant seals and mesoscale eddies east of kerguelen islands. *Progress in Oceanography*, 87(1):61–71, 2010.

M. R. Droop. 25 years of algal growth kinetics a personal view. *Botanica marina*, 26(3):99–112, 1983.

C. O. Dufour. *Rôle des tourbillons océaniques dans la variabilité récente des flux air-mer de CO2 dans l'océan Austral*. PhD thesis, October 2011.

Carolina O. Dufour, Julien Le Sommer, Marion Gehlen, James C. Orr, Jean-Marc Molines, Jennifer Simeon, and Bernard Barnier. Eddy compensation and controls of the enhanced sea-to-air CO2 flux during positive phases of the southern annular mode. *Global Biogeochem. Cycles*, 27(3):950–961, September 2013. ISSN 1944-9224. doi: 10.1002/gbc.20090. URL http://onlinelibrary.wiley.com/doi/10.1002/gbc.20090/abstract.

J.-L. Dufresne, M.-A. Foujols, S. Denvil, A. Caubel, O. Marti, O. Aumont, Y. Balkanski, S. Bekki, H. Bellenger, R. Benshila, S. Bony, L. Bopp, P. Braconnot, P. Brockmann, P. Cadule, F. Cheruy, F. Codron, A. Cozic, D. Cugnet, N. Noblet, J.-P. Duvel, C. Ethé, L. Fairhead, T. Fichefet, S. Flavoni, P. Friedlingstein, J.-Y. Grandpeix, L. Guez, E. Guilyardi, D. Hauglustaine, F. Hourdin, A. Idelkadi, J. Ghattas, S. Joussaume, M. Kageyama, G. Krinner, S. Labetoulle, A. Lahellec, M.-P. Lefebvre, F. Lefevre, C. Levy, Z. X. Li, J. Lloyd, F. Lott, G. Madec, M. Mancip, M. Marchand, S. Masson, Y. Meurdesoif, J. Mignot, I. Musat, S. Parouty, J. Polcher, C. Rio, M. Schulz, D. Swingedouw, S. Szopa, C. Talandier, P. Terray, N. Viovy, and N. Vuichard. Climate change projections using the ipsl-cm5 earth system model: from cmip3 to cmip5. *Climate Dynamics*, 40(9-10):2123–2165, May 2013. URL http://nora.nerc.ac.uk/505579/.

D Durand. Globcolour full validation report, vol. 1.1, acri-st, 2007.

Richard W. Eppley. Temperature and phytoplankton growth in the sea. *Fish. Bull*, 70(4): 1063–1085, 1972.

Geoffrey T. Evans and John S. Parslow. A model of annual plankton cycles. *Biological Oceanography*, 3(3):327–347, 1985. ISSN 0196-5581. doi: 10.1080/01965581.1985.10749478. URL http://www.tandfonline.com/doi/abs/10.1080/01965581.1985.10749478.

Nicolas Fauchereau, Alessandro Tagliabue, Laurent Bopp, and Pedro M. S. Monteiro. The response of phytoplankton biomass to transient mixing events in the southern ocean. *Geophys. Res. Lett.*, 38(17):L17601, September 2011. ISSN 0094-8276. doi: 10.1029/2011GL048498. URL http://www.agu.org/pubs/crossref/2011/2011GL048498.shtml.

Raffaele Ferrari, Sophia T. Merrifield, and John R. Taylor. Shutdown of convection triggers increase of surface chlorophyll. *Journal of Marine Systems*, February 2014. ISSN 09247963. doi: 10.1016/j.jmarsys.2014.02.009. URL http://linkinghub.elsevier.com/retrieve/pii/S0924796314000384.

Michel Fiala, Elzbieta E Kopczynska, Catherine Jeandel, Louise Oriol, and Giles Vetion. Seasonal and interannual variability of size-fractionated phytoplankton biomass and community structure at station kerfix, off the kerguelen islands, antarctica. *J. Plankton Res.*, 20(7): 1341–1356, January 1998. ISSN 0142-7873, 1464-3774. doi: 10.1093/plankt/20.7.1341. URL http://plankt.oxfordjournals.org/content/20/7/1341.

Peter J. S. Franks. Has sverdrup's critical depth hypothesis been tested? mixed layers vs. turbulent layers. *ICES Journal of Marine Science: Journal du Conseil*, page fsu175, October 2014. ISSN 1054-3139, 1095-9289. doi: 10.1093/icesjms/fsu175. URL http://icesjms.oxfordjournals.org/content/early/2014/10/17/icesjms.fsu175.

N. P. Gillett and J. C. Fyfe. Annular mode changes in the CMIP5 simulations. *Geophys. Res. Lett.*, 40(6):1189–1193, March 2013. ISSN 1944-8007. doi: 10.1002/grl.50249. URL http://onlinelibrary.wiley.com/doi/10.1002/grl.50249/abstract.

H. H. Gran and Trygve Braarud. A quantitative study of the phytoplankton in the bay of fundy and the gulf of maine (including observations on hydrography, chemistry and turbidity). *J. Biol. Board Can.*, 1(5):279–467, September 1935. ISSN 0368-1424. doi: 10.1139/f35-012. URL http://www.nrcresearchpress.com/doi/abs/10.1139/f35-012.

C Guinet, P Jouventin, and H Weimerskirch. Population changes, movements of southern elephant seals on crozet and kerguelen archipelagos in the last decades. *Polar Biology*, 12(3-4): 349–356, 1992.

C. Guinet, X. Xing, E. Walker, P. Monestiez, S. Marchand, B. Picard, T. Jaud, M. Authier, C. Cotté, A. C. Dragon, E. Diamond, D. Antoine, P. Lovell, S. Blain, F. D'Ortenzio, and H. Claustre. Calibration procedures and first dataset of southern ocean chlorophyll <i>a</i> profiles collected by elephant seals equipped with a newly developed CTD-fluorescence tags. *Earth System Science Data*, 5(1):15–29, February 2013. ISSN 1866-3516. doi: 10.5194/essd-5-15-2013. URL http://www.earth-syst-sci-data.net/5/15/2013/.

Christoph Heinze. Assessing the importance of the southern ocean for natural atmospheric pCO2 variations with a global biogeochemical general circulation model. *Deep Sea Research Part II: Topical Studies in Oceanography*, 49(16):3105–3125, 2002. ISSN 0967-0645. doi: 10.1016/S0967-0645(02)00074-7. URL http://www.sciencedirect.com/science/article/pii/S0967064502000747.

S. Henson, H. Cole, C. Beaulieu, and A. Yool. The impact of global warming on seasonality of ocean primary production. *Biogeosciences Discussions*, 10(1):1421–1450, January 2013. ISSN 1810-6285. doi: 10.5194/bgd-10-1421-2013. URL http://www.biogeosciences-discuss.net/10/1421/2013/.

S. A. Henson, J. P. Dunne, and J. L. Sarmiento. Decadal variability in north atlantic phytoplankton blooms. *Journal of Geophysical Research*, 114(C4):C04013, 2009. URL http://www.agu.org/pubs/crossref/2009/2008JC005139.shtml.

MA Hindell, DJ Slip, and HR Burton. The diving behavior of adult male and female southern elephant seals, mirounga-leonina (pinnipedia, phocidae). *Australian Journal of Zoology*, 39(5): 595–619, 1991.

J. Huisman, P. van Oostveen, and Franz J. Weissing. Critical depth and critical turbulence: Two different mechanisms for the development of phytoplankton blooms. 1999.

C. Jeandel, D. Ruiz-Pino, E. Gjata, A. Poisson, C. Brunet, E. Charriaud, F. Dehairs, D. Delille, M. Fiala, C. Fravalo, et al. KERFIX, a time-series station in the southern ocean: a presentation. *Journal of Marine Systems*, 17(1-4):555–569, 1998.

R. Ji, M. Edwards, D. L. Mackas, J. A. Runge, and A. C. Thomas. Marine plankton phenology and life history in a changing climate: current research and future directions. *Journal of Plankton Research*, 32(10):1355–1368, June 2010. ISSN 0142-7873, 1464-3774. doi: 10.1093/plankt/fbq062. URL http://www.plankt.oxfordjournals.org/cgi/doi/10.1093/plankt/fbq062.

Robert Johnson, Peter G. Strutton, Simon W. Wright, Andrew McMinn, and Klaus M. Meiners. Three improved satellite chlorophyll algorithms for the southern ocean. *J. Geophys. Res. Oceans*, 118(7):3694–3703, July 2013. ISSN 2169-9291. doi: 10.1002/jgrc.20270. URL http://onlinelibrary.wiley.com/doi/10.1002/jgrc.20270/abstract.

Mati Kahru and B. Greg Mitchell. Blending of ocean colour algorithms applied to the southern ocean. *Remote Sensing Letters*, 1(2):119–124, June 2010. ISSN 2150-704X, 2150-7058. doi: 10.1080/01431160903547940. URL http://www.tandfonline.com/doi/abs/10.1080/01431160903547940.

Hannele Korhonen, Kenneth S. Carslaw, Piers M. Forster, Santtu Mikkonen, Neil D. Gordon, and Harri Kokkola. Aerosol climate feedback due to decadal increases in southern hemisphere wind speeds. *Geophys. Res. Lett.*, 37(2):L02805, January 2010. ISSN 1944-8007. doi: 10.1029/2009GL041320. URL http://onlinelibrary.wiley.com/doi/10.1029/2009GL041320/abstract.

Corinne Le Quéré, Christian Rödenbeck, Erik T Buitenhuis, Thomas J Conway, Ray Langenfelds, Antony Gomez, Casper Labuschagne, Michel Ramonet, Takakiyo Nakazawa, Nicolas Metzl, Nathan Gillett, and Martin Heimann. Saturation of the southern ocean CO2 sink due to recent climate change. *Science*, 316(5832):1735–1738, June 2007. ISSN 0036-8075, 1095-9203. doi: 10.1126/science.1136188. URL http://www.sciencemag.org/content/316/5832/1735.

Andrew Lenton and Richard J. Matear. Role of the southern annular mode (SAM) in southern ocean CO2 uptake. *Global Biogeochem. Cycles*, 21(2):GB2016, June 2007. ISSN 1944-9224. doi: 10.1029/2006GB002714. URL http://onlinelibrary.wiley.com/doi/10.1029/2006GB002714/abstract.

Alan Longhurst, Shubha Sathyendranath, Trevor Platt, and Carla Caverhill. An estimate of global primary production in the ocean from satellite radiometer data. *J. Plankton Res.*, 17 (6):1245–1271, January 1995. ISSN 0142-7873, 1464-3774. doi: 10.1093/plankt/17.6.1245. URL http://plankt.oxfordjournals.org/content/17/6/1245.

Alan R. Longhurst. Chapter 12 - the southern ocean. In Alan R. Longhurst, editor, *Ecological Geography of the Sea (Second Edition)*, pages 443–475. Academic Press, Burlington, 2007. ISBN 978-0-12-455521-1. URL http://www.sciencedirect.com/science/article/pii/B9780124555211500139.

Nicole S. Lovenduski and Nicolas Gruber. Impact of the southern annular mode on southern ocean circulation and biology. *Geophysical Research Letters*, 32(11):n/a–n/a, 2005. ISSN 1944-8007. doi: 10.1029/2005GL022727. URL http://onlinelibrary.wiley.com/doi/10.1029/2005GL022727/abstract.

M. Susan Lozier, Apurva C. Dave, Jaime B. Palter, Lisa M. Gerber, and Richard T. Barber. On the relationship between stratification and primary productivity in the north atlantic. *Geophys. Res. Lett.*, 38(18):L18609, September 2011. ISSN 0094-8276. doi: 10.1029/2011GL049414. URL http://www.agu.org/pubs/crossref/2011/2011GL049414.shtml.

M. Lévy, Y. Lehahn, J. M. André, L. Mémery, H. Loisel, and E. Heifetz. Production regimes in the northeast atlantic: A study based on sea-viewing wide field-of-view sensor (SeaWiFS) chlorophyll and ocean general circulation model mixed layer depth. *Journal of geophysical research*, 110(C7):C07S10, 2005. URL http://www.agu.org/pubs/crossref/2005/2004JC002771.shtml.

Marina Lévy, Laurent Mémery, and Jean-Michel André. Simulation of primary production and export fluxes in the northwestern mediterranean sea. *Journal of Marine Research*, 56(1):197–238, 1998. doi: 10.1357/002224098321836163.

Marina Lévy, Patrice Klein, and Anne-Marie Treguier. Impact of sub-mesoscale physics on production and subduction of phytoplankton in an oligotrophic regime. *Journal of Marine Research*, 59(4):535–565, July 2001. doi: 10.1357/002224001762842181.

G Madec. Nemo ocean engine. note du pole de modélisation, institut pierre-simon laplace (ipsl), france, no 27 issn no 1288-16193, 2008.

Amala Mahadevan, Eric D'Asaro, Craig Lee, and Mary Jane Perry. Eddy-driven stratification initiates north atlantic spring phytoplankton blooms. *Science*, 337(6090):54–58, June 2012. ISSN 0036-8075, 1095-9203. doi: 10.1126/science.1218740. URL http://www.sciencemag.org/content/337/6090/54.

John Marra and Richard T. Barber. Phytoplankton and heterotrophic respiration in the surface layer of the ocean. *Geophysical Research Letters*, 31(9), 2004. URL http://onlinelibrary.wiley.com/doi/10.1029/2004GL019664/full.

John H. Martin, Steve E. Fitzwater, and R. Michael Gordon. Iron deficiency limits phytoplankton growth in antarctic waters. *Global Biogeochem. Cycles*, 4(1):5–12, March 1990. ISSN 1944-9224. doi: 10.1029/GB004i001p00005. URL http://onlinelibrary.wiley.com/doi/10.1029/GB004i001p00005/abstract.

Pierre Mathiot. *Influence du forçage atmosphérique sur la représentation de la glace de mer et des eaux de plateau en Antarctique dans une étude de modélisation numérique.* PhD thesis, Université Joseph-Fourier-Grenoble I, 2009.

BJ McConnell, C Chambers, and MA Fedak. Foraging ecology of southern elephant seals in relation to the bathymetry and productivity of the southern ocean. *Antarctic Science*, 4(04): 393–398, 1992.

A. J. S. Meijers. The southern ocean in the coupled model intercomparison project phase 5. *Phil. Trans. R. Soc. A*, 372(2019):20130296, July 2014. ISSN 1364-503X, 1471-2962. doi: 10.1098/rsta.2013.0296. URL http://rsta.royalsocietypublishing.org/content/372/2019/20130296.

N Metzl, B Tilbrook, and A Poisson. The annual fco2 cycle and the air–sea co2 flux in the sub-antarctic ocean. *Tellus B*, 51(4):849–861, 1999.

J. Monod. Recherches sur la croissance des cultures bacteriennes, hermann. 1942.

C. M. Moore, M. M. Mills, K. R. Arrigo, I. Berman-Frank, L. Bopp, P. W. Boyd, E. D. Galbraith, R. J. Geider, C. Guieu, S. L. Jaccard, T. D. Jickells, J. La Roche, T. M. Lenton, N. M. Mahowald, E. Marañón, I. Marinov, J. K. Moore, T. Nakatsuka, A. Oschlies, M. A. Saito, T. F. Thingstad, A. Tsuda, and O. Ulloa. Processes and patterns of oceanic nutrient limitation. *Nature Geosci*, 6(9):701–710, September 2013. ISSN 1752-0894. doi: 10.1038/ngeo1765. URL http://www.nature.com/ngeo/journal/v6/n9/full/ngeo1765.html.

J. K. Moore and M. R. Abbott. Phytoplankton chlorophyll distributions and primary production in the southern ocean. *Journal of Geophysical Research*, 105(C12):28–709, 2000.

J. Keith Moore, Mark R. Abbott, James G. Richman, Walker O. Smith, Timothy J. Cowles, Kenneth H. Coale, Wilford D. Gardner, and Richard T. Barber. SeaWiFS satellite ocean color data from the southern ocean. *Geophys. Res. Lett.*, 26(10):PP. 1465–1468, 1999. doi: 199910.1029/1999GL900242. URL http://www.agu.org.biblioplanets.gate.inist.fr/pubs/crossref/1999/1999GL900242.shtml.

J.Keith Moore and Mark R Abbott. Surface chlorophyll concentrations in relation to the antarctic polar front: seasonal and spatial patterns from satellite observations. *Journal of Marine Systems*, 37(1–3):69–86, November 2002. ISSN 0924-7963. doi: 10.1016/S0924-7963(02)00196-3. URL http://www.sciencedirect.com/science/article/pii/S0924796302001963.

Richard H Moss, Jae A Edmonds, Kathy A Hibbard, Martin R Manning, Steven K Rose, Detlef P Van Vuuren, Timothy R Carter, Seita Emori, Mikiko Kainuma, Tom Kram, et al. The next generation of scenarios for climate change research and assessment. *Nature*, 463(7282):747–756, 2010.

David M. Nelson and Walker O. Smith. Sverdrup revisited: Critical depths, maximum chlorophyl levels, and the control of southern ocean productivit by the irradiance-mixing regime. 1991.

Atsushi Obata, Joji Ishizaka, and Masahiro Endoh. Global verification of critical depth theory for phytoplankton bloom with climatological in situ temperature and satellite ocean color data. *Journal of Geophysical Research*, 101(C9):20657, 1996. ISSN 0148-0227. doi: 10.1029/96JC01734. URL http://www.agu.org/pubs/crossref/1996/96JC01734.shtml.

Y.-H. Park, E. Charriaud, D.Ruiz Pino, and C. Jeandel. Seasonal and interannual variability of the mixed layer properties and steric height at station KERFIX, southwest of kerguelen. *Journal of Marine Systems*, 17(1–4):571–586, November 1998. ISSN 0924-7963. doi: 10.1016/S0924-7963(98)00065-7. URL http://www.sciencedirect.com/science/article/pii/S0924796398000657.

Raymond Pollard, Richard Sanders, Mike Lucas, and Peter Statham. The crozet natural iron bloom and export experiment (CROZEX). *Deep Sea Research Part II: Topical Studies in Oceanography*, 54(18–20):1905–1914, September 2007. ISSN 0967-0645. doi: 10.1016/j.dsr2.2007.07.023. URL http://www.sciencedirect.com/science/article/pii/S0967064507001452.

A.C. Redfield. On the proportions of organic derivations in sea water and their relation to the composition of plankton. in james johnstone memorial volume. (ed. r.j. daniel). university press of liverpool. 1934.

G.A. Riley. The relationship of vertical turbulence and spring diatom flowerings. *J. Mar. Res.*, 1942.

S. R. Rintoul. Antarctic circumpolar current. In John H. Steele, editor, *Encyclopedia of Ocean Sciences (Second Edition)*, pages 178–190. Academic Press, Oxford, 2009. ISBN 978-0-12-374473-9. URL http://www.sciencedirect.com/science/article/pii/B9780123744739006032.

S.R. Rintoul, M. Sparrow, M.P. Meredith, V. Wadley, K. Speer, E. Hofmann, C. Summerhayes, E. Urban, and R. Bellerby. The southern ocean observing system. 2010.

J. B. Sallée, Kevin Speer, R. Morrow, and Rick Lumpkin. An estimate of lagrangian eddy statistics and diffusion in the mixed layer of the southern ocean. *Journal of Marine Research*, 66(4):441–463, 2008. URL http://www.ingentaconnect.com/content/jmr/jmr/2008/00000066/00000004/art00002.

J. B. Sallée, K. G. Speer, and S. R. Rintoul. Zonally asymmetric response of the southern ocean. 2010a.

J.-B. Sallée, E. Shuckburgh, N. Bruneau, A. J. S. Meijers, T. J. Bracegirdle, and Z. Wang. Assessment of southern ocean mixed-layer depths in CMIP5 models: Historical bias and forcing response. *Journal of Geophysical Research: Oceans*, 118(4):1845–1862, April 2013. ISSN 21699275. doi: 10.1002/jgrc.20157. URL http://doi.wiley.com/10.1002/jgrc.20157.

Jean-Baptiste Sallée, Nicolas Wienders, Kevin Speer, and Rosemary Morrow. Formation of subantarctic mode water in the southeastern indian ocean. *Ocean Dynamics*, 56(5-6):525–542, February 2006. ISSN 1616-7341, 1616-7228. doi: 10.1007/s10236-005-0054-x. URL http://www.springerlink.com/index/10.1007/s10236-005-0054-x.

Jean-Baptiste Sallée, Kevin Speer, Steve Rintoul, and S. Wijffels. Southern ocean thermocline ventilation. *Journal of Physical Oceanography*, 40(3):509–529, March 2010b. ISSN 0022-3670, 1520-0485. doi: 10.1175/2009JPO4291.1. URL http://journals.ametsoc.org/doi/abs/10.1175/2009JPO4291.1.

M. R. P. Sapiano, C. W. Brown, S. Schollaert Uz, and M. Vargas. Establishing a global climatology of marine phytoplankton phenological characteristics. *J. Geophys. Res.*, 117 (C8):C08026, August 2012. ISSN 0148-0227. doi: 10.1029/2012JC007958. URL http://www.agu.org/pubs/crossref/2012/2012JC007958.shtml.

J. L. Sarmiento, N. Gruber, M. A. Brzezinski, and J. P. Dunne. High-latitude controls of thermocline nutrients and low latitude biological productivity. *Nature*, 427(6969):56–60, January 2004. ISSN 0028-0836. doi: 10.1038/nature02127. URL http://www.nature.com/nature/journal/v427/n6969/full/nature02127.html.

Jorge Louis Sarmiento and Nicolas Gruber. *Ocean biogeochemical dynamics*. Princeton University Press, Princeton, N.J., 2006. ISBN 0691017077 9780691017075. URL http://press.princeton.edu/titles/8223.html.

Alexander Sen Gupta, Agus Santoso, Andréa S. Taschetto, Caroline C. Ummenhofer, Jessica Trevena, and Matthew H. England. Projected changes to the southern hemisphere ocean and sea ice in the IPCC AR4 climate models. *Journal of Climate*, 22(11):3047–3078, June 2009. ISSN 0894-8755, 1520-0442. doi: 10.1175/2008JCLI2827.1. URL http://journals.ametsoc.org/doi/abs/10.1175/2008JCLI2827.1.

Jonathan Sharples, Oliver N. Ross, Beth E. Scott, Simon P.R. Greenstreet, and Helen Fraser. Inter-annual variability in the timing of stratification and the spring bloom in the north-western north sea. *Continental Shelf Research*, 26(6):733–751, April 2006. ISSN 0278-4343. doi: 10.1016/j.csr.2006.01.011. URL http://www.sciencedirect.com/science/article/pii/S0278434306000392.

D. A. Siegel. The north atlantic spring phytoplankton bloom and sverdrup's critical depth hypothesis. *Science*, 296(5568):730–733, April 2002. ISSN 00368075, 10959203. doi: 10.1126/science.1069174. URL http://www.sciencemag.org/cgi/doi/10.1126/science.1069174.

Serguei Sokolov and Stephen R. Rintoul. On the relationship between fronts of the antarctic circumpolar current and surface chlorophyll concentrations in the southern ocean. *Journal of Geophysical Research*, 112(C7), July 2007. ISSN 0148-0227. doi: 10.1029/2006JC004072. URL http://www.agu.org/pubs/crossref/2007/2006JC004072.shtml.

H. U. Sverdrup. On conditions for the vernal blooming of phytoplankton. *Journal du Conseil*, 18(3):287–295, 1953. URL http://icesjms.oxfordjournals.org/content/18/3/287.full.pdf.

S. Swart, S.J. Thomalla, and P.M.S. Monteiro. The seasonal cycle of mixed layer dynamics and phytoplankton biomass in the sub-antarctic zone: a high-resolution glider experiment. *Journal of Marine Systems*, June 2014. ISSN 09247963. doi: 10.1016/j.jmarsys.2014.06.002. URL http://linkinghub.elsevier.com/retrieve/pii/S0924796314001535.

Mimi Szeto, PJ Werdell, TS Moore, and JW Campbell. Are the world's oceans optically different? *Journal of Geophysical Research: Oceans (1978–2012)*, 116(C7), 2011.

A. Tagliabue, T. Mtshali, O. Aumont, A. R. Bowie, M. B. Klunder, A. N. Roychoudhury, and S. Swart. A global compilation of over 13 000 dissolved iron measurements: focus on distributions and processes in the southern ocean. *Biogeosciences Discussions*, 8(6):11489–11527, November 2011. ISSN 1810-6285. doi: 10.5194/bgd-8-11489-2011. URL http://www.biogeosciences-discuss.net/8/11489/2011/.

Alessandro Tagliabue, Olivier Aumont, and Laurent Bopp. The impact of different external sources of iron on the global carbon cycle. *Geophysical Research Letters*, pages n/a–n/a, 2014a. ISSN 1944-8007. doi: 10.1002/2013GL059059. URL http://onlinelibrary.wiley.com/doi/10.1002/2013GL059059/abstract.

Alessandro Tagliabue, Jean-Baptiste Sallée, Andrew R. Bowie, Marina Lévy, Sebastiaan Swart, and Philip W. Boyd. Surface-water iron supplies in the southern ocean sustained by deep winter mixing. *Nature Geoscience*, 7(4):314–320, March 2014b. ISSN 1752-0894, 1752-0908. doi: 10.1038/ngeo2101. URL http://www.nature.com/doifinder/10.1038/ngeo2101.

John R. Taylor and Raffaele Ferrari. Shutdown of turbulent convection as a new criterion for the onset of spring phytoplankton blooms. *Limnology and Oceanography*, 56(6):2293–2307, 2011. ISSN 00243590. doi: 10.4319/lo.2011.56.6.2293. URL http://www.aslo.org/lo/toc/vol_56/issue_6/2293.html.

Karl E. Taylor, Ronald J. Stouffer, and Gerald A. Meehl. An overview of CMIP5 and the experiment design. *Bulletin of the American Meteorological Society*, 93(4):485–498, April 2012. ISSN

0003-0007, 1520-0477. doi: 10.1175/BAMS-D-11-00094.1. URL http://journals.ametsoc.org/doi/abs/10.1175/BAMS-D-11-00094.1.

S. J. Thomalla, N. Fauchereau, S. Swart, and P. M. S. Monteiro. Regional scale characteristics of the seasonal cycle of chlorophyll in the southern ocean. *Biogeosciences*, 8(10): 2849–2866, October 2011. ISSN 1726-4189. doi: 10.5194/bg-8-2849-2011. URL http://www.biogeosciences.net/8/2849/2011/.

David W. J. Thompson, Susan Solomon, Paul J. Kushner, Matthew H. England, Kevin M. Grise, and David J. Karoly. Signatures of the antarctic ozone hole in southern hemisphere surface climate change. *Nature Geoscience*, 4(11):741–749, October 2011. ISSN 1752-0894, 1752-0908. doi: 10.1038/ngeo1296. URL http://www.nature.com/doifinder/10.1038/ngeo1296.

David W. Townsend, Maureen D. Keller, Michael E. Sieracki, and Steven G. Ackleson. Spring phytoplankton blooms in the absence of vertical water column stratification. *Nature*, 360(6399): 59–62, November 1992. ISSN 0028-0836. doi: 10.1038/360059a0. URL http://www.nature.com/doifinder/10.1038/360059a0.

Detlef P. van Vuuren, Jae Edmonds, Mikiko Kainuma, Keywan Riahi, Allison Thomson, Kathy Hibbard, George C. Hurtt, Tom Kram, Volker Krey, Jean-Francois Lamarque, Toshihiko Masui, Malte Meinshausen, Nebojsa Nakicenovic, Steven J. Smith, and Steven K. Rose. The representative concentration pathways: an overview. *Climatic Change*, 109(1-2):5–31, November 2011. ISSN 0165-0009, 1573-1480. doi: 10.1007/s10584-011-0148-z. URL http://link.springer.com/10.1007/s10584-011-0148-z.

Martin Vancoppenolle, Laurent Bopp, Gurvan Madec, John Dunne, Tatiana Ilyina, Paul R. Halloran, and Nadja Steiner. Future arctic ocean primary productivity from CMIP5 simulations: Uncertain outcome, but consistent mechanisms. *Global Biogeochem. Cycles*, 27 (3):605–619, September 2013. ISSN 1944-9224. doi: 10.1002/gbc.20055. URL http://onlinelibrary.wiley.com/doi/10.1002/gbc.20055/abstract.

H.J. Venables, R.T. Pollard, and E.E. Popova. Physical conditions controlling the development of a regular phytoplankton bloom north of the crozet plateau, southern ocean. *Deep Sea Research Part II: Topical Studies in Oceanography*, 54(18):1949–1965, 2007.

Joanna J. Waniek. The role of physical forcing in initiation of spring blooms in the northeast atlantic. *Journal of Marine Systems*, 39(1–2):57–82, February 2003. ISSN 0924-7963. doi: 10.1016/S0924-7963(02)00248-8. URL http://www.sciencedirect.com/science/article/pii/S0924796302002488.

Ben Weeding and Thomas W. Trull. Hourly oxygen and total gas tension measurements at the southern ocean time series site reveal winter ventilation and spring net community

production. *Journal of Geophysical Research: Oceans*, pages n/a–n/a, 2013. ISSN 2169-9291. doi: 10.1002/2013JC009302. URL http://onlinelibrary.wiley.com/doi/10.1002/2013JC009302/abstract.